DEVELOPMENT OF A CFD-BASED MODEL FOR THE SIMULATION OF IMMOBILIZED PHOTOCATALYTIC REACTORS FOR WATER TREATMENT

by

José Esteban Durán Herrera

M.Sc. (Hons), Universidad de Costa Rica, 2005

A THESIS SUBMITTED IN PARTIAL FULFILLMENT OF
THE REQUIREMENTS FOR THE DEGREE OF

DOCTOR OF PHILOSOPHY

in

The Faculty of Graduate Studies

(Chemical and Biological Engineering)

THE UNIVERSITY OF BRITISH COLUMBIA
(Vancouver)

August 2010

© José Esteban Durán Herrera, 2010

ABSTRACT

A computational fluid dynamics (CFD) model for the simulation of immobilized photocatalytic reactors for water treatment was developed and evaluated experimentally. The model integrated hydrodynamics, species mass transport, chemical reaction kinetics, and irradiance distribution within the reactor. For the development of this integrated CFD model, each of the above phenomena was individually evaluated against experimental data and proper models were identified. The experimental evaluation was performed using various configurations of annular reactors and UV lamp sizes, over a wide range of hydrodynamic conditions ($350<Re<11,000$).

The comparison of modeling and experimental data indicated that the developed CFD model was able to successfully predict the photocatalytic degradation rate of model pollutants (benzoic acid and 2,4-D) in the analyzed reactors. In terms of hydrodynamic models, the results demonstrated that the laminar model performed well for systems under laminar flow conditions (error < 8%), whereas the Abe-Kondoh-Nagano (AKN) low Reynolds number (error < 12%) and the Reynolds stress (RSM) (error < 19%) turbulence models gave accurate predictions of the coated photoreactor performances under transitional or turbulent flow regimes. The degradation prediction capability of the CFD model was largely determined by the external mass transfer prediction performance of the hydrodynamic models utilized.

The developed radiation field model included the lamp within the computational domain allowing to incorporate important interactions between the UV radiation, the quartz walls, and the Hg vapour inside the lamp. A modification of the extensive source volumetric lamp emission model that incorporates the high photon absorbance/re-emission effect produced by the Hg vapour in the lamp (ESVERA model) showed excellent agreement with near- and far-field experimental data.

An effective optimization design approach which combines CFD modeling and the Taguchi design of experiments (DOE) method was presented for annular reactors with repeated ribs as external mass transfer promoters. The statistical analysis showed that the reactor performance was improved using small outer tube diameters, large inner/outer tube diameter ratios, intermediate (rib height)/(hydraulic diameter) ratio, and small (rib pitch)/(rib height) ratios. Moreover, the (rib height)/(hydraulic diameter) ratio was the design parameter having the greatest impact (57%) on photoreactor performance.

TABLE OF CONTENTS

LIST OF TABLES

LIST OF FIGURES

NOMENCLATURE

a	annulus diameter ratio, d_1/d_2
A	area, m^2
C	molar concentration, mol m^{-3}
Co	contribution ratio
d	diameter, m
Da	Damköhler number
D_m	molecular diffusivity of species i in the mixture, m^2 s^{-1}
D_t	eddy (or turbulent) diffusivity for species concentration, m^2 s^{-1}
e	rib height, m
E	radiation irradiance (photon flux), W m^{-2}
E_{ex}	external effectiveness factor
ESDE	extensive source superficial diffuse emission model (refer to Table 4.1)
ESVE	extensive source volumetric emission model (refer to Table 4.1)
ESVEA	modified ESVE model that accounts for photon absorption/re-emission in the lamp plasma
ESVERA	modified ESVEA model that accounts for radiation reflection, refraction and absorption at the lamp quartz envelope
ESDER	modified ESDE model that accounts for radiation reflection, refraction and absorption at the lamp quartz envelope
ESVER	modified ESVE model that accounts for radiation reflection, refraction and absorption at the lamp quartz envelope
F	design parameter

G	fluence rate, W m^{-2}
h	local mass transfer coefficient, m s^{-1}
h_m	average mass transfer coefficient, m s^{-1}
H	lamp arc length, m
I	unit tensor
j^e	emission (source) term, W m^{-3} sr^{-1}
J_i	diffusive flux of species i, kg s^{-1} m^{-2}
k	first order reaction rate constant, s^{-1}
k''	first-order surface reaction rate constant, m s^{-1}
k_c	mass transfer coefficient, m s^{-1}
k_1	adsorption rate constant, s^{-1}
k_{-1}	desorption rate constant, mol m^{-3} s^{-1}
k_2	surface reaction rate constant, mol m^{-3} s^{-1}
K	calibration factor, m^2
K_{ads}	adsorption equilibrium constant, m^3 mol^{-1}
K_{ads}^{app}	apparent adsorption equilibrium constant, m^3 mol^{-1}
l	mass transfer section length, m
L	photon radiance, W m^{-2} sr^{-1}
LSDE	line source diffuse emission model (refer to Table 4.1)
LSDER	modified LSDE model that accounts for radiation reflection, refraction and absorption at the lamp quartz envelope
LSSE	line source spherical emission model (refer to Table 4.1)
LSSS	line source spherical sources model (refer to Table 4.1)
m_i	mass fraction of species i

m'_i	fluctuating mass fraction of species *i*
M_W	molar weight, kg $kmol^{-1}$
MPSS	multiple point source summation model (refer to Table 4.1)
MSSS	multiple segment source summation model (refer to Table 4.1)
n	refractive index
$\hat{n}$	unit vector normal to the surface
N	total number of species
p	phase function for the in-scattering of photons
P	pressure, Pa
ΔP	pressure drop, Pa
Q	flow rate, $m^3\ s^{-1}$
r	volumetric reaction rate, mol $m^{-3}\ s^{-1}$
r''	surface reaction rate, mol $m^{-2}\ s^{-1}$
$\vec{r}$	position vector, m
R	distance from center of lamp to the detector, m
Re	Reynolds number, $\rho U d_e/\mu$
Re_y	wall-distance-based turbulent Reynolds number
R_i^S	surface rate of production/depletion of species *i*, kg $s^{-1}\ m^{-2}$
s	path length, m
$\vec{s}$	propagation direction vector, m
$\vec{s}'$	scattering direction vector, m
S	signal (response) function
Sc	Schmidt number

Sc_t	turbulent Schmidt number
Sh_{av}	Sherwood number based on the average mass transfer coefficient, $k_c d_e/D_m$
t	time, s
T	absolute temperature of the medium, K
TI	turbulence intensity
u	fluctuating flow velocity, m s^{-1}
U	velocity, m s^{-1}
V	volume, m^3
w	irradiated window width, m
W	power output of the lamp, W
x	axial position, m
X	nondimensional axial position, $4x(1-a)/(\mathrm{Re}\ d_2)$
X_S	reactant conversion per pass
y	normal distance from the lamp center , m
y^+	nondimensional distance from the wall
Z_i	range of parameter i
Z_{total}	total range

Greek symbols

α	reaction rate constant, $m^3\ W^{-1}\ s^{-1}$
β	half angle subtended by the lamp at the sensor position, rad
γ	power constant
ε	angle from the normal axis of the lamp, rad
θ	residence time, s

κ	absorption coefficient, m^{-1}
μ	molecular viscosity, $m^2\ s^{-1}$
μ_t	turbulent viscosity, $m^2\ s^{-1}$
ξ	surface coverage
π	distance between repeated ribs, m
ρ	density, $kg\ m^{-3}$
σ	scattering coefficient, m^{-1}
$\sigma_{S\text{-}B}$	Stefan-Boltzmann constant, $5.672\times10^{-8}\ W\ m^{-2}\ K^{-4}$
τ	viscous stress tensor, $N\ m^{-2}$
ϕ	function defined as $[(1-a)/a]\ [1/2-(a^2/(1-a^2))\ \ln(1/a)]\ /\ [((1+a^2)/(1-a^2))\ \ln(1/a) - 1]$
Φ	quantum yield, mol $einstein^{-1}$
Ω	solid angle about the propagation direction, sr
$\hat{\Omega}$	unit vector in the direction of propagation
Ω'	solid angle about the scattering direction vector $\vec{s}'$, sr

Subscripts

0	initial condition ($t = 0$)
1	inner annular cylinder
2	outer annular cylinder
a	adjacent to the wall
air	refers to the lamp running in air
app	apparent
b	bulk value

B	bulk fluid phase
BA	benzoic acid
cat	catalyst
e	equivalent or hydraulic
eff	effective
Fe^{2+}	ferrous ion
HP	hydrogen peroxide
i	inlet condition
M	Refers to the mixed tank
o	outlet condition
overall	overall (catalyst + system)
reactor	refers to the lamp running inside the annular reactor
R	reactor
sat	saturation condition
sys	system
S	catalyst surface
T	total amount of liquid solution
window	refers to the irradiated window
x	along the axial position

ACKNOWLEDGEMENTS

I would like to express my sincere gratitude to my supervisors, Dr. Fariborz Taghipour and Dr. Madjid Mohseni, for their continuous guidance, support, encouragement, and valuable feed-back throughout this research work.

I also thank Dr. Kevin Smith and Dr. Tom Troczynski for serving on my Ph.D. committee, and Dr. Naoko Ellis and Dr. Eric Hall for agreeing to be examiners in the final dissertation defence. Thanks to all of them for their valuable comments.

I would like to give special thanks to all my fellow researchers, particularly to Gustavo Imoberdorf, Adrián Vega, Siva Sarathy, Daniel Medeiros, Clara Gómez, Mehdi Bazri, and Sona Kazemi who offered countless hours of assistance and companionship during my time at UBC.

I am deeply grateful to my parents (Lilliana and Enrique) and family (Mao, Jess, Ary, Naty, Sofy, Cris, Tita, Andy and Faby) for their love, thrust, and continuous support.

Finally, I would like to acknowledge the support received from the Natural Sciences and Engineering Research Council of Canada (NSERC), UBC University Graduate Fellowship, BI PureWater (Canada) Inc., and Universidad de Costa Rica.

DEDICATION

To my parents, Lilliana & Enrique

CO-AUTHORSHIP STATEMENT

All manuscript based chapters of this thesis were co-authored with research supervisors Dr. Madjid Mohseni and Dr. Fariborz Taghipour. My contribution was the conduction of the CFD simulations, the collection and the analysis of experimental data and the writing of the manuscripts. Dr. Madjid Mohseni and Dr. Fariborz Taghipour largely contributed to the development of experimental plans, the discussion of results, and the revision of the manuscript drafts.

1. INTRODUCTION

The contamination of drinking water sources with harmful organic substances has been recognized as a major problem worldwide. Among many contaminants, pesticides, pharmaceuticals, and personal care products are now frequently found in water resources and outflows from sewage treatment plants (Boyd et al., 2003; Jasim et al., 2006; Kolpin et al., 2002; Na et al., 2006; Pasternak, 2006; Ternes, 1998). The removal of these contaminants using conventional water treatment processes has shown to be very difficult; therefore, an increasing number of new treatment technologies is being developed and evaluated. One such group of technologies is advanced oxidation processes (AOPs) (Oppenländer, 2004; Poyatos et al., 2009). Through a high yield of hydroxyl radicals (•OH) and other reactive species, AOPs can offer significant removal of such contaminants.

A particularly emerging and promising AOP for air and water purification is heterogeneous photocatalysis (Herrmann, 2005; Hoffmann et al., 1995; Ollis & Turchi, 1990). More than 1200 different organic pollutants have been reported as degraded using this technology (Adesina, 2004). Photocatalytic processes involve the use of nano-structured photocatalyst materials, predominantly titanium dioxide (TiO_2), activated by ultraviolet (UV) irradiation. In the TiO_2 particles, the absorbed UV photons generate energetic electron-hole pairs which interact with the surrounding medium inducing redox reactions that result in the decomposition of the contaminants. One of the main appeals of this technology lies in its capability to potentially mineralize the pollutants into harmless compounds (carbon dioxide, water and mineral acids) without producing any other waste streams (Ollis et al., 1991), this is in addition to the inactivation of pathogens including protozoa and viruses.

Two major configurations of photocatalytic reactors have been employed in photodegradation studies: those with the photocatalyst particles suspended (slurry reactors); and those with the catalyst immobilized in layers to a reactor surface (immobilized reactors) (de Lasa et al., 2005; Hoffmann et al., 1995). The slurry reactors are efficient due to the large surface area of catalyst available for the reaction and the efficient mass transfer within such systems; however, the need for a post-process separation of the nano-size semiconductor particles from the fluid adds to the complexity of the overall treatment process and decreases the economic viability and commercialization of slurry reactors. On the other hand, supported catalyst configurations eliminate the need for photocatalyst recovery, but some limitations such as low surface area-to-volume ratios and significant influence of external mass transfer lessen the efficiency of such treatment systems. Nevertheless, many authors agree that the immobilized catalyst configuration is a promising alternative for an efficient reactor scalable to industrial sizes (Dijkstra et al., 2002; Krýsa et al., 2006; McMurray et al., 2004; Mehrotra et al., 2005).

Despite the many advantages of photocatalysis and the extensive laboratory research done in this field, there are still some factors that stymie the development of large scale photocatalytic oxidation reactors for water treatment. Lack of proper models and simulation tools for predicting and analyzing the performance of full-scale systems, and therefore lack of adequate scale-up strategies, is among the key factors hindering the development of commercial water treatment systems utilizing this technology (Adesina, 2004; Mukherjee & Ray, 1999). An effectual approach to this issue is the application of computational fluid dynamics (CFD), which has extensively demonstrated to be a very effective tool in the design, optimization and scaling-up of reacting systems (Kuipers & van Swaaij, 1998; Ranade, 2002). Through simultaneous modeling of hydrodynamics, species mass transport, chemical reaction

kinetics, and photon flux distribution, CFD allows for comprehensive analysis of photocatalytic reactor performance by providing the local values of the parameters of interest (i.e., fluid velocity, pollutant concentration, reaction rate, UV irradiance, etc.). In addition, applying CFD analysis to scaled-up reactors minimizes experimental effort and fabrication costs at the pilot-scale level (Adesina, 2004).

Although CFD modeling has extensively demonstrated to be a very effective tool in the analysis and design of reacting systems, little research has focused on its application to photocatalytic water treatment. The modeling of immobilized photocatalytic reactors used for water treatment is a complicated task. The complex interactions among transport processes, reaction kinetics, and radiation propagation require proper definition and incorporation of appropriate turbulence models for the hydrodynamics and mass transfer, UV radiation field model, and the kinetics of the surface reactions in the photoreactor. In particular, near-wall modeling needs special attention as the thickness of the mass transfer boundary layer in liquid systems (where $Sc \approx 1000$) is just a few micrometers.

The primary objective of this thesis was to develop and evaluate experimentally a CFD-based model for the simulation of photocatalytic reactors, comprising of nano-size TiO_2 coated surfaces, used for water treatment. The computational model integrates hydrodynamics, species mass transport, chemical reaction kinetics, and irradiance distribution within the reactor. Each of these aspects were individually analyzed and experimentally evaluated over a wide range of conditions to guarantee its applicability. Since the annular reactor geometry is considered to be perhaps the simplest and most efficient configuration for photocatalytic applications using artificial radiation sources (Romero et al., 2003), and besides it is the most commonly found commercial photoreactor geometry, this reactor configuration was selected as model geometry in the investigation.

The developed CFD-model is a valuable tool for the design, scale-up, and optimization of heterogeneous immobilized photocatalytic reactors, and is an important contribution towards the implementation of large-scale commercial treatment systems.

1.1. Photocatalysis on TiO_2 surfaces

1.1.1. Photocatalysis as a remediation technology

The discovery of Fujishima & Honda (1972) of the photocatalytic splitting of water on UV-illuminated TiO_2 electrodes is considered to be the genesis of current research and development activities on the application of photocatalysis for environmentally friendly technologies (Adesina, 2004). The applications began as photoelectrochemical solar energy conversion technologies and then, after the experiments of Frank & Bard (1977) of the oxidation of cyanide ion in aqueous solutions using UV-illuminated TiO_2 suspensions, they shifted into technologies of environmental cleanup of polluted air, water and soil (Fujishima & Zhang, 2006). Since that time, more than 1200 different organic pollutants have been reported as degraded using TiO_2 photocatalysis (Adesina, 2004).

Much of the interest in TiO_2 photocatalysis is due to the many advantages it has over traditional water and air treatment technologies; one such advantage being the fact that organic pollutants can be potentially degraded to carbon dioxide, water and mineral acids (Ollis et al., 1991). Reaction equation (1.1) summarizes the mineralization process produced by the TiO_2 photocatalytic oxidation of organic compounds.

$$Organic\ \ compound + O_2 + h\nu \xrightarrow{TiO_2} CO_2 + H_2O + \text{mineral acids} \qquad (1.1)$$

Some other advantages of this technology are: mild reaction conditions and modest reaction times; lesser chemical input requirement; minimal secondary waste generation; and capacity for using renewable and pollution-free solar energy (Kabra et al., 2004).

The photocatalytic phenomenon is not exclusive to TiO_2. Other semiconductors such as ZnO, CdS and ZnS show organic compound degradation under UV irradiation. Nevertheless, it has been extensively demonstrated that TiO_2 is the most advantageous of all because it shows higher efficiencies, is chemically and biologically inert, photostable, non-toxic, cheap and commercially available (Herrmann, 2005; Hoffmann et al., 1995; Mills et al., 1993; Oppenländer, 2004).

Some of the main applications of photocatalysis investigated are: color removal and the destruction of dyes; reduction of COD (chemical oxygen demand); mineralization of hazardous organics; destruction of hazardous inorganics such as cyanides; treatment of heavy metals; degradation of harmful fungicides, herbicides, and pesticides; purification and disinfection of water; destruction of malodorous compounds; decontamination of soil; purification and decontamination of indoor air; and destruction of cancer cells and viruses (Kabra et al., 2004). More recently, some applications in the area of self-cleaning surfaces and photoinduced superhydrophilicity have also been under investigation (Fujishima et al., 2000; Thompson & Yates, 2006).

1.1.2. Mechanism of photocatalysis

In semiconductors, the electrons (e^-) are confined to energy bands (valence band and conduction band). Electrons cannot have any values of energy that lie outside these bands. This forbidden region, which separates both bands, is called the energy band gap of the material. If the semiconductor is irradiated with photons with energy equal or greater than the

energy band gap, electrons can absorb this energy and be promoted from the valence band to the conduction band. As the latter process occurs, electron vacancies or positive charges called holes (h^+) are generated in the valence band (Mills et al., 1993). In the case of TiO_2, which has a band gap of 3.2 eV, the photons should have a wave length shorter than approximately 388 nm to generate an $e^- – h^+$ pair (Mills & Hunte, 1997).

In heterogeneous photocatalysis of organic and inorganic compounds by semiconductors, the initial process is precisely the generation of electron-hole pairs in the semiconductor particles (Linsebigler et al., 1995). Although the lifetime of an $e^–h^+$ pair is a few nanoseconds before it spontaneously recombines (Hoffmann et al., 1995), it is still long enough to alternatively migrate to the surface of the particle and promote redox reactions in the fluid phase that is in contact with it. A simplified scheme of the physical and chemical processes that take place in a TiO_2 particle during photocatalysis is presented in Fig. 1.1.

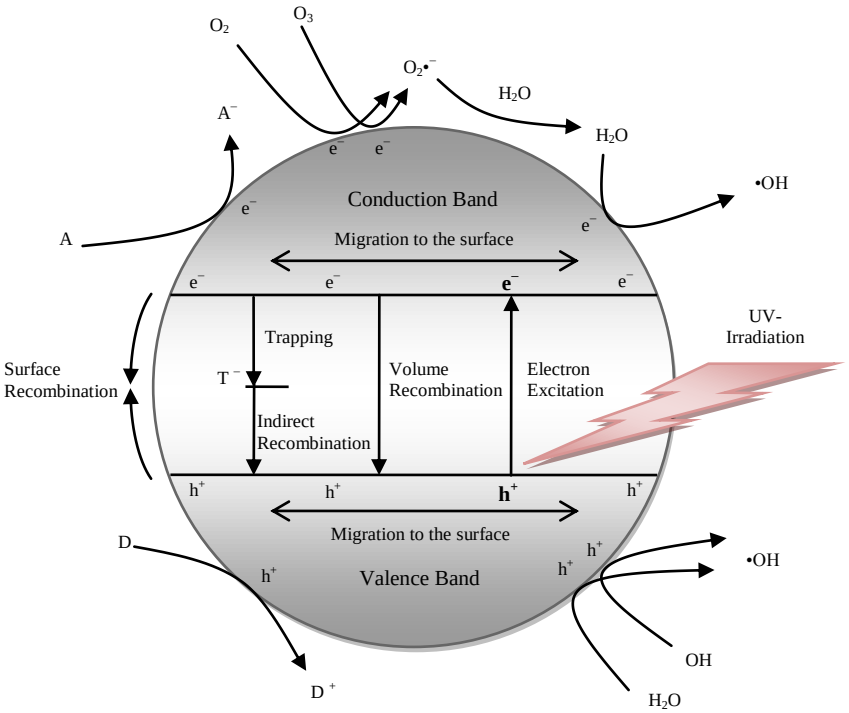

Fig. 1.1. Schematic illustration of the mechanism of photocatalysis in a TiO_2 particle.

Table 1.1. Main reactions occurring during the photocatalytic degradation of formic acid (Dijkstra et al., 2002)

Process	Reaction	
Excitation	$TiO_2 + h\nu \rightarrow e^- + h^+$	(R1)
Trapping	$e^- + O_{2,ads} \leftrightarrow \bullet O^-_{2,ads}$	(R2)
	$e^- + T \leftrightarrow T^-$	(R3)
	$h^+ + OH^-_{ads} \leftrightarrow \bullet OH_{ads}$	(R4)
	$h^+ + H_2O_{ads} \leftrightarrow \bullet OH_{ads} + H^+$	(R5)
Recombination		
(direct)	$e^- + h^+ \rightarrow$ heat	(R6)
(indirect)	$e^- + T \leftrightarrow T^-$	(R7a)
	$h^+ + T^- \rightarrow T$	(R7b)
Reaction	$\bullet OH_{ads} + HCOOH_{ads} \rightarrow HCOO\bullet + H_2O$	(R8)
	$h^+ + HCOOH \leftrightarrow HCOO\bullet + H^+$	(R9)
	$HCOO\bullet + O_2 \rightarrow CO_2 + H^+ + \bullet O^-_2$	(R10)
Radical reactions	$\bullet O^-_2 + H^+ \rightarrow HO_2\bullet$	(R11)
	$HO_2\bullet + e^- \rightarrow HO^-_2$	(R12)
	$HO^-_2 + H^+ \rightarrow H_2O_2$	(R13)
	$2\ HO_2\bullet \rightarrow H_2O_2 + O_2$	(R14)
	$\bullet O^-_2 + HO_2\bullet \rightarrow O_2 + HO^-_2$	(R15)
	$H_2O_2 + e^- \rightarrow \bullet OH + OH^-$	(R16)
	$H_2O_2 + \bullet OH \rightarrow H_2O + HO_2\bullet$	(R17)
	$2\ \bullet OH \rightarrow H_2O_2$	(R18)
Adsorption	$site_{O2} + O_2 \leftrightarrow O_{2,ads}$	(R19)
	$site_{FA} + HCOOH_{ads} \leftrightarrow HCOOH_{ads}$	(R20)

Table 1.1 exemplifies the main reactions occurring during the photocatalytic degradation of formic acid (Dijkstra et al., 2002) and they are described as follows. To prevent the recombination of the charge carriers, the electrons and holes have to be trapped. The electrons can be trapped by molecular oxygen (or any other electron acceptor *A*) present in the water, thus forming superoxide radicals (R2). Surface defect states can also trap electrons (R3). The holes can be trapped by hydroxide ions or water adsorbed at the semiconductor surface forming hydroxyl radicals (R4 and R5). If the electrons and holes are not trapped, they will recombine and the energy will be lost as heat. Recombination can occur either directly (R6) or indirectly via a trap T (R7). In titanium dioxide, the recombination will mainly proceed via indirect recombination. The hydroxyl radicals are reported to be the main

reactants in the degradation of pollutants (R8), but the photogenerated holes can also attack the pollutants (electron donator *D*) directly (R9). Hydroxyl radicals are formed both by holes via reaction (R5) and by electrons via the superoxide radical, $O^{-}_{2}\bullet$, which via various radical reactions (R11)–(R15) can lead to the formation of a hydroxyl radical from hydrogen peroxide (R16).

1.1.3. Kinetics of liquid phase photocatalyzed reactions

Analyses of liquid-phase kinetics for suspended or immobilized photocatalytic systems relied for many years on the Langmuir-Hinshelwood (L-H) kinetic model to interpret the experimental observations. This kinetic model, in its simplest form, assumes one relatively rapid reaction achieving adsorption equilibrium, followed by a single, slow surface reaction step (rate determining step) (Emeline et al., 2005; Ollis, 2005). The following equations describe the mechanism:

$$A_{liq} \underset{k_{-1}}{\overset{k_1}{\rightleftarrows}} A_{ads} \tag{1.2}$$

$$A_{ads} \xrightarrow[slow]{k_2} Products \tag{1.3}$$

where *A* represents the reacting specie in bulk solution (*liq*) or adsorbed on the catalyst surface (*ads*), k_1 and k_{-1} are the adsorption and desorption rate constants, respectively, and k_2 is the surface reaction rate constant. The L-H adsorption model assumes that (i) at equilibrium, the number of surface adsorption sites is fixed; (ii) only one substrate may bind at each surface site; (iii) the heat of adsorption by the substrate is identical for each site and is independent of surface coverage; (iv) there is no interaction between adjacent adsorbed molecules; (v) the rate of surface adsorption of the substrate is greater than the rate of any subsequent chemical

reactions; and (vi) no irreversible blocking of active sites by binding to product occurs (Fox & Dulay, 1995). Under these assumptions, the surface coverage ξ is related to the concentration of the substrate C, and to the adsorption equilibrium constant $K_{ads} = k_1/k_{-1}$ by:

$$\xi = \frac{K_{ads}C}{1 + K_{ads}C} \tag{1.4}$$

and the reaction rate would be

$$-r = k_2\xi = \frac{k_2 K_{ads}C}{1 + K_{ads}C} \tag{1.5}$$

where k_2 is expected to be dependent on the photon flux (E) incident over the TiO_2 surface. Nevertheless, during the last decade, some key experiments have brought evidence that this mechanism is not consistent with the obtained results (Emeline et al., 2005; Ollis, 2005). Some of the flaws of the L-H kinetic model analyzed by Ollis (2005) are: (i) while adsorption isotherm and reaction rate may each follow the same analytic form, i.e., a saturation function of the Langmuir adsorption isotherm form, the dark adsorption equilibrium constant K_{ads} is not found to be the same as the apparent adsorption constant (K_{ads}^{app}) in the rate equation; (ii) some reactions and adsorption systems have different analytic forms; (iii) the L-H parameters k and K_{ads}^{app} collected from nine different studies of phenol and 4-chlorophenol have positive correlations; (iv) several recent papers that explored the influence of reactant concentration and photon flux in the same photocatalyzed reaction, found out that both the rate constant k and the apparent binding constant K_{ads}^{app} depends on photon flux.

Based on the preceding facts, Ollis (2005) in his recent "illuminating" approach, proposed a new simple model; it can be described with the same Eqs. (1.2) and (1.3), but instead of assuming equilibrated adsorption of reactants and, correspondingly, a slow, rate-

controlling surface step, it assumes a pseudo-steady-state hypothesis to the surface coverage ($d\xi/dt = 0$). Under these assumptions, the reaction rate expression is:

$$-r = \frac{k_2 K_{ads}^{app} C}{1 + K_{ads}^{app} C} \tag{1.6}$$

where

$$K_{ads}^{app} = \frac{k_1}{k_{-1} + k_2} \tag{1.7}$$

As it can be easily identified, Eq. (1.6) has exactly the same mathematical form as the L-H model; however, it can explain the dependence of K_{ads}^{app} on the photon flux (E). Turchi & Ollis (1990) suggested, that k_2 is related to E via the following expression:

$$k_2 = \alpha E^{\gamma} \tag{1.8}$$

where α is a proportional constant and γ has been traditionally reported with a value of 0.5 under high-photon-flux conditions "when e^-–h^+ pair recombination dominates", and 1 under low-photon-flux conditions "when the surface reaction dominates". Nevertheless, this asseveration for the value of γ has been recently classified by Emeline et al. (2005), as one of the "dogmas and misconceptions in heterogeneous photocatalysis". In their paper, Emeline et al. (2005) state that their data explicitly showed that, depending on the concentration of the reactant molecules, the dependence of the reaction rate on photon flux does in fact vary from zero-order kinetics at low concentrations of reactant to first-order kinetics at sufficiently high concentrations in the same range of light irradiance. Accordingly, at intermediate concentrations, the order of the reaction on photon flux is between 0 and 1, and the square-root dependence is simply a particular case lying within this range. Confirming results for this statement have been recently reported by Brosillon et al. (2008).

Molecular oxygen plays an important role in the photooxidation process; its primary role is to act as an electron sink for photogenerated carriers (Kabra et al., 2004). Oxygen adsorption appears to be in a non-dissociated form and non-competitive; it is believed that it exclusively attracts to Ti^{III} sites, whereas hydroxyl radicals and organic substrates adsorb at Ti^{IV} and lattice oxygen sites (Ollis et al., 1989; Turchi & Ollis, 1990). The dependence of the photocatalytic degradation rate on the dissolved oxygen concentration (C_{O2}) has been modeled successfully by an L-H type expression, i.e.:

$$r \propto \frac{K_{O_2} C_{O_2}}{1 + K_{O_2} C_{O_2}} \tag{1.9}$$

where K_{O2} is the binding apparent constant for oxygen. Recently, Mills et al. (2006) investigated and confirmed the dependence of the K_{O2} on the photon flux, the same way that is predicted by the new kinetic model of Ollis (2005).

The overall process of semiconductor photocatalysis is not usually found to be very temperature sensitive; reported activation energies generally lie in the range between 5 and 16 kJ/mol (Mills et al., 1993). A similar situation occurs with the pH of the aqueous solution, since it does not strongly affect the rate of photocatalysis. For example, in some studies of degradation of dyes utilizing coated photocatalysis, the reaction rate varied by less than a factor of two from pH=3 to pH=11 (Aris et al., 2002; Fernández et al., 2004).

1.1.4. The quantum yield

A way to quantify the efficiency of photocatalytic processes is through the quantum yield (Φ). It is defined as the number of molecules of a given product formed (or alternatively of a given reactant disappeared) per photon of light of a given wavelength absorbed by the photocatalyst (Serpone & Emeline, 2002). However, in heterogeneous photocatalysis, the

measurement of quantum yield is very difficult since the semiconductor particles absorb, scatter and transmit radiation. Therefore, a more practical term to be used is the apparent quantum yield (Φ_{app}), which is defined as the number of molecules of a given product formed (or alternatively of a given reactant disappeared) per photon of light of a given wavelength incident on the photocatalyst (Mills & Hunte, 1997). For cases where the catalyst is immobilized, the apparent quantum yield can be calculated as:

$$\Phi_{app} = \frac{r_i \cdot V}{E \cdot A_{cat}} \tag{1.10}$$

where r_i is the rate of formation/disappearance of the product/reactant i per unit reaction volume V, and E is the photon flux (photon irradiance) over the coated area A_{cat}. Φ_{app} may vary over a wide range according to the nature of the catalyst, the experimental conditions used, and especially the nature of the reaction considered. Values comprised between 0.02% and 70% have been found and the analysis of this parameter is fundamental, since it enables one to (i) compare the activity of different catalysts for the same reaction, (ii) estimate the relative feasibility of different reactions, and (iii) calculate the energetic yield of the process and the corresponding cost (Herrmann, 2005).

1.2. The CFD simulation process

CFD can be defined as the science of predicting fluid flow, heat transfer, mass transfer, chemical reactions, and related phenomena by solving the mathematical equations that govern these processes using numerical algorithms on a digital computer (Bakker et al., 2001; Ranade, 2002). The extent of chemical process applications where CFD is being successfully used varies widely. Some of the areas with recent reported studies are: chemical reaction engineering (Dixon et al., 2006; Fox, 2006), fuel cells (Carcadea, et al., 2007), combustion

chamber design (Miltner et al., 2007; Smail et al., 2006), crystallization processes (Hatakka et al., 2006), metallurgy (Scheepers et al., 2006), cyclone design (Shi et al., 2006), multiphase reactors analysis (Wang et al., 2006; Zimmermann & Taghipour, 2005), environmental engineering (Templeton et al., 2006; Zhang & Chen, 2007) water disinfection (Elyasi & Taghipour, 2006; Greene et al., 2006), occupational and environmental hygiene (Salim et al., 2006) and photocatalysis (Taghipour & Mohseni, 2005; Trujillo et al., 2007).

For many years, the design, scale-up, and running of unit operations in the chemical process industries have heavily relied upon empiricism and correlations of overall parameters for nonideal or nonequilibrium conditions. This situation has come because the design correlations do not take local effects into account and nonidealities introduced by scaling up of lab or pilot-scale equipment are difficult, if not impossible, to predict empirically. Nevertheless, every time, more and more CFD is being used to analyze the flow and performance of process equipment. CFD allows for an indepth analysis of the fluid mechanics and local effects in these types of equipment and in many cases, this results in improved performance, better reliability, more confident scale-up, improved product consistency, and higher plant productivity (Bakker et al., 2001).

CFD solvers usually utilize the finite volume method. In this method, the geometry of interest is first divided, or discretized, into a number of computational cells. Discretization is the method of approximating the differential equations by a system of algebraic equations for the variables at some set of discrete locations in space and time. The discrete locations are referred to as grid or mesh. In this way, the continuous information from the exact solution of the partial differential governing equations is replaced with discrete values. Once the grid has been created, boundary conditions need to be specified. Pressures, velocities, mass flows, and scalars such as temperature may be specified at inlets; temperature, UV-irradiance, wall shear

rates, or heat fluxes may be set at walls; and pressure or flow-rate splits may be fixed at outlets. The component material properties, such as density, viscosity, diffusion coefficient, UV-absorbance and heat capacity, need to be prescribed. With the grid created, the boundary conditions and physical properties defined, the calculations can be performed. A CFD code will solve the appropriate conservation equations for all grid cells using an iterative procedure. Typical chemical process problems involve solving for: (i) mass conservation (using a continuity equation); (ii) momentum (using the Navier-Stokes equations); (iii) enthalpy; (iv) turbulent kinetic energy; (v) turbulent energy dissipation rate; (vi) chemical species conservation; (vii) local reaction rates; and (viii) local volume fractions for multiphase problems (Bakker et al., 2001). After the numerical solving process, a convergence analysis is recommended. Convergence is reached when changes in solution variables, from one iteration to the next, are negligible. Residuals provide a mechanism to help monitor this trend. It is also recommended to check the overall conservation of mass and energy in the system. Lastly, a grid dependence analysis should be performed, which involves performing the simulation on two or more successively finer grids to determine if the results change. The solution must be grid-independent. The results can be post-processed via graphical visualizations or by numerical reports computed by the CFD code.

Bakker et al. (2001) also mention that the three most commonly made mistakes while doing a CFD simulation are: (i) using a low-quality, coarse grid; (ii) using unconverged results; and (iii) using the wrong physical property data. Fortunately, none of these problems is fundamental to CFD technology itself and can be avoided, if proper attention is paid to them.

1.3. Photocatalytic reactor modeling

In the area of photocatalysis, as in all other fields of chemical reaction engineering, engineers have recognized the importance of finding and developing models to describe the fundamentals that govern reaction systems. Once the models are developed, they can be used to predict the reactor performance, and serve as a valuable tool in the design, scale-up, and optimization process of such systems.

The modeling of photocatalytic reactors requires the resolution of the momentum and mass-transfer equations, the radiation transfer equation in the fluid phases and across the flow physical boundaries, and the heterogeneous photocatalytic reaction kinetics (Imoberdorf et al., 2006). The resolution of this set of equations might be a complicated task, not only due to the mathematical complexity of the equations, but also because in many systems they are strongly coupled. Because of this fact, in many of the models reported in the literature, simplifying assumptions in one or more of these equations have needed to be made in order to simplify the mathematical solutions. However, the resolution of the governing equations under simplification assumptions (e.g., plug-flow, perfectly mixed or fully developed laminar regimes) limits the applicability of the model to those simple systems where those conditions apply. In order to properly predict the behaviour of the photoreactor under different operating conditions and scales, the rigorous solution of the governing equations of the system is desired. In this sense, the development of CFD-based models provides valuable tools for the design, optimization and scale-up of photocatalytic reactors.

In chapters 2-5, detailed literature reviews of photocatalytic reactor modeling are presented. The reviews include modeling of individual model components (i.e., hydrodynamics and mass transfer (chapter 2), surface reaction (chapter 3) and radiation field (chapter 4)), as well as integrated models (chapter 5).

1.4. Thesis scope and objectives

The overall objective of this research was to develop and experimentally evaluate a CFD-based model for the simulation of immobilized photocatalytic reactors used for water treatment. The developed model integrates four fundamental phenomena that determine the physicochemical behaviour of the reactor (i.e., hydrodynamics, external mass transfer, surface chemical reactions, and UV-radiation field). For the development of this integrated CFD model, each of the above phenomena was individually evaluated against experimental data and proper models were identified. The annular reactor geometry was utilized as model geometry taking into account its simplicity and efficiency for photocatalytic applications. This configuration is the most commonly found commercial photoreactor geometry found in the market.

The overall goal was realized by focusing on specific objectives as outlined below:

1. Propose a model that correctly describes the hydrodynamics and the external mass transfer in the reactor.
2. Identify a model that properly predicts the performance of reactors with surface reaction operating under diffusion limiting conditions.
3. Propose a radiation model that accurately computes the UV-photon flux (irradiance) at the catalyst surface.
4. Develop a CFD-based model, which integrates hydrodynamics, mass transfer, UV-radiation, and surface photoreactions, for simulating the performance of surface-coated UV photocatalytic reactors.
5. Experimentally evaluate the CFD-based model in prototype photocatalytic reactors degrading a model contaminant.

6. Examine the application of the developed CFD-based model for the conceptual design of photocatalytic reactors, by analyzing and suggesting possible design improvements to the investigated reactors.

1.5. Thesis layout

This dissertation presents the results, analyses, and conclusions obtained throughout the course of the research in the form of five manuscripts. Each manuscript constitutes one of the following five chapters and contributes to meeting one (or two) of the thesis objectives. Additionally, preliminary research results obtained in a simple photocatalytic reactor were included in a manuscript that is presented in Appendix A. Following is a detailed description of how each of the above objectives has been met with respect to their presentation in the following chapters and/or appendices.

Chapter 2 contributes to meeting Objective 1. This manuscript presents a study in which experiments and CFD simulations were carried out in order to evaluate the accuracy of different hydrodynamic models for the prediction of surface mass transfer in reactors. Two common annular reactor configurations (with the inlet normal (U-shape) and parallel (L-shape) to the main reactor body) were tested as model photoreactors. The hydrodynamic models were evaluated in a wide range of hydrodynamic conditions ($500<Re<11,000$) which include laminar, transitional and turbulent flow within the reactor annulus. Different near-wall models were also considered in the evaluation. As a result of this study, a CFD model that properly predicts external mass transfer was identified.

Chapter 3 contributes to meeting Objective 2. In this chapter, the capability of several hydrodynamic models to predict successfully the kinetic behaviour of the reactor under diffusion limiting conditions was assessed against experimental data. For this, CFD

simulations and experiments using an L-shape coated-wall annular reactor were performed. The thermal decomposition of H_2O_2 catalyzed by Mn/Al oxides was used as model surface reaction. A wide range of flow rates and intrinsic reaction rate constants were utilized for evaluating the model performances. A CFD model capable of predicting the kinetic behaviour of the reactor under different degrees of mass transfer limitation was identified in this study.

Chapter 4 contributes to meeting Objective 3. In this manuscript, a computational radiation field model for simulating the irradiance in single-phase annular photoreactors was developed and evaluated experimentally. For achieving this, several lamp emission models, computed utilizing a CFD-based approach, were evaluated against far- and near-field experimental data obtained using radiometric and actinometric techniques.

Chapter 5 contributes to meeting Objectives 4 and 5. This chapter reports on the integration into a CFD-based model of the hydrodynamic and external mass transfer, surface chemical reaction, and UV-irradiance models that were developed in the earlier chapters. The experimental evaluation of the integrated CFD model was performed using various configurations of annular reactors and UV lamp sizes, over a wide range of hydrodynamic conditions ($350<Re<11{,}000$). The photocatalytic degradation of benzoic acid over a TiO_2 composite sol-gel coating was used as model system in the study.

Chapter 6 contributes to meeting Objective 6. In this chapter, the application of the developed CFD-based model in conceptual design of photocatalytic reactors was explored. For this, an optimization design approach which combines CFD modeling and the Taguchi design of experiments method is presented. The effect of different geometrical factors and mass transfer enhancement elements on the pollutant degradation achieved in an annular photocatalytic reactor was examined. The CFD model was experimentally evaluated against degradation data of 2,4-D (model pollutant).

In Appendix A, a manuscript containing preliminary research results on the evaluation of the individual CFD model components are presented. The evaluation of different hydrodynamic models was performed against experimental data obtained in a differential plate photocatalytic reactor. The surface chemical reaction model was evaluated against an analytical solution valid for reacting fluids under laminar flow. The use of the finite-volume method for solving the radiative transfer equation was assessed against the analytical solution found for the case of a radiation emitting disc.

1.6. References

Adesina, A. (2004). Industrial exploitation of photocatalysis: progress, perspectives and prospects. *Catalysis Surveys from Asia , 8* (4), 265–273.

Aris, A., Din, M.M., Salim, M., Yunus, S., & Bakar, W.A. (2002). Influence of varying reacting conditions in the degradation of azo dye using immobilized TiO_2 photocatalyst. *Water Science and Technology , 46* (9), 255–262.

Bakker, A., Haidari, A.H., & Oshinowo, L.M. (2001). Realize Greater Benefits from CFD. *Chemical Engineering Process , 97* (3), 45–53.

Boyd, G.R., Reemtsma, H., Grimm, D.A., & Mitra, S. (2003). Pharmaceuticals and personal care products (PPCPs) in surface and treated waters of Louisiana, USA and Ontario, Canada. *Science of the Total Environment , 311* (1–3), 135–149.

Brosillon S., Lhomme L., Vallet C., Bouzaza A., & Wolbert D. (2008). Gas phase photocatalysis and liquid phase photocatalysis: Interdependence and influence of substrate concentration and photon flow on degradation reaction kinetics. *Applied Catalysis B: Environmental, 78*, 232–241.

Carcadea, E., Ene, H., Ingham, D.B., Lazar, R., Ma, L., Pourkashanian, M., & Stefanescu, I. (2007). A computational fluid dynamics analysis of a PEM fuel cell system for power generation. *International Journal of Numerical Methods for Heat & Fluid Flow, 17*(3), 302–312.

de Lasa H., Serrano B., & Salaices M. (2005). *Photocatalytic reaction engineering*. New York: Springer.

Dijkstra, M.F., Panneman, H.J., Winkelman, J.G., Kelly, J.J., & Beenackers, A.A. (2002). Modeling the photocatalytic degradation of formic acid in a reactor with immobilized catalyst. *Chemical Engineering Science , 57*, 4895–4907.

Dixon, A.G., Nijemeisland, M., & Stitt, E.H. (2006). Packed tubular reactor modeling and catalyst design using computational fluid dynamics. *Advances in Chemical Engineering, 31*, 307–389

Elyasi, S., & Taghipour, F. (2006). Simulation of UV photoreactor for water disinfection in Eulerian framework. *Chemical Engineering Science , 61* (14), 4741–4749.

Emeline, A.V., Ryabchuk, V.K., & Serpone, N. (2005). Dogmas and Misconceptions in Heterogeneous Photocatalysis. Some Enlightened Reflections. *Journal of Physical Chemistry B,109*, 18515–18521.

Fernández, J., Kiwi, J., Baeza, J., Freer, J., Lizama, C., & Mansilla, H. (2004). Orange II photocatalysis on immobilised TiO_2: Effect of the pH and H_2O_2. *Applied Catalysis B: Environmental,48*, 205–211.

Fox, M.A., & Dulay, M.T. (1995). Heterogeneous Photocatalysis. *Chemical Reviews , 83*, 341–357.

Fox, R.O. (2006). CFD models for analysis and design of chemical reactors. *Advances in Chemical Engineering , 31*, 231–305.

Frank, S.N., & Bard, A.J. (1977). Heterogeneous photocatalytic oxidation of cyanide ion in aqueous solutions at titanium dioxide powder. *Journal of the American Chemical Society , 99* (1), 303–304.

Fujishima, A., & Honda, K. (1972). Electrochemical photolysis of water at a semiconductor electrode. *Nature , 238* (5358), 37–38.

Fujishima, A., & Zhang, X. (2006). Titanium dioxide photocatalysis: present situation and future approaches. *C.R. Chimie , 9*, 750–760.

Fujishima, A., Rao, T.N., & Tryk, D.A. (2000). Titanium dioxide photocatalysis. *Journal of Photochemistry and Photobiology C: Photochemistry Reviews , 1*, 1–21.

Greene, D.J., Haas, C.N., & Farouk, B. (2006). Computational Fluid Dynamics Analysis of the Effects of Reactor Configuration on Disinfection Efficiency. *Water Environment Reseach, 78* (9), 909–919.

Hatakka, H., Alatalo, H., Kallas, J., Liiri, M., & Aittamaa, J. (2006). CFD modelling for crystallization processes and crystallizer design. *VTT Tiedotteita , 2340*, 12–49.

Herrmann J. (2005). Heterogeneous photocatalysis: state of the art and present applications. *Topics in Catalysis, 34*, 49–65.

Hoffmann M.R., Martin S.T., Choi W., Bahnemannt D.W. (1995). Environmental applications of semiconductor photocatalysis. *Chemical Reviews, 95*, 69–96.

Imoberdorf, G.E., Cassano, A.E., Alfano, O.M., & Irazoqui, H.A. (2006). Modeling of a Multiannular Photocatalytic Reactor for Perchloroethylene Degradation in Air. *AIChE Journal , 52* (5), 1814–1823.

Jasim, S.Y., Irabell, A., Yang, P., Ahmed, S., & Schweitzer, L. (2006). Presence of Pharmaceuticals and Pesticides in Detroit River Water and the Effect of Ozone on Removal. *Ozone: Science & Engineering , 28* (6), 415–423.

Kabra, K., Chaudhary, R., & Sawhney, R.L. (2004). Treatment of Hazardous Organic and Inorganic Compounds through Aqueous-Phase Photocatalysis: A Review. *Industrial & Engineering Chemistry Research , 43* (24), 7683–7696.

Kolpin, D.W., Furlong, E.T., Meyer, M.T., Thurman, E., Zaugg, S.D., & Buxton, L.B. (2002). Pharmaceuticals,Hormones, and Other Organic Wastewater Contaminants in U.S.Streams, 1999–2000: A National Reconnaissance. *Environmental Science and Technology , 36*, 1202–1211.

Krýsa, J., Waldner, G., Měšťánková, H., Jirkovský, J., & Grabner, G. (2006). Photocatalytic degradation of model organic pollutants on an immobilized particulate TiO_2 layer: Roles of adsorption processes and mechanistic complexity. *Applied Catalysis B: Environmental , 64* (3–4), 290–301.

Kuipers, J.A., & Van Swaaij, W.P. (1998). Computational fluid dynamics applied to chemical reaction engineering. *Advances in Chemical Engineering , 24*, 227–328.

Linsebigler, A.L., Lu, G., & Yates, J.T. (1995). Photocatalysis on TiO_2 Surfaces: Principles, Mechanisms, and Selected Results. *Chemical Reviews , 95* (3), 735–758.

McMurray, T., Byrne, J., Dunlop, P., Winkelman, J., Eggins, B., & McAdamsa, E. (2004). Intrinsic kinetics of photocatalytic oxidation of formic and oxalic acid on immobilised TiO_2 films. *Applied Catalysis A: General , 262*, 105–110.

Mehrotra, K., Yablonsky, G.S., & Ray, A.K. (2005). Macro kinetic studies for photocatalytic degradation of benzoic acid in immobilized systems. *Chemosphere , 60*, 1427–1436.

Mills, A., & Hunte, S.L. (1997). An overview of semiconductor photocatalysis. *Journal of Photochemistry and Photobiology A: Chemistry , 108*, 1–35.

Mills, A., Davies, R.H., & Worsley, D. (1993). Water Purification by Semiconductor Photocatalysis. *Chemical Society Reviews , 22* (6), 417–425.

Mills, A., Wang, J., & Ollis, D.F. (2006). Dependence of the kinetics of liquid-phase photocatalyzed reactions on oxygen concentration and light intensity. *Journal of Catalysis, 243*, 1–6.

Miltner, M., Miltner, A., Harasek, M., & Friedl, A. (2007). Process simulation and CFD calculations for the development of an innovative baled biomass-fired combustion chamber. *Applied Thermal Engineering , 27* (7), 1138–1143.

Mukherjee, P.S., Ray, A.K. (1999). Major challenges in the design of a large-scale photocatalytic reactor for water treatment. *Chemical Engineering Technology, 22*, 253–260.

Na, T., Fang, Z., Zhanqi, G., Cheng, Z., Ming, S. (2006). The Status of Pesticide Residues in the Drinking Water Sources in Meiliangwan Bay, Taihu Lake of China. *Environmental Monitoring and Assessment , 123* (1–3), 351–370.

Ollis, D.F. (2005). Kinetics of Liquid Phase Photocatalyzed Reactions: An Illuminating Approach. *Journal of Physical Chemistry B , 109*, 2439–2444.

Ollis, D.F., & Turchi, C. (1990). Heterogeneous photocatalysis for water purification: contaminant mineralization kinetics and elementary reactor analysis. *Environmental Progress , 9* (4), 229–234.

Ollis, D.F., Pelizzetti, E., & Serpone, N. (1989). Heterogeneous Photocatalysis in the Environment: Application to Water Purification. In N. Serpone, & E. Pelizzetti, *Photocatalysis: Fundamentals and Applications* (p.p. 603–637). New York: John Wiley & Sons.

Ollis, D. F., Pelizzetti, E., & Serpone, N. (1991). Photocatalyzed destruction of water contaminants. *Environmental Science & Technology , 25* (9), 1522–1529.

Oppenländer T. (2004). *Photochemical purification of water and air*. Weinheim: Wiley–VCH.

Pasternak, J. (2006). Agricultural Pesticide Residues in Farm Ditches of the Lower Fraser Valley, British Columbia, Canada. *Journal of Environmental Science and Health, Part B: Pesticides, Food Contaminants, and Agricultural Wastes , 41* (5), 647–669.

Poyatos, J., Muñio, M., Almecija, M., Torres, J., Hontoria, E., & Osorio, F. (2010). Advanced oxidation processes for wastewater treatment: state of the art. *Water, Air, and Soil Pollution , 205*, 187–204.

Ranade, V. (2002). *Computational Flow Modeling for Chemical Reaction Engineering*. London: Academic Press.

Romero, R.L., Alfano, O.M., & Cassano, A.E. (2003). Radiation field in an annular, slurry photocatalytic reactor. 2. Model and experiments. *Industrial & Engineering Chemistry Research, 42,* 2479–2488.

Salim, S., Viswanathan, S., & Madhumita, B.R. (2006). Evaluation of source model coupled computational fluid dynamics (CFD) simulation of the dispersion of airborne contaminants in a work environment. *Journal of occupational and environmental hygiene, 3* (12), 684–693.

Scheepers, E., Adema, A.T., Yang, Y., & Reuter, M.A. (2006). The development of a CFD model of a submerged arc furnace for phosphorus production. *Minerals Engineering , 19* (10), 1115–1125.

Serpone, N., & Emeline, A.V. (2002). Suggested terms and definitions in photocatalysis and radiocatalysis. *International Journal of Photoenergy , 4*, 91–131.

Shi, L., Bayless, D.J., Kremer, G., & Stuart, B. (2006). CFD Simulation of the influence of temperature and pressure on the flow pattern in cyclones. *Industrial & Engineering Chemistry Research , 45* (22), 7667–7672.

Smail, K., Alain, D., & Detlef, K. (2006). Hybrid modeling approach to predict gas turbine combustor performance. *Heat and Technology , 24* (2), 15–21.

Taghipour, F., & Mohseni, M. (2005). CFD Simulation of UV Photocatalytic Reactors for Air Treatment. *AIChE Journal , 51* (11), 3039–3047.

Templeton, M.R., Hofmann, R., & Andrews, R.C. (2006). Case study comparisons of computational fluid dynamics (CFD) modeling versus tracer testing for determining clearwell residence times in drinking water treatment. *Journal of Environmental Engineering and Science , 5* (6), 529–536.

Ternes T. (1998). Occurrence of drugs in German sewage treatment plants and rivers. *Water Research, 32*, 3245–3260.

Thompson, T.L., & Yates, J.T. (2006). Surface Science Studies of the Photoactivation of TiO_2–New Photochemical Processes. *Chemical Reviews , 106*, 4428–4453.

Trujillo, F. J., Safinski, T., & Adesina, A.A. (2007). CFD Analysis of the radiation distribution in a new immobilized catalyst bubble column externally illuminated photoreactor. *Journal of Solar Energy Engineering , 129*, 27–36.

Turchi, C.S., & Ollis, D.F. (1990). Photocatalytic degradation of organic water contaminants: mechanisms involving hydroxyl radical attack. *Journal of Catalysis , 122* (1), 178–192.

Wang, F., Mao, Z.-S., Wang, Y., & Yang, C. (2006). Measurement of phase holdups in liquid-liquid-solid three-phase stirred tanks and CFD simulation. *Chemical Engineering Science, 61* (22), 7535–7550.

Zhang, T.F., & Chen, Q. (2007). Identification of contaminant sources in enclosed environments by inverse CFD modeling. *Indoor air , 17* (3), 167–177.

Zimmermann, S., & Taghipour, F. (2005). CFD Modeling of the Hydrodynamics and Reaction Kinetics of FCC Fluidized-Bed Reactors. *Industrial & Engineering Chemistry Research, 44*, 9818–9827.

2. CFD MODELING OF MASS TRANSFER IN ANNULAR REACTORS [1]

2.1. Introduction

The annular reactor geometry has been finding increasingly many applications in chemical engineering processes. Some of the most common configurations include tube wall reactors (Kapteijn et al., 2005; Karim et al., 2005), membrane reactors (Moueddeb et al., 1996), electrochemical reactors (Pickett, 1979), dialyzers (Castro et al., 2008), and immobilized photocatalytic reactors (Taghipour & Mohseni, 2005; Tomasic et al., 2008). Despite their potential success and applications, mass-transfer limitations could be an issue in these reactors depending on the kinetics, operating conditions, and the geometrical properties of the system. Hence, when modeling these reactors, an accurate prediction of fluid flow and thus, local mass transfer is needed.

Most of the previous studies on mass transfer in annular reactors reported in the open literature have concentrated on obtaining correlations of dimensionless numbers for different configurations and operating conditions. Rai et al. (1998) compiled several correlations for both developed and developing boundary layers under laminar and turbulent flow conditions. More recently, Mobarak et al. (1997) measured the rates of solid-liquid mass transfer at the inner surface (smooth and rough) of an annular duct by the electrochemical technique under developing flow conditions. Table 2.1 provides a list of some of the correlations available in the literature. Even though the design of annular reactors has relied for many years on the use of such correlations, they present the disadvantage of being applicable only to a specific reactor configuration operated under a certain range of hydrodynamic conditions. Besides, this type of design correlations does not take into account local effects. Moreover, the nonidealities

[1] A version of this chapter has been published.
Duran, J.E., Taghipour, F., & Mohseni, M. (2009). CFD modeling of mass transfer in annular reactors. *International Journal of Heat and Mass Transfer, 52*, 5390–5401.

introduced by scaling up of the lab or pilot-scale equipment are difficult, if not impossible, to predict empirically (Bakker, 2001).

Table 2.1. Some correlations reported in the literature for mass transfer in annuli.

Hydrodynamic condition	Source	Correlation	Condition	Eq. no.
Laminar flow				
Fully developed	(Ross & Wragg, 1965)	$Sh_{av} = 1.614\left(\mathrm{Re}\, Sc\, \phi\, d_e / l\right)^{1/3}$		(2.1)
Developing	(Mobarak et al., 1997)	$Sh_{av} = 1.029 Sc^{1/3}\, \mathrm{Re}^{0.55}\left(d_e / l\right)^{0.472}$		(2.2)
	(Ould-Rouis et al., 1995)	$Sh_{av} = 0.66\, Sc^{1/3}\left(\mathrm{Re}\, \phi\, d_e / l\right)^{0.52}$	$X \le 42\times10^{-4}$	(2.3)
		$Sh_{av} = 1.56\, Sc^{1/3}\left(\mathrm{Re}\, \phi\, d_e / l\right)^{0.34}$	$X \ge 42\times10^{-4}$	(2.4)
	(Ghosh & Upadhyay, 1985)	$Sh_{av} = 2.703\left(\mathrm{Re}\, Sc\, \phi\, d_e / l\right)^{1/3}$		(2.5)
Turbulent flow				
Fully developed	(Ross & Wragg, 1965)	$Sh_{av} = 0.276 Sc^{1/3}\, \mathrm{Re}^{0.58}\left(d_e / l\right)^{1/3}$	$l/d_e < 2$	(2.6)
		$Sh_{av} = 0.023 Sc^{1/3}\, \mathrm{Re}^{0.8}$	$l/d_e > 2$	(2.7)
	(Rai et al., 1988)	$Sh_{av} = 0.027 Sc^{1/3}\, \mathrm{Re}^{0.8}\left(d_2 / d_1\right)^{0.53}$		(2.8)
	(Pickett, 1979)	$Sh_{av} = 0.145 Sc^{1/3}\, \mathrm{Re}^{2/3}\left(d_e / l\right)^{0.25}$	$l/d_e < 7.5$	(2.9)
Developing	(Mobarak et al., 1997)	$Sh_{av} = 0.095 Sc^{0.33}\, \mathrm{Re}^{0.85}\left(d_e / l\right)^{0.472}$	$6.8 < l/d_e < 34.4$	(2.10)
	(Ghosh & Upadhyay, 1985)	$Sh_{av} = 0.305 Sc^{1/3}\, \mathrm{Re}^{2/3}\left(\phi\, d_e / l\right)^{1/3}$		(2.11)
	(Rai et al., 1988)	$Sh_{av} = 0.032 Sc^{1/3}\, \mathrm{Re}^{0.8}\left(1+\left(d_e / l\right)^{2/3}\right)\left(d_2 / d_1\right)^{0.53}$	$l/d_e < 7$	(2.12)

A better approach to estimate mass transfer in annular reactors is finding suitable models that allow predicting the concentration fields inside the reactor. Several researchers have taken this approach; for instance, Houzelot & Villermaux (1977) performed a numerical simulation of radial diffusional mass transfer in a fluid flowing in fully developed laminar

flow in a reactor in which a first order heterogeneous reaction was taking place at the wall. The simulation results were in excellent agreement with those yielded by the experiments and the investigation revealed that annular reactors exhibit a mass transfer efficiency which is noticeably higher than that of empty tubes. Other researchers have proposed and evaluated several mathematical models which included mass transfer in annular reactors used for different applications, but their systems were limited either to laminar, or to fully developed turbulent flow conditions (Farias et al., 2001; Imoberdorf et al., 2007; Legrand et al., 1997; Legrand & Martemyanov, 1994; Maestri et al., 2007; Martemyanov et al., 1999; Ould-Rouis et al., 1995; Papadias et al., 2001; Ross & Wragg, 1965). Practical annular reactors, however, often do not have an entrance length to assure a fully developed flow. In fact, in most of the cases, developing flow is desirable since it gives rise to enhanced mass transfer. In this sense, inlet and outlet port configurations, so as internal accessories (e.g., internal baffles) usually play an important role in improving mass transfer performance of the reactor.

Mass transfer modeling under developing flow condition is a complex task. However, the application of computational fluid dynamics (CFD) has demonstrated to be a very effective approach for tackle this challenge. Taghipour & Mohseni (2005) and Mohseni & Taghipour (2004) applied computational fluid dynamics (CFD) and simulated laminar flow annular photocatalytic reactors treating chlorinated VOCs. The CFD-models were capable of predicting the reactor performance and provided insight into the concentration gradients of the species in the reactor. For the case of annular reactors operating under developing turbulent flow regime, little modeling work has been done. Sozzi & Taghipour (2006) performed a detailed CFD simulation of the hydrodynamics of two annular photoreactor configurations (concentric and normal inlets), and evaluated the results with the velocity profiles from particle imagine velocimetry (PIV). Under the evaluated operational conditions, the realizable

k-ε and the Reynolds stress model (RSM) turbulence models displayed the best overall match to the experimental PIV measurements. Even though this investigation brought an important outcome in terms of recommending appropriate turbulence models for computing the fluid velocity field inside annular reactors, further investigation is needed to assess their applicability to mass transfer modeling. Since the wall-liquid mass transfer phenomenon takes place almost completely within the near-wall region, near-wall modeling significantly impacts the validity of numerical solutions and requires experimental evaluation. To the author's knowledge, no research has been performed on modeling and experimentally evaluating mass transfer of transient and turbulent flow with simultaneous development of velocity and concentration boundary layers in commonly used annular reactor configurations.

This research has focused on applying CFD for modeling single-phase liquid fluid flow and mass transfer phenomena in commercial-type annular reactors. CFD allows for an in-depth analysis of the fluid mechanics, local mass transfer, and other physicochemical processes occurring in chemical reactors, thereby offering the possibility of achieving an improved performance, a better reliability, and a more confident scale-up of the equipment. The aim of this work was to carry out a comprehensive CFD study in which simulation results obtained using different hydrodynamics models were evaluated with experimental measurements of external mass transfer in annular reactors. The case of mass transfer from the inner surface of the outer tube (at constant concentration) was analyzed. The experimental determination of the mass transfer rates was achieved by coating the inner wall with benzoic acid (as a model chemical) and then measuring the dissolution of the slightly soluble acid into the flow stream. Two commonly used annular reactor configurations were studied: with the

inlet normal (U-shape); and parallel (L-shape) to the main reactor body. Commercial CFD code Fluent® 6.3.26 was used to perform the simulations.

2.2. CFD modeling

2.2.1. Governing equations

In the present study, it is assumed that the fluid (water) is Newtonian, incompressible, isothermal, non-reactive, with constant physical properties and under turbulent steady-state flow. Under these assumptions and following the Reynolds averaged Navier-Stokes (RANS) turbulence modeling approach (Ranade, 2002), the CFD model involves solving the continuity equation (2.13), Reynolds average Navier-Stokes equation (2.14) and time-average conservation of species equation (2.15) which are expressed as:

$$\nabla \cdot \left(\overline{U}\right) = 0 \tag{2.13}$$

$$\nabla \cdot \left(\rho \overline{U}\,\overline{U} + \rho \overline{uu}\right) = -\nabla \overline{P} - \nabla \cdot \overline{\tau} \tag{2.14}$$

$$\nabla \cdot \left(\rho \overline{U}\,\overline{m_i} + \rho \overline{u m'_i}\right) = -\nabla \cdot \overline{J}_i \tag{2.15}$$

where the overbar indicates a time-averaged value, ρ is density, U is velocity, P is pressure, τ is viscous stress tensor, m_i is mass fraction of species i, J_i is diffusive flux of species i, and u and m'_i are fluctuating flow velocity and mass fraction of species i, respectively. Time averaging of the basic governing equations of flow processes leads to the appearance of apparent stress gradients $\left(\rho \overline{uu}\right)$ and mass transfer fluxes $\left(\rho \overline{u m'_i}\right)$ associated with turbulent motion. The main challenge in modeling turbulent flow lies in the specification of these turbulent stresses and mass fluxes in terms of the time-averaged variables. Generally, for most engineering flow modeling applications, this so-called closure problem is solved by

introducing a turbulence model. Several turbulence models have been proposed in the open literature (Nallasamy, 1987; Wilcox, 2006), but unfortunately, there is none that can be used universally. Proper turbulence models need to be selected according to the problem under consideration.

This investigation intended to evaluate CFD modeling of mass transfer in annular reactors over a broad range of hydrodynamic conditions. The Reynolds number (Re) range analyzed was between 500 and 11000, in which laminar, transitional and turbulent flow regimes were present. For the simulations having $500<Re<2100$, the laminar hydrodynamic model was used, whereas for those simulations with $2100<Re<11000$ four different turbulence models were evaluated. In the first place, the widely used standard k-ε model (S k-ε) (Launder & Spalding, 1974) was evaluated. Then, based on the results obtained by Sozzi & Taghipour (2006), the realizable k-ε model (R k-ε) (Shih et al., 1995) and the Reynolds stress model (RSM) (Launder et al., 1975) were chosen for evaluation. Finally, the low Reynolds number turbulence model developed by Abe, Kondoh and Nagano (AKN) (Abe et al., 1994) was selected for evaluation. This later model was chosen based on the successful predictions of mass and heat transfer obtained by other researchers in similar systems such as pipe expansions, turbulent pipes and impinging jets (Hsieh & Chang, 1996; Wang et al., 1996; Wang & Mujumdar, 2005). The five hydrodynamic models are briefly discussed in the following section.

2.2.2. Hydrodynamic models

2.2.2.1. Laminar model

When modeling laminar flow, identical equations to (2.13)-(2.14), but excluding the apparent stress gradients $\left(\rho\overline{uu}\right)$ associated with turbulent motion, need to be solved. These equations combined with the Newton's law of viscosity, as a constitutive equation to relate the viscous stress tensor to the motion of the continuous fluid, allow computing the velocity field within the reactor. Further details and solved examples for this model can be found in Bird et al. (2002).

2.2.2.2. Standard k-ε model (S k-ε)

The S *k*-ε model is a two-equation eddy viscosity model which is based on the Boussinesq hypothesis (approximation). The Boussinesq hypothesis makes the assumption that the Reynolds stresses can be expressed in terms of mean velocity gradients and that the turbulent eddy viscosity is related to the turbulence kinetic energy *k* and the dissipation rate ε. The advantage of this approach is the relatively low computational cost associated with the computation of the turbulent viscosity; however, it also presents the disadvantage of assuming the turbulent viscosity as an isotropic scalar quantity, which is not strictly true. The S *k*-ε model has proved reasonably accurate for many flows without highly curved streamlines or significant swirl. It usually underestimates flow separation and overestimates turbulence production by normal straining (Perry & Green, 1997). In the derivation of the model, the flow is assumed fully turbulent, and the effects of molecular viscosity are neglected. These assumptions therefore make the S *k*-ε model valid only for fully turbulent flows. Nonetheless,

this turbulence model has been one of the most widely validated and used in engineering applications. The S *k*-ε model is described by Launder & Spalding (1974).

2.2.2.3. Realizable k-ε model (R k-ε)

The R *k*-ε model is a modification of the S *k*-ε model which incorporates a new formulation for the turbulent viscosity and a new transport equation for the dissipation rate ε. A benefit of the R *k*-ε model, compared with the S *k*-ε model, is that it predicts more accurately the spreading rate of planar and round jets, and it is also likely to provide superior performance for flows involving rotation, boundary layers under strong adverse pressure gradients, separation, and recirculation (Fluent-Inc., 2006). The details of this turbulence model can be found in Shih, et al. (1995).

2.2.2.4. Reynolds stress model (RSM)

The RSM is the most elaborate turbulence model among the RANS based models. It does not use the Boussinesq hypothesis and rather than assuming isotropic turbulent viscosity, the RSM closes the RANS equations by solving individual transport equations for the Reynolds stresses, together with an equation for the dissipation rate. This turbulence model should be considered whenever non-isotropic effects are important; for example, in flows with strong curvature, swirling flows, and flows with strong acceleration/retardation. The fidelity of RSM predictions is still limited by the closure assumptions employed to model various terms in the exact transport equations for the Reynolds stresses. The modeling of the pressure-strain and dissipation-rate terms is particularly challenging, and often considered to be responsible for compromising the accuracy of RSM predictions (Fluent-Inc., 2006). Among some of the

disadvantages of the RSM, Ranade (2002) mentions that the model is computationally expensive, that it performs as poor as the *k*-ε model in some flows due to problems with the dissipation rate equation, and that it has not been widely validated yet. Launder et al. (1975) present details of the RSM.

2.2.2.5. Enhanced wall treatment

The S *k*-ε, R *k*-ε, and RSM models are primarily valid for turbulent core flows (i.e., the flow in the regions somewhat far from walls). Therefore, special consideration needs to be given as to how to make these models suitable for wall-bounded flows. There are two main approaches to modeling the near-wall region. In one approach, the so-called 'wall function' approach, the viscosity-affected inner regions (viscous and buffer layers) are not modeled; instead, semi-empirical formulae (wall functions) are used to bridge the viscosity-affected region between the wall and the fully turbulent region (Ranade, 2002). This approach, although less memory and CPU intensive, misses important features of the mass transfer boundary layer if it is deeply embedded within the viscous sublayer. This situation makes the wall function approach inappropriate when modeling wall-mass or heat transfer in liquid flows. In the other approach, special low Reynolds number turbulence models are developed to simulate the near-wall region flow, allowing for extending the turbulence model all the way to the wall (Jones & Launder, 1972; Wolfstein, 1969). This latter approach has given the best results when modeling wall mass and heat transfer, and thus it is the recommended method in these applications. In this investigation, when the S *k*-ε, R *k*-ε or RSM models were used to perform CFD simulations, the enhanced wall treatment available in the commercial CFD software was enabled. This treatment is a near-wall modeling method that combines a two-

layer model applicable in regions with fine near-wall meshes, with enhanced wall functions used in regions with coarse meshes. When using the enhanced wall treatment, it is necessary thus to construct a proper fine mesh where the viscosity-affected near-wall region is desired to be fully resolved. Details of this method can be found in Fluent-Inc. (2006).

2.2.2.6. AKN low Reynolds number turbulence model

Over the past few years, low Reynolds number (LRN) *k*-ε models have been widely used to predict wall-bounded flows due to their simplicity and capability of predicting the near wall flow, so as mass and heat transfers (Dhotre & Joshi, 2004; Nesic et al., 1993; Wang & Postlethwaite, 1997). The low Reynolds number *k*-ε modeling approach incorporates either a wall-damping effect or a direct effect of molecular viscosity, or both, on the empirical constants and functions in the turbulence transport equations. This approach enables the extension of the *k*-ε turbulence model all the way to the wall. The low Reynolds number does not refer to the global Reynolds number, but the local turbulent Reynolds number formed by a turbulent fluctuation and turbulent length scale. This Reynolds number varies throughout the computational domain and is proportional to the ratio of the turbulent and physical viscosity (Davidson, 2003). Fairly complete reviews of low Reynolds number *k*-ε models have been presented by Patel et al. (1984), Hrenya et al. (1995), and Thakre & Joshi (2000, 2002).

Among many others, the AKN model has shown promising results in modeling near-wall heat and mass transfers (Hsieh & Chang, 1996; Wang et al., 1996; Wang & Mujumdar, 2005). Abe et al. (1994) modified the Nagano & Tagawa (1990) LRN *k*-ε turbulence model, suggesting the use of the Kolmogorov velocity scale instead of the friction velocity to account

for the near-wall and LRN effects in both attached and detached flows. Doing so, the model improved the prediction of the flows with separation and reattachment (Abe et al., 1994).

2.2.3. Mass transfer models

2.2.3.1. Laminar flow

When modeling mass transfer under laminar flow regime, Eq. (2.15), excluding the mass transfer fluxes $\left(\rho\overline{um'_i}\right)$ associated with turbulent motion, needs to be solved. The diffusive flux of species *i* can be estimated using Fick's first law of diffusion:

$$J_i = -D_m \nabla\left(\rho m_i\right) \tag{2.16}$$

where D_m is the molecular diffusivity of species *i* in the mixture. Substituting Eq. (2.16) in (2.15) with $\left(\rho\overline{um'_i}\right)=0$, gives the convection-diffusion mass transfer equation for laminar flow:

$$\nabla\cdot\left(\rho U m_i\right) = \nabla\cdot\left(D_m\nabla\left(\rho m_i\right)\right) \tag{2.17}$$

2.2.3.2. Turbulent flow

The closure problem associated with the specification of the mass transfer fluxes $\left(\rho\overline{um'_i}\right)$ associated with turbulent motion modeling has been typically solved by analogy to the linear approximation for the Reynolds stresses (or to Fick's first law of diffusion):

$$\rho\overline{um'_i} = -D_t\nabla\left(\rho\overline{m_i}\right) \tag{2.18}$$

where D_t is the so-called eddy (or turbulent) diffusivity for species concentration. Combining Eqs. (2.18) and (2.15) results in the convection-diffusion turbulent mass transfer equation applicable to our case:

$$\nabla \cdot \left(\rho \overline{U}\, \overline{m_i} \right) = \nabla \cdot \left[\left(\rho D_m + \frac{\mu_t}{Sc_t} \right) \nabla \overline{m_i} \right] \tag{2.19}$$

with μ_t the turbulent viscosity and Sc_t the turbulent Schmidt number defined as the ratio between the turbulent viscosity and the turbulent diffusion:

$$Sc_t = \frac{\mu_t}{\rho D_t} \tag{2.20}$$

This dimensionless number typically is close to unity. Koeltzsch (2000) reviewed the previous experimental investigations and found that most authors use a constant for Sc_t ranging from 0.5 to 0.9. In this investigation a value of 0.7 was used as recommended in various references (Fluent-Inc., 2006; Spalding, 1971; Yimer et al., 2002). The assumption of using a constant turbulent Schmidt number across the whole flow field has been questioned recently and some researchers have elaborated models that consider the dependence of Sc_t on global quantities of the flow (Rosen & Traegaardh, 1995), or as algebraic turbulence models (Aravinth, 2000). More accurate predictions of mass and heat transfer have been reported using this approach (Wolfstein, 1969; Nelissen et al., 2003). Also, more complex models for solving the turbulent mass transfer equation have been recently proposed, like the two-equation model of B.T. Liu (Sun et al., 2005).

2.2.4. Geometrical models

The two model annular reactor geometries studied in the present work are shown in Fig. 2.1. Both reactors share the same main dimensions: 33 mm outer tube diameter, 21 mm

inner tube diameter, 295 mm total length, 12 mm inlet and outlet diameter tubes. The inlet and outlet ports of the U-shape reactor were placed 20 mm from each respective end, so as the outlet port of the L-shape reactor. The inlet port of the L-shape reactor was centered on the front plate. The inlet and outlet tubes were chosen to be at least 45 diameters in length to ensure that a fully developed flow was established at the entrance of the reactor and at the outlet boundary. The L-shape reactor inner tube began 20 mm away from the front plate and its holder was placed 30 mm from the front plate. The holder consisted of three prongs (3 mm wide × 6 mm long × 3 mm thick) located 120° one from another. Both annular reactors had three sections on the inner wall of the outer tube that could be set at constant concentration. Experimentally, this condition was achieved by depositing a benzoic acid coating onto the inner walls. This feature allowed for studying the mass transfer process at different regions along the annular volume of the reactors. Each section was 76 mm long and they were coded as follows: A for the inlet section, B for the middle section, and C for the outlet section.

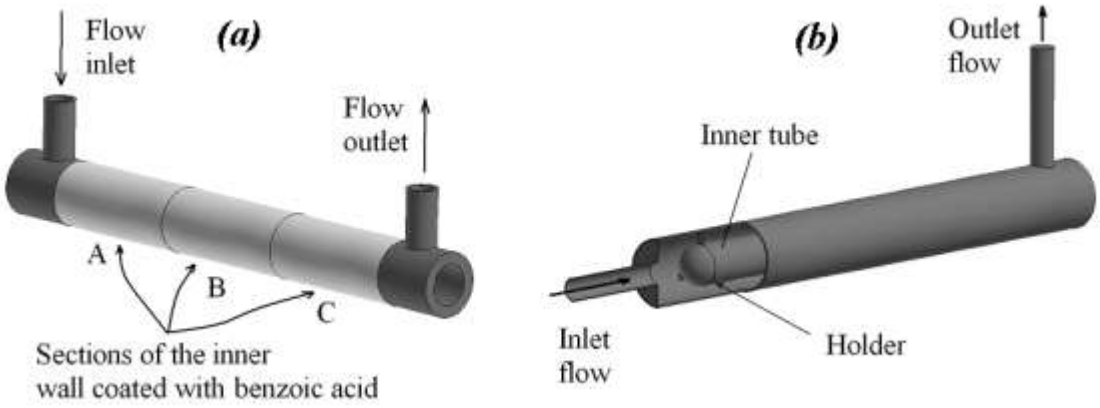

Fig. 2.1. Schematic diagram of the U-shape (a) and L-shape (b) annular reactors. The schematic of the U-shape reactor indicates the inner wall sections coded as A, B and C. The L-shape reactor is illustrated with a partial cut-off to show the inner tube with its holder.

2.2.5. Mesh design

When modeling turbulent mass transfer from a wall using the enhanced wall treatment or the low Reynolds number turbulence model approaches, it is fundamental to have a mesh fine enough that allows solving the governing equations all the way to the wall. Typical recommendations for being able to resolve the mean velocity and turbulent quantities in the near-wall region are to have a $y^+ \approx 1$ and at least 10 cells within the viscosity-affected near-wall region ($Re_y < 200$) (Fluent-Inc., 2006). Nevertheless, for high Schmidt number systems, the concentration boundary layer is much smaller than the velocity boundary layer. This fact makes it necessary to have even finer meshes within the near-wall region in order to be able to solve properly the concentration profiles. To define the mesh requirements in the sections of the reactor geometry where mass transfer from the wall was taking place, a preliminary study was performed. In this study, simulations of mass transfer in a straight pipe (10 mm diameter × 1 m long) with its internal wall coated with benzoic acid, and therefore at constant concentration, were performed. The four turbulence models (S k-ε, R k-ε, RSM and AKN) were evaluated. Eleven different meshes for the pipe operating under three water flow rates (Re=7500, 35000, 75000) were evaluated not only in terms of mesh independent results, but also in terms of result accuracy. The benzoic acid outlet concentrations computed by the CFD simulation were compared with the predictions of the empirical correlation obtained by Harriott & Hamilton (1965), which is reported to have an average deviation of 5.4% from the experimental data. The conclusions of the simulations under the three different water flow rates were basically the same; therefore, only some of the data corresponding to Re = 7500 are presented in Table 2.2 as the representative results. The results showed that a y^+ smaller than 0.5 at the wall-adjacent cell and at least 10 cells within the viscosity-affected near-wall region

(Re_y < 200) were needed to obtain consistent and accurate results. These near-wall mesh requirements were then utilized in all the simulations performed in this investigation. It is also worth highlighting that the computations using the RSM and the AKN models provided the closest agreement with the estimations of the empirical correlation.

Table 2.2. Difference (%) in the exit concentrations of benzoic acid predicted by the empirical correlation of Harriott & Hamilton (1965) and the CFD simulations. Four different turbulence models and several near-wall meshes were evaluated.

Mesh	#1	#2	#3	#4	#5	#6
y^+	0.06	0.13	0.25	0.25	0.5	1.3
# cells Re_y < 200	19	14	19	15	14	11
RSM % Error	2.5	3.9	1.8	2.8	1.4	23.8
AKN % Error	4.3	5.1	3.1	3.3	6.8	31.1
R k-ε % Error	17.7	17.6	17.4	17.7	14.4	33.5
S k-ε % Error	17.7	18.4	17.4	18.0	14.4	33.9

The commercial mesh generator Gambit® was used to create the grid. For the case of the U-shape reactor, structured hexahedral cells were used to discretise the entire physical domain, whereas for the L-shape reactor it was necessary to split the reactor domain and use unstructured cells in the region where the inner tube holder was located (see Fig. 2.2a). For the annular region, where the mass transfer took place, a boundary-layer mesh accomplishing a y^+ < 0.5 and having at least 10 cells within the viscosity-affected near-wall region was setup (see Fig. 2.2b). The utilized grids for both reactors had approximately 1.3 million volume cells and they were verified to give mesh-independent results.

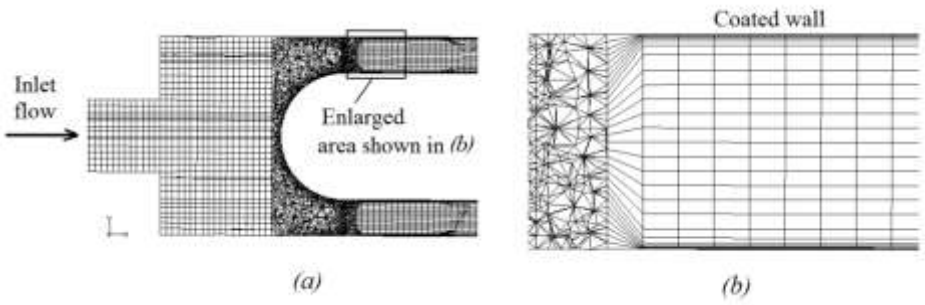

Fig. 2.2. Sections of the mesh used in the L-shape reactor. (a) Longitudinal cut of the entrance zone where an unstructured mesh was required in the region of the inner tube holder. (b) Enlargement of the annular region where a boundary-layer mesh is utilized.

2.2.6. Boundary conditions

The boundary conditions for the CFD model were defined as follows. At the inlet, the mass flow rate of the fluid was specified. The direction of the flow was defined normal to the boundary. The hydraulic diameter was fixed at 12 mm and the turbulence intensity (TI) was set with values close to 5%. The turbulence intensity was estimated for each case based on the formula $TI = 0.16\ Re^{-1/8}$. This formula calculates the turbulence intensity at the core of fully developed flows (Fluent-Inc., 2006). At the outlet, a fully developed flow (outflow) condition was applied. At all the walls, a no-slip boundary condition was imposed. Also, zero diffusive flux of species was specified at the wall, except for the walls coated with benzoic acid, where a constant concentration of 3.4×10^{-3} (mass fraction) was fixed. This concentration corresponds to the saturation concentration of benzoic acid in water at 298 K (Kirk & Othmer, 2001).

2.2.7. Physical properties

The physicochemical process studied in this investigation is the isothermal convective mass transfer of benzoic acid in water at 298 K. Because at this temperature the saturation concentration of benzoic acid in water is very low, the physical properties of water can be

assumed for the system. At 298 K the viscosity and the density of water are 8.9×10^{-4} Pa·s and 997 kg/m^3 respectively (Lide, 2007). The assumed diffusion coefficient of benzoic acid in water was 9.32×10^{-10} m^2/s, which is the integral diffusion coefficient computed by Noulty & Lealst (1987) over the concentration range from zero to saturation.

2.2.8. Numerical solution method and strategy

Commercial CFD code Fluent® 6.3.26 was used to perform the simulations. Fluent® has the S *k*-ε, R *k*-ε and RSM turbulence models, as well as six LRN models, among them being the AKN model. The AKN model constants were set to the software's default values which are identical to those in the high Reynolds number S *k*-ε model. Some researchers have found that when using this set of constants, the model performs better (Wang et al., 1996).

The segregated steady-state solver was used to solve the governing equations. Second order upwind discretization scheme was employed except for pressure for which PRESTO! was selected. The SIMPLE algorithm was chosen for the pressure-velocity coupling. Convergence of the numerical solution was ensured by monitoring the scaled residuals to a criterion of at least 10^{-4} for the continuity and momentum variables, and 10^{-6} for the concentration. Additionally, the variation of velocity magnitude at several points of the computational domain located in areas of high velocity gradients was used as indicator of convergence.

Taking advantage of the fact that the very low concentrations of benzoic acid did not affect the velocity field within the reactor, the CFD model was solved in two steps. First, equations of continuity (2.13) and motion (2.14) were solved for getting the flow field across the computational domain. Then, the velocity values were kept "frozen" and the equation of

conservation of species (2.15) was solved using the converged flow solution. This solving strategy saves computation time and brings stability to the solution.

2.3. Experimental setup and procedure

The experimental work focused to generate data of the external mass transfer in both (U-shape and L-shape) annular reactors under different hydrodynamic conditions. The U-shape and L-shape annular reactors described in Section 2.2.4 were used in the experiments. The main reactor structure was made of PVC and included a union that allowed for setting up either reactor configuration as needed (see Fig. 2.3a). The coatings of benzoic acid, as a model chemical, were deposited on glass tubes (76 mm long and 33 mm inner diameter) with an outer diameter slightly smaller than the inner diameter of the PVC unit, so that the glass tubes could fit inside the PVC structure (see Fig. 2.3b). The coated glass tubes could be located at positions A, B or C as indicated in Fig. 2.1. When only one of the sections was desired to be coated with benzoic acid, two more glass tubes without any coating were placed at the other two positions. The glass tubes were coated by dipping them into molten benzoic acid (Fisher Scientific certified ACS). On contact with the cold glass, the benzoic acid solidified immediately, yielding a layer of the organic acid that presented a smooth and uniform appearance. Because the coating was desired only on the inner wall of the tubes, the outer walls and the borders were cleaned of the solidified acid using a sharp blade and then a wet cloth. The mass transfer rate was quantified in terms of the average mass transfer coefficient and was obtained by operating the reactors in recirculated batch mode using the experimental setup shown schematically in Fig. 2.4. The operation of the system involved recycling a constant flow rate of water at 25°C into the reactor causing the dissolution of the slightly soluble benzoic acid into the bulk fluid. The coated tubes were used as long as a smooth layer

of benzoic acid was present and covered all the internal surface of the tubes. The concentration of benzoic acid was monitored over time and determined via a UV spectrophotometer (UV-Mini 1240, Shimadzu) at 231 nm or 271 nm depending on the concentration range.

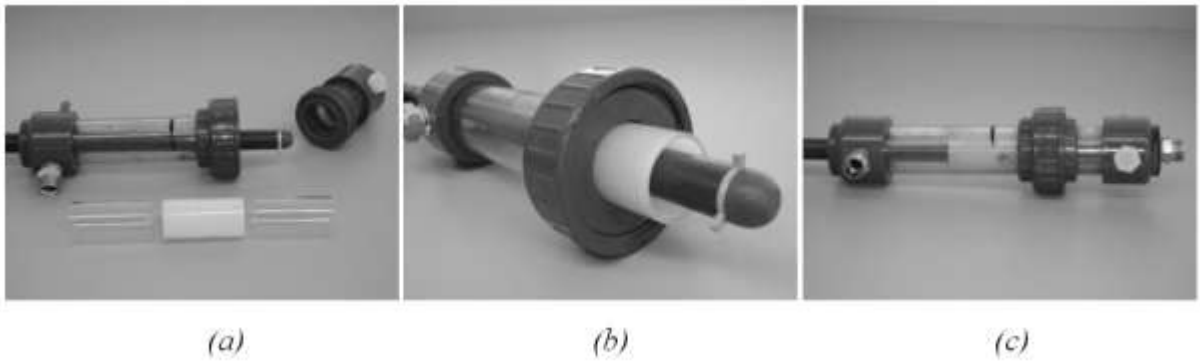

Fig. 2.3. L-shape annular reactor used in the experiments. (a) Disarmed PVC structure with glass tubes next to it. The inner wall of the glass tube located in the middle is coated with benzoic acid. (b) Coated glass tube fitted in the PVC structure. (c) Armed PVC structure with the coated glass tube placed at position B.

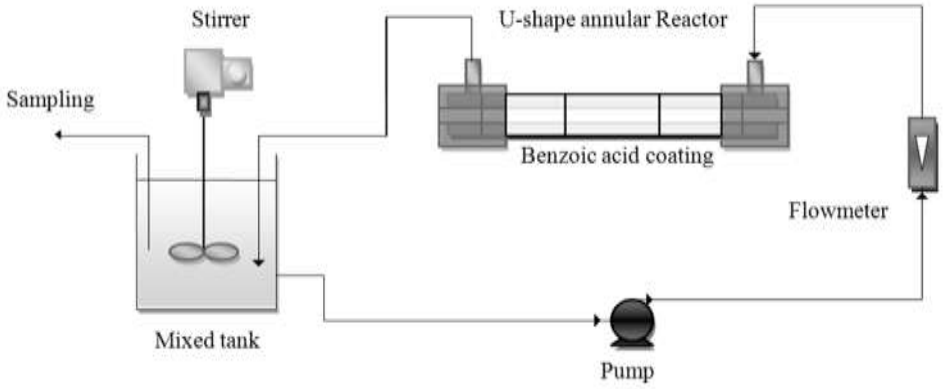

Fig. 2.4. Schematic of the recirculated batch annular reactor system used for determining the average mass transfer coefficients.

A mass balance of benzoic acid in the solution gives the following equation for the variation of the concentration with respect to time in the system:

$$C = C_{sat} + (C_0 - C_{sat})\, e^{-\frac{h_m A}{V} t} \qquad (2.21)$$

where C is the concentration of benzoic acid in the mixed tank, C_{sat} is the saturation concentration of benzoic acid in water, C_0 is the concentration of the acid at t = 0, h_m is the average mass transfer coefficient, A is the area of mass transfer, V is the total volume of liquid and t is the elapsed time. Using a non-linear regression method for fitting the concentration versus time data, the average mass transfer coefficients were estimated. Flow rates of 1.2, 3.4, 6.6, 8.5, 11.4, 18.0 and 24.6 L/min were used, representing a range of Reynolds numbers of approximately 500<Re<11000 (based on the annulus of the reactor). The total volume of liquid used in the system was 15.0 L of distilled water. For each flow rate, the average mass transfer coefficient was determined by triplicate runs. Each of the following configurations were studied in both reactors: coating of benzoic acid in all sections A, B and C (A+B+C); only section A (A) coated; only section B (B) coated; only section C (C) coated.

2.4. Results and discussion

2.4.1. Mass transfer experimental results

The benzoic acid concentration versus time data obtained in the recirculated batch system were fitted to the model given by Eq. (2.21) utilizing a non-linear regression method, from which the average mass transfer coefficients of the system were estimated. The model fit the experimental data closely, presenting correlation coefficients > 0.999 and standard errors for the mass transfer coefficients < 2%. The average mass transfer coefficients obtained for both reactor types operated under various hydrodynamic conditions and coating configurations are presented in Fig. 2.5. As expected, mass transfer coefficients increased monotonically with

flow rates. For both reactor configurations the average mass transfer coefficients in section A were much higher than those in sections B, and those in section B were in turn slightly higher than the ones in section C. Mass transfer coefficient in section A was nearly twice that of sections B and C indicating that more than half of the total mass transfer in the reactor happened in the first third of its volume. This result was the same for all the hydrodynamic conditions investigated (500<Re<11000). An important result is that the values of the average mass transfer coefficients obtained at each of the different sections were very similar for both reactor types. This finding indicates that in terms of average mass transfer efficiency, both annular reactor configurations perform similarly and therefore, there is no particular advantage of one over the other.

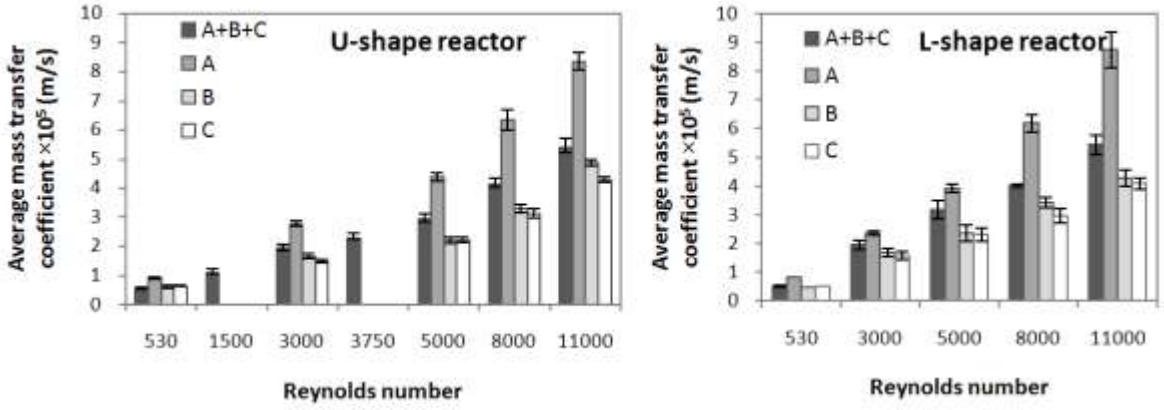

Fig. 2.5. Average mass transfer coefficients obtained for the U-shape and L-shape annular reactors operating under different hydrodynamic conditions. A, B and C indicate the sections coated with benzoic acid. The error bars represent the standard deviation obtained with triplicate runs.

The mass transfer data obtained in this work showed good agreement with those from other reported investigations where similar annular configurations were used. Fig. 2.6 compares the average mass transfer coefficients obtained for transitional and turbulent flows (3000<Re<11,000) with the values predicted by some of the correlations tabulated in Table

2.1. The average mass transfer coefficients obtained in section A coincided well with the results calculated with the correlations corresponding to developing flow, in particular with Eqs. (2.10) and (2.11). The experimental data from sections B and C were in close agreement with the predictions of the correlations proposed for completely developed flow. These results suggest that the abrupt expansion and change of direction that the fluid experiences at the inlet zone of both reactor geometries generate high turbulence, as well as a large near-surface concentration gradient, which results in high mass transfer in section A. The turbulence created in this region is then transported by convection and mass transfer decreases as the flow redevelops downstream of the entrance in sections B and C. Although not presented here, similar results were obtained for the laminar-flow data when compared with Eqs. (2.1) to (2.5).

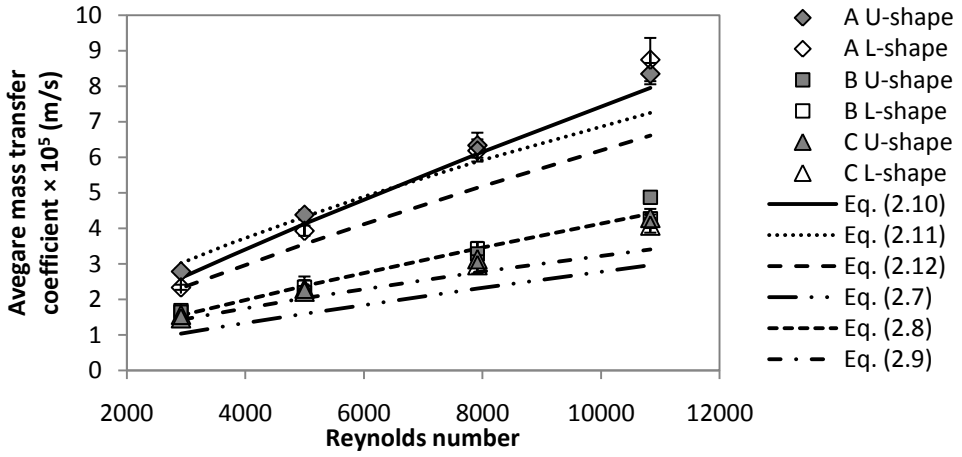

Fig. 2.6. Comparison of the average mass transfer coefficients obtained in the experiments with the ones estimated using different correlations reported in the literature. A, B and C indicate the sections coated with benzoic acid. The error bars represent the standard deviation obtained with triplicate runs.

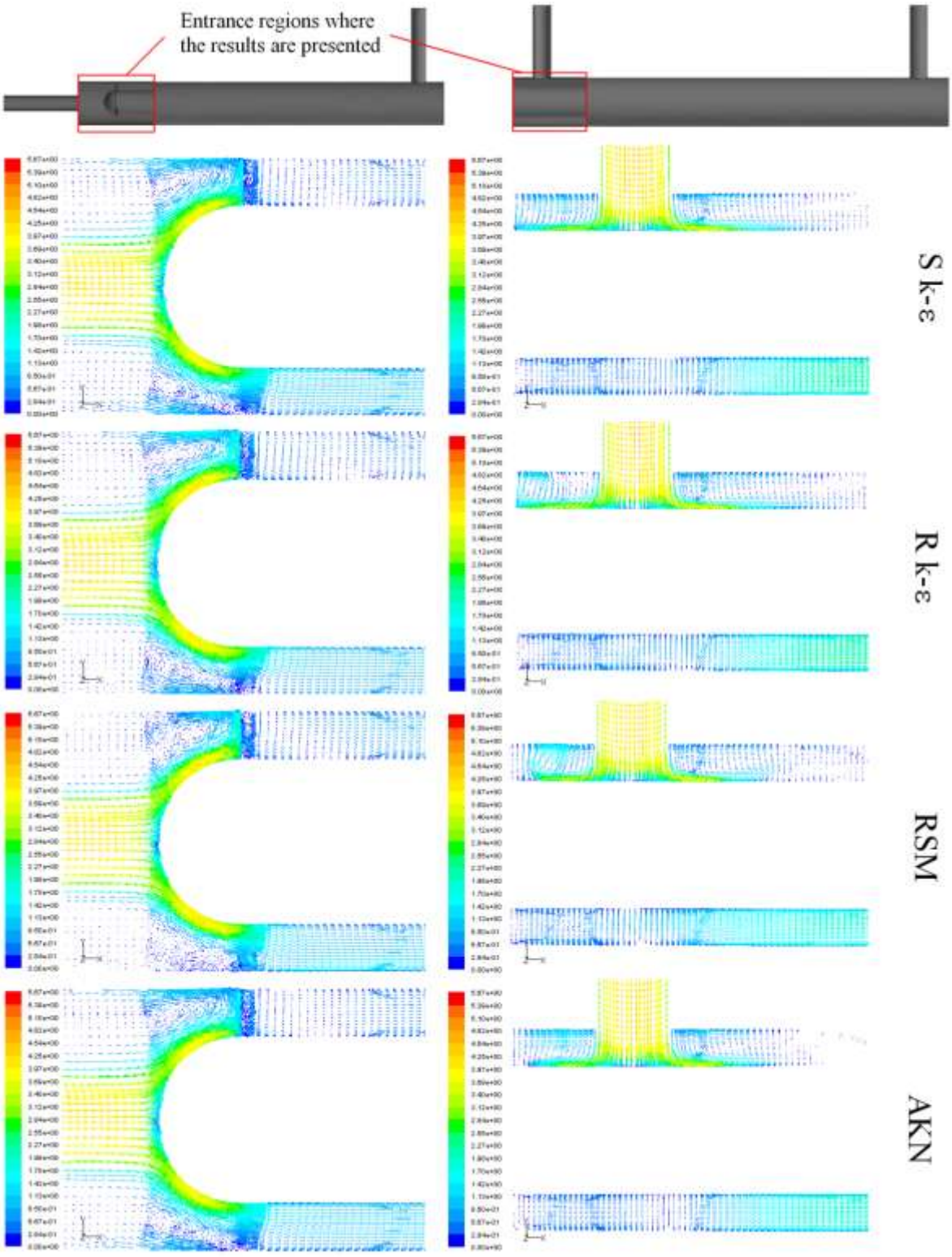

Fig. 2.7. Velocity vectors (m/s) on the longitudinal center plane at the inlet region of the L-shape (left) and U-shape (right) reactors using different turbulence models. The results correspond to a flow rate of 24.6 L/min (Re = 11,000).

2.4.2. CFD hydrodynamic simulations

CFD simulations of the annular reactors (U-shape and L-shape) operating at the same flow rates and conditions of the experiments were performed. From the perspective of hydrodynamic modeling, the inlet region of both annular reactors is the more challenging zone. The inlet flow impinges on the inner tube, from the top in the case of the U-shape reactor and from the front for the L-shape configuration, causing the split of the flow and the creation of flow separation, recirculation, and reattachment zones. Fig. 2.7 shows the velocity vector field at the inlet regions of both reactors which were obtained from the simulations performed at a flow rate corresponding to Re=11,000. The results correspond to the longitudinal center plane of the reactors. Similar velocity vector patterns were obtained in the simulations at the other flow rates. As it can be seen, the core velocity fields computed using the different turbulence models look somewhat similar. For example, all the simulations predicted the same recirculation zones, which in the case of the L-shape reactor were located at the entrance of the annular region (between the inner tube rounded end and the outer wall) and behind the holder prongs. The generation and location of such recirculation zones in similar reactor geometries were observed experimentally by Sozzi & Taghipour (2006) using PIV techniques.

Fig. 2.8 shows the velocity magnitude contours along the U-shape and L-shape reactor volumes computed using the R k-ε turbulence model and for Re=11,000. The same flow patterns were also found when using the other turbulence models as well as for the other flow rates. As seen in Fig. 2.8, the velocity magnitude distribution along the annular space for the L-shape reactor is more uniform than that for the U-shape reactor. The U-shape reactor shows higher velocities in the section opposite the inlet and outlet ports (bottom of the reactor) and a

low velocity region at the top. Such dissimilar velocity fields will produce very different local mass transfer at the walls of both reactor configurations (this topic is discussed further in Section 2.4.3). The veracity of these particular velocity distributions predicted by the CFD simulations was verified by letting the water flow in the reactors for a long time, so that the benzoic acid coatings were eroded by the stream at the regions of high velocity. The analysis of erosion patterns observed in both reactor configurations agreed with the CFD simulation predictions.

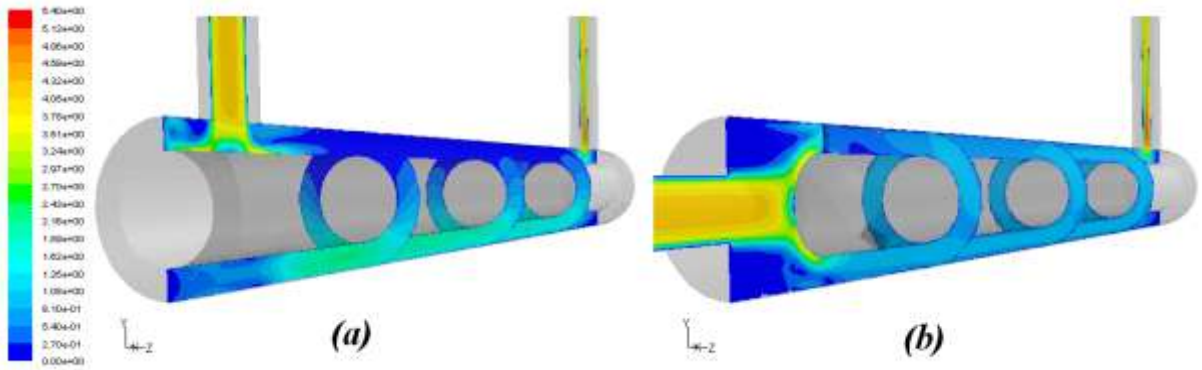

Fig. 2.8. Contours of velocity magnitude (m/s) in the U-shape (a) and L-shape (b) annular reactors calculated using the R *k*-ε model. The figure shows the longitudinal center plane and transversal planes at the middle of sections A, B and C. The results correspond to a flow rate of 24.6 L/min (Re = 11,000).

The previously analyzed results indicate that all the turbulence models under evaluation (S *k*-ε, R *k*-ε, RSM and AKN), indistinctly of the near-wall region model they utilized, were capable of somehow predicting the main characteristics of the core flow hydrodynamics within both annular reactors. However, accurate mass transfer prediction depends largely on the near-wall region flow modeling; consequently, the fact that a turbulence model can describe appropriately the core flow field does not guarantee its correct

prediction of the surface mass transfer phenomenon. This subject matter will be analyzed in the following section.

2.4.3. Comparison of CFD mass transfer predictions with experimental data

Having the CFD simulation results obtained for different flow rates and hydrodynamic models, the corresponding average mass transfer coefficients in the reactors were calculated using:

$$h_m = \frac{Q}{A}\ln\left(\frac{C_{sat} - C_i}{C_{sat} - C_o}\right) \tag{2.22}$$

where Q is the flow rate, C_i and C_o are the concentrations of benzoic acid at the inlet and outlet of the reactor, respectively. Eq. (2.22) is obtained by performing a mass balance over the system, assuming that the concentration of benzoic acid at the wall is constant and corresponds to the saturation concentration of the acid in water. Fig. 2.9 presents the average mass transfer coefficients calculated using the CFD simulation results for the U-shape configuration. Also, the experimental results are presented for comparison with the CFD simulations. The results obtained for the L-shape annular configuration were very similar to those of the U-shape and therefore not shown here.

Fig. 2.9a shows the results corresponding to the case where mass transfer was taking place at all the sections (A+B+C). It can be seen that the results for laminar flow regimes showed excellent agreement with the predictions by the laminar model. However, all the evaluated turbulence models to some extent underestimated the global mass transfer rates associated with all the flow rates. The AKN predictions were the ones having the closest agreement with the experimental data (around 10% error), followed by those of the RSM. More insight on the capabilities of the turbulence models to predict mass transfer is obtained

via the analysis of the results acquired for the individual sections (see Figs. 9b, c, d). All the turbulence models underestimated the mass transfer in section A, but the agreement between the results in sections B and C were quite close over the whole evaluation range (3000<Re<11,000). This result demonstrates that the disagreement found in the case corresponding to sections (A+B+C) is due to the underprediction computed by the turbulence models at section A. One possible reason for this discrepancy is that the turbulence models were not able to capture all the small eddies generated at the inlet, due to the sudden expansion of the flow. However, once the flow redeveloped through sections B and C, turbulence decreased and the models performed better.

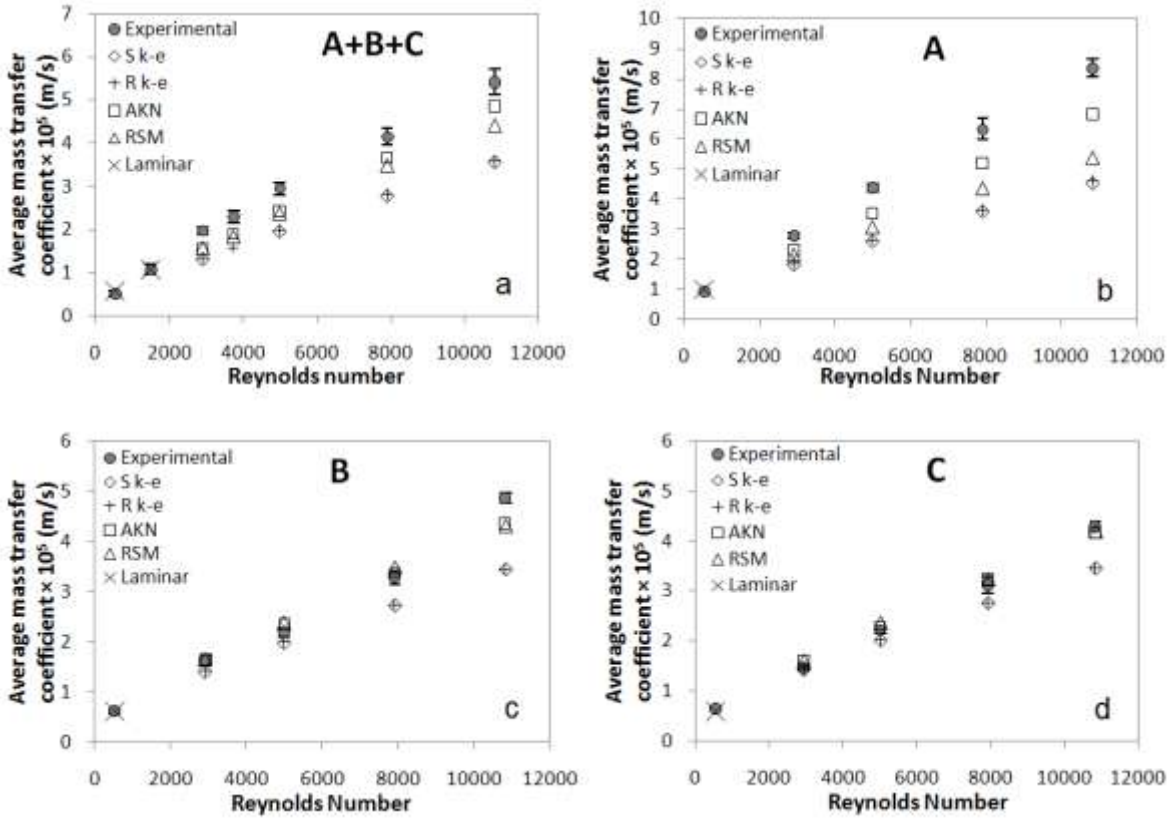

Fig. 2.9. Comparison of the average mass transfer coefficients obtained in the CFD simulations with the experimental values for the U-shape reactor. The results presented were obtained using different hydrodynamic models and at sections A, B and C of the reactor. The error bars represent the standard deviation obtained with triplicate runs.

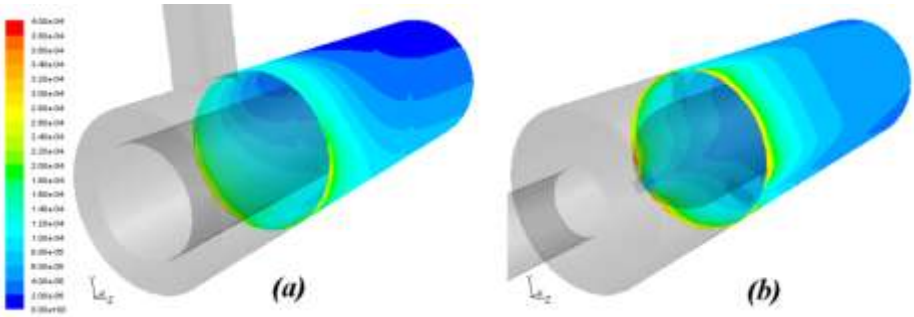

Fig. 2.10. Local mass transfer coefficient (m/s) distributions at entrance section A as computed using the AKN model and for a flow rate of 24.6 L/min (Re = 11,000). (a) U-shape, and (b) L-shape reactor configuration.

Further investigation on the liquid-to-wall mass transfer predicting capabilities of the hydrodynamic and near-wall models was carried out by analyzing their ability to predict local mass transfer coefficients. A user defined function (UDF) for calculating the local mass transfer coefficient (h) at the wall of the reactors was programmed and integrated into the CFD model using the following equation:

$$h = \frac{D_m\left(C_{sat} - C_a\right)}{\delta\left(C_{sat} - C_b\right)} \tag{2.23}$$

where C_a and C_b are the benzoic acid concentrations in the wall-adjacent cell and in the bulk of the fluid, respectively, and δ is the distance from the wall-adjacent-cell center to the wall. The three-dimensionality of the flow in the analyzed annular reactors, generated mainly by the specific inlet configurations, creates a two-dimensional local mass transfer distribution at the reactor wall. Fig. 2.10 shows the maps of local mass transfer coefficients in section A for both reactor configurations as computed utilizing the AKN model (Re=11,000). In the case of the L-shape configuration, local mass transfer at the wall is more uniform; however, three regions of low mass transfer are evident behind each of the lamp holder prongs. The local mass transfer distribution in the U-shape reactor presents high values at the bottom and low values

at the top of section A. These results are in accordance with the velocity field results obtained in Section 2.4.2, since higher mass transfer rates are expected in areas with higher fluid velocity gradients near the wall.

The most desirable way to evaluate these CFD simulations would be to compare the predictions with experimental measurements of local mass transfer throughout the walls. Unfortunately, such measurements were not within the scope of this work, nor there were any found in the open literature for the studied configurations. As a result, an alternative evaluation was performed utilizing the one-dimensional correlations reported in Table 2.1. From these correlations, a local mass transfer coefficient was calculated through differentiation according to:

$$h_x = \frac{\mathrm{d}\left(h_m x\right)}{\mathrm{d}x} \tag{2.24}$$

where x is the axial position. These data were compared with the average values at axial position x, calculated from the CFD-computed local mass transfer coefficients. The averaging was done around the circumference of the wall at each axial position (x). Fig. 2.11 presents the results obtained for both reactor configurations operating at Re=530, and for the L-shape configuration operating at Re=11,000. The results for the U-shape configuration and for other turbulent flow rates were similar and therefore not shown here.

As it can be seen in Fig. 2.11a, laminar CFD-computed local mass transfer coefficients were consistent with those calculated from the correlations, especially with the data of Ould-Rouis et al. (1995). Even though the different types of reactor inlets produced different local mass transfer distributions on the reactor wall (as shown in Fig. 2.10), the average values at an axial position x were not much different from one another. These results demonstrate the advantage of applying CFD modeling as it brings more insight into the analyzed system by

providing the local mass transfer coefficient at each point; information which cannot be obtained from the correlations. For the predictions of the turbulence models, the results presented in Fig. 2.11b show a better performance for the AKN model, followed by the RSM. AKN was able to predict higher local mass transfer coefficients in the entrance region and as a consequence, provided values closer to the data obtained from correlations (2.10) and (2.11). It should be noted that Eq. (2.10) had the closest agreement with the average mass transfer coefficients experimentally obtained in this work. For values of $x/d_e > 2$ ($x > 0.024$ m), the agreement with Eqs. (2.10) and (2.11) was excellent, but for values of $x/d_e < 2$ ($x < 0.024$ m) some underprediction with respect to Eq. (2.10) was found. Other investigations reported that the AKN model could successfully predict separating and reattaching flows downstream of a backward-facing step (Abe et al., 1994), so as liquid-to-wall mass transfer in pipes (Wang et al., 1996). The analyzed L-shape annular reactor involves most of the essential physics of these two systems. Fig. 2.11b also evidences that the difference in the predictions of the turbulence models happens in the entrance region. After $x/d_e > 5$ ($x > 0.06$ m) the predictions of all of the turbulence models are basically the same.

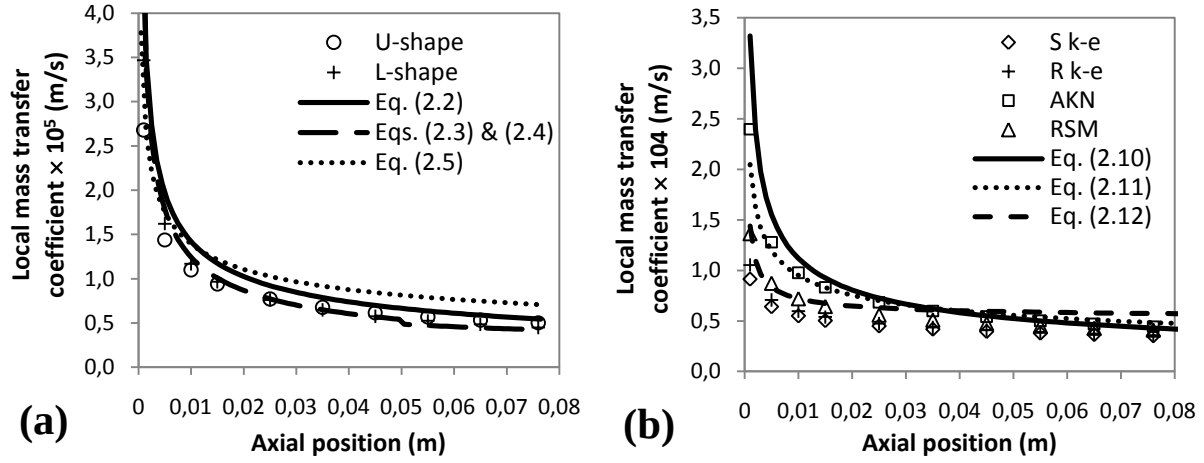

Fig. 2.11. CFD predictions of the local mass transfer coefficient along the reactor axis compare with values calculated from correlations. (a) Re=530, (b) Re=11,000, L-shape configuration.

Overall, AKN model provided better mass transfer predictions, particularly in section A. Based on the hydrodynamic simulations and the experimental evidences obtained in this investigation, it was not possible to find any significant difference between the flow fields computed using any of the *k*-ε-based turbulence models. Consequently, the better performance of the AKN model might be explained in terms of the large impact that near-wall region modeling has on surface mass transfer predictions. In this sense, it appears that for the systems under investigation, the LRN approach simulates better the near-wall region than the two-layer approach employed in the enhanced wall treatment.

The effect of perturbing flows, created by the inlet sections, on the average mass transfer coefficients in section A was investigated utilizing the AKN model. The values computed for both reactor configurations were compared with the results obtained for a long (0.6 m) annular configuration without inlet/outlet ports. In this way, no extra phenomena, such as recirculation, or flow expansion/compression exist at the inlet/outlet boundaries. This configuration was achieved by defining a plug-flow at the inlet and a fully developed flow at the outlet as the boundary conditions in the model. The results are presented in Table 2.3 as the ratio between mass transfer coefficients with and without the inlet sections. For the transitional and turbulent flow conditions, the mass transfer enhances with Reynolds number due to the presence of inlet ports. At Re=11,000 the average mass transfer coefficient in section A obtained with either a parallel or perpendicular inlet port is twice the value obtained without these ports. Interestingly, in the case of laminar flow, the mass transfer coefficient is lower when an inlet section is present. These results demonstrate the significant impact of the

inlet section on the reactor overall mass transfer performance, so as the importance of considering the inlet/outlet ports when modeling commercial-type annular reactors.

Table 2.3. Enhancement in the average mass transfer coefficient in section A due to perturbing flows created by the inlet sections. Results correspond to the ratio between the mass transfer coefficients obtained with and without inlet ports as computed by laminar (Re=530) and AKN (3000<Re<11000) hydrodynamic models.

Re	L-shape	U-shape
530	0.83	0.87
3,000	1.25	1.22
5,000	1.66	1.61
8,000	1.89	1.83
11,000	2.02	1.96

2.5. Conclusions

In this study, experiments and CFD simulations were carried out in order to evaluate the accuracy of different hydrodynamic models for the prediction of surface mass transfer in annular reactors. Two common reactor configurations (U-shape and L-shape) were tested within a range of flow rates corresponding to 500<Re<11,000.

The experiments performed in both annular reactors revealed that half of the surface mass transfer took place near the entrance region of the reactor. Also, both annular reactors provided similar mass transfer efficiencies; indicating that there was no particular advantage for either configuration in terms of mass transfer. However, if erosion of the surface material (e.g. catalyst) is an issue, the L-shape reactor which provides a more uniform near-wall velocity gradient might be a better option.

The turbulence models under evaluation (S *k*-ε, R *k*-ε, RSM and AKN) predicted comparable core flow hydrodynamics which were in agreement with previous PIV investigations of similar systems. The mass transfer measurements demonstrated that the laminar model was able to predict successfully the mass transport in laminar flows. On the other hand, the AKN and the RSM models performed well and predicted turbulent mass transfer in both annular reactors, except for a moderate underestimation at the entrance region where high turbulence and mass transfer rates were found. For the case where the entire reactor was analyzed, the relative error of the estimations for the AKN and RSM models were approximately 10% and 20%, respectively. The predictions of both turbulence models were accurate within the entire range of flow rates investigated, which included flows under transitional regime. Near-wall modeling was found to be critical in surface mass transfer simulations.

Inlet sections of annular reactors play an important role in the reactor hydrodynamics and consequently on its mass transfer performance. For that reason, these sections should be included in the annular reactor model.

The results obtained in this investigation make the AKN and RSM models very attractive for CFD-based simulations of turbulent annular reactors. The AKN model presents the advantage of being less memory and computational intensive than the RSM.

2.6. Acknowledgements

The author acknowledges financial support from the Natural Sciences and Engineering Research Council of Canada (NSERC) and BI PureWater (Canada) Inc. J. Esteban Durán also thanks the Universidad de Costa Rica.

2.7. References

Abe, K., Kondoh, T., & Nagano, Y. (1994). A new turbulence model for predicting fluid flow and heat transfer in separating and reattaching flows- I. Flow field calculations. *International Journal of Heat and Mass Transfer , 37* (1), 139–151.

Aravinth, S. (2000). Prediction of heat and mass transfer for fully developed turbulent fluid flow through tubes. *International Journal of Heat and Mass Transfer , 43*, 1399–1408.

Bakker, A., Haidar, A., & Oshinowo, L. (2001). Realize Greater Benefits from CFD. Chemical Egineering Process. *97* (3), 45–53.

Bird, R., Stewart, W., & Lightfoot, E. (2002). *Transport Phenomena, Second Ed.* New York: JohnWiley & Sons.

Castro, M. L., Priego, F., & Sanchez, N. (2008). Is dialysis alive as a membrane-based separation technique? *Trends in Analytical Chemistry , 27* (4), 315–326.

Davidson, L. (2003). *An Introduction to Turbulence Models.* Chalmers University of Technology, Sweden: Department of Thermo and Fluid Dynamics.

Dhotre, M., & Joshi, J. (2004). CFD Simulation of Heat Transfer in Turbulent Pipe Flow. *Industrial & Engineering Chemistry Research , 43*, 2816–2829.

Farias, S. R., Legentilhomme, P., & Legrand, J. (2001). Finite element simulation of mass transfer in laminar swirling decaying flow induced by means of a tangential inlet in an annulus. *Computer Methods in Applied Mechanics and Engineering , 190*, 4713–4731.

Fluent-Inc. (2006). *FLUENT 6.3 User's Guide. Chapter 12. Modeling Turbulence.* Lebanon, NH.

Ghosh, U., & Upadhyay, S. (1985). Mass Transfer to Newtonian and Non-Newtonian Fluids in Short Annuli. *AIChE Journal , 31* (10), 1721–1724.

Harriott, P., & Hamilton, R. (1965). Solid-liquid mass transfer in turbulent pipe flow. *Chemical Engineering Science , 20*, 1073–1078.

Houzelot, J., & Villermaux, J. (1977). Mass transfer in annular cylindrical reactors in laminar flow. *Chemical Engineering Science , 32*, 1465–1470.

Hrenya, C., Boilo, E., Chakrabarti, D., & Sinclair, J. (1995). Comparison of Low Reynolds Number *k*-ε Turbulence Model in Predicting Fully Developed Pipe Flow. *Chemical Engineering Science 1995 , 50* (12), 1923–1941.

Hsieh, W., & Chang, K. (1996). Calculation of wall heat transfer in pipe-expansion turbulent flows. *International Journal of Heat and Mass Transfer , 39* (18), 3813–3822.

Imoberdorf, G., Cassano, A., Irazoqui, H., & Alfano, O. (2007). Optimal design and modeling of annular photocatalytic wall reactors. *Catalysis Today , 129*, 118–126.

Jones, W., & Launder, B. (1972). The Prediction of Laminarization with a Two-Equation Model of Turbulence. *International Journal of Heat and Mass Transfer , 15*, 301–314.

Kapteijn, F., Deugd, R. M., & Moulijn, J. A. (2005). Fischer-Tropsch synthesis using monolithic catalysts. *Catalysis Today , 105*, 350–356.

Karim, A., Bravo, J., Gorm, D., Conant, T., & Datye, A. (2005). Comparison of wall-coated and packed-bed reactors for steam reforming of methanol. *Catalysis Today , 110*, 86–91.

Kirk, R., & Othmer, D. (2001). *Kirk-Othmer Encyclopedia of Chemical Technology* . New Jersey: John Wiley & Sons, Inc.

Koeltzsch, K. (2000). The height dependence of the turbulent Schmidt number within the boundary layer. *Atmospheric Environment , 34*, 1147–1151.

Launder, B., & Spalding, D. (1974). The numerical computation of turbulent flows. *Computer Methods in Applied Mechanics and Engineering , 3*, 269–289.

Launder, B., Reece, G., & Rodi, W. (1975). Progress in the development of a Reynolds-Stress turbulence closure. *Journal of Fluid Mechanics , 68*, 537–566.

Legrand, J., & Martemyanov, S. A. (1994). Turbulent mass transfer in small radius ratio annuli. *Journal of Applied Electrochemistry , 24* (8), 737–744.

Legrand, J., Legentilhomme, P., Neto, S. F., & Aouabed, H. (1997). Mass transfer in developing flows. *Electrochimica Acta , 42* (5), 805–811.

Lide, D. (2007). *CRC Handbook of Chemistry and Physics, 88th Edition* . Boca Raton: CRC.

Maestri, M., A.Beretta, Faravelli, T., Groppi, G., & Tronconi, E. (2007). Role of gas-phase chemistry in the rich combustion of H_2 and CO over a Rh/Al_2O_3 catalyst in annular reactor. *Chemical Engineering Science , 62*, 4992–4997.

Martemyanov, S., Skurygin, E., & Legrand, J. (1999). Turbulent mass transfer in the developing diffusion layer at large Schmidt numbers. *International Journal of Heat and Mass Transfer , 42* (13), 2357–2362.

Mobarak, A. A., Farag, H. A., & Sedahmed, G. H. (1997). Mass transfer in smooth and rough annular ducts underdeveloping flow conditions. *Journal of Applied Electrochemistry , 27*, 201–207.

Mohseni, M., & Taghipour, F. (2004). Experimental and CFD analysis of photocatalytic gas phase vinyl chloride (VC) oxidation. *Chemical Engineering Science , 59* (7), 1601–0609.

Moueddeb, H., Sanchez, J., Bardot, C., & Fick, M. (1996). Membrane bioreactor for lactic acid production. *Journal of Membrane Science , 114*, 59–71.

Nagano, Y., & Tagawa, M. (1990). An Improved *k*-ε Model in Boundary Layer Flows. *Journal of Fluids Engineering , 112*, 33–39.

Nallasamy, M. (1987). Turbulence models and their applications to the prediction of internal flows: A review. *Computers & Fluids , 15* (2), 151–194.

Nelissen, G., Bossche, B. v., Deconinck, J., Theemsche, A., & DAN, C. (2003). Laminar and turbulent mass transfer simulations in a parallel plate reactor. *Journal of Applied Electrochemistry , 33*, 863–873.

Nesic, S., Adamopoulos, G., Postlethwaite, J., & Bergstrom, D. (1993). Modelling of turbulent flow and mass transfer with wall function and low-Reynolds number closures. *The Canadian Journal of Chemical Engineering , 71*, 28–34.

Noulty, R., & Lealst, D. (1987). Diffusion Coefficient of Aqueous Benzoic Acid at 25°C. *Journal of chemical and engineering data , 32*, 418–420.

Ould-Rouis, M., Salem, A., Legrand, J., & Nouar, C. (1995). Etude numérique et expérimentale des transferts de matière et de quantité de mouvement dans un écoulement annulaire laminaire non établi. *International Journal of Heat and Mass Transfer , 38* (6), 953–967.

Papadias, D., Edsberg, L., & Björnbom, P. (2001). E!ect of eccentricity and interaction between kinetics and mass transfer on the behaviour of catalytic annular reactors: a comparison between lumped and distributed models. *Chemical Engineering Science , 56*, 4863–4878.

Patel, V., Rodi, W., & Scheuerer, G. (1984). Turbulence Models forNear Wall and Low Reynolds Number Flows: A Review. *AIAA Journal , 23*, 1308–1319.

Perry, R., & Green, D. (1997). *Perry's Chemical Engineers' Handbook* (7 ed.). New York: McGraw-Hill.

Pickett, D. J. (1979). *Electrochemical Reactor Design, 2nd Ed.* Amsterdam: Elsevier Scientific Publishing Company.

Rai, B., Sinha, A., Ghosh, U., Gupta, S., & Upadhyay, S. (1988). Force convective mass transfer in annuli. *Chemical Engineering Communications , 68*, 15–30.

Ranade, V. (2002). *Computational Flow Modeling for Chemical Reaction Engineering.* London: Academic Press.

Rosen, C., & Traegaardh, C. (1995). Prediction of turbulence high Schmidt number mass transfer using a low Reynolds number *k*-ε turbulence model. *The Chemical Engineering Journal , 59*, 153–159.

Ross, T., & Wragg, A. (1965). Electrochemical mass transfer studies in annuli. *Electrochimica Acta , 10*, 1093–1106.

Shih, T., Liou, W., Shabbir, A., Yang, Z., & Zhu, J. (1995). A new *k*-ε eddy viscosity model for high Reynolds number turbulent flows - model development and validation. *Computers Fluids , 24*, 227–238.

Sozzi, D., & Taghipour, F. (2006). Computational and experimental study of annular photo-reactor hydrodynamics. *International Journal of Heat and Fluid Flow , 27* (6), 1043–1053.

Spalding, D. (1971). Concentration Fluctuations in a Round Turbulent Free Jet. *Chemical Engineering Science , 26*, 95–107.

Sun, Z. M., Liu, B. T., Yuan, X. G., Liu, C. J., & Yu, K. T. (2005). New Turbulent Model for Computational Mass Transfer and Its Application to a Commercial-Scale Distillation Column. *Industrial Engineering Chemistry Research , 44*, 4427–4434.

Taghipour, F., & Mohseni, M. (2005). CFD Simulation of UV Photocatalytic Reactors for Air Treatment. *AIChE Journal , 51* (11), 3039–3047.

Thakre, S., & Joshi, J. (2000). CFD Modeling of Heat Transfer in Turbulent Pipe Flows. *AIChE Journal , 46* (9), 1798–1812.

Thakre, S., & Joshi, J. (2002). Momentum, Mass and Heat Transfer in Single Phase Turbulent Flow. *Reviews in Chemical Engineering , 18*, 83–293.

Tomasic, V., Jovic, F., & Gomzi, Z. (2008). Photocatalytic oxidation of toluene in the gas phase: Modelling an annular photocatalytic reactor. *Catalysis Today , 137*, 350–356.

Wang, S., & Mujumdar, A. (2005). A comparative study of five low Reynolds number *k*-ε models for impingement heat transfer. *Applied Thermal Engineering , 25*, 31–44.

Wang, Y., & Postlethwaite, J. (1997). The application of low Reynolds number *k*-ε turbulence model to corrosion modelling in the mass transfer entrance region. *Corrosion Science , 39* (7), 1265–1283.

Wang, Y., Postlethwaite, J., & Bergstrom, D. (1996). Modelling mass transfer entrance lengths in turbulent pipe-flow with applications to small cathodes for measuring local mass transfer rates. *Journal of Applied Electrochemistry , 26*, 471–479.

Wilcox, D. (2006). *Turbulence modeling for CFD.* La Cañada, Calif.: DCW Industries.

Wolfstein, M. (1969). The Velocity and Temperature Distribution of One-Dimensional Flow with Turbulence Augmentation and Pressure Gradient. *International Journal of Heat and Mass Transfer , 12*, 301–318.

Yimer, I., Campbel, I., & Jiang, L.-Y. (2002). Estimation of the Turbulent Schmidt Number from Experimental Profiles of Axial Velocity and Concentration for High-Reynolds-Number Jet Flows. *Canadian Aeronautics and Space Journal , 48* (3), 195–200.

Zahran, R. R., Sedahmed, G. H., Abdelwahab, O. E., & El-Sarraf, W. M. (2006). Mass-Transfer-Controlled Impingement Corrosion at the Jet Inlet Zone of an Annulus under Turbulent Flow. *Industrial & Engineering Chemistry Research , 45*, 1160–1166.

3. MODELING OF ANNULAR REACTORS WITH SURFACE REACTION USING COMPUTATIONAL FLUID DYNAMICS (CFD) [2]

3.1. Introduction

Coated-wall reactors with surface reaction have gained special attention among the chemical engineering community since the early 1950's (Baron et al., 1952). In this type of reactors, the catalyst is located in a layer attached to the inner wall while the fluid, gas or liquid, flows along the tube. Low pressure drop, easy temperature control of the catalytic surface, and nearly isothermal reaction conditions are the recognized advantages for this reactor configuration (Goyal et al., 1988). However, mass-transfer limitations could be an issue in these reactors depending on the kinetics of the surface reaction, and the operating conditions of the system. In addition to the tubular reactor shape, the annular shape is commonly utilized. This latter configuration offers lower diffusion path (which lowers the radial mass transfer resistance) and higher surface-to-volume ratios (Houzelot & Villermaux, 1977).

Coated-wall tubular and annular reactors have been investigated for many different heterogeneous reactions such as hydrogenation of carbon monoxide to methane (Dalai & Bakhshi, 1992; Schehl et al., 1977), the catalytic partial oxidation of propene to acrolein (Redlingshöfer et al., 2002), partial oxidation of methane into syngas (Deutschmann & Schmidt, 1998), steam reforming of methanol (Karim et al., 2005), Fischer-Tropsch synthesis (Kapteijn et al., 2005), indirect internal reforming solid oxide fuel cells (Dokamaingam et al., 2009), and photocatalytic degradation of organic compounds in aqueous and gaseous streams

[2] A version of this chapter has been published.
Duran, J.E., Mohseni, M., & Taghipour, F. (2010). Modeling of annular reactors with surface reaction using computational fluid dynamics (CFD). *Chemical Engineering Science*, *65*, 1201–1211.

(Boulinguieza et al., 2008; Mohseni & Taghipour, 2004; Pareek et al., 2003; Tomasic et al., 2008).

Models of isothermal coated-wall tubular and annular reactors have been developed at different levels of complexity. The most simple and less computationally expensive is the one-dimensional (1-D) model which considers plug flow in the axial direction and mass transfer occurring through the fluid boundary layer near the catalyst surface. Mass transfer coefficients are estimated by semiempirical correlations applicable to laminar (Biard et al, 2007; Tomasic et al., 2008) or turbulent flow regimes (Senkan et al., 1976; Schehl et al., 1977). 1-D models have shown accurate predictions in simple reaction systems where the corresponding model assumptions are valid and for which proper semiempirical correlations exist. Berger & Kapteijn (2007) recently developed criteria based on the observed conversion to allow for neglecting radial concentration gradients and using the simple plug-flow model to describe the reactor performance and to determine reaction kinetics. Two-dimensional (2-D) models have also been developed. In most of these works, laminar flow regime with a parabolic or plug-flow profile of fluid velocity has been assumed and the governing equations have been solved by means of analytical (Gill et al., 1975; Lupa & Dranoff, 1966; Schmidt, 1963) or numerical methods (Goyal et al., 1988; Houzelot & Villermaux, 1977; Imoberdorf et al., 2007; Tomasic et al., 2008). In some investigations, 2-D Navier–Stokes equations coupled with energy and mass balances have been directly solved by the use of computational fluid dynamic (CFD) methods giving more accurate results (Benedetto et al., 2003; Deutschmann & Schmidt, 1998; Dokamaingam et al., 2009; Duran et al., 2009b). The most computationally expensive are the three-dimensional (3-D) models. The solution of these models involves solving the mass, momentum and species conservation equations, and if applicable, the energy conservation equation using CFD methods. As expected, the computer time increases with the complexity

of CFD based models, but so does the accuracy and applicability of their predictions. Some of the systems simulated and analyzed with 3-D CFD models include oxidation processes in monoliths (Canu & Vecchi, 2002; Holmgren & Andersson, 1998) and heterogeneous photocatalysis for air treatment (Mohseni & Taghipour, 2004; Taghipour & Mohseni, 2005).

Most of the research carried out to date on modeling the coated-wall tubular and annular reactors has dealt with gaseous systems under laminar flow regime. However, the applications of this reacting system in emerging water purification processes (e.g., photocatalytic degradation of pollutants, residual H_2O_2 decomposition), in membrane reactors, and in some other technologies, warrants investigation of proper models for simulating liquid systems operating under either laminar or turbulent flow conditions. Since the efficiency of coated-wall systems with surface reaction is prone to mass transfer limitation, it is essential that these models perform correctly over the whole spectrum of possible operating conditions: from completely mass transport limited to surface reaction rate limited. In particular, the experimental evaluation of turbulence and near-wall models is required. To the author's knowledge, no research has been reported in the open literature in this area. Near-wall modeling of turbulent flows needs special attention, as the thickness of the mass transfer boundary layer in liquid systems (where $Sc \approx 1{,}000$) is just a few micrometers and also the chemical reaction is taking place at the wall.

This work has focused on applying CFD for modeling single-phase liquid fluid flow with an isothermal heterogeneous surface reaction occurring at the catalyst-coated outer wall of an annular reactor. The objective was to experimentally evaluate the performance of different hydrodynamic models to predict the kinetic behaviour of the reactor under different diffusion limiting conditions. The heterogeneous decomposition of hydrogen peroxide over a Mn/Al oxide catalyst at 298 K was utilized as a model reaction. An annular reactor

configuration with inlet parallel and outlet perpendicular to the main reactor axis (L-shape), which is commonly found in industrial reactor geometries, was studied. Commercial CFD code Fluent® 6.3.26 was used to perform the simulations.

3.2. CFD modeling

3.2.1 Governing equations

The evaluation of CFD modeling of annular reactors under different diffusion limiting conditions was achieved by analyzing the reactor over a broad range of hydrodynamic conditions and surface reaction rate constants. The Reynolds number (Re) range analyzed was between 500 and 11,000 (calculated based on the equivalent diameter of the annular region of the reactor), in which laminar, transient, and turbulent flow regimes were present. For the simulations having 500<Re<2,100, the laminar hydrodynamic model was used, whereas for those with 2100<Re<11,000 a Reynolds-averaged Navier–Stokes Equations (RANS) approach was taken.

3.2.1.1. Laminar flow

Assuming that the fluid (water) is Newtonian, incompressible, isothermal, non-reactive, with constant physical properties and under laminar steady state flow, the governing equations for modeling the system are as follows (Ranade, 2002):

Continuity equation:

$$\nabla \cdot (U) = 0 \qquad (3.1)$$

Momentum conservation equation:

$$\nabla \cdot (\rho UU) = -\nabla P - \nabla \cdot \tau \tag{3.2}$$

with the viscous stress tensor:

$$\tau = \mu\left(\nabla U + \nabla U^T\right) - \frac{2}{3}\mu \nabla \cdot UI \tag{3.3}$$

Conservation of species equation:

$$\nabla \cdot (\rho U m_i) = -\nabla \cdot J_i \quad , \quad i = 1, 2, \ldots, N-1 \tag{3.4}$$

with the diffusive flux of species *i* estimated using Fick's first law of diffusion:

$$J_i = -D_m \nabla(\rho m_i) \tag{3.5}$$

In Eqs. (3.1) – (3.5), ρ is density, U is velocity, P is pressure, τ is viscous stress tensor, μ is molecular viscosity, I is unit tensor, m_i is mass fraction of species i, J_i is diffusive flux of species i, N is the total number of species, and D_m is the molecular diffusivity of species i in the mixture.

3.2.1.2. Turbulent flow

Under the same assumptions stated for the laminar flow model, the Reynolds averaged Navier-Stokes (RANS) turbulence modeling approach involves solving the time-averaged continuity equation (3.6), momentum conservation equation (3.7), and conservation of species equation (3.8) which are expressed as (Ranade, 2002):

$$\nabla \cdot \left(\overline{U}\right) = 0 \tag{3.6}$$

$$\nabla \cdot \left(\rho \overline{U}\,\overline{U} + \rho \overline{uu}\right) = -\nabla \overline{P} - \nabla \cdot \overline{\tau} \tag{3.7}$$

$$\nabla \cdot \left(\rho \overline{U}\,\overline{m_i} + \rho \overline{um'_i}\right) = -\nabla \cdot \overline{J}_i \quad , \quad i = 1, 2, \ldots, N-1 \tag{3.8}$$

where the overbar indicates a time-averaged value, and u and m'_i are fluctuating flow velocity and mass fraction of species i, respectively. Time averaging of the basic governing equations

of flow processes leads to the appearance of apparent stress gradients $\left(\rho\overline{uu}\right)$ and mass transfer fluxes $\left(\rho\overline{um'_i}\right)$ associated with turbulent motion. The main challenge in modeling turbulent flow lies in the specification of these turbulent stresses and mass fluxes in terms of the time-averaged variables. Generally, for most engineering flow modeling applications, this so-called closure problem is solved by introducing a turbulence model. Several turbulence models have been proposed (e.g., Nallasamy, 1987; Wilcox, 2006), but no turbulence model is universally accepted to be superior for all conditions. Proper turbulence models need to be selected according to the problem under consideration.

The closure problem associated with the specification of the mass transfer fluxes $\left(\rho\overline{um'_i}\right)$ has been typically solved by analogy to the linear approximation for the Reynolds stresses (or to Fick's first law of diffusion):

$$\rho\overline{um'_i} = -D_t\nabla\left(\rho\overline{m_i}\right) \tag{3.9}$$

where D_t is the so-called eddy (or turbulent) diffusivity for species concentration. Combining Eqs. (3.9), (3.8), and the time-averaged version of Fick's first law of diffusion (Eq. (3.5)), results in the convection-diffusion turbulent mass transfer equation applicable to our case:

$$\nabla\cdot\left(\rho\overline{U}\,\overline{m_i}\right) = \nabla\cdot\left[\left(\rho D_m + \frac{\mu_t}{Sc_t}\right)\nabla\overline{m_i}\right] \tag{3.10}$$

with μ_t, the turbulent viscosity and Sc_t, the turbulent Schmidt number, defined as the ratio between the turbulent viscosity and the turbulent diffusion:

$$Sc_t = \frac{\mu_t}{\rho D_t} \tag{3.11}$$

A value of $Sc_t = 0.7$ was used in the simulations as recommended in various references (e.g., Spalding, 1971; Yimer et al., 2002).

Four hydrodynamic turbulence models were evaluated against experimental results in this investigation: the widely used standard k–ε model (S k–ε) (Launder & Spalding, 1974), the realizable k–ε model (R k–ε) (Shih et al., 1995), the Reynolds stress model (RSM) (Launder et al., 1975), and the low Reynolds number k–ε turbulence model developed by Abe et al. (1994) (AKN). Near-wall modeling for the S k–ε, R k–ε and RSM models were performed with the enhanced wall treatment approach available in the commercial CFD software utilized in the study (Fluent). This near-wall modeling method combines a two-layer model applicable in regions with fine near-wall meshes, with enhanced wall functions used in regions with coarse meshes. When using the enhanced wall treatment, it is necessary thus to construct a proper fine mesh where the viscosity-affected near-wall region is desired to be fully resolved. Details of this near-wall modeling method can be found in the Fluent manual (Fluent-Inc., 2006). On the other hand, the AKN near-wall modeling approach incorporates wall-damping effects on the empirical constants and functions in the turbulence transport equations. This approach enables the extension of the k–ε turbulence model all the way to the wall. The AKN model has shown promising results in modeling near-wall heat and mass transfers (Duran et al., 2009a; Wang & Mujumdar, 2005; Wang et al., 1996). Further details of all five hydrodynamic models can be found in the cited references.

3.2.2 Geometrical model

The model annular reactor geometry studied in the present work is shown with its dimensions in Fig. 3.1. For the simulations corresponding to transient and turbulent flows, the inlet and outlet tubes were chosen to be at least 45 diameters in length to ensure that a fully developed flow was established at the entrance of the reactor, and at the outlet boundary. For

the case of laminar flow simulations, the outlet tube was defined as 75 diameters in length. The reactor inner tube holder consisted of three prongs (3 mm wide × 6 mm long × 3 mm thick) located 120° one from another.

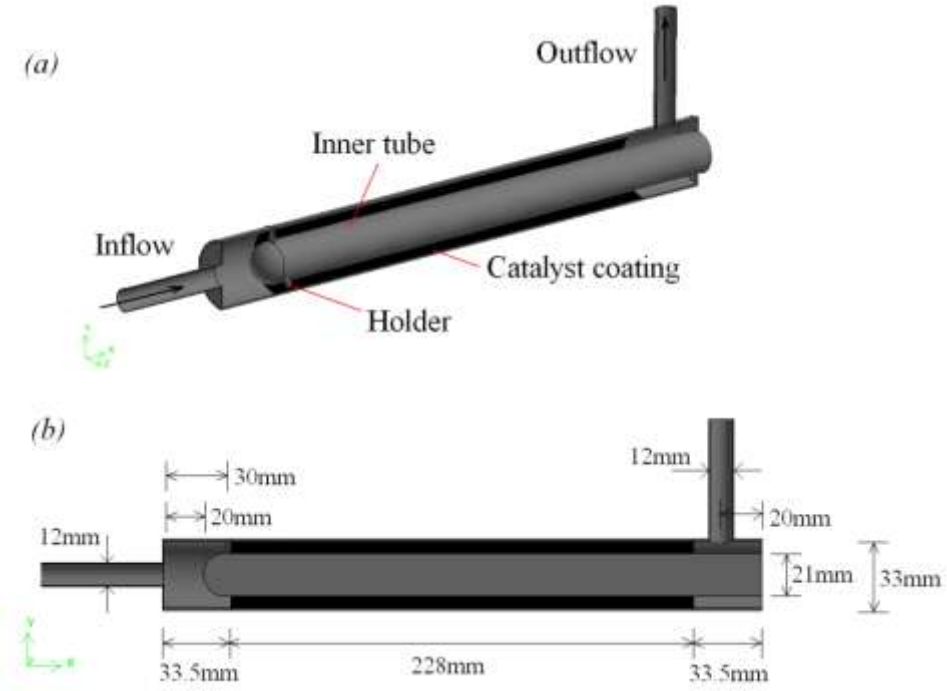

Fig. 3.1. Schematic diagram of the L-shape coated-wall annular reactor: (a) reactor cut-off showing the internal components, (b) reactor dimensions.

3.2.3. Mesh structure

When modeling turbulent flow using either enhanced wall treatment or low Reynolds number turbulence model approaches, it is fundamental to apply a mesh fine enough that allows solving the governing equations all the way to the wall. Based on the results of our previous study (Duran et al., 2009a), a y^+ smaller than 0.5 at the wall-adjacent cell, and at least 10 cells within the viscosity-affected near-wall region ($Re_y < 200$) were defined in all the

simulations performed in this investigation. A commercial mesh generator (Gambit® 2.2.30) was used to create the grid. Structured hexahedral cells were used to discretize the physical domain, except for the region of the inner tube holder, where it was necessary to split the reactor domain and use unstructured cells (Fig. 3.2). For the annular region, where the surface reaction took place, a boundary-layer mesh was setup. The utilized grids had approximately 1.3 million volume cells and they were verified to give mesh-independent results.

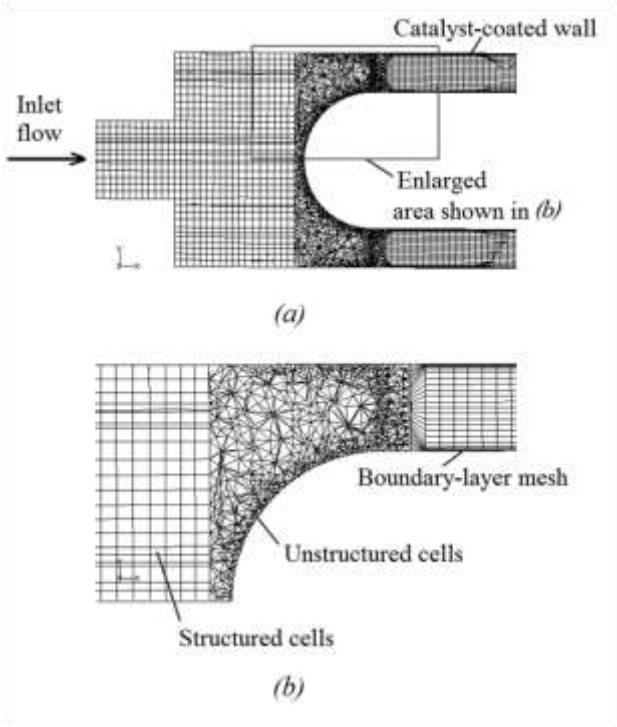

Fig. 3.2. Sections of mesh used in the L-shape reactor: (a) longitudinal cut of the entrance zone, (b) enlargement of the inner-tube-holder region showing different types of mesh cells utilized.

3.2.4. Boundary conditions

The boundary conditions for the CFD models were defined as follows. At the inlet, the mass flow rate of the fluid was specified. The direction of the flow was defined normal to the boundary. For the cases corresponding to turbulent flow, the hydraulic diameter was fixed at

12 mm and the turbulence intensity (TI) was set with values close to 5%. The TI was estimated for each case based on the formula TI = 0.16 $Re^{-1/8}$. This formula calculates the turbulence intensity at the core of fully developed flows (Fluent-Inc., 2006). At the outlet, a fully developed flow (outflow) condition was applied. At all the walls, a no-slip boundary condition was imposed. Also, zero diffusive flux of species was specified at the walls, except for the walls coated with the catalyst where the following boundary condition was defined:

$$J_i \cdot \hat{n} = R_i^S \qquad (3.12)$$

here $\hat{n}$ is a unit vector normal to the surface and R_i^S is the rate of production/depletion of species *i* arising from the surface.

3.2.5. Physical properties

The process studied in this investigation was the isothermal heterogeneous decomposition of hydrogen peroxide in an aqueous stream at 298 K. The concentrations of hydrogen peroxide utilized were very low (below 20 mg/L); consequently, the physical properties of water were assumed for the system. At 298 K the viscosity and the density of water are 8.9×10^{-4} Pa·s and 997 kg/m^3, respectively (Lide, 2007). The assumed diffusion coefficient of hydrogen peroxide in water was 1.3×10^{-9} m^2/s (Csoka & Nagy, 2004).

3.2.6. Surface chemistry model

The isothermal heterogeneous decomposition of hydrogen peroxide over a Mn/Al oxide catalyst ($H_2O_2 \rightarrow H_2O + ½\ O_2$) was selected as a model reaction for the experimental evaluation performed in this investigation. Under the experimental conditions utilized, the

reaction followed first-order kinetics (refer to Section 3.4). Thus, the rate of decomposition of hydrogen peroxide in the system was given by

$$R^{S}_{H_2O_2} = M_W k'' C_{H_2O_2,S} \quad (3.13)$$

where M_W is the H_2O_2 molar weight, $C_{H2O2,S}$ the H_2O_2 molar concentration at the catalyst surface, and k'' is the intrinsic surface reaction rate constant.

The "laminar finite rate" model which ignores the effect of turbulent fluctuations on reaction rates was chosen for reaction modeling. When chemical reactions are slow with respect to mixing (Da<< 1), turbulent mixing will be complete before the reaction can take place, and the contributions of fluctuating concentrations may therefore be neglected (Ranade, 2002).

3.2.7. Numerical solution method and strategy

Commercial CFD code Fluent® 6.3.26 was used to perform the simulations. The segregated steady-state solver was used to solve the governing equations. Second order upwind discretization scheme was employed except for pressure for which PRESTO! was selected. The SIMPLE algorithm was chosen for the pressure-velocity coupling. Convergence of the numerical solution was assured by monitoring the scaled residuals to a criterion of at least 10^{-4} for the continuity and momentum variables, and 10^{-6} for concentration. Additionally, the variation of velocity magnitude at several points of the computational domain located in areas of high velocity gradients was used as the indicator of convergence.

Taking advantage of the fact that the reaction of hydrogen peroxide did not affect the velocity field within the reactor, the CFD model was solved in two steps. First, the equations of continuity and conservation of momentum were solved for getting the flow field across the

computational domain. Then, the velocity values were kept "frozen" and the equation of conservation of species was solved using the converged flow solution. This solving strategy saves computation time and brings stability to the solution.

3.3. Experimental

3.3.1. Catalyst preparation and characterization

The manganese/aluminum oxide based catalyst was simultaneously synthesized and deposited on the required surface as explained next. 12 g of aluminum nitrate ($Al(NO_3)_3$ certified ACS from Fisher Sci.) were dissolved in 10 mL of high purity deionized water, and then mixed with 10 mL of manganese nitrate solution ($Mn(NO_3)_2$ 45–50% + HNO_3 <5% from Aldrich) to prepare a batch of the coating solution. The surfaces to be coated (previously sandblasted to improve the adhesion of the coating) were impregnated with the coating solution. Once the surfaces presented a uniform film of the coating solution, the pieces were heated in an oven at 180°C for at least 5 hours. Under those conditions, the metal nitrates decomposed and formed the corresponding Mn/Al oxides (Pacewska & Keshr, 2002; De Bruijn, et al., 1981). Several (at least five) coating layers (one over the other) were deposited onto the surface to obtain a uniform coating. Each time a new layer was deposited, the surface was washed with deionized water to remove any loose material. Also, when a used catalyst surface needed to be "regenerated", fresh coating layers were deposited onto the surface.

Two characterization studies, namely X-ray diffraction (XRD) (Siemens D5000) and scanning electron microscopy (SEM) combined with energy dispersive X-ray analysis (EDX) (Philips XL-30), were performed on fresh synthesized and used catalyst samples.

3.3.2. Experimental setups and methods

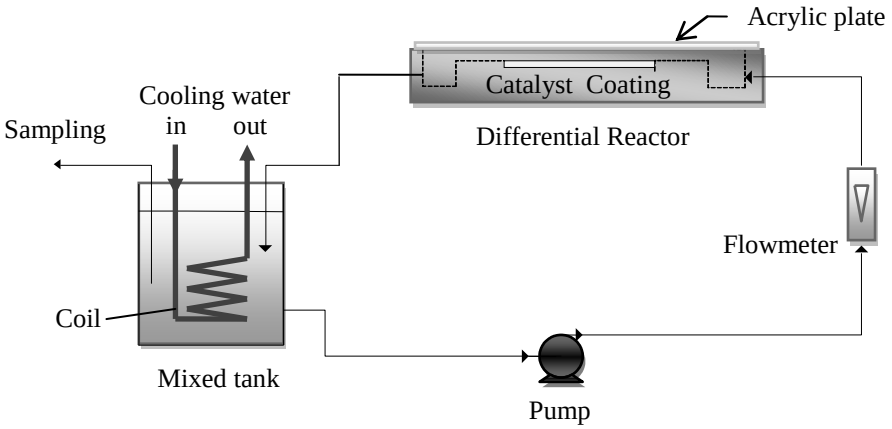

Fig. 3.3. Schematic of the re-circulating batch system used for determining the intrinsic kinetics of the reaction.

3.3.2.1. Determination of intrinsic reaction kinetics

The first part of the experimental work involved the determination of the intrinsic kinetics for the decomposition of hydrogen peroxide over the synthesized Mn/Al oxide catalyst at 298 K. The experiments were conducted in a differential reactor (i.e., a reactor with very low conversion per pass) equipped with three glass slides (25mm×75mm each) coated with the catalyst according to the previously described method (Section 3.3.1). The reactor consisted of a 63-mm-wide aluminum block designed to allow the H_2O_2 solution to flow through a 225 mm long passage of 25 mm (width) and 3 mm (height), and over the coated glass plates. The differential reactor was set up in a re-circulating batch system as shown schematically in Fig. 3.3. 700 mL of hydrogen peroxide solution (prepared with ACS-grade 30% H_2O_2 solution from Fisher Sci.) with an initial concentration of approximately 20 mg/L was charged in the mixed tank (800 mL glass beaker), and then pumped through the reactor

using a gear pump (Micropump 221/56C). Samples were collected from the well mixed tank every 10 min over a period of 80 min. Good mixing conditions in the tank were achieved due to the high re-circulating flow rates used; however, in a few runs where the flow rates were low, a magnetic stirrer was utilized. The temperature of the system was kept at 298.0 K ± 0.5 K, and was measured with a mercury thermometer (H-B, USA). Temperature control was achieved passing cold water through a copper coil submerged in the tank.

3.3.2.2. Quantification of coated-wall annular reactor performance

The second part of the experimental work sought the quantification of the performance of a coated-wall annular reactor prototype in decomposing H_2O_2 under different hydrodynamic conditions (flow rates). This information was then used to evaluate CFD simulations. The reactor prototype had the same dimensions as the geometrical model described in Fig. 3.1. The reactor structure was made of PVC and included a union that allowed for fitting catalyst-coated glass tubes in the inside (see Fig. 3.4). The Mn/Al oxide catalyst was coated on the inner wall of glass tube halves (76 mm long and 33 mm inner diameter) as shown in Fig. 3.4a. Six tube halves were put together using electrical tape to form a 228-mm-long 33-mm-inner-diameter coated tube. This coated tube had an outer diameter slightly smaller than the inner diameter of the PVC unit, so that the glass tube could fit inside the PVC structure (see Fig. 3.4b). The reacting system was operated in re-circulating batch mode using an experimental setup similar to the one shown schematically in Fig. 3.3, in which the differential reactor was substituted with the coated-wall annular reactor. In this experimental setup, the tank was a 3 L plastic beaker and the pump was a magnetic drive centrifugal pump (Flotec MDR6OT-X03). The temperature measurement and control were performed with the same equipment explained in Section 3.3.2.1. The operation of the system

involved re-circulating the H_2O_2 aqueous solution (approximately 20 mg/L initial concentration) at 25°C and constant flow rate through the reactor for 80 min, and taking samples every 10 min. Flow rates of 1.2, 3.4, 6.6, 11.4, and 24.6 L/min were used, representing a range of Reynolds numbers between 500 and 11,000. The total volume of liquid in the system was 2.50 L of H_2O_2 solution prepared using distilled water. Triplicate runs were performed for each studied flow rate.

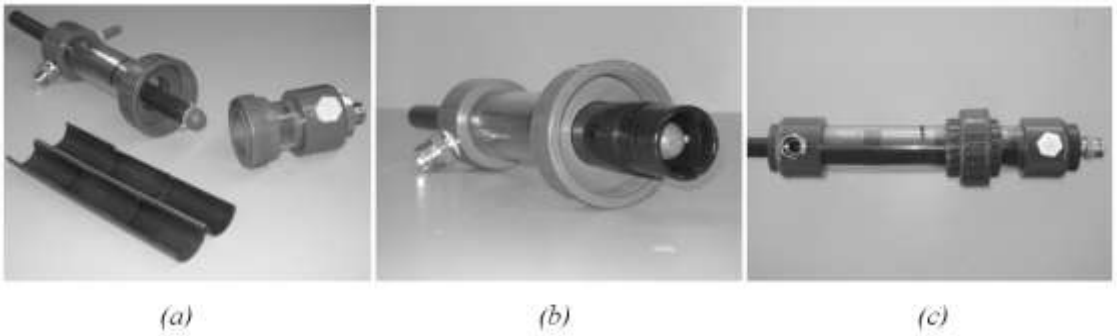

Fig. 3.4. Coated-wall annular reactor used in the experiments: (a) disarmed PVC structure with catalyst-coated glass halves next to it, (b) catalyst-coated glass tube fitted in the PVC structure, (c) armed PVC structure.

3.3.2.3. Analytical methods

The concentration of hydrogen peroxide was determined via UV spectrophotometry utilizing the I_3^- method (Klassen et al., 1994). The spectrophotometer used was a Shimadzu UV-Mini 1240 and all the chemicals employed (KI, NaOH, $(NH_4)_6Mo_7O_{24}{\cdot}4\ H_2O$, and HKP, all certified ACS) were used as received from Fisher Scientific.

3.4. Dynamics of a real first-order catalytic reactor in re-circulating batch mode operation

Catalytic reactors that exhibit low conversion of reactants in one single pass are commonly operated in re-circulating batch mode. Typical examples are heterogeneous photocatalytic reactors and differential reactors utilized for determining reaction rate kinetics. A simplified schematic diagram of such a system is shown in Fig. 3.5. A model for the dynamic process of the catalytic reaction within the reactor as well as mixing within the tank is developed next. The case of a first-order catalytic reaction is considered.

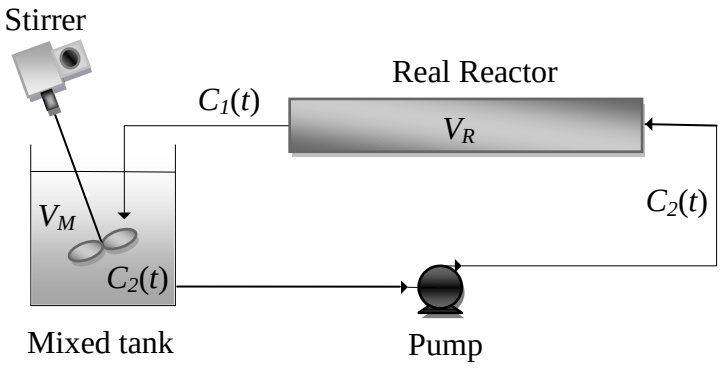

Fig. 3.5. Simplified schematic diagram of a re-circulating batch system.

3.4.1. General case

In reference to Fig. 3.5, a mass balance in the tank (assuming perfect mixing) gives

$$\frac{dC_2}{dt} = \frac{C_1 - C_2}{\theta_M} \tag{3.14}$$

where C_1 is the concentration of the reactant leaving the reactor, C_2 is its concentration in the mixed tank and entering the reactor, and θ_M is the residence time in the mixed tank defined as

$$\theta_M = \frac{V_M}{Q} \tag{3.15}$$

where V_M is the tank volume, and Q is the volumetric flow rate of operation. To obtain an expression only in terms of C_2, it is necessary to relate C_1 and C_2 in the reactor. The conversion per pass, X_S, relates the reactant concentration leaving the reactor (C_1) at time t, with the concentration entering the reactor (C_2) but at one reactor-residence time, θ_R, earlier as

$$X_S = 1 - \frac{C_1(t)}{C_2(t-\theta_R)} \tag{3.16}$$

where

$$\theta_R = \frac{V_R}{Q} \tag{3.17}$$

and V_R the reactor volume. Now, the relation between $C_2(t\text{-}\theta_R)$ and $C_2(t)$ can be approximated by the first-order backward difference equation (valid for small values of θ_R)

$$C_2(t-\theta_R) \approx C_2(t) - \frac{dC_2(t)}{dt}\theta_R \tag{3.18}$$

For the experimental conditions used in this work, the error associated with using this approximation was estimated not to exceed 0.07%. Upon substitution of Eq. (3.18) into Eq. (3.16), substitution of the result into Eq. (3.14), and rearrangement, we obtain

$$\frac{dC_2}{dt} = -\frac{X_S}{\theta_R + \theta_M - X_S\theta_R} C_2 = -\frac{X_S}{\theta_T - X_S\theta_R} C_2 \tag{3.19}$$

where θ_T is the total residence time of the system. In any reactor (real or ideal) where a first-order reaction is taking place, the conversion per pass (X_S) is independent of concentration (Fogler, 2006), and thus a constant value. This also implies that the conversion per pass would be the same if the reactor is being operated in either continuous or re-circulating batch mode. Integrating Eq. (3.19) gives the model that describes the dynamic behaviour of a real or ideal

reactor operated at constant volumetric flow rate in a re-circulating batch system in terms of the reactant concentration in the tank,

$$C_2 = C_{2,0}\, e^{-\frac{X_S}{\theta_T - X_S\theta_R}t} = C_{2,0}\, e^{-k_{app}t} \qquad (3.20)$$

where $C_{2,0}$ is the initial concentration in the tank, and k_{app} is an apparent reaction rate constant.

3.4.2. Case of a differential reactor

For the case of differential reactors utilized in the determination of intrinsic surface reaction rate constants, it can be assumed that $k\theta_R$ is small and that the reactor performs as an ideal plug flow reactor (PFR). In that case,

$$X_S = 1 - e^{-k\theta_R} \approx 1 - (1 - k\theta_R) = k\theta_R \qquad (3.21)$$

where k is the intrinsic volumetric reaction rate constant. In Eq. (3.21), the exponential function is approximated using the first two terms of its Taylor series. In the case of the present study, the product $k\theta_R$ was in the order of 10^{-3} for all the experimental conditions used; hence, the error for using this approximation was $< 1\times10^{-3}$ %. Substituting Eq. (3.21) into Eq. (3.20), and neglecting the term $k\theta_R^2$, gives:

$$C_2 = C_{2,0}\, e^{-k\frac{\theta_R}{\theta_T}t} = C_{2,0}\, e^{-k\frac{V_R}{V_T}t} \qquad (3.22)$$

which is consistent with the model obtained by Wolfrum & Turchi (1992). Writing Eq. (3.22) in terms of the intrinsic surface reaction rate constant k'' gives

$$C_2 = C_{2,0}\, e^{-k''\frac{A_{cat}}{V_T}t} \qquad (3.23)$$

where A_{cat} is the catalytic surface area (in the case of immobilized-catalyst reactors, A_{cat} is preferably defined as the area coated with catalyst). Using Eq. (3.23) and data of concentration

versus time free of mass transfer limitations, it is possible to estimate the intrinsic reaction rate constant of the catalytic reaction.

3.5. Results and discussion

3.5.1. Catalyst characterization

The coatings of the synthesized catalyst exhibited excellent adhesion and uniformity characteristics. The XRD analysis of the synthesized catalyst revealed that the coating material is amorphous, probably due to the relatively low heat treatment temperature used in the preparation process. The simultaneous processes of dehydration and of elimination of nitrogen compounds usually result in rapid collapse of the hydrate structure and amorphization of the obtained products (Pacewska & Keshr, 2002). The SEM and EDX analyses confirmed the presence of manganese and aluminum oxides in the samples. Fig. 3.6 shows a SEM micrograph and the EDX results for a sample of fresh coated catalyst. The analysis performed on samples of used catalyst did not show any appreciable difference with respect to the fresh catalyst samples.

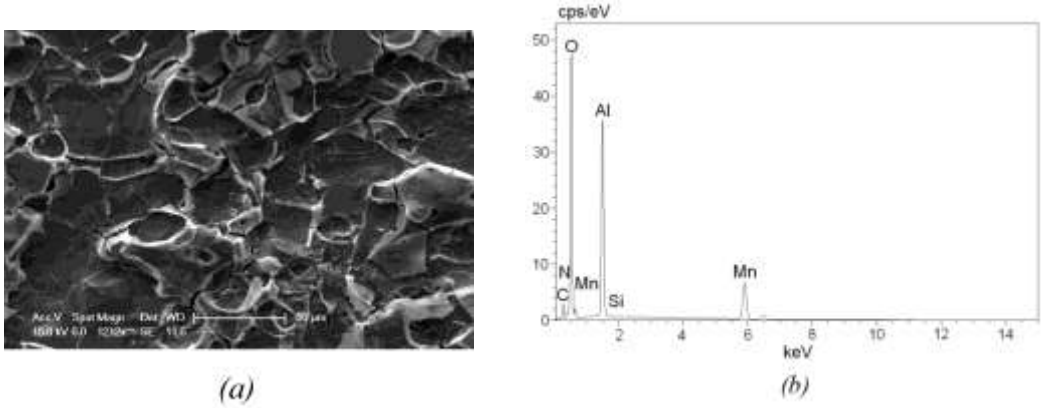

Fig. 3.6. Catalyst characterization: (a) SEM micrograph and (b) EDX results made to a sample of fresh coated catalyst.

3.5.2. Intrinsic reaction kinetics

In the experiments for determining the reaction kinetics conducted in the differential reactor, the decomposition of H_2O_2 followed an exponential decay and also showed dependence on flow rate. According to the model derived in Section 3.4, which describes the dynamics of a catalytic reactor operated in re-circulating batch mode, the exponential degradation implied that the intrinsic reaction rate followed first-order kinetics (see Eq. (3.23)). This result is also consistent with the ones reported in the literature, proposing this heterogeneous reaction to follow first-order kinetics (Salem et al., 2000). The dependence on flow rate indicated the presence of mass transfer limitation. To overcome this problem and determine the intrinsic kinetics, the experiments were conducted with increasing flow rates until mass transfer resistance was eliminated.

For the case when mass transfer limitation exists in the system, Eq. (3.23) can be rewritten as

$$\frac{C}{C_0} = e^{-k''_{eff}\frac{A_{cat}}{V_T}t} = e^{-k_{app}t} \qquad (3.24)$$

where C is the hydrogen peroxide concentration measured in the mixed tank at time t, C_0 is its initial concentration, k''_{eff} is the effective surface reaction rate constant, A_{cat} is the area of the reactor coated with catalyst, V_T is the total volume of the solution , and k_{app} is the apparent reaction rate constant related to the catalyst activity. The effective surface reaction rate constant k''_{eff} is a combination of the transport and intrinsic surface reaction rates. For the specific case of a system with a dilute reacting solution with first-order intrinsic reaction kinetics at a catalyst surface, the effective rate constant can be defined as (Fogler, 2006):

$$k''_{eff} = \frac{k_c\, k''}{k_c + k''} \tag{3.25}$$

where k_c is the mass transfer coefficient in the system. From Eq. (3.25) it is clear that as the flow rate (and hence, the mass transfer coefficient) increases in the system, k''_{eff} approaches the intrinsic rate constant, k''.

Experiments without any Mn/Al oxide catalyst (control runs) were carried out to quantify the non-catalytic decomposition of hydrogen peroxide in the system. The results showed a small decomposition (< 15% of the total conversion obtained using the Mn/Al oxide catalyst), likely due to volumetric and/or surface reactions. This small decomposition reaction was assumed to follow first-order kinetics as well. Taking into account this parallel reaction, Eq. (3.24) can be rewritten as

$$\frac{C}{C_0} = e^{-\left(k''_{eff}\frac{A_{cat}}{V_T} + k_{sys}\right)t} = e^{-\left(k_{app} + k_{sys}\right)t} = e^{-k_{overall}\,t} \tag{3.26}$$

where k_{sys} is the rate constant inherent to the system, and $k_{overall}$ is the overall rate constant of hydrogen peroxide decomposition (catalyst + system). From these control experiments, k_{sys} was estimated as $(4.5\pm0.5) \times 10^{-2}$ min^{-1}.

From the experiments using catalyst-coated plates in the reactor, the effective surface reaction rate constants were calculated fitting the concentration versus time data to Eq. (3.26). A non-linear regression method was used and the results are shown in Fig. 3.7. As seen, the values increased with flow rate demonstrating the presence of mass transfer limitation in the system up to a flow rate of approximately 6 L/min. From that point on, the rate constant reached a constant value of $(2.0 \pm 0.1) \times 10^{-5}$ m/s which was assumed to be the intrinsic reaction rate constant k''.

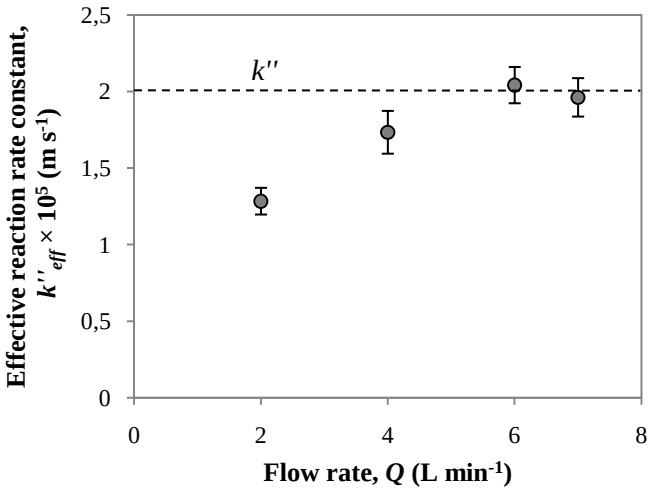

Fig. 3.7. Apparent reaction rate constants obtained in the differential reactor under different hydrodynamic conditions. The error bars represent the 95% confidence interval obtained with triplicate runs.

3.5.3. Kinetic performance of the coated-wall annular reactor

To quantify the performance of the coated-wall annular reactor in decomposing H_2O_2 due exclusively to the catalyst activity, control experiments without the Mn/Al oxide catalyst were conducted at different flow rates. The data presented the same exponential decay trend for all the flow rates, indicating a first-order decomposition rate inherent to the system. This reaction rate constant was estimated by means of a non-linear regression method as $k_{sys}=(1.3\pm0.2)\times10^{-3}$ min^{-1}. As it can be noted, the k_{sys} value reported in Section 3.5.2 for the differential reactor setup was higher than that of the annular reactor. It is speculated that the differential reactor, due to its aluminum structure, has contributed to the higher decomposition rate of peroxide in the system. Based on the dynamic model for re-circulating batch reactors derived in Section 3.4, Eq. (3.20) can be modified to account for this parallel reaction (k_{sys}) to obtain:

$$\frac{C}{C_0} = e^{-\left(\frac{X_S}{\theta_T - X_S\,\theta_R} + k_{sys}\right)t} = e^{-\left(k_{app} + k_{sys}\right)t} = e^{-k_{overall}\,t} \qquad (3.27)$$

The annular reactor was then operated with the catalyst immobilized on the inner wall. Several runs at different hydrodynamic conditions (flow rates) allowed investigating the kinetic performance of the reactor under diverse diffusion limiting conditions. The apparent reaction rate constant for each hydrodynamic condition was calculated by non-linear regression of the data fitted to Eq. (3.27). The computed values and their corresponding 95% confidence intervals are reported in Fig. 3.8. The rate of decomposition of hydrogen peroxide increased with the flow rate with the rate constant approaching a plateau at high flow rates.

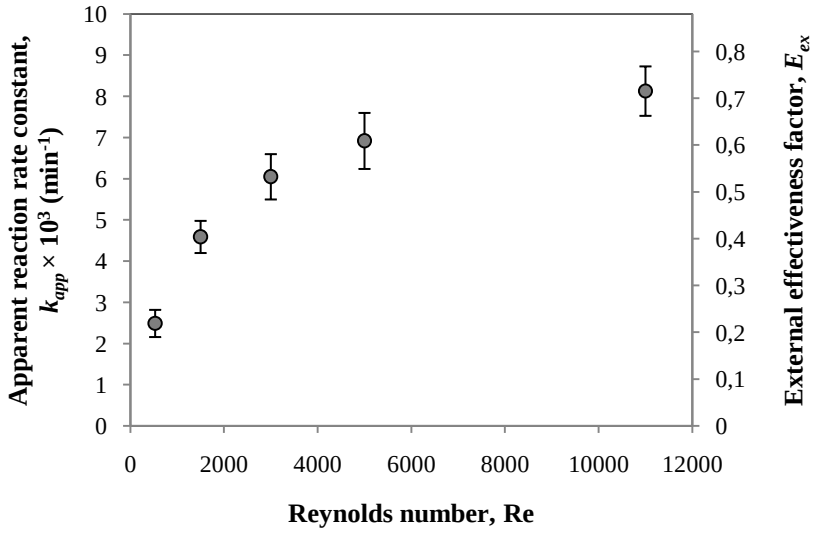

Fig. 3.8. Apparent reaction rate constants obtained for coated-wall annular reactors operating in re-circulating batch mode under different hydrodynamic conditions. The error bars represent the 95% confidence interval obtained with triplicate runs.

The degree of mass transfer limitation in the reacting system can be quantified by means of the external effectiveness factor (E_{ex}) which is defined (Dekker et al., 1995) as the ratio between the observed reaction rate and the reaction rate without external mass transport limitations (i.e., the intrinsic rate). For a first-order isothermal reaction,

$$E_{ex} = \frac{k'' C_s}{k'' C_b} = \frac{k''_{eff}\, C_b}{k'' C_b} = \frac{k''_{eff}}{k''} \tag{3.28}$$

where C_s and C_b are the concentrations at the surface of the catalyst and in the bulk fluid phase, respectively. The magnitude of E_{ex} ranges from 0 to 1 indicating the relative importance of diffusion and reaction limitations. As E_{ex} approaches 1, the overall reaction is surface-reaction-limited, whereas when E_{ex} is much smaller than 1 (i.e., E_{ex} <<1), the overall reaction is diffusion-limited. A common criterion used for neglecting external mass transport limitations in heterogeneous reactions states that E_{ex} must be larger than 0.95 (Dekker et al., 1995). Fig. 3.8 shows the E_{ex} calculated for each of the experimental conditions under investigation. The factors were computed using the k''_{eff} derived from the k_{app} values and the intrinsic reaction rate constant (k'') obtained in Section 3.5.2. The results evidence the transition of the system from mass transport to surface reaction rate limited operation ($E_{ex} \rightarrow$ 1) as the flow rate increases. This particular situation was desired in this study since the aim was to evaluate the hydrodynamic models under various mass transfer limiting conditions.

3.5.4. CFD simulations

One approach to evaluate the performance of the hydrodynamic models against the experimental data obtained in the present investigation was to perform CFD simulations of the reactor operating under the exact operational conditions of the experiments. Taking this

approach, the coated-wall reactor needed to be simulated under unsteady state conditions, since the system was run in re-circulating batch mode. However, performing unsteady state CFD simulations of the reactor for a typical operation time of 80 min was practically impossible (the computational power and time required were inhibitory). Hence, an alternative method based on steady state CFD simulations was developed to perform the experimental evaluation of the hydrodynamic models.

The steady state CFD simulations allow for performing comprehensive analysis of the reactor performance by providing the local values of the parameters of interest. Fig. 3.9 shows the local reaction rate at the catalyst surface as computed using the AKN turbulence model for the reactor operating at a flow rate of 24.6 L/min (Re=11,000). As it can be noticed, lower reaction rates are found in the regions behind the inner tube holder prongs. These results can be explained in light of the detailed hydrodynamics and mass transfer information obtained for this reactor configuration by Duran et al. (2009a), in which it was found that the inner tube holder prongs generate a wake of low velocity and external mass transfer behind them; resulting in reduced reaction rate. These results make evident that the local reaction rate distribution is highly influenced by the hydrodynamics and external mass transfer in the system, and that their interaction can be properly studied through CFD analysis.

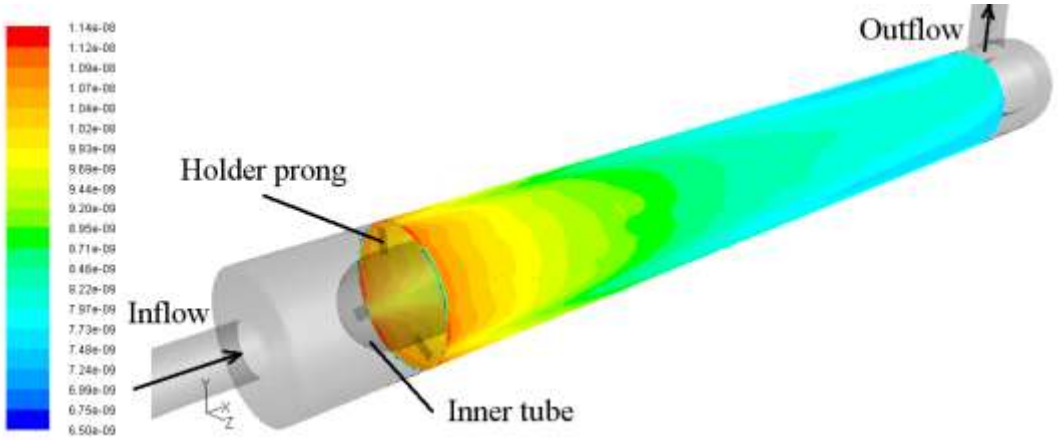

Fig. 3.9. Local reaction rate (kmol s^{-1} m^{-2}) distribution at the catalyst surface as computed using the AKN model and for a flow rate of 24.6 L/min (Re = 11,000).

As discussed in Section 3.4, the conversion per pass X_S in any reactor with first-order reaction kinetics (real or ideal) is independent of the reactant concentration (Fogler, 2006). This fact implies that the conversion per pass is the same for the reactor operating in either continuous or re-circulating batch mode. Given this property, it was possible to evaluate the results of steady state CFD simulations with experimental data that were collected under unsteady state operation. This was achieved by performing the steady state CFD simulations of the reactor operating at each of the flow rates utilized in the experiments, and calculating the corresponding X_S using the defined inlet and the predicted outlet concentrations. Given X_S is the same for the reactor operating in either continuous or re-circulating batch mode, the apparent reaction rate constants k_{app} of the system under the re-circulating batch mode were estimated as (see Eq. (3.27))

$$k_{app} = \frac{X_S}{\theta_T - X_S \theta_R} \tag{3.29}$$

and compared with the values obtained in the experiments.

Fig. 3.10 shows a comparison of the CFD-estimated apparent reaction rate constants obtained using different hydrodynamic models with the ones obtained from the experimental data. For the two simulations corresponding to laminar flow regime (Re=530 and 1,500), the laminar model was able to predict the experimental reaction rate constants very closely, with the predicted values falling within the 95% confidence intervals of the experimental values (% differences < 7%). For the case of transient and turbulent flow simulations, the predictions by the turbulence models were in fair agreement with the experimental data as well (disagreements not > 17%). Among the analyzed turbulence models, AKN model performed the best (with 9% disagreement in the worst case, Re=3,000) followed by RSM (disagreement<11%).

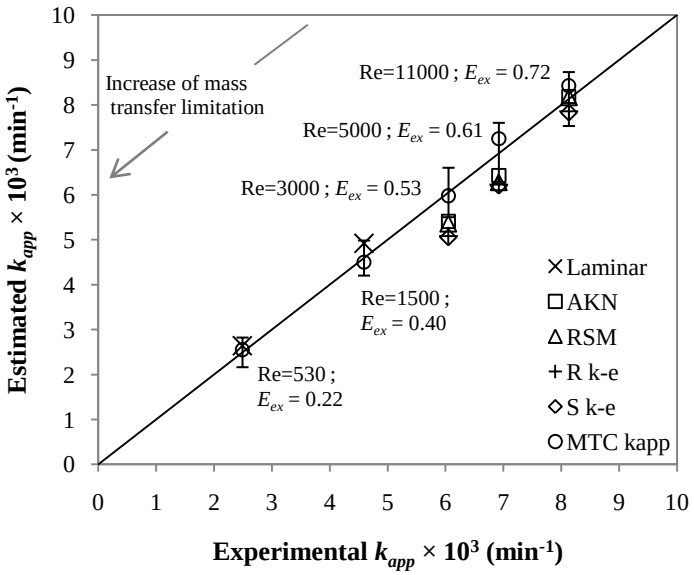

Fig. 3.10. Comparison of the apparent reaction rate constants estimated based on CFD simulations with the ones obtained experimentally. The error bars over the unit line represent the 95% confidence interval of the experimental results.

Another aspect that can be noticed in Fig. 3.10 is that for the case of transient and turbulent flow simulations, the disagreement between the CFD-predicted rate constants and

the experimental values decreased with increasing Re number. Even more, all the turbulence models provided an excellent prediction at Re=11,000. Based on these results, it would be hasty to conclude that the studied turbulence models perform better as Re increases, or that at high Re numbers all the models generate very good predictions. Rather, as demonstrated by the decrease of the external effectiveness factors (E_{ex}), increases in the Re number lead to the process becoming less limited by mass transfer and more affected/controlled by the surface reaction rate. Under these latter circumstances, the reactant concentration gradient towards the reactive wall is small, and thus, the prediction of the apparent reaction rate constants is less sensitive to the accuracy of the turbulence models predicting mass transfer. To further investigate this hypothesis, the turbulence models were evaluated under new mass-transport-limited conditions. For this, the system was studied at constant flow rate (Re=11,000), but with different intrinsic surface reaction rate constant magnitudes. The CFD simulation predictions obtained using the turbulence models were evaluated and will be discussed later on.

Fig. 3.10 shows also a series of apparent reaction rate constants labeled "MTC k_{app}". These rate constants were calculated utilizing the experimental mass transfer coefficients of benzoic acid in the studied annular reactor reported elsewhere (Duran et al., 2009a). The calculation was as follows: using the average mass transfer coefficients of benzoic acid ($k_{c.BA}$) measured for the annular reactor under investigation, the mass transfer coefficients of hydrogen peroxide ($k_{c.HP}$) were estimated as

$$k_{c,HP} = k_{c,BA}\left(\frac{D_{m,HP}}{D_{m,BA}}\right)^{2/3} \tag{3.30}$$

where $D_{m,HP}$ (1.3×10^{-9} m^2/s) and $D_{m,BA}$ (9.32×10^{-10} m^2/s) are the molecular diffusion coefficients of hydrogen peroxide and benzoic acid, respectively. Eq. (3.30) is based on the general dependence of mass transfer coefficients with the diffusion coefficient to the power of 2/3 (Perry & Green, 1997). The estimated average mass transfer coefficients of hydrogen peroxide in the system are reported in Table 3.1. These coefficients, together with the intrinsic surface reaction rate determined in Section 3.5.2, were used for calculating the apparent reaction rate constants applying Eqs. (3.24) and (3.25). As Fig. 3.10 indicates, the match between the calculated values based on the mass transfer coefficients and the direct experimental measurements of the reaction rate constants was excellent for all the hydrodynamic conditions studied (% difference < 5%). Therefore, it was determined that the mass transfer coefficients could be utilized to accurately predict the apparent reaction rate constant of the system for any intrinsic surface reaction rate constant of other magnitude. Consequently, it would potentially be possible to use the apparent reaction rate constants estimated based on mass transfer coefficients for assessing CFD simulation results (instead of measuring the apparent reaction rate constant directly).

Table 3.1. Estimated average mass transfer coefficients for hydrogen peroxide in the system.

Re	$k_{c,HP} \times 10^5$ ($m\ s^{-1}$)
530	0.61
1500	1.41
3000	2.43
5000	3.96
11,000	6.79

The analysis of the annular reactor operating at Re=11,000 and under different mass transfer limitation conditions was carried out setting five different intrinsic surface reaction

rate constant values, i.e. 5×10^{-6}, 2×10^{-5}, 6×10^{-5}, 2×10^{-4}, and 1 m/s. Given the average mass transfer coefficient for hydrogen peroxide at Re=11,000 (6.79×10^{-5} m/s), the selected range of reaction rate constants covers the spectrum of reactor operation from completely surface reaction rate limited (E_{ex}= 0.93) to entirely mass transfer limited (E_{ex}= 7×10^{-5}). Fig. 3.11 shows the comparison of the apparent reaction rate constants predicted by CFD using different turbulence models with the ones calculated using the mass-transfer-based reaction rate constant, so as the corresponding E_{ex} values. It is clear from Fig. 3.11 that increasing the intrinsic reaction rate constant, and consequently mass transfer limitation (lower E_{ex} values), leads to poorer predictions by CFD with various turbulence models. Nonetheless, AKN performed relatively well (% difference of k_{app} <11%), followed by RSM (% difference of k_{app} <17%), and both k–ε models performed similarly for all the conditions analyzed (% difference of k_{app} <30%).

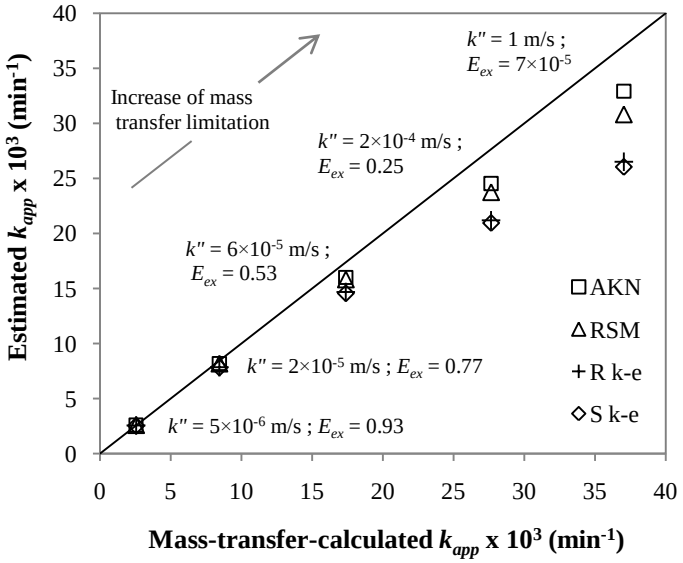

Fig. 3.11. Comparison of the apparent reaction rate constants estimated based on CFD simulations with the ones calculated based on the mass transfer coefficients obtained experimentally. The intrinsic reaction rate constants analyzed cover the spectrum from surface reaction rate to mass transfer limitation at Re = 11,000.

Duran et al. (2009a) performed a comprehensive study of the capabilities of the analyzed hydrodynamic models for predicting mass transfer in annular reactors. They found that the laminar model was able to predict successfully the mass transport in laminar flows (Re<1500). For transitional and turbulent conditions (3000<Re<11,000), it was found that the AKN and RSM provided a better prediction of the average mass transfer rates in the systems, whereas the *k*–ε-based turbulence models performed poorly. In light of those and the present results, it can be derived that the performance of the models is a function of their mass transfer predicting capabilities and ultimately, the degree of mass transfer limitation in the system. A model that predicts mass transfer properly will predict accurately the surface reaction phenomenon regardless of the degree of mass transfer limitation in the system. On the other hand, a model that poorly predicts mass transfer will perform well only in reacting systems that are under surface-reaction limitation.

In all the evaluations performed, the AKN model yielded better CFD simulation results. This outcome is in agreement with the ones in the literature, in which low Reynolds number models have been consistently reported to model better near-wall region processes (Duran et al., 2009a; Wang & Mujumdar, 2005; Wang et al., 1996). For instance, S *k*–ε and AKN turbulence models share the same core flow high Reynolds number model; however, their predictions of the kinetic performance of the reactor were very different. These results evidence the impact of near-wall models (enhanced wall treatment for S *k*–ε and low Reynolds number damping functions for AKN) on CFD predictions of the coated-wall reactors.

Overall, the results demonstrated that the performance of CFD, applying the analyzed models, is a function of their mass transfer prediction capabilities and ultimately, the degree of mass transfer limitation in the reacting system. For surface reaction rate limiting conditions

(high E_{ex} values), all the hydrodynamic models perform well. As the degree of mass transfer limitation increases, the predictions given by the models differ to some extent from the experimental observations according to their capability in predicting external mass transfer within the system. The better performance of AKN and RSM over the whole range of mass transfer limitation makes them promising turbulence models for being incorporated in the CFD simulations of coated-wall annular reactors.

3.6. Conclusions

The performance of different CFD hydrodynamic models in predicting the kinetic behaviour of an isothermal annular reactor with surface reaction under different diffusion limiting conditions was evaluated experimentally. A Mn/Al oxide catalyst was synthesized to carry out the decomposition of hydrogen peroxide. The reaction rate showed to follow first-order intrinsic reaction kinetics.

The performance of the hydrodynamic models was found to be related to their efficacy to predict mass transfer and consequently, the degree to which mass transfer limitation governs the system behaviour. The laminar model was able to predict the kinetic behaviour of the reactor under laminar flow conditions. For transient and turbulent flows, the performance of the turbulence models depended upon the degree in which the reacting system was limited by mass transfer. When the process was controlled by the surface reaction, all the analyzed turbulence models provided good predictions of the system. When the system presented some degree of mass transfer limitation, AKN and RSM exhibited better performance. AKN and RSM predicted apparent reaction rate constants with percentage differences < 11% and 17%,

respectively. Besides being more accurate, AKN has the advantage of being less memory and computationally intensive than RSM.

For the system under investigation, the low Reynolds number approach for simulating the near-wall region gave better results than the two-layer approach employed in the enhanced wall treatment. The developed CFD-based model was able to correctly simulate the performance of annular reactors with surface reaction over the whole range of diffusion controlled conditions.

3.7. Acknowledgments

The author acknowledges financial support from the Natural Sciences and Engineering Research Council of Canada (NSERC) and BI PureWater (Canada) Inc. J. Esteban Durán also thanks the Universidad de Costa Rica.

3.8. References

Abe, K., Kondoh, T., & Nagano, Y. (1994). A new turbulence model for predicting fluid flow and heat transfer in separating and reattaching flows- I. Flow field calculations. *International Journal of Heat and Mass Transfer, 37* (1), 139–151.

Baron, T., Manning, W.R., & Johnstone, H.F. (1952). Reaction kinetics in a tubular reactor. *Chemical Engineering Progress, 48*, 125–132.

Benedetto, A.D., Marra, F., & Russo, G. (2003). Heat and mass fluxes in presence of superficial reaction in a not completely developed laminar flow. *Chemical Engineering Science, 58*, 1079 – 1086.

Berger, R., & Kapteijn, F. (2007). Coated-wall reactor modeling: Criteria for neglecting radial concentration gradients. 1. Empty reactor tubes. *Industrial and Engineering Chemistry Research, 46*, 3863–3870.

Biard, P., Bouzaza, A., & Wolbert, D. (2007). Photocatalytic degradation of two volatile fatty acids in an annular plug-flow reactor: kinetic modeling and contribution of mass transfer rate. *Environmental Science and Technology, 41*, 2908–2914.

Boulinguieza, B., Bouzaza, A., Merabet, S., & Wolbert, D. (2008). Photocatalytic degradation of ammonia and butyric acid in plug-flow reactor: degradation kinetic modeling with contribution of mass transfer. *Journal of Photochemistry and Photobiology A: Chemistry, 200*, 254–261.

Canu, P., & Vecchi, S. (2002). CFD simulation of reactive flows: catalytic combustion in a monolith. *A.I.Ch.E. Journal, 48* (12), 2921–2935.

Csoka, B., & Nagy, G. (2004). Determination of diffusion coefficient in gel and in aqueous solutions using scanning electrochemical microscopy. *Journal of Biochemical and Biophysical Methods, 61*, 57–67.

Dalai, A., & Bakhshi, N. (1992). Carbon monoxide hydrogenation over cobalt catalyst in a tube-wall reactor. Part 1. Experimental studies. *Canadian Journal of Chemical Engineering, 70* (2), 269–277.

De Bruijn, T.J.W., Ipekoglu, A.N., De Jong, W.A., & van den Berg, P.J. (1981). Thermal decomposition of aqueous manganese nitrate solutions and anhydrous manganese nitrate. Part 3. Isothermal kinetics. *Thermochimica Acta, 45*, 293–303.

Dekker, F. H. M., Bliek, A., Kapteijn, F., & Moulijn, J. A. (1995). Analysis of mass and heat transfer in transient experiments over heterogeneous catalysts. *Chemical Engineering Science, 50* (22), 3573–3580.

Deutschmann, O., & Schmidt, L. (1998). Modeling the partial oxidation of methane in a short-contact-time reactor. *A.I.Ch.E. Journal, 44* (11), 2465–2477.

Dokamaingam, P., Assabumrungrat, S., Soottitantawat, A., Sramala, I., & Laosiripojana, N. (2009). Modeling of SOFC with indirect internal reforming operation: comparison of conventional packed-bed and catalytic coated-wall internal reformer. International Journal of Hydrogen Energy 34, 410–421.

Duran, J.E., Taghipour, F., & Mohseni, M. (2009a). CFD modeling of mass transfer in annular reactors. *International Journal of Heat and Mass Transfer, 52*, 5390–5401.

Duran, J.E., Taghipour, F., & Mohseni, M. (2009b). Evaluation of model parameters for simulating TiO_2 coated UV reactors. *Water Science and Technology: Water Supply*, in press.

Fluent-Inc. (2006). *FLUENT 6.3 User's Guide. Chapter 12. Modeling Turbulence.* Lebanon, NH.

Fogler, H.S. (2006). *Elements of Chemical Reaction Engineering*. Upper Saddle River, NJ: Prentice Hall.

Gill, W., Ruckenstein, E., & Hsieh, H. (1975). Homogeneous models for porous catalyst and tubular reactors with heterogeneous reactions. *Chemical Engineering Science*, *30*, 685–694.

Goyal, S.K., Esmail, M.N., & Bakhshi, N.N. (1988). Tube-wall reactor modeling for multiple reaction networks with nonlinear kinetics and volume change. *Canadian Journal of Chemical Engineering, 66* (5), 776–786.

Holmgren, A., & Andersson, B. (1998). Mass transfer in monolith catalyst: CO oxidation experiments and simulations. *Chemical Engineering Science, 53* (13), 2285–2298.

Houzelot, J., & Villermaux, J. (1977). Mass transfer in annular cylindrical reactors in laminar flow. *Chemical Engineering Science, 32*, 1465–1470.

Imoberdorf, G., Cassano, A., Irazoqui, H., & Alfano, O. (2007). Optimal design and modeling of annular photocatalytic wall reactors. *Catalysis Today, 129*, 118–126.

Kapteijn, F., Deugd, R.M., & Moulijn, J.A. (2005). Fischer-Tropsch synthesis using monolithic catalysts. *Catalysis Today, 105*, 350–356.

Karim, A., Bravo, J., Gorm, D., Conant, T., & Datye, A. (2005). Comparison of wall-coated and packed-bed reactors for steam reforming of methanol. *Catalysis Today*, *110*, 86–91.

Klassen, N., Marchington, D., & McGowan, H. (1994). H_2O_2 determination by the I_3^- method and $KMnO_4$ titration. *Analytical Chemistry, 66*, 2921–2925.

Launder, B., & Spalding, D. (1974). The numerical computation of turbulent flows. *Computer Methods in Applied Mechanics and Engineering, 3*, 269–289.

Launder, B., Reece, G., & Rodi, W. (1975). Progress in the development of a Reynolds-Stress turbulence closure. *Journal of Fluid Mechanics, 68*, 537–566.

Lide, D. (2007). *CRC Handbook of Chemistry and Physics*, 88th ed. Boca Raton:CRC.

Lupa, A., & Dranoff, J. (1966). Chemical reaction on the wall of an annular reactor. *Chemical Engineering Science, 21*, 861–866.

Mohseni, M., & Taghipour, F. (2004). Experimental and CFD analysis of photocatalytic gas phase vinyl chloride (VC) oxidation. *Chemical Engineering Science, 59* (7), 1601–1609.

Nallasamy, M. (1987). Turbulence models and their applications to the prediction of internal flows: a review. *Computers & Fluids, 15* (2), 151–194.

Pacewska, B., & Keshr, M. (2002). Thermal transformations of aluminium nitrate hydrate. *Thermochimica Acta, 385*, 73–80.

Pareek, V.K., Cox, S.J., Brungs, M.P., Young, B., & Adesina, A.A. (2003). Computational fluid dynamic (CFD) simulation of a pilot-scale annular bubble column photocatalytic reactor. *Chemical Engineering Science, 58*, 859–865.

Perry, R.H., & Green, D.W. (1997). *Perry's Chemical Engineers' Handbook*, 7th ed. New York:McGraw-Hill.

Ranade, V.V. (2002). *Computational Flow Modeling for Chemical Reactor Engineering*, Academic Press, London.

Redlingshöfer, H., Kröcher, O., Böck, W., Huthmacher, K., & Emig, G. (2002). Catalytic wall reactor as a tool for isothermal investigations in the heterogeneously catalyzed oxidation of propene to acrolein. *Industrial & Engineering Chemistry Research, 41*, 1445–1453.

Salem, I., El-Maazawi, M., & Zaki, A. (2000). Kinetics and mechanisms of decomposition reaction of hydrogen peroxide in presence of metal complexes. *International Journal of Chemical Kinetics, 32* (11), 643–666.

Schehl, R.R., Weber, J., Kuchta, M., & Haynes, W. (1977). Application of a diffusion limiting model to a tube-wall methanation reactor. *Industrial & Engineering Chemistry Process Design and Development, 16* (2), 227–230.

Schmidt, H. (1963). Berechnungen zum Einfluss des Stofftransportes bei Wandreaktionen im Ringspalt. *International Journal of Heat and Mass Transfer, 6*, 719–725.

Senkan, S., Evans, L., & Howard, J. (1976). An analysis of the tube-wall reactor under diffusion limiting conditions. *Industrial & Engineering Chemistry Process Design and Development, 15* (1), 184–187.

Shih, T., Liou, W., Shabbir, A., Yang, Z., & Zhu, J. (1995). A new *k*–ε eddy viscosity model for high Reynolds number turbulent flows: model development and validation. *Computers & Fluids, 24*, 227–238.

Spalding, D. (1971). Concentration fluctuations in a round turbulent free jet. *Chemical Engineering Science, 26*, 95–107.

Taghipour, F., & Mohseni, M. (2005). CFD simulation of UV photocatalytic reactors for air treatment. *A.I.Ch.E Journal, 51* (11), 3039–3047.

Tomasic, V., Jovic, F., & Gomzi, Z. (2008). Photocatalytic oxidation of toluene in the gas phase: modelling an annular photocatalytic reactor. *Catalysis Today, 137*, 350–356.

Wang, S., & Mujumdar, A. (2005). A comparative study of five low Reynolds number *k*–ε models for impingement heat transfer. *Applied Thermal Engineering, 25*, 31–44.

Wang, Y., Postlethwaite, J., & Bergstrom, D. (1996). Modelling mass transfer entrance lengths in turbulent pipe-flow with applications to small cathodes for measuring local mass transfer rates. *Journal of Applied Electrochemistry, 26*, 471–479.

Wilcox, D. (2006). *Turbulence Modeling for CFD*. La Cañada, CA:DCW Industries.

Wolfrum, E., & Turchi, C. (1992). Comments on "Reactor Dynamics in the Evaluation of Photocatalytic Oxidation Kinetics". *Journal or Catalysis, 136*, 626–628.

Yimer, I., Campbel, I., & Jiang, L.-Y. (2002). Estimation of the turbulent Schmidt number from experimental profiles of axial velocity and concentration for high-Reynolds-number jet flows. *Canadian Aeronautics and Space Journal, 48* (3), 195–200.

4. IRRADIANCE MODELING IN ANNULAR PHOTOREACTORS USING THE FINITE-VOLUME METHOD [3]

4.1. Introduction

The degradation rate of contaminants in photocatalytic reactors is directly dependent on the UV irradiance at the photocatalyst surface; therefore, the radiation field (photon distribution) within the reaction volume is one of the critical factors that determine the overall conversion and photoreactor performance. In this sense, when modeling immobilized photocatalytic reactors, the accurate prediction of the radiation field (and consequently the UV irradiance on the catalyst-coated surface) is of paramount importance.

Modeling the radiation field in a given photoreactor involves solving the radiative (photon) transfer equation (RTE) (Cassano, et al., 1995; Fluent-Inc., 2006). For monochromatic radiation, the RTE is defined as:

$$\frac{\mathrm{d}L(\vec{r},\vec{s})}{\mathrm{d}s}+(\kappa+\sigma)L(\vec{r},\vec{s})=j^{e}(\vec{r})+\frac{\sigma}{4\pi}\int_{4\pi}L(\vec{r},\vec{s}')p(\vec{s}'\rightarrow\vec{s})d\Omega' \qquad (4.1)$$

where L is the photon radiance, $\vec{r}$ is the position vector, $\vec{s}$ is the propagation direction vector, s is the path length, κ is the absorption coefficient, σ is the scattering coefficient, j^e is the emission (source) term, p is the phase function for the in-scattering of photons, and Ω' is the solid angle about the scattering direction vector $\vec{s}'$. In Eq. (4.1), the terms on the left-hand side represent the radiance change along the path length s, and the loss due to absorption and out-scattering. The terms on the right-hand side correspond to the radiance source and the gain in radiation radiance due to in-scattering. An analytical solution for this integro-differential

[3] A version of this chapter has been accepted for publication. Duran, J.E., Taghipour, F., & Mohseni, M. (2010). Irradiance modeling in annular photoreactors using the finite-volume method. Journal of Photochemistry and Photobiology A: Chemistry. doi:10.1016/j.jphotochem.2010.07.027

equation is only possible for very simple cases (Ozisik, 1973); for most practical engineering applications a numerical approach is necessary (Carvalho & Farias, 1998).

Several numerical methods have been developed for solving the RTE. Carvalho & Farias (1998) presented a review of some of these methods. Among the proposed methods, three of them have been mostly utilized and studied in the simulation of photoreactors: the Monte Carlo (MC) method, the discrete ordinate (DO) method, and the finite volume (FV) method (Pareek, et al., 2008). In particular, the FV method has been gaining much acceptance due to very favourable characteristics. In the FV method, the RTE is integrated over both the control angle and the control volume (Pareek & Adesina, 2004), which allows for conserving radiant energy and easily incorporating the method in computational fluid dynamics (CFD) simulations. CFD is a very attractive modeling approach since it allows an integrated analysis of photoreactors through simultaneous modeling of hydrodynamics, species mass transport, chemical reaction kinetics, and photon flux distribution.

Even though the FV method has been used in many CFD-based studies (Denny, et al., 2009; Pareek, et al., 2008; Pareek, 2005; Pareek & Adesina, 2004; Pareek, et al., 2003; Trujillo, et al., 2008; Trujillo, et al., 2007), few of them involved experimental evaluation of the radiation field simulations (Denny, et al., 2009; Trujillo, et al., 2008). Additionally, the radiation source (the UV lamp) was not included in the computational domain; instead, the radiation entering the reacting fluid was defined as a boundary condition using a lamp emission model. The main drawback of this approach is its inability to account for important effects and interactions happening not only inside the lamp, but also between the lamp and the quartz sleeve. Such effects include radiation reflection, refraction and absorption at the quartz walls (lamp envelope and sleeve), as well as absorption and re-emission of photons by the mercury vapour inside the lamp (Imoberdorf, et al., 2008). Neglecting these effects can

potentially imply large errors in the radiation field calculation. For instance, Imoberdorf et al. (2008) reported that the effective transmittance of the lamp quartz sleeve used in their multi-lamp setup was only 39%, as opposed to 100% which would be the predicted/estimated value had there been no consideration for the aforementioned effects.

Table 4.1. Lamp emission models commonly employed in the simulations of the radiation field in photoreactors.

Type	Name	Abbreviation	Characteristics	Reference
Multiple Point Source	Multiple Point Source Summation	MPSS	The lamp is modeled as a finite number of emission points equally spaced along the lamp axis.	(Jacob & Dranoff, 1970)
	Multiple Segment Source Summation	MSSS	The lamp is modeled as a series of differential cylindrical segments. The radiation is emitted normal to the cylinder surface and decreases with the cosine of the emission angle.	(Liu, et al., 2004; Rahn, et al., 2006)
Line Source	Spherical Emission	LSSE	The lamp is modeled as a line emitting radiation isotropically.	(Blatchley, 1997)
	Diffuse Emission	LSDE	The lamp is modeled as a line emitting radiation diffusely (following the cosine law).	(Akehata & Shirai, 1972)
	Spherical Sources	LSSS	The lamp is modeled as a series of differential spheres where the light is generated at the center. Only the component of radiation which is normal to the lamp walls is transmitted.	(Tsekov, et al., 1997)
Extensive Source	Superficial Diffuse Emission	ESDE	The lamp is modeled as a perfect cylinder. Radiation is diffusely emitted by point emitters uniformly distributed on the lamp surface.	(Yokota, et al., 1976)
	Volumetric Emission	ESVE	The lamp is modeled as a perfect cylinder. Radiation is isotropically emitted by point emitters uniformly distributed inside the lamp volume.	(Irazoqui, et al., 1973)

A key component in the development of a radiation field model is the definition of the lamp emission model (i.e., how UV radiation is emitted by the lamp). Several conceptual and mathematical models have been proposed in the literature (Alfano, et al., 1986; Imoberdorf, et al., 2008; Irazoqui, et al., 2000; Liu, et al., 2004; Pareek, et al., 2008; Tsekov, et al., 1997). A

list with some of the lamp emission models most commonly employed in photoreactor modeling is given in Table 4.1. Imoberdorf et al. (2008) recently proposed a more exhaustive lamp emission model that includes the reflection and refraction effects on/in the quartz envelope, so as the photon absorption/re-emission by the mercury vapour inside the lamp. The model was applied to the simulation of multi-lamp, homogeneous photoreactors, showing good agreement with the experimental data.

All the lamp emission models mentioned so far have been experimentally evaluated for lamps running in air, or inside homogeneous photoreactors (Alfano, et al., 1986; Imoberdorf, et al., 2008; Jin, et al., 2005; Liu, et al., 2004; Quan, et al., 2004; Rahn, et al., 2006; Salaices, et al., 2002). Nonetheless, the radiation model evaluation close to the lamp (which is likely to be the location of the photocatalyst in the case of immobilized reactors) has been particularly challenging. Most studies utilized either a UV radiometer or a chemical actinometer for performing the irradiance/fluence rate measurements. Radiometers, however, are not reliable for measuring irradiance in close proximity to the radiation source, mainly due to the geometry and the variable response of the photometer within a nonparallel radiation field (Severin & Roessler, 1998). On the other hand, under high radiation fluxes, some actinometers can experience saturation of the reacting solution due to diffusional resistance effects. This phenomenon has been reported, for example, for the iodide/iodate actinometer for 254 nm radiation (Forney & Pierson, 2003a; Forney & Pierson, 2003b; Jin, et al., 2005; Liu, et al., 2004).

Another shortcoming of some evaluation studies is related to the estimation of the radiation output of the lamp under the working (experimental) conditions. In many cases, the lamp output was measured while running the lamp in air at ambient temperature. However, experiments were conducted with the lamp inside a reactor, enclosed in a quartz sleeve, and

submerged in water at another temperature. Hence, the radiation outputs of the lamp during the experiments were likely different. For low-pressure mercury (Hg) lamps, fluctuations of 10°C in the lamp temperature can produce changes in the emission efficiency as high as 50% (Australasia, 1999; Bahnfleth, et al., 2009; USEPA, 1986). In this sense, new measurement methods that address this issue have been recently proposed (Robinson, 2007).

This investigation has focused on developing an FV-based model for predicting the irradiance inside single-phase annular photoreactors. The model is primarily intended to be applied to the CFD simulation of immobilized photocatalytic reactors. In the developed model, the UV lamp (monochromatic) is part of the computational domain. Hence, the reflection, refraction, and absorption of radiation at the air/quartz/water interface, as well as the absorption and re-emission of photons by the lamp plasma, could be considered. For defining an appropriate emission model for the lamp, several lamp emission models were evaluated against far-field (measuring position located away from the lamp) and near-field (measuring position close to the lamp) experimental data. The employed measurement techniques aimed to eliminate the previously discussed errors associated with irradiance determinations. To perform accurate evaluations, the power output of the low-pressure Hg lamp employed in the experiments was carefully measured under the operating conditions.

4.2. Experimental

4.2.1. Far-field evaluation

Several lamp emission models were evaluated against far-field irradiance measurements for a low-pressure Hg lamp (arc length=277mm, tube diameter=15mm, nominal UV-output at 254 nm=5.7 W, GPH357T5L/4P, Light Sources Inc.) running in air at 22 °C.

The actual UV-output of the lamp was first determined using the goniometric method (i.e., a series of irradiance measurements in a plane containing the lamp and along an arc scribed at a fixed radius from the center of the lamp) described by the USEPA (1986). Fig. 4.1 shows a schematic representation of the experimental setup utilized for this test. The irradiance was measured at different radial angles using a calibrated research radiometer (IL1700, SED240 detector, NS254 filter, International Light) once the lamp reached steady emission. The radius from the center of the lamp to the radiometer detector was 1 m, and the readings were recorded rotating the lamp around its transverse axis from 0° to 345° in 15° increments, while the radiometer was kept static. The lamp was then rotated 90° around its longitudinal axis and the measurement process was repeated. Assuming that the emission of the lamp was symmetrical, eight different measurements for each of the angles in the interval from 0° to 90° (0 to $\pi/2$) were obtained.

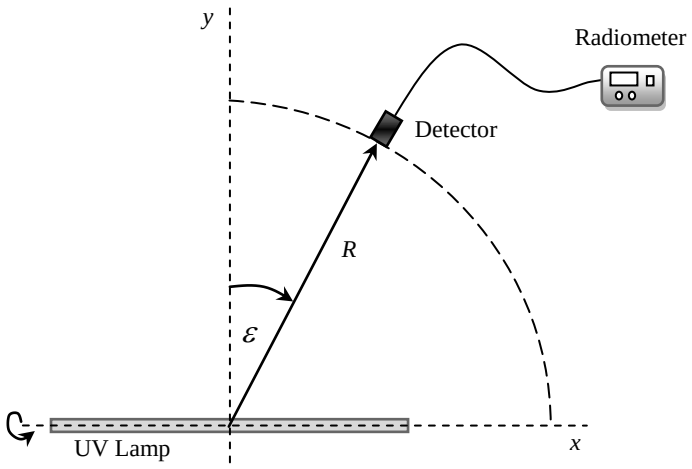

Fig. 4.1. Schematic of the experimental setup utilized for performing far-field evaluation of lamp emission models.

The power output of the lamp (P) was calculated using the following equation:

$$P = 4\pi R^2 \int_0^{\pi/2} E(\varepsilon)\cos\varepsilon \, d\varepsilon \tag{4.2}$$

where R is the distance from lamp center to the detector, ε is the angle of the detector from the normal axis of the lamp, and $E(\varepsilon)$ is the irradiance as a function of ε. The integral in Eq. (4.2) was solved numerically.

The determined UV output and the dimensions of the lamp were fed into different emission models and the irradiances at the same measurement points were predicted. A comparison of the model predictions against the experimental data was performed.

4.2.2. Near-field evaluation

The near-field evaluation was performed using an annular reactor in which both tubes were made of quartz (inner tube: 23 mm OD/20 mm ID, outer tube: 50mm OD/46 mm ID, quartz type GE 124, CANSCI Glass Products Ltd.). A schematic with the details of the experimental setup is presented in Fig. 4.2. This setup allowed measuring the irradiance at specific axial locations around the reactor's outer wall using a chemical actinometer that ran inside a PVC annular jacket (Fig. 4.2c). Evaluating the irradiance at the outer tube was important since in annular immobilized photocatalytic reactors the catalyst is likely coated on the inner wall of the outer tube. The PVC annular jacket dimensions were 25.4 mm width, 102 mm OD and 54 mm ID. The actinometer solution run inside a 13 mm wide × 7 mm deep channel formed between the quartz tube and the jacket inner wall. This space was sealed by two o-rings which also allowed moving the jacket to different positions along the reactor. The irradiance measurements were performed on the surface of ~5 mm wide gaps (windows)

created on the outer tube wall using several layers of electrical tape (3M) (see Fig. 2b). These measurement windows were located ± 5, ± 11, ± 13 and ± 14 cm from the center of the lamp. For calculating the area of each window, the gap widths were carefully measured at several

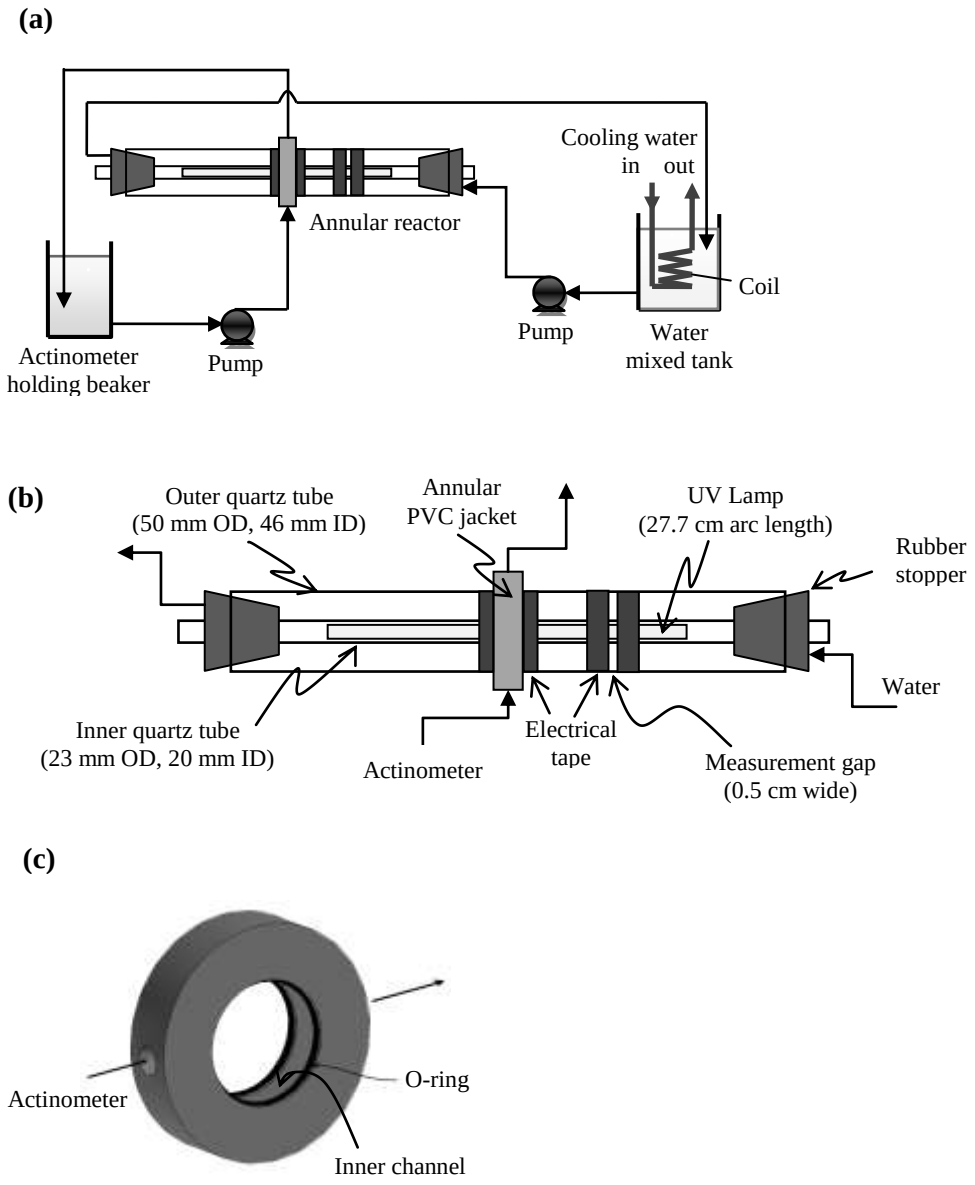

Fig. 4.2. Schematic of the equipment and experimental setup employed for the near-field irradiance measurements. Details of: (a) experimental setup (b) the annular reactor, and (c) annular PVC jacket.

points along the tube circumference using an electronic digital calliper (General, No. 147). The experimental setup also allowed running water with different transmittances and at constant temperature through the annular space of the reactor. In this study, water with 98% UV transmittance and at 22°C was circulated at a flow rate of 4 L/min in the system. As a safety measure, the reactor's outer tube was covered with black construction paper during the experimental runs.

The actinometer used in this investigation was potassium ferrioxalate solution (0.02 M) prepared and utilized as described by Murov et al. (1993). This actinometer has the advantage that its quantum yield is relatively insensitive to radiation flux (Murov, et al., 1993), making it suitable for near-field measurements. All the chemicals employed were ACS certified, obtained from Fisher Scientific, and used as received. The same low-pressure Hg lamp used in the far-field tests was employed in these experiments.

The experimental runs were carried out as follows. While running water in the reactor annulus, the UV lamp was placed inside the quartz sleeve (inner tube) and turned on. At least 20 min were given for the system to stabilize and for the lamp to reach steady emission. Following that, 500 mL of actinometric solution were circulated through the PVC jacket at 4 L/min and samples were taken from the container beaker at different time intervals. The concentration of Fe^{2+} was measured via UV spectrophotometry at 510 nm (Carry 100 UV-Visible spectrophotometer, Varian) and the irradiance was calculated (Murov, et al., 1993; Romero, et al., 2003) as

$$E = \frac{4.72 \times 10^5 \cdot V_T}{\Phi \cdot \pi d_2 w} \cdot \frac{\mathrm{d}C_{Fe^{2+}}}{\mathrm{d}t} \cdot 0.89 \qquad (4.3)$$

where V_T is the total volume of actinometric solution, Φ is the quantum yield of potassium ferrioxalate at 254 nm, d_2 is the external tube outer diameter, w is the irradiated window width, dC_{Fe}^{2+}/dt is the slope obtained from the linear regression of Fe^{2+}-concentration versus time data, 4.72×10^5 is a factor to convert Einstein to Joule (valid only for 254 nm radiation), and 0.89 is a correction factor for deducting the contributions made by the lamp emitting radiation at wavelengths other than 254 nm (Rahn, et al., 2003). The quantum yield used in the calculations was Φ=1.41 in accordance with a recent study by Goldstein & Rabani (2008).

The power output of the lamp operating inside the annular reactor was verified using a method adopted from Robinson (2007). According to this method ("method 2" in reference (Robinson, 2007)), the UV output of the lamp inside the submerged quartz sleeve can be calculated from an irradiance reading made with a fibre optic placed against the sleeve wall. The "calibration" of the fibre optic irradiance reading with respect to the real output of the lamp is made by performing simultaneous near-field and far-field measurements for the lamp running in air. For this, the UV output of the lamp running in air is determined using a standard far-field test with the modification that a short section of quartz sleeve is included in the setup. This sleeve section is positioned such that its radial distance from the lamp is the same as that for the sleeve during normal operation in the reactor. The irradiance at the short sleeve section is then measured using the fibre optic and a calibration factor can be computed.

The annular reactor utilized in this study did not allow making irradiance measurements at the wall of the quartz sleeve using our fibre optic input (P2/FFO2500, International Light) because the annular space was too narrow. However, this measurement was possible at the wall of the outer quartz tube. Robinson's "method 2" (Robinson, 2007) was therefore adopted by substituting the sleeve section by a section of annular reactor, and by

taking the irradiance measurements at the outer tube wall. Fig. 4.3 shows some pictures of the section of annular reactor built for performing the measurements (Figs. 4.3a and 4.3b), and that of the annular reactor (Fig. 4.3c). The section of annular reactor was built using quartz tube halves (same tubes as in the actual reactor) held together by means of a PVC housing. The annular space of the section was filled with water (having the same transmittance as in the actual experiments) through a small hole bored at one side of the piece and sealed with a rubber stopper. The power output of the lamp inside the reactor ($P_{reactor}$) was calculated as:

$$P_{reactor} = P_{air} \frac{E_{reactor}}{E_{air}} = K \cdot E_{reactor} \tag{4.4}$$

where E_{air} is the fibre optic irradiance readings at the wall of the annular reactor section with the lamp running in air, $E_{reactor}$ is the irradiance reading at the wall of the annular reactor with the lamp running inside, P_{air} is the far-field power output, and K ($=P_{air}/E_{air}$) is the calibration factor.

(a) (b) (c)

Fig. 4.3. Section of annular reactor used for relating the UV lamp output with near-field irradiance measurements (a), irradiance measurement using the fibre optic input: at the wall of the section of annular reactor (b), and at the wall of the annular reactor (c).

Simulation of the radiation field in the annular reactor was performed using the estimated power output of the lamp and different emission models. The simulation results were evaluated against the irradiance measurements.

4.3. Radiation field model

4.3.1. Solving the governing equation

The RTE (Eq. (4.1)) is the governing equation required to be solved for obtaining the radiation field in the photoreactor. In this investigation, the RTE was solved using the FV method programmed in commercial CFD code Fluent® 6.3.26. This method considers the RTE in the direction $\vec{s}$ as a field equation (Fluent-Inc., 2006). Eq. (4.1) is rewritten and solved as:

$$\nabla \cdot \left(L(\vec{r},\vec{s})\vec{s}\right) + (\kappa+\sigma)L(\vec{r},\vec{s}) = \kappa n^2 \frac{\sigma_{S-B}T^4}{\pi} + \frac{\sigma}{4\pi}\int_{4\pi} L(\vec{r},\vec{s}')p(\vec{s}'\rightarrow\vec{s})d\Omega' \qquad (4.5)$$

where n is the refractive index, $\sigma_{S\text{-}B}$ is the Stefan-Boltzmann constant (5.672×10^{-8} W m^{-2} K^{-4}), and T is the absolute temperature of the medium. Inside the photoreactor there is no UV radiation emission (generation), except for the lamp. Therefore, the source term (first term in the right-hand side of Eq. (4.5)) was almost inactivated by setting the computational domain temperature (everywhere except the lamp) to 1 K (minimum temperature allowed by Fluent). The definition of the UV radiation emitted by the lamp is described in Section 4.3.2. Note that because the domain zone temperatures are set equal to constant values, this approach can only be used for the simulation of systems that can be treated as isothermal reactors (this is usually the case for photocatalytic reactors). However, for cases where the reacting system is not isothermal, the emission terms of the different domain zones can be defined utilizing a sub-program (a user defined function in Fluent).

The segregated steady-state solver was used for solving the governing equation. An angular discretization of 40 divisions was used. This number was found to be sufficient to avoid the appearance of the "ray effect" (Pareek & Adesina, 2004; Raithby, 1999). To overcome control angle overhang (Pareek & Adesina, 2004; Raithby, 1999), a 1×1 pixelation was used. Due to the symmetry of the studied system, 2-D axisymmetric simulations were performed. This approach was preferred since it is much less computationally intensive than 3-D simulations. Moreover, little difference (<1%) between 2-D and 3-D solutions was found in preliminary evaluations. Second order upwind discretization scheme was employed. Convergence of the numerical solution was assured by monitoring the scaled residuals to a criterion of at least 10^{-6}. Additionally, the variation of fluence rate at several points (or irradiance at different surfaces) of the computational domain was used as the indicator of convergence.

Commercial mesh generator Gambit® 2.2.30 was used to create the grid. Structured quadrilateral cells were used to discretize the physical domain. Boundary-layer mesh was setup at the lamp wall where high radiation gradients occur. The utilized grids were verified to give mesh-independent results. In the simulations performed, approximately 20,000 cells were used.

4.3.2. Lamp emission models and boundary conditions

In the present investigation, the lamp (radiation source) was part of the computational domain. As discussed in the introduction, there are different ways to model the radiation emission of a lamp. Therefore, different approaches were taken to simulate these emission patterns using the CFD software. For the ESVE, the plasma volume (a cylinder) was defined as a fluid or solid continuum. The lamp emission power was defined by the absorption

coefficient, the refractive index, and the temperature of the plasma (see source term in Eq. (4.5)). The ESVE model assumes that the absorption coefficient is zero (Irazoqui, et al., 1973), even though a small value was needed to be defined (e.g., 0.01 m^{-1}). The refractive index was assumed as 1 given that the lamp is filled with an inert gas and Hg at a very low concentration. The temperature was then determined using the following iterative procedure: a first guess of the temperature was set in the model and the simulation was run; the power output coming out of the lamp envelope was checked; if the obtained value disagreed with the desired one, a new plasma temperature was calculated realizing that the power output is proportional to T^4. The lamp envelope was defined as a zero-thickness, semi-transparent, fully specular wall (diffuse fraction=0); the cylinder end caps were semi-transparent, fully diffused walls that absorbed all the incident radiation. Complete radiation absorption at these walls was set in Fluent assigning a thickness (e.g., 2 mm) and a high absorption coefficient (e.g., 10,000 m^{-1}).

The ESDE was simulated the same way as the ESVE, except that the lamp envelope needed to be set as a purely diffused wall (diffuse fraction =1). Another alternative to simulate the ESDE was defining only the external walls of the lamp (lamp=hollow cylinder). In this case, the lamp envelope was a semi-transparent, purely diffused exterior wall with external irradiation. The external irradiation was calculated dividing the power output of the lamp by the envelope surface area. The cylinder end caps were semi-transparent, fully diffused walls that absorbed all the incident radiation.

The LSSE and LSDE were simulated in the same way as the ESVE and ESDE, respectively; except that the diameter of the lamp cylinder was made so small that a linear approximation could be achieved. In the simulations performed, the ratio between the lamp length and diameter was 1385. The LSSS model is mathematically identical to LSDE, except

for a $\pi/4$ factor (refer to Table 4.3). Thus, the LSSS model was simulated as the LSDE, but with the power emission reduced by $\pi/4$.

Additional lamp emission models were evaluated in this study; however, they were basically modifications of the ESDE and ESVE models in which reflection/refraction/ absorption effects at the quartz envelope, and/or a higher photon absorption/re-emission in the Hg plasma were included. Reflection/refraction/absorption at the quartz envelope was considered in Fluent by giving some thickness (e.g., 1 mm) to the envelope wall (Fluent-Inc., 2006). Higher photon absorption/re-emission in the Hg plasma was accomplished by increasing the photon absorption coefficient. It is important to mention that since these changes caused modifications in the radiation emission inside the lamp, the plasma temperature needed to be checked and properly adjusted every time to guarantee the desired lamp output.

The quartz sleeve and the external quartz tube were simulated as solid continuums enclosed by zero-thickness, semi-transparent, fully specular walls. This was done to better simulate radiation refraction and propagation inside these walls, and also because the thickness of the walls were considerable when compared to the radial length of the computational domain (~14%). Both, the air surrounding the lamp and the water inside the annulus were defined as fluid continuums (solid continuum is also adequate if the fluid is static). The annular jacket with the actinometric solution was also included in the computational domain. The actinometer was defined as a fluid continuum and the jacket walls were zero-thickness, opaque, fully diffused, non-reflective walls. This was also the case for the external side walls of the reactor. Non-reflectivity of opaque walls was defined making the emissivity equal to 1 (Fluent-Inc., 2006; Pareek & Adesina, 2004). Due to the symmetry of the

system, a symmetry boundary condition (BC) was imposed at the center of the reactor. The computational domain of the annular reactor simulated in the present work is shown in the 2-D geometrical model of Fig. 4.4.

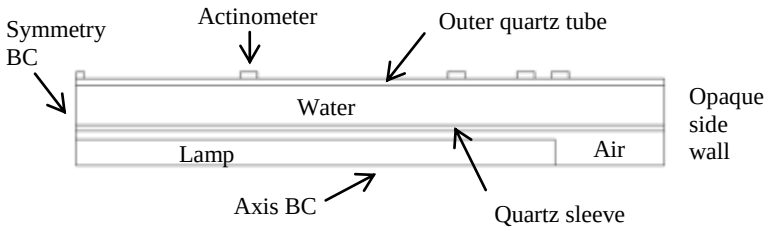

Fig. 4.4. 2-D geometrical model of the annular reactor utilized in the near-field evaluation study. Boundary conditions (BC) and continuums of the computational domain are shown.

4.3.3. Optical properties

The refractive index and the absorption coefficient are the optical properties of the materials necessary for the simulations. Table 4.2 lists the values for these two properties for each of the materials present in the simulations.

Table 4.2. Refractive indexes (n) and absorption coefficients (κ) used in the simulations.

Material	n (–)	κ (m^{-1})
Lamp plasma	1.00	0.01[a]/191[b]
Air	1.00	0
Water	1.38 [c]	2.02 [d]
GE 124 Quartz	1. 52 [e]	22 [f]
Actinometer	1.38 [g]	0 [h]

[a] Used for transparent plasma
[b] Used for absorbing plasma (Imoberdorf et al., 2008)
[c] (Thormählen, et al., 1985)
[d] Calculated for water with 98% transmittance
[e] (Lide, 2007; Momentive)
[f] (Momentive)
[g] The same value of water was assumed
[h] Assumed zero because the absorption effect was not modeled.

4.4. Results and discussion

4.4.1. Verification of the lamp emission models

In the present investigation, it was desired to include the lamp in the computational domain of the simulations since this approach facilitates the definition of the radiation model. In addition, it allows for accounting the radiation reflection, refraction and absorption at the reactor quartz sleeve and at the lamp envelope, so as the absorption and re-emission of photons in the lamp plasma. However, before starting to evaluate the radiation models against the experiments where all the aforementioned complex effects take place, a verification of the emission models was performed for the simple case of an emitting lamp running in air (5.7 W power output, 277 mm arc length, 15 mm diameter).

The lamp emission models were verified against analytical (LSSE, LSDE and LSSS) or numerical solutions (ESVE and ESDE) of the corresponding mathematical models. The fluence rate (G) and the irradiance (E) were calculated applying the following definitions (Cassano, et al., 1995):

$$G = \int_{\Omega} L \, \mathrm{d}\Omega \tag{4.6}$$

$$E = \int_{\Omega} L \, \hat{\Omega} \cdot \hat{\mathrm{n}} \, \mathrm{d}\Omega \tag{4.7}$$

where $\hat{\Omega}$ is the unit vector in the direction of propagation, $\hat{\mathrm{n}}$ is the unit vector normal to the area, and Ω is the solid angle about the propagation direction. Table 4.3 presents the analytical solutions obtained for LSSE, LSDE, and LSSS where H is the arc length, x is axial coordinate (origin=lamp center), and y is the normal distance from the lamp center. Equations for ESVE

and ESDE can be found elsewhere (Alfano, et al., 1986; Pareek, et al., 2008) and were numerically solved using the software Mathematica.

Table 4.3. Fluence rate (G) and irradiance (E) analytical solutions for LSSE, LSDE and LSSS models. The irradiance solutions apply to areas parallel to the lamp longitudinal axis.

Model	Analytical solution	Eq.
LSSE	$G = \frac{P}{4\pi Hy}\left[\arctan\left(\frac{H/2+x}{y}\right)+\arctan\left(\frac{H/2-x}{y}\right)\right]$	(4.8)
	$E = \frac{P}{4\pi Hy}\left[\frac{H/2+x}{\sqrt{(H/2+x)^2+y^2}}-\frac{x-H/2}{\sqrt{(x-H/2)^2+y^2}}\right]$	(4.9)
LSDE	$G = \frac{P}{\pi^2 Hy}\left[\frac{H/2+x}{\sqrt{(H/2+x)^2+y^2}}-\frac{x-H/2}{\sqrt{(x-H/2)^2+y^2}}\right]$	(4.10)
	$E = \frac{P}{2\pi^2 Hy}\left[\frac{(x+H/2)y}{(x+H/2)^2+y^2}-\frac{(x-H/2)y}{(x-H/2)^2+y^2}+\arctan\left(\frac{H/2+x}{y}\right)-\arctan\left(\frac{x-H/2}{y}\right)\right]$	(4.11)
LSSS	$G = \frac{P}{4\pi Hy}\left[\frac{H/2+x}{\sqrt{(H/2+x)^2+y^2}}-\frac{x-H/2}{\sqrt{(x-H/2)^2+y^2}}\right]$	(4.12)
	$E = \frac{P}{8\pi Hy}\left[\frac{(x+H/2)y}{(x+H/2)^2+y^2}-\frac{(x-H/2)y}{(x-H/2)^2+y^2}+\arctan\left(\frac{H/2+x}{y}\right)-\arctan\left(\frac{x-H/2}{y}\right)\right]$	(4.13)

Fig. 4.5 presents some of the results obtained for the analysis made at the region close to the lamp (2 cm<y<3 cm). The calculations were performed along the lines parallel to the longitudinal lamp axis at different normal distances from the lamp center. Different normal distances were chosen to prevent overlapping of the results since the computations of the

models are somewhat similar at the same distance. The agreement between the model predictions and the analytical/numerical solutions of the mathematical models was excellent for both, irradiance and fluence rate. Other normal distances (up to 15 cm away from the lamp) were also analyzed and the results matched well. These results confirm the suitability of using the proposed approach for simulating different lamp emission models.

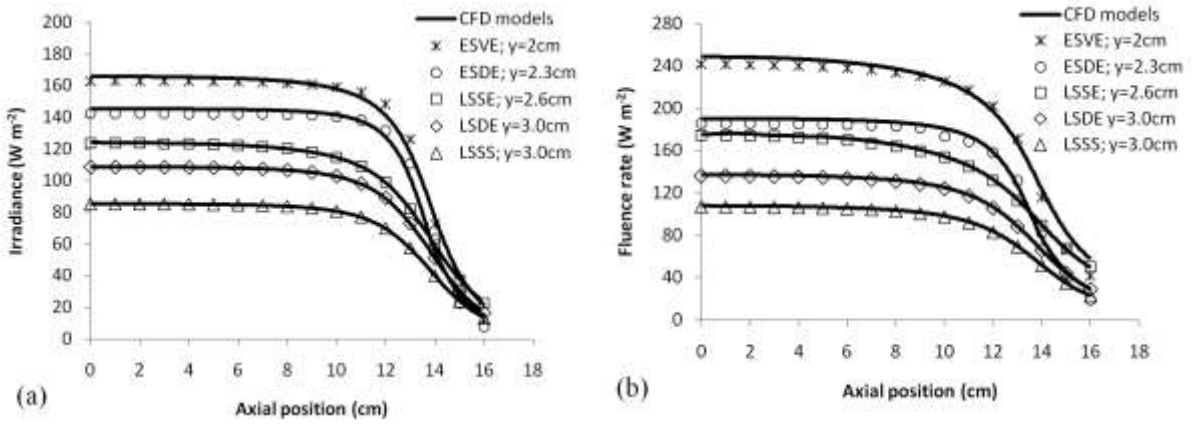

Fig. 4.5. Irradiance (a) and fluence rate (b) predicted by the CFD-based lamp emission models compared against the analytical/numerical solutions of the corresponding mathematical models. The data were computed parallel to the lamp longitudinal axis and at different normal distances from the lamp center (*y*). The lines and the symbols represent the CFD-based and mathematical predictions, respectively.

4.4.2. Far-field evaluation

Fig. 4.6 shows the irradiance values obtained using the goniometric method described in Section 4.2.1. The irradiance measurements presented a cosine-like functionality, very similar to the ones reported in other investigations (Sasges, et al., 2007; USEPA, 1986). A cosine response is distinctive of diffused (lambertian) emitters; thus, these results suggest that the lamp has an emission pattern similar to that of a diffused emitter. Using Eq. (4.2), the power output of the lamp was calculated as 4.5 W.

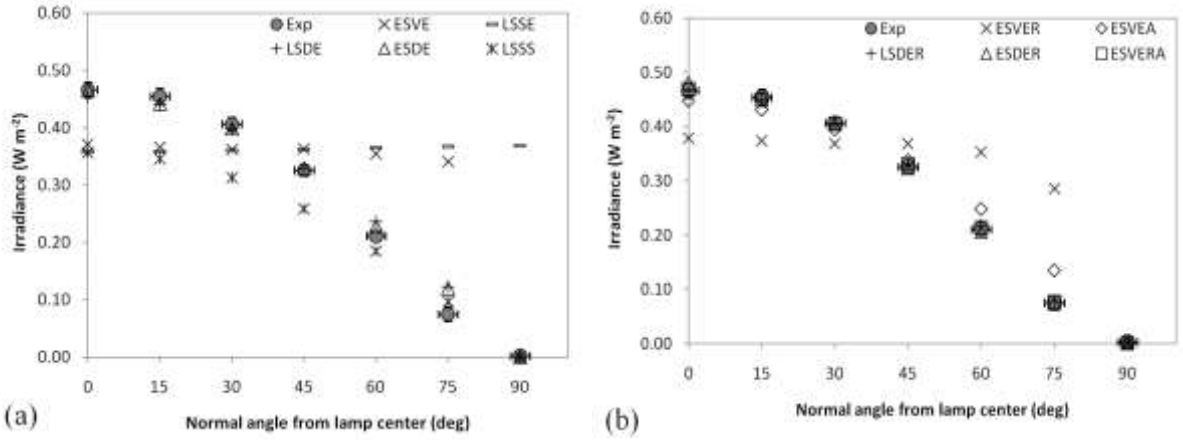

Fig. 4.6. Goniometric irradiance measurements obtained 1 m away from the lamp center (Exp) and their comparison with different lamp emission model predictions: (a) LSSE, LSDE, LSSS, ESDE, and ESVE, (b) LSDER, ESDER, ESVER, ESVEA, and ESVERA. The error bars represent the 95% confidence interval calculated for eight measurements.

The determined lamp power output was fed into different lamp emission models to predict the irradiance at the locations where the goniometric measurements were performed. As a first stage in the analysis, the traditional LSSE, LSDE, LSSS, ESDE and ESVE models were evaluated (Fig. 4.6a). Irradiance predictions based on the LSSE and ESVE models did not match the experimental data at all. These models predicted that the irradiance at the sensor would gradually rise as the lamp is rotated; and in the case of the ESVE, it would sharply drop to zero as the angle reaches 90°. This same behaviour was reported by other researchers (Sasges, et al., 2007) for the LSSE model. Moreover, calculations made using other systems with different H/R ratios verified that these are general model behaviours and that the irradiance rise is steeper as H/R increases. These model behaviours are consequence of assuming isotropic emission from the lamp emitting elements. With this assumption the

radiation emitted by each element towards the sensor is the same irrespective of the sensor position. In addition, the radiometer sensor gets closer to the lamp as the angle increases in the goniometric measurements. These results clearly indicate that LSSE and ESVE do not model the emission pattern of the lamp properly, and that they should not be utilized for far-field predictions. LSSS model predictions showed cosine functionality; however, the irradiance predictions were ~$\pi/4$ lower than the experimental values. LSSS predictions were lower because this model is not energy conservative, i.e., the integration of irradiance over an enclosing surface around the lamp does not yield the total power output of the lamp; it only yields $\pi/4$ of the lamp output. In the development of this model, the irradiance of the MPSS is simply multiplied by the cosine function, resulting in a lower emitted power of the differential elements (Sasges, et al., 2007). The same analysis applies to the MSSS, since MSSS is mathematically identical to the LSSS in the limit as the number of point sources becomes infinite. LSSS and MSSS are therefore not recommended to be utilized as emission models. On the other hand, LSDE and ESDE predictions had a much closer agreement with the experimental measurements. For $0 < \varepsilon < 50$, the estimated and measured values agreed quite well and for $50 < \varepsilon < 90$, a small overprediction was found. These models consider that radiation is diffusely emitted by the lamp, implying that the real lamp emission must be to some extent similar to that of a lambertian emitter. Evidence of cosine-liked emission from a low-pressure mercury UV lamp was also obtained by André et al. (1985) who made irradiance measurements very close to the lamp envelope wall using a fibre optic.

Even though the irradiance predictions of LSDE and ESDE were not completely accurate for all the directions around the lamp, their overall performance was good and acceptable. As a matter of fact, a formula based on the LSDE model has been recently

proposed (Lawal, et al., 2008) to be used in a standard method for calculating the total UV output of a monochromatic lamp. According to this method, the irradiance at a normal distance from the center of a lamp is measured using a radiometer (x=0, $y \geq 2H$). The power output is calculated using the Keitz formula (Keitz, 1971):

$$P = \frac{E 2\pi^2 yH}{2\beta + \sin 2\beta} \tag{4.14}$$

where β is the half angle subtended by the lamp at the sensor position (i.e., $\tan\beta = H/(2y)$). Eq. (4.14) can be derived from Eq. (4.11) at x=0 and through the mathematical simplification of the resulting expression. On the other hand, an older method based on the LSSE model, which assumes that at considerable distance the lamp can be taken as a point source emitter ($P=4\pi y^2 E$) has been proven to considerably overestimate (~20%) the UV output of the lamp (Whitby, et al., 2009).

To analyze if better model predictions could be achieved, the LSDE, ESDE, and ESVE models were modified to account for radiation reflection, refraction and absorption at the lamp quartz envelope (these modified models were abbreviated as LSDER, ESDER, and ESVER, respectively). These effects were included in the FV-based model assigning a 1 mm thickness to the envelope wall and adjusting the plasma temperature to obtain 4.5 W power output. As can be seen in Fig. 4.6b, the incorporation of reflection, refraction and absorption to LSDE and ESDE made the model predictions fit the experimental data very well; this not being the case for ESVE. These results suggest that radiation is diffusely emitted from a thin layer of plasma next to the inner envelope wall, after which it suffers reflection, refraction and absorption at the quartz envelope. Computations performed for LSDE in which only reflection was incorporated into the model demonstrated that this effect accounts for practically all the correction given to the model predictions.

The results obtained here can be explained by analyzing the physical processes occurring inside a low-pressure Hg lamp. It is well known that photons are emitted all over the lamp plasma volume. However, since this emission process is reversible, photons can be absorbed and isotropically re-emitted by another mercury atom before escaping the lamp envelope (Masschelein, 2002). This absorption/re-emission process is significant due to the high absorption coefficient of the Hg plasma, and it becomes more important in those directions implying a longer pathway for the photons (i.e., for increasing ε values). As a consequence, compared to that from inside parts of the plasma, higher emission rates occur near the walls of the lamp, and diffused emission takes place. Based on this analysis, the ESVE model was modified to account for the absorption/re-emission effect (model abbreviation: ESVEA). This modification was made in the computational model by setting a high absorption coefficient for the lamp plasma (191 m^{-1} as reported by Imoberdorf et al. (2008)), and again, adjusting the plasma temperature to obtain 4.5 W power output. As it can be seen in Fig. 4.6b, the irradiance predictions obtained with the ESVEA model were practically the same as the ones obtained with LSDE and ESDE. This result proves that the absorption/re-emission process can adequately explain the diffused radiation emission observed in the experimental measurements. Moreover, when reflection, refraction, and absorption at the lamp envelope were included to the ESVEA model (model abbreviated as ESVERA), the irradiance predictions fitted the experimental measurements fully (see Fig. 4.6b). The ESVERA model coincides fundamentally with the model proposed and evaluated by Imoberdorf et al. (2008) for multi-lamp, homogeneous photoreactors.

The ESVERA emission model shows great potential for being applied in CFD simulations. The model is very easy to set up and its far-field irradiance predictions agreed

fully with the measurements. As a second alternative, the ESDE should be considered. The capability of these models to predict near-field irradiance was also evaluated. The results are presented and analyzed in the following section.

4.4.3. Near-field evaluation

Before evaluating the irradiance prediction capabilities of different emission models in the near-field region, the power output of the lamp while operating inside the annular reactor was verified. For this, the method proposed and described in Section 4.2.2 was implemented. The calibration of the fibre optic irradiance measurement at the outside wall of the annular reactor section was carried out against the power output determined in the far-field measurements (Section 4.4.2). The calibration factor *K* (see Eq. (4.4)) obtained for our specific system was 0.137 m^2. The irradiance was also measured at the outer wall of the annular reactor while operating under normal conditions. This value substituted in Eq. (4.4) allowed for calculating the actual power output of the lamp, indicating that under the experimental conditions, the lamp output was the same (within the experimental error estimated at 5%) as when the lamp was running in air. This result can be explained by the fact that the generated heat in the annular reactor was removed by the water of the same temperature as ambient air (22°C). This situation propitiates comparable heat transfer conditions in both systems resulting in similar lamp temperatures and consequently, the same power outputs.

The temperature of the water in the reactor was varied to study its effect on the lamp power output. Fig. 4.7 presents the normalized power output obtained at different water temperatures (reference temperature=22°C). This normalized power output can also be understood as a temperature correction factor. As can be seen in Fig. 4.7, different operating water temperatures produced variations of up to 15% in the lamp output. The general trend of

the obtained curve in which a maximum output is found agrees with the results reported by different researchers and by the UV-lamp manufactures (Australasia, 1999; Bahnfleth, et al., 2009; USEPA, 1986). However, a direct comparison cannot be made since our results are reported with respect to the surrounding water temperature, whereas in those other references the lamp UV output is given as a function of the lamp wall temperature. The results corroborate, however, the importance of performing the determination of the lamp UV output under the actual operating conditions of the reactor.

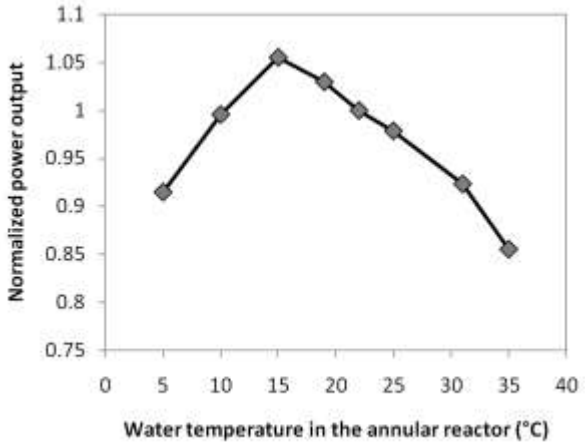

Fig. 4.7. Effect of water temperature on the power output of the lamp. The power output was normalized with respect to the result obtained at 22°C.

When a lamp is operated inside a quartz sleeve, there are important phenomena that need to be taken into account for the simulation of radiation distribution. These phenomena are schematically illustrated in Fig. 4.8. From the radiation coming from the lamp and reaching the quartz sleeve, a fraction is transmitted through the quartz wall and the other part is reflected backwards. Part of this reflected radiation reaches the lamp envelope where a fraction suffers reflection again; however, the rest of radiation re-enters the lamp body. These photons that re-enter the lamp body are absorbed and re-emitted multiple times by Hg atoms

until they finally escape the lamp (Imoberdorf, et al., 2008). Consequently, since each photon that re-enters will exit the lamp again, the net photon emission of the lamp remains constant. When simulating this system using the developed FV-based model, the part of radiation that re-enters the lamp and is absorbed by the Hg plasma is correctly taken into account, but the effect of re-emission of these absorbed photons is not considered in the governing equation and thus, not computed. Nonetheless, this additional generation of photons (due to re-emission) can be simulated by simply increasing the plasma temperature until the corresponding net power output is met. Following this approach, a net lamp power output of 4.5 W was assured in all the annular reactor simulations performed.

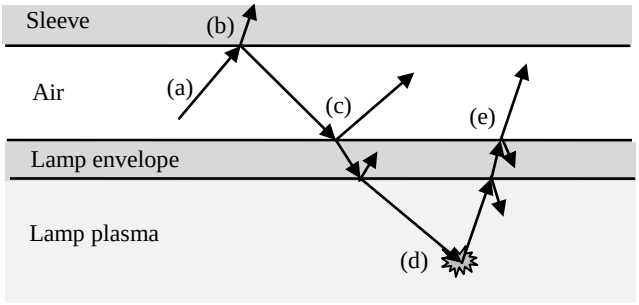

Fig. 4.8. Schematic representation of the phenomena and interactions taking place when a lamp is operated inside of a quartz sleeve: (a) radiation coming from the lamp, (b) reflection and refraction at the quartz sleeve, (c) reflection and refraction at the lamp envelope, (d) absorption and re-emission of photons by Hg atoms, and (e) radiation re-escaping from the lamp envelope.

A corollary of the previous analysis on the interaction between the quartz sleeve and the lamp is that practically all the radiation that is generated in the lamp will end up being transmitted into the sleeve wall; there is consequently no "loss" of radiation because of reflection at the air/quartz sleeve interface. The reflected radiation re-enters the lamp, is absorbed and subsequently re-emitted towards the sleeve; or if it misses the lamp, it will

continue travelling until it reaches the sleeve at some other position. This results from the conservation of radiative energy in the lamp-sleeve control volume. Under this approach, the use of radiation models that deduct the reflected radiation at the air/sleeve interface might result in underprediction of the irradiance (or fluence rate) inside the photoreactor.

Simulations of the radiation field in the experimental system were performed using various lamp emission models and the experimentally determined lamp power output. Fig. 4.9 illustrates the computed fluence rate distribution in the system using the ESVERA lamp emission model. Some details that can be observed are the radiation reflection at the quartz sleeve, and some disturbances in the fluence rate contours due to the presence of the actinometric solution. This latter effect happens because radiation is transmitted more easily through the measurement windows (which are in contact with an aqueous solution), than through the quartz tube (which is in contact with air).

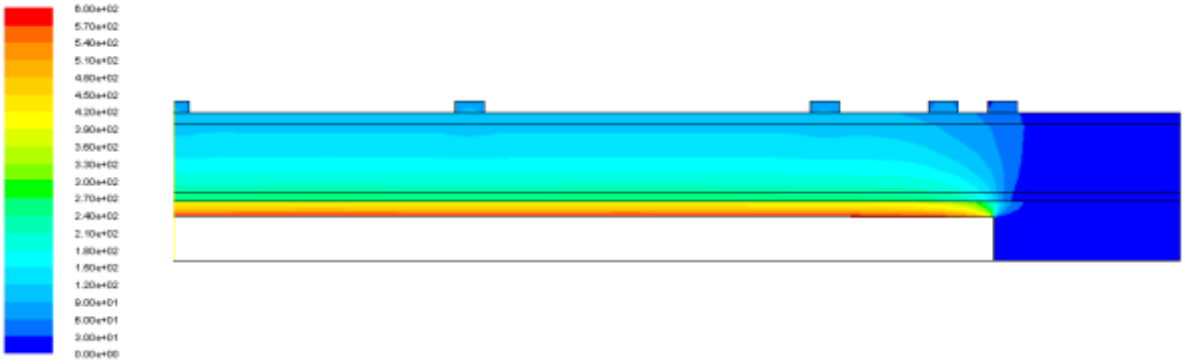

Fig. 4.9. Fluence rate (W m^{-2}) distribution in the experimental system as predicted using ESVERA lamp emission model. Due to the scale in this figure, the distribution inside the lamp is not shown. Each component of the system including the UV lamp, sleeve, and actinometers are shown in Fig. 4.4.

Using the quartz tube annular reactor and the actinometer solution running inside the annular PVC jacket, the irradiance at different axial positions was determined (Fig. 4.10). It is evident that the studied lamp had symmetrical emission and that the irradiance at the wall had a flat profile within ~70% of the irradiated area (-11cm<x<+11cm), followed by a steep decrease in the region 12 cm<|x|<15 cm.

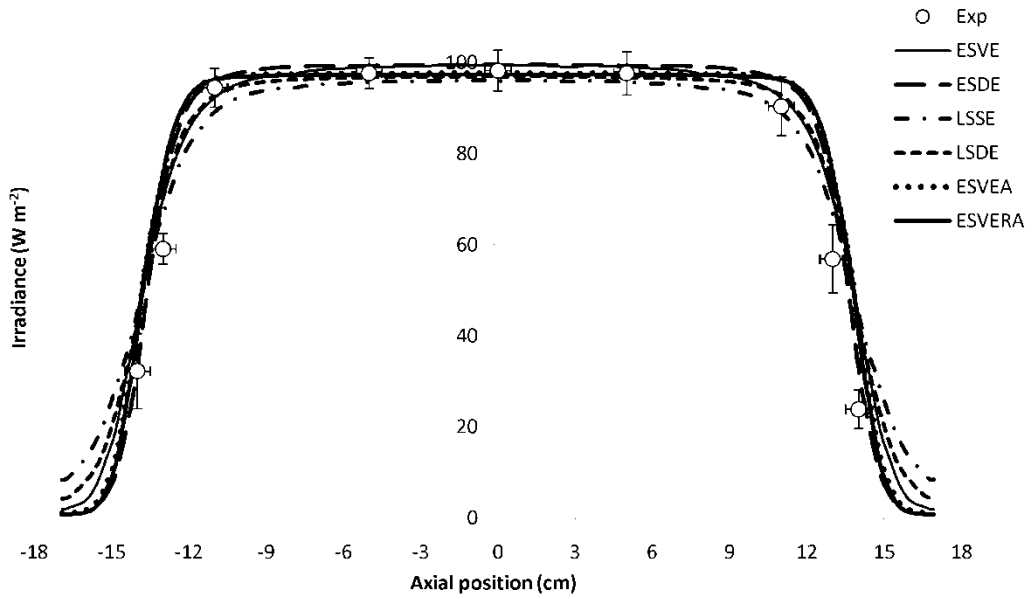

Fig. 4.10. Irradiance measured at different positions of the reactor outer wall compared with the predictions of different lamp emission models. The error bars represent the 95% confidence interval obtained with triplicate runs.

Fig. 4.10 also shows the predicted irradiance at the reactor outer tube wall using the FV-based model with different radiation emissions. Analyzing the region with practically flat irradiance profile (-11cm<x<+11cm), it can be noticed that the prediction of the different models were somewhat similar. Due to the experimental error (~5%) associated with the actinometric determinations in that zone, it is not possible to affirm whether one particular model performs better than the others. Nonetheless, it is interesting to see how exactly ESVERA and ESVEA predicted the average of the experimental measurements. In the region of steep decrease of the irradiance (12 cm<|x|<15 cm), all the models somehow overpredicted the irradiance at the tube wall. Note that in this region the experimental error was much larger (~15%). The models that predicted the steepest decrease and thus the closest agreement with the experimental data were ESVERA, ESVEA, and ESDE. This latter result is consistent with the far-field evaluation since these three models showed good irradiance predictions in high-normal-angle propagation directions.

While the irradiance profiles predicted using LSSE and ESVE were somehow in fair agreement with the experimental data, their far-field predictions fell far away from the experimental points. This result demonstrates that in the region close to the lamp, the radiation emission pattern (isotropic or diffused) has little effect on the irradiance prediction profiles. Nevertheless, this is not the case for other radiation field variables such as the fluence rate. Fig. 4.11 shows the fluence rate profiles computed by different lamp emission models along the radial coordinate in the annular space at the center and one side (x=13cm) of the reactor. As can be seen, significant prediction differences can be found among the different models. These results have important implications for the simulation of photoreactors with volumetric reactions, since photochemical reaction rates are determined by the local fluence rate.

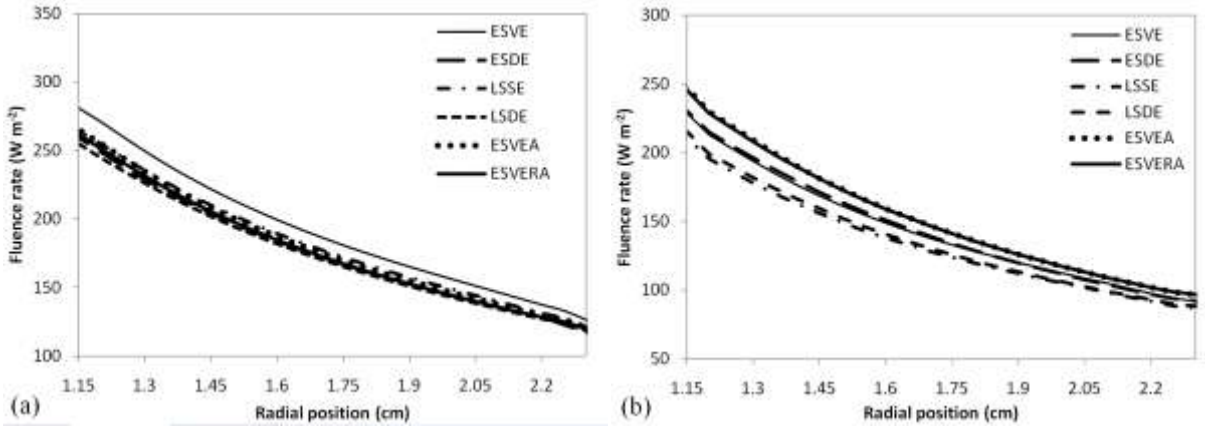

Fig. 4.11. Fluence rate profiles along the radial coordinate in the annular space as computed using different lamp emission models. The results correspond to (a) the center, and (b) one side (x = 13cm) of the reactor.

The models that assumed (or resulted in) diffused radiation emission (LSDE, ESDE, ESVEA, and ESVERA) were the ones that showed better overall irradiance prediction capabilities. In other investigations (Akehata & Shirai, 1972; Alfano, et al., 1986; Imoberdorf, et al., 2008; Liu, et al., 2004; Quan, et al., 2004; Rahn, et al., 2006; Yokota, et al., 1976), diffused emission models have also shown good results not only in terms of irradiance, but also fluence rate prediction accuracy. In few of those studies (Liu, et al., 2004; Rahn, et al., 2006), the authors utilized the MSSS model in the radiation distribution calculations. As mentioned before, this model reduces the radiation output of the lamp by $\pi/4$. However, the two studies referred above have used the method based on LSSE (which overestimates the real output in about $\pi/4$) for estimating the lamp output. As a consequence, the predictions they obtained are equivalent to LSDE model predictions.

The annular reactor simulations performed in all the previous evaluations considered the quartz sleeve and the outer tube as solid continuums enclosed by zero-thickness, semi-transparent, fully specular walls. This was originally done to better simulate radiation

refraction and propagation inside these walls, and because the wall thicknesses were considerable when compared to the radial length of the reactor. To analyze if the model geometry could be simplified without sacrificing prediction accuracy, a simulation in which the quartz sleeve was defined as a regular BC wall was performed. For this, the 15 mm-thick solid continuum enclosed by zero-thickness, semi-transparent, fully specular, BC walls were substituted by one 15 mm-thick, semi-transparent, fully specular, BC wall located 21.5 mm from the lamp center. ESVERA was used as the lamp emission model. As it can be seen in Fig. 4.12, the irradiance predicted at the inner wall of the outer tube is practically the same for both systems. Consequently, for future works, it is recommended to treat the sleeve as a regular BC wall. It is important to notice that if reflection/refraction/absorption effects are to be modeled at the wall, a thickness must be specified (Fluent-Inc., 2006).

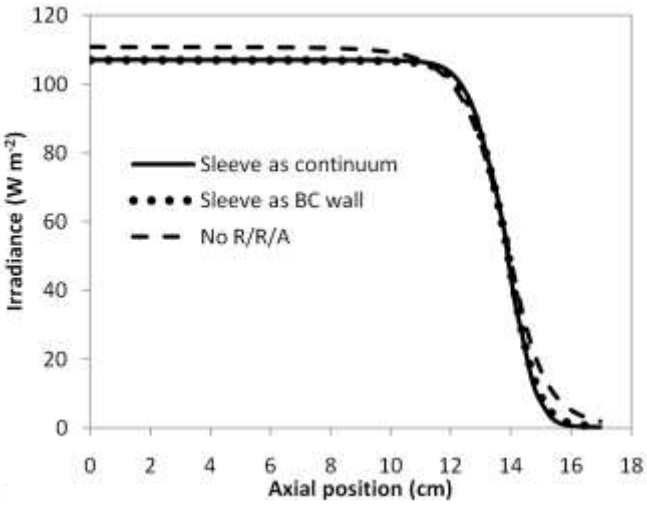

Fig. 4.12. Effect of quartz sleeve definition on the irradiance prediction at the inner wall of the reactor outer tube. Three cases are presented: the sleeve as a solid continuum, as a BC wall, and removing all the reflection/refraction/absorption at the air/quartz/water interfaces. ESVERA model was used in the simulations.

Fig. 4.12 also shows the irradiance obtained at the inner wall of the outer tube for the case where reflection/reflection/absorption effects at the air/sleeve/water interfaces were removed from the radiation model. In the region of flat irradiance profile (-11cm<x<+11cm), the prediction resulted in an overestimation of only 3%. This difference is basically the consequence of not considering radiation absorption in the sleeve. As it can be noticed, no radiation is "lost" in the lamp-sleeve system due to reflection at the sleeve internal wall. On the other hand, in the regions of low irradiance, the overprediction is more significant (up to 700%) as a result of the higher absorption and refraction effects suffered by the radiation traveling at high-normal-angle directions.

4.5. Conclusions

A computational radiation field model based on the finite-volume method was developed for simulating the irradiance in single-phase annular photoreactors. As part of the model, a CFD-based approach for modeling lamp radiation emission was proposed. Under this approach, the lamp is included in the computational domain and the lamp plasma emission is simulated by defining proper physical properties and boundary conditions, allowing for different emission patterns to be defined in the model.

For developing the radiation model, several lamp emission models were evaluated against near- and far-field irradiance measurements. The far-field evaluation showed that LSSE, LSSS and ESVE model predictions were in complete disagreement with the experimental data. Thus, these models are not recommended for far-field predictions. On the other hand, diffused emission models (LSDE and ESDE) predicted fairly well the irradiance distribution around the lamp. Moreover, incorporating reflection/refraction/absorption effects

at the lamp quartz envelope to these diffused models allowed for even better far-field irradiance predictions.

When the high photon absorbance/re-emission effect produced by the Hg vapour was considered in the ESVE model (ESVEA model), it was able to explain the diffused emission behaviour of the lamp. Moreover, adding reflection/refraction/absorption effects at the lamp quartz envelope (ESVERA model) resulted in an excellent match between predictions and experimental data.

Near-field evaluation revealed that the radiation emission pattern (isotropic or diffused) has little effect on the irradiance prediction close to the lamp. However, important differences were observed for the fluence rate predictions. Even though the predicted irradiance profile using different emission models was somehow similar, ESDE, ESVEA, and ESVERA presented the closest agreement with the experimental data.

ESVERA is a promising emission model to be incorporated in integrated models, such as the CFD-based simulations of photoreactors, particularly immobilized photocatalytic reactors. The model is very easy to set up, it comprises the main physical phenomena occurring in the lamp, it allows taking into account important lamp-sleeve interactions, and it shows excellent agreement with near- and far-field experimental data.

Experiments obtained for the lamp operating inside the quartz sleeve of the annular reactor demonstrated the strong effect of surrounding temperature on the lamp power output. Consequently, to perform accurate simulations, it is essential to obtain and use a real estimate of the lamp power output under the actual operating conditions in the reactor.

4.6. Acknowledgements

The author acknowledges Dr. Gustavo Imoberdorf for his valuable input and discussions, and the Natural Sciences and Engineering Research Council of Canada (NSERC) for financial support. J. Esteban Durán also thanks the support received from Universidad de Costa Rica.

4.7. References

Akehata, T., & Shirai, T. (1972). Effect of light-source characteristics on the performance of circular annular photochemical reactor. *Journal of Chemical Engineering of Japan , 5* (4), 385–391.

Alfano, O., Romero, R., & Cassano, A. (1986). Radiation field modelling in photoreactors - I. Homogeneous media. *Chemical Engineering Science , 41* (3), 421–444.

André, J., Roger, M., & Villermaux, J. (1985). Répartition de la Luminière dans un Réacteur Photochimique de Symétrie Cylindrique. *The Chemical Engineering Journal , 31*, 199–208.

Australasia, U. T. (1999). *The critical factors in ultraviolet disinfection systems.* www.uvta.com.au/pdf/critical_factors.pdf.

Bahnfleth, W., Lau, J., Kremer, P., Clark, D., & Freihaut, J. (2009). *Emerging filter and UV devices for energy efficient IAQ in commercial buildings Volume 2: Germicidal lamp testing.* Indoor Environment Center, The Pennsylvania State University.

Blatchley, E. I. (1997). Numerical modelling of UV intensity: Application to collimated-beam reactors and continuous-flow systems. *Water Research , 31*, 2205–2218.

Carvalho, M., & Farias, T. (1998). Modelling of heat transfer in radiating and combusting systems. *Trans IChemE: Part A , 76*, 175–184.

Cassano, A. E., Martin, C. A., Brandi, R. J., & Alfano, O. M. (1995). Photoreactor Analysis and Design: Fundamentals and Applications. *Industrial & Engineering Chemistry Research , 34* (7), 2155–2201.

de Lasa, H., Serrano, B., & Salaices, M. (2005). *Photocatalytic Reaction Engineering.* New York: Springer.

Denny, F., Scott, J., Pareek, V., Peng, G., & Amal, R. (2009). CFD modelling for a TiO2-coated glass-bead photoreactor irradiated by optical fibres: Photocatalytic degradation of oxalic acid. *Chemical Engineering Science , 64*, 1695–1706.

Dijkstra, M. F., Panneman, H. J., Winkelman, J. G., Kelly, J. J., & Beenackers, A. A. (2002). Modeling the photocatalytic degradation of formic acid in a reactor with immobilized catalyst. *Chemical Engineering Science , 57*, 4895–4907.

Fluent-Inc. (2006). *FLUENT 6.3 User's Guide. Chapter 13.3. Modeling Radiation.* Lebanon, NH.

Forney, L., & Pierson, J. (2003a). Optimum Photolysis in Taylor–Couette Flow. *AIChE Journal, 49* (3), 727–733.

Forney, L., & Pierson, J. (2003b). Photolytic Reactors: Similitude in Taylor–Couette and Channel Flows. *AIChE Journal , 49* (5), 1285–1292.

Goldstein, S., & Rabani, J. (2008). The ferrioxalate and iodide-iodate actinometers in the UV region. *Journal of Photochemistry and Photobiology, A: Chemistry , 193*, 50–55.

Herrmann, J. (2005). Heterogeneous photocatalysis: state of the art and present applications. *Topics in Catalysis , 34* (1–4), 49–65.

Hoffmann, M. R., Martin, S. T., Choi, W., & Bahnemannt, D. W. (1995). Environmental Applications of Semiconductor Photocatalysis. *Chemical Reviews , 95*, 69–96.

Imoberdorf, G., Taghipour, F., & Mohseni, M. (2008). Radiation field modeling of multi-lamp, homogeneous photoreactors. *Journal of Photochemistry and Photobiology A: Chemistry , 198*, 169–178.

Irazoqui, H., Cerdá, J., & Cassano, A. (1973). Radiation profiles in an empty annular photoreactor with a source of finite spatial dimensions. *AIChE Journal , 19* (3), 460–467.

Irazoqui, H., Isla, M. A., & Cassano, A. E. (2000). Simplified Extense Source Model for Photoreactor Analysis and Design. *Industrial Engineering Chemistry Research , 39*, 4260–4271.

Jacob, S., & Dranoff, J. (1970). Light intensity profiles in a perfectly mixed photoreactor. *AIChE Journal , 16*, 359–363.

Jin, S., Linden, K., Ducoste, J., & Liu, D. (2005). Impact of lamp shadowing and reflection on the fluence rate distribution in a multiple low-pressure UV lamp array. *Water Research , 39*, 2711–2721.

Keitz, H. (1971). *Light Calculations and Measurements* (2nd ed.). New York: St. Martin's Press Inc.

Krýsa, J., Waldner, G., Měšťánková, H., Jirkovský, J., & Grabner, G. (2006). Photocatalytic degradation of model organic pollutants on an immobilized particulate TiO2 layer: Roles of adsorption processes and mechanistic complexity. *Applied Catalysis B: Environmental , 64* (3–4), 290–301.

Lawal, O., Dussert, B., Howarth, C., Platzer, K., Sasges, M., Muller, J., Whitby, E., Stowe, R., Adam, V., Witham, D., Engel, S., Posy, P., & van der Pol, A. (2008). Proposed Method

for measurement of the output of monochromatic (254 nm) low pressure UV lamps. *IUVA News , 10* (1), 14–17.

Lide, D. (2007). *CRC Handbook of Chemistry and Physics*, 88th ed. Boca Raton:CRC.

Liu, D., Ducoste, J., Jin, S., & Linden, K. (2004). Evaluation of alternative fluence rate distribution models. *Journal of Water Supply: Research and Technology - AQUA , 53* (6), 391–408.

Masschelein, W. (2002). *Ultraviolet Light in Water and Wastewater Sanitation.* Boca Raton: Lewis Publishers/CRC Press.

McMurray, T., Byrne, J., Dunlop, P., Winkelman, J., Eggins, B., & McAdamsa, E. (2004). Intrinsic kinetics of photocatalytic oxidation of formic and oxalic acid on immobilised TiO2 films. *Applied Catalysis A: General , 262*, 105–110.

Mehrotra, K., Yablonsky, G. S., & Ray, A. K. (2005). Macro kinetic studies for photocatalytic degradation of benzoic acid in immobilized systems. *Chemosphere , 60*, 1427–1436.

Momentive. (n.d.). Retrieved 08 22, 2009, from http://www.gequartz.com/en/optical.htm

Murov, S., Carmichael, I., & Hug, G. (1993). *Handbook of Photochemistry* (Second ed.). New York: Marcel Dekker, Inc.

Ollis, D. F., & Turchi, C. (1990). Heterogeneous photocatalysis for water purification: contaminant mineralization kinetics and elementary reactor analysis. *Environmental Progress , 9* (4), 229–234.

Ozisik, M.N. (1973). *Radiative Transfer and Interactions with Conduction and Convection*, New York: Wiley.

Pareek, V. K., Cox, S. J., Brungs, M. P., Young, B., & Adesina, A. A. (2003). Computational fluid dynamic (CFD) simulation of a pilot-scale annular bubble column photocatalytic reactor. *Chemical Engineering Science , 58* (3–6), 859–865.

Pareek, V. (2005). Light intensity distribution in a dual-lamp photoreactor. *International Journal of Chemical Reactor Engineering , 3*, Article A56.

Pareek, V., & Adesina, A. (2004). Light Intensity Distribution in a Photocatalytic Reactor Using Finite Volume. *AIChE Journal , 50* (6), 1273–1288.

Pareek, V., Chong, S., Tadé, M., & Adesina, A. A. (2008). Light intensity distribution in heterogenous photocatalytic reactors. *Asia-Pacific Journal of Chemical Engineering, 3*, 171–201.

Quan, Y., Pehkonen, S. O., & Ray, M. B. (2004). Evaluation of Three Different Lamp Emission Models Using Novel Application of Potassium Ferrioxalate Actinometry. *Industrial & Engineering Chemistry Research , 43*, 948–955.

Rahn, R. O., Bolton, J., & Stefan, M. I. (2006). The Iodide/Iodate Actinometer in UV Disinfection: Determination of the Fluence Rate Distribution in UV Reactors. *Photochemistry and Photobiology , 82*, 611–615.

Rahn, R., Stefan, M., Bolton, J., Goren, E., Shaw, P., & Lykke, K. (2003). Quantum yield of the iodide-iodate chemical actinometer: Dependence on wavelength and concentration. *Photochemistry and Photobiology , 78* (2), 146–152.

Raithby, G. (1999). Evaluation of discretization errors in finite-volume radiant heat transfer predictions. *Numerical Heat Transfer, Part B , 36*, 241–264.

Robinson, J. (2007). Determination of the output of a UV lamp running in a quartz sleeve submerged in water. *World Congress on Ozone and Ultraviolet Technologies.* Los Angeles: International Ozone Association and International Ultraviolet Association.

Romero, R., Alfano, O., & Cassano, A. (2003). Radiation Field in an Annular, Slurry Photocatalytic Reactor. 2. Model and Experiments. *Industrial & Engineering Chemistry Research , 42*, 2479–2488.

Salaices, M., Serrano, B., & Lasa, H. d. (2002). Experimental evaluation of photon absorption in an aqueous TiO2 slurry reactor. *Chemical Engineering Journal , 90*, 219–229.

Sasges, M., Pol, A. v., Voronov, A., & Robinson, J. (2007). A Standard Method for Quantifying the Output of UV Lamps. *World Congress on Ozone and Ultraviolet Technologies.* Los Angeles: International Ozone Association and International Ultraviolet Association.

Severin, B., & Roessler, P. (1998). Resolving UV photometer outputs with modeled intensity profiles. *Water Research , 32* (5), 1718–1724.

Thormählen, I., Straub, J., & Grigull, U. (1985). Refractive index of water and its dependence on wavelength, temperature and density. *Journal of Physical and Chemical Reference Data , 14*, 933–945.

Trujillo, F. J., Safinski, T., & Adesina, A. A. (2007). CFD Analysis of the Radiation Distribution in a New Immobilized Catalyst Bubble Column Externally Illuminated Photoreactor. *Journal of Solar Energy Engineering , 129*, 27–36.

Trujillo, F., Lee, I., Hsu, C., Safinski, T., & Adesina, A. (2008). Hydrodynamically-Enhanced Light Intensity Distribution in an Externally-Irradiated Novel Aerated Photoreactor: CFD Simulation and Experimental Studies. *International Journal of Chemical Reactor Engineering , 6,* Article A58.

Tsekov, R., & Smirniotis, P. (1997). Radiation field in continuous annular photocatalytic reactors: role of the lamp finite size. *Chemical Engineering Science , 52* (10), 1667–1671.

USEPA. (1986). *Design Manual: Municipal Wastewater Disinfection.* Cincinnati, OH: EPA/625/1–86/021.

Whitby, G., Sotirakos, B., & Bolton, J. (2009). A comparison of two methods for measuring the UV output of low pressure mercury lamps in air. Boston: International Ozone Association and International Ultraviolet Association.

Yokota, T., Iwano, T., & Tadaki, T. (1976). Light intensity in an annular photochemical reactor. *Kagaku Kogaku Ronbunshu , 2,* 298–303.

5. CFD MODELING OF IMMOBILIZED PHOTOCATALYTIC REACTORS FOR WATER TREATMENT [4]

5.1. Introduction

Most of the CFD models of photocatalytic reactors reported in the literature are related to the simulation of immobilized photocatalytic reactors used for air treatment (Jarandehei & Visscher, 2009; Mohseni & Taghipour, 2004; Romero-Vargas, et al., 2006; Romero-Vargas & de Lasa, 2007; Salvado-Estivill, et al., 2007; Taghipour & Mohseni, 2005; Yang, et al., 2007). For example, Mohseni & Taghipour (2004), and Taghipour & Mohseni (2005) simulated annular photocatalytic reactors treating chlorinated VOCs under laminar flow regime. The CFD models were capable of predicting the reactor performance and provided insight into the concentration gradient of the species in the reactor. Romero-Vargas et al. (2006) and Romero-Vargas & de Lasa (2007) made a turbulent flow field investigation of a photocatalytic reactor for air treatment and identified several design issues.

There are few CFD investigations of photocatalytic reactors used for water treatment (Denny, et al., 2009; Mehrotra & Ray, 2003; Pareek, et al., 2003; Sengupta, et al., 2001). For example, Pareek et al. (2003) applied CFD to simulate a suspended TiO_2 pilot-scale annular bubble column photocatalytic reactor and obtained good agreement between the simulations and the experimental results. More recently, Denny et al. (2009) developed and evaluated experimentally a laminar flow CFD model for simulating a TiO_2-coated glass-bead photoreactor irradiated by optical fibres. The model successfully predicted the radiation distribution in the reactor and the photocatalytic degradation of oxalic acid.

[4] A version of this chapter has been accepted for publication.
Duran, J.E., Mohseni, M., & Taghipour, F. CFD modeling of immobilized photocatalytic reactors for water treatment. AIChE Journal (in press).

For the case of turbulent flow immobilized photocatalytic reactor for water treatment, to the author's knowledge, only two investigations are reported in the literature. In one of them (Periyathamby & Ray, 1999; Ray, 1998), a series of simulations were run in order to determine the effects of flow rates, diffusion coefficients, reaction rate constants and inter lamp spacing on the performance of a multi-lamp reactor. One of the main findings of the investigation was that the conversion in the reactor was primarily controlled by the flow and diffusion of the pollutant, and was practically independent of the surface reaction rate. However, the publications neither offer much information about the computational model (boundary conditions, radiation model, near-wall modeling approach, mesh quality, etc.), nor evaluate the simulation results against experimental data. The other investigation is reported by Duran et al. (2010b). In this study, different hydrodynamic models (laminar, realizable k-ε, and Reynolds stress models) were evaluated in terms of their external mass transfer and photocatalytic oxidation prediction capabilities. A flat-plate differential reactor and formic acid as a model compound were used in the evaluation. Based on radiation field simulations of the system, the UV irradiance over the photocatalyst plates in the reactor was assumed constant. As a consequence, irradiance modeling was excluded from the model and was not evaluated. The study showed good agreement between the model predictions and the experimental data for those cases where completely laminar or turbulent flow regimens were present in the system.

The modeling of immobilized photocatalytic reactors used for water treatment is a complicated task. The complex interactions among transport processes, reaction kinetics, and radiation propagation require proper definition and incorporation of appropriate turbulence models for the hydrodynamics and mass transfer, UV radiation field model, and the kinetics of

the surface reactions in the photoreactor. In particular, near-wall modeling needs special attention as the thickness of the mass transfer boundary layer in liquid systems (where $Sc \approx 1000$) is just a few micrometers.

The primary objective of this study was to develop and evaluate experimentally a CFD-based model for the simulation of photocatalytic reactors, comprising of nano-size TiO_2 coated surfaces, used for water treatment. The computational model integrates hydrodynamics, species mass transport, chemical reaction kinetics, and irradiance distribution within the reactor. Each of these aspects have been individually analyzed and experimentally evaluated in previous investigations (Sozzi & Taghipour, 2006; Duran, et al., 2009; Duran, et al., 2010a; Duran, et al., 2010c). Three annular reactors presenting different inlet configurations, dimensions, and lamp sizes were used for the experimental evaluation. Benzoic acid (BA) was chosen as a model pollutant and the CFD-based model was evaluated over a wide range of hydrodynamic conditions ($350<Re<11,000$) in which laminar, transient, and turbulent flow regimes were present. Comprehensive methodologies were followed to obtain accurate estimations of the experimental surface reaction rate kinetics and UV lamp power outputs. The model predictions using different hydrodynamic models and near-wall modeling approaches were compared against the experimental data collected. Commercial CFD code Fluent® 6.3.26 was used to perform the simulations.

5.2. CFD model

5.2.1. Laminar flow governing equations

Assuming that the fluid is Newtonian, incompressible, isothermal, non-reactive, with constant physical properties and under laminar steady state flow, the hydrodynamic and species transport governing equations are as follows (Ranade, 2002):

Mass conservation equation:

$$\nabla \cdot (U) = 0 \tag{5.1}$$

Momentum conservation equation:

$$\nabla \cdot (\rho UU) = -\nabla P - \nabla \cdot \tau \tag{5.2}$$

where the viscous stress tensor is:

$$\tau = \mu\left(\nabla U + \nabla U^T\right) - \frac{2}{3}\mu \nabla \cdot UI \tag{5.3}$$

Species conservation equation:

$$\nabla \cdot (\rho U m_i) = -\nabla \cdot J_i \quad , \quad i = 1, 2, \ldots, N-1 \tag{5.4}$$

where the diffusive flux of species *i* is estimated using Fick's first law of diffusion:

$$J_i = -D_m \nabla(\rho m_i) \tag{5.5}$$

In Eqs. (5.1) – (5.5), ρ is density, U is velocity, P is pressure, τ is viscous stress tensor, μ is molecular viscosity, I is unit tensor, m_i is mass fraction of species i, J_i is diffusive flux of species i, N is the total number of species, and D_m is the molecular diffusivity of species i in the mixture.

5.2.2. Turbulent flow governing equations

Under the same assumptions stated for the laminar flow model, the Reynolds averaged Navier-Stokes (RANS) turbulence modeling approach involves solving the following time-average equations (Ranade, 2002):

Mass conservation equation:

$$\nabla \cdot \left(\overline{U}\right) = 0 \tag{5.6}$$

Momentum conservation equation:

$$\nabla \cdot \left(\rho \overline{U}\,\overline{U} + \rho \overline{uu}\right) = -\nabla \overline{P} - \nabla \cdot \overline{\tau} \tag{5.7}$$

Species conservation equation:

$$\nabla \cdot \left(\rho \overline{U}\,\overline{m_i} + \rho \overline{um'_i}\right) = -\nabla \cdot \overline{J}_i \quad , \quad i = 1, 2, \ldots, N\text{–}1 \tag{5.8}$$

where the overbar indicates a time-averaged value, and u and m'_i are fluctuating flow velocity and mass fraction of species i, respectively.

The specification of the apparent stress gradients $\left(\rho \overline{uu}\right)$ was made by means of a turbulence model (Nallasamy, 1987; Wilcox, 2006). Since no turbulence model is universally accepted to be superior for all conditions, four hydrodynamic turbulence models were evaluated against experimental results in this investigation: the widely used standard k–ε model (S k–ε) (Launder & Spalding, 1974), the realizable k–ε model (R k–ε) (Shih, et al., 1995), the Reynolds stress model (RSM) (Launder, et al., 1975), and the low Reynolds number k–ε turbulence model developed by Abe, Kondoh and Nagano (AKN) (Abe, et al., 1994). Near-wall modeling for the S k–ε, R k–ε and RSM models were performed with the enhanced wall treatment approach, which combines a two-layer model applicable in regions with fine near-wall meshes, with enhanced wall functions used in regions with coarse meshes

(Fluent-Inc., 2006a). On the other hand, the AKN near-wall modeling approach incorporates wall-damping effects on the empirical constants and functions in the turbulence transport equations. This approach enables the extension of the *k*–ε turbulence model all the way to the wall. The AKN model has given promising results in modeling near-wall heat and mass transfers in various applications (Wang & Mujumdar, 2005; Wang, et al., 1996), and more recently modeling external mass transfer (Duran, et al., 2009) and surface reaction (Duran, et al., 2010) in annular reactors.

The specification of the mass transfer fluxes $\left(\rho\overline{um'_i}\right)$ was made by analogy to the linear approximation for the Reynolds stresses (or to Fick's first law of diffusion):

$$\rho\overline{um'_i} = -D_t \nabla\left(\rho\overline{m_i}\right) \tag{5.9}$$

where D_t is the so-called eddy (or turbulent) diffusivity for species concentration. Combining Eqs. (5.9), (5.8), and (5.5) results in the convection-diffusion turbulent mass transfer equation applicable to our case:

$$\nabla\cdot\left(\rho\overline{U}\,\overline{m_i}\right) = \nabla\cdot\left[\left(\rho D_m + \frac{\mu_t}{Sc_t}\right)\nabla\overline{m_i}\right] \tag{5.10}$$

with Sc_t, the turbulent Schmidt number, defined as the ratio between the turbulent viscosity, μ_t, and the turbulent diffusivity:

$$Sc_t = \frac{\mu_t}{\rho D_t} \tag{5.11}$$

A value of Sc_t = 0.7 was used in the simulations as recommended in various references (Spalding, 1971; Yimer, et al., 2002).

5.2.3. Radiation field governing equations

Modeling the radiation field in a given photoreactor involves solving the radiative (photon) transfer equation (RTE) (Cassano, et al., 1995; Fluent-Inc., 2006b). For monochromatic radiation the RTE is defined as:

$$\frac{\mathrm{d}L(\vec{r},\vec{s})}{\mathrm{d}s}+(\kappa+\sigma)L(\vec{r},\vec{s})=j^{e}(\vec{r})+\frac{\sigma}{4\pi}\int_{4\pi}L(\vec{r},\vec{s}')p(\vec{s}'\rightarrow\vec{s})d\Omega' \qquad (5.12)$$

where L is the photon radiance, $\vec{r}$ is the position vector, $\vec{s}$ is the propagation direction vector, s is the path length, κ is the absorption coefficient, σ is the scattering coefficient, j^e is the emission (source) term, p is the phase function for the in-scattering of photons, and Ω' is the solid angle about the scattering direction vector $\vec{s}'$. Fluent solves the RTE using the finite volume method which considers the RTE in the direction $\vec{s}$ as a field equation (Fluent-Inc., 2006b); thus, Eq. (5.12) is rewritten and solved as:

$$\nabla\cdot\left(L(\vec{r},\vec{s})\vec{s}\right)+(\kappa+\sigma)L(\vec{r},\vec{s})=\kappa n^{2}\frac{\sigma_{S-B}T^{4}}{\pi}+\frac{\sigma}{4\pi}\int_{4\pi}L(\vec{r},\vec{s}')p(\vec{s}'\rightarrow\vec{s})d\Omega' \qquad (5.13)$$

where n is the refractive index, $\sigma_{S\text{-}B}$ is the Stefan-Boltzmann constant (5.672×10^{-8} W m^{-2} K^{-4}), and T is the absolute temperature of the medium.

In this investigation, the reactor lamp was included in the computational domain. The lamp emission model implemented was a modification of the extensive source volumetric emission model (Irazoqui, et al., 1973) that incorporates the photon absorbance/re-emission effect produced by the mercury vapour in the lamp, so as the reflection/refraction/absorption at the lamp quartz envelope (ESVERA model). All the details about this lamp emission model and its corresponding CFD-based modeling approach can be found elsewhere (Duran, et al., 2010c).

5.2.4. Surface chemistry model

The heterogeneous photocatalytic decomposition of benzoic acid (BA) over a composite sol-gel TiO_2 coating was selected as the model reaction for the experimental evaluation of the developed CFD-based model. Photocatalytic reactions carried out in a porous photocatalyst layer are "volumetric" reactions. The rates of these reactions vary with position within the layer because of UV irradiance gradients caused by radiation absorption and concentration gradients of the reacting species caused by conversion or diffusion resistance (Herz, 2004). For the photocatalytic reaction to occur within the catalyst layer, simultaneous presence of the reagents and photons is necessary. As a consequence, the overall photocatalytic process within the catalyst layer may be controlled by the kinetics of the reaction, the internal transport of the reagents, the transport of the photons, or a combination of these processes (Camera-Roda & Santarelli, 2007). This overall reaction, however, can be treated as a surface reaction by simply expressing the observed overall degradation reaction rate (free of external mass transfer limitation) in per unit area of coated catalyst. The overall surface reaction rate expression obtained using this approach will be a function of the concentration of the reacting species and UV irradiance at the liquid-catalyst layer interface, and of a series of properties inherent to the catalyst layer (i.e., UV absorption coefficient, thickness, tortuosity, porosity, etc.) (Camera-Roda & Santarelli, 2007; Edwards, et al., 1996; Herz, 2004). Hence, these kinetic rate expressions are not intrinsic kinetics, but are rate expressions inherent to the photocatalyst layer and can therefore be utilized for predicting the pollutant degradation rate in any other immobilized system which uses the same TiO_2 coating (same preparation, coating technique, coating thickness) as in the kinetic determination study. Besides, in this investigation 254 nm UV radiation was utilized. For this radiation, the absorption coefficient on TiO_2 is reported as 5.1×10^7 m^{-1} (Mills et al., 2002), implying that

99% of the incident radiation will be absorbed within the first 90 nm of the catalyst layer. This implies that photocatalytic reactions in thick TiO_2 catalyst layers using 254 nm radiation will likely be limited by the transport of photons and no internal mass transfer limitation will occur.

Under the experimental conditions utilized in this study, the surface photocatalytic decomposition of benzoic acid ($-R_{BA}^{S}$) followed pseudo-first-order kinetics with respect to the concentration of benzoic acid and the UV irradiance (refer to Section 5.4.2). Thus, the rate expression was defined by:

$$-R_{BA}^{S} = M_W \alpha E C_{BA,S} \tag{5.14}$$

where M_W is the BA molar weight, α is the rate constant obtained from the kinetic experiments and is inherent to the photocatalyst coating, BA initial concentration, and dissolved oxygen concentration utilized in the experiments (α=4.75×10^{-6} m^3 W^{-1} s^{-1} in this study), E is the UV irradiance reaching the catalyst surface, and $C_{BA,S}$ is the BA molar concentration at the catalyst surface exposed to the fluid medium. This reaction rate expression was programmed as a sub-program (user defined function in Fluent) and it was integrated to the surface reaction rate model of Fluent. Since an overall reaction is required to be set in the CFD software, complete mineralization of BA was assumed ($C_6H_5COOH + 15/2\ O_2 \rightarrow 7\ CO_2 + 3\ H_2O$).

The "laminar finite rate" model which ignores the effect of turbulent fluctuations on reaction rates was chosen for reaction modeling. When chemical reactions are slow with respect to mixing (Da<< 1), turbulent mixing will be complete before the reaction can take place, and the contributions of fluctuating concentrations may therefore be neglected (Ranade, 2002).

5.2.5. Geometrical models and mesh structure

Two commonly used annular reactor configurations were studied, with the inlet normal (U-shape) and parallel (L-shape) to the main reactor body. The reactor geometries are shown with their dimensions in Fig. 5.1. The inlet and outlet tubes were chosen to be 100 diameters in length to ensure that a fully developed flow was established at the entrance and at the outlet boundaries of the reactor. The L-shape reactor sleeve holder consisted of three prongs (3 mm wide × 5.5 mm long × 3 mm thick) located 120° one from another.

When modeling turbulent flow using either enhanced wall treatment or low Reynolds number turbulence model approaches, it is fundamental to apply a mesh fine enough that allows solving the governing equations all the way to the wall (Fluent-Inc., 2006a). For that reason, a boundary-layer mesh was setup in the annular region where the surface reaction took place. Based on the results obtained in a previous study (Duran, et al., 2009), a $y^+ < 0.5$ at the wall-adjacent cell, and at least 10 cells within the viscosity-affected near-wall region ($Re_y < 200$) were defined. A boundary-layer mesh was also set up at the lamp envelope where high radiation gradients occur. The commercial mesh generator Gambit® 2.2.30 was used to create the grid. Structured hexahedral cells were used to discretize the physical domains, except for the region of the sleeve holder of the L-shape reactor, where it was necessary to split the reactor domain and use unstructured cells. The utilized grids had approximately 1.7 million volume cells and they were verified to give mesh-independent results.

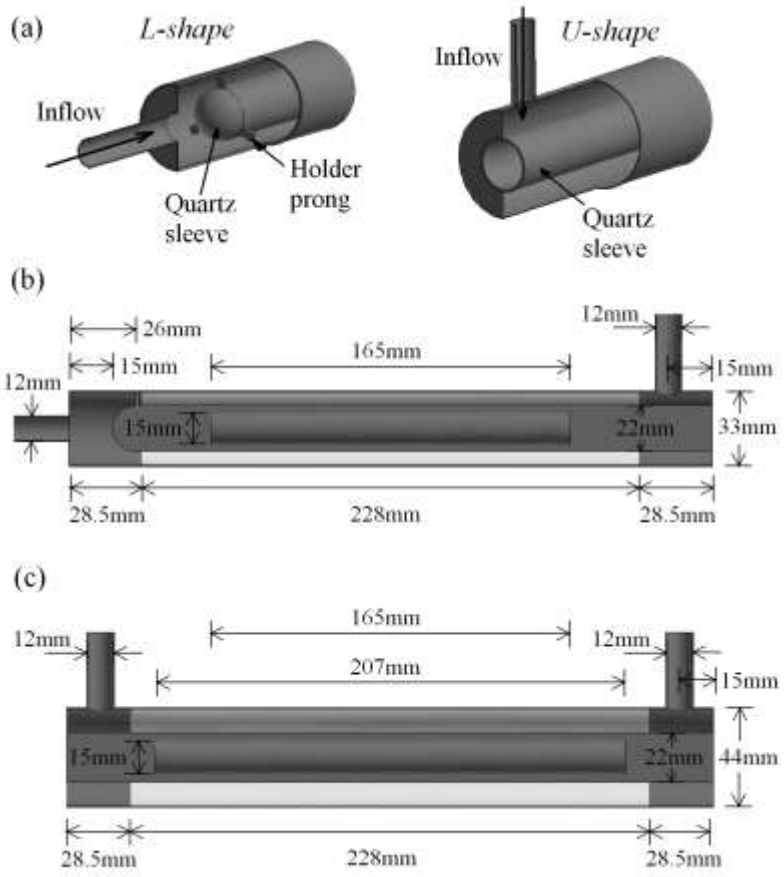

Fig. 5.1. Schematic diagram and dimensions of the U-shape and L-shape TiO_2-coated annular reactors: (a) reactor entrance details, (b) L-shape reactor dimensions, (c) U-shape reactor dimensions (with two UV lamp lengths of 165 and 207 mm). The 228 mm-long-white areas shown in both reactors correspond to the photocatalyst coatings. The cylinders inside the sleeves represent the UV lamps.

5.2.6. Boundary conditions

The boundary conditions related to the hydrodynamics and mass transport in the CFD model were defined as follows. At the inlet, the mass flow rate of the fluid was specified. The direction of the flow was defined normal to the boundary. For the cases corresponding to turbulent flow, the hydraulic diameter was fixed at 12 mm and the turbulence intensity (TI) was set according to the formula $TI = 0.16\ Re^{-1/8}$ (Fluent-Inc., 2006a). The inlet mass fractions of BA, dissolved oxygen, and carbon dioxide were specified as 4.41×10^{-6}, 8.0×10^{-6}, and 0,

respectively. These conditions were defined considering that in a typical experimental run, the initial concentration of BA was around 4.41 ppm, the dissolved oxygen concentration was kept constant at saturation (8 ppm at 25°C) and no CO_2 was present initially. At the outlet, a fully developed flow (outflow) condition was applied. At all the walls, a no-slip boundary condition was imposed. Also, zero diffusive flux of species was specified at the walls, except for the walls coated with the photocatalyst where the following boundary condition was defined:

$$J_i \cdot \hat{\mathrm{n}} = R_i^S \tag{5.15}$$

where $\hat{\mathrm{n}}$ is the unit vector normal to the surface, and R_i^S is the rate of production/depletion of species *i* arising from the surface.

The radiation field boundary conditions were defined as follows. The lamp plasma was defined as a solid continuum cylinder surrounded by a 1mm-thick, semi-transparent, fully specular wall. The temperature of the entire computational domain was set at 1 K (to eliminate any volumetric radiation effect), except for the temperature of the lamp plasma which was defined so that the radiation power generated matched the corresponding power output of the lamp. The lamp end caps were semi-transparent, fully diffused absorbent walls. The air surrounding the lamp was also defined as a solid continuum. The quartz sleeve was set as a 1mm-thick, semi-transparent, fully specular wall. The water inside the annulus was defined as a fluid continuum and all the remaining walls (including the photocatalyst-coated wall) were set as zero-thickness, opaque, fully diffused, non-reflective walls. A detailed explanation of these radiation field boundary conditions can be found elsewhere (Duran, et al., 2010c).

5.2.7 Physical properties

The concentrations of BA utilized in this study were very low (< 5 mg/L); consequently, the physical properties of water were assumed for the solution. At 298 K the following values were used (Lide, 2008; Noulty & Lealst, 1987; Thormählen, et al., 1985): μ = 8.9×10^{-4} Pa·s, ρ = 997 kg/m^3, D_m = 9.32×10^{-10} m^2/s, n = 1.38, and κ = 1.3 m^{-1} (measured for a 2.5 ppm BA solution). The optical properties assumed for the other materials were as follows: air (n = 1.00, and κ = 0 m^{-1}) (Lide, 2008), GE 124 quartz (n = 1.52, and κ = 22 m^{-1}) (Momentive; Lide, 2008), lamp plasma (n = 1.00, and κ = 191 m^{-1}) (Imoberdorf, et al., 2008). All the optical properties were estimated for 254 nm UV radiation.

5.2.8. Numerical solution method and strategy

Commercial CFD code Fluent® 6.3.26 was used to perform the simulations. The segregated steady-state solver was used to solve the governing equations. Second order upwind discretization scheme was employed except for pressure for which the standard scheme was selected. The SIMPLE algorithm was chosen for the pressure-velocity coupling. An angular discretization of 40 divisions was used for solving the RTE. This number was found to be sufficient to avoid the appearance of the "ray effect"; and to overcome control angle overhang, 1×1 pixelation was used (Pareek & Adesina, 2004; Raithby, 1999). Convergence of the numerical solution was assured by monitoring the scaled residuals to a criterion of at least 10^{-4} for the continuity and momentum, and 10^{-6} for the concentration and radiation variables. Additionally, the variation of velocity magnitude, BA concentration and radiation fluence rate at several points of the computational domain was used as an indicator of convergence.

Taking advantage of the facts that in the studied system the velocity and radiation fields did not interact, and that the photocatalytic reaction development did not affect these fields, the CFD model was solved in three steps. First, the equations of conservation of mass and momentum were solved for getting the flow field across the computational domain. Then, the velocity values were kept "frozen" and the RTE was solved for obtaining the radiation field. Finally, keeping "frozen" the converged flow and radiation field solutions, the conservation of species equation was solved for computing the BA concentration map within the system. This solving strategy saves computation time and brings stability to the solution.

5.3. Experimental

5.3.1. Catalyst preparation and characterization

The photocatalyst utilized in the experiments was a composite sol-gel TiO_2 coating (Keshmiri, et al., 2004). The preparation method for a batch of photocatalyst was as follows. 96 mL of denatured ethanol (85% ethanol+15% methanol from Fisher Sci.) was mixed with 6.4 mL of high purity deionized water and 16 mL of concentrated HCl (36.5% from Fisher Sci.). After a few minutes of agitation, 120 mL of titanium tetraisopropoxide (97% from Sigma-Aldrich) was added to the mixture. This mixture was agitated for 2 hours after which 38 g of TiO_2 Degussa P-25 was added and stirred for 12 hours. The prepared mixture was deposited on the desired surfaces (previously sandblasted using Brown Alumina Grit No 80 to improve the adhesion of the coating) using dip-coating technique at a withdrawal speed of 1.25 cm/min. The coated samples were dried at room temperature for 1 hour and then heat-treated at 500 °C for 2 h. The heating up and cooling down rate for all the samples were approximately 11 and 2 °C/min, respectively.

Two characterization analyses, namely scanning electron microscopy (SEM) (Philips XL-30), and Brunauer-Emmet-Teller (BET) surface area (Micromeritics ASAP 2020) were performed on the prepared photocatalyst coating samples. In addition, experiments for exploring the decay of the photocatalytic degradation activity were carried out utilizing the procedure and equipment detailed in Section 5.3.2. Also, the release/detachment of the synthesized photocatalyst coatings from the surface with the repeated use of the samples was gravimetrically quantified (AND GR-200 analytical balance). A more exhaustive characterization of the photocatalyst, including quantitative analyses of the resulting polymorphs of TiO_2 and scratch coating adhesion tests, has been reported elsewhere (Keshmiri, et al., 2004).

5.3.2. Determination of the surface reaction kinetics

The surface kinetics for the photocatalytic decomposition of BA over the coated TiO_2 catalyst was determined in a separate study under controlled conditions. Surface kinetics of liquid-phase photocatalytic reactions are usually functions of the pollutant concentration, dissolved oxygen concentration, and UV irradiance at the photocatalyst surface (Mills, et al., 1993; Ollis, et al., 1989; Turchi & Ollis, 1990). However, photocatalytic systems are typically operated under conditions of constant dissolved oxygen concentration. For that reason, in our experiments the dissolved oxygen concentration was maintained constant by continuous aeration of the BA solution and the determined kinetic expression related the surface reaction rate with the BA concentration and the UV irradiance only.

For obtaining the surface kinetics, experiments were conducted in a differential reactor (i.e., a reactor with very low conversion per pass) equipped with three glass slides (25mm×75mm each) coated with the photocatalyst according to the previously described

method (Section 5.3.1). The reactor consisted of a 63-mm-wide aluminum block designed to allow the BA solution to flow through a 225 mm long passage of 25 mm (width) and 3 mm (height), and over the coated glass plates. The reactor was covered by a diffused quartz plate and was irradiated by two low-pressure mercury UV lamps (GPH357T5L/4P, Atlantic Ultraviolet) mounted under an aluminum reflector. Radiometer measurements and irradiance CFD simulations reported elsewhere (Duran, et al., 2010b) demonstrated that the irradiance over the coated glass slides was fairly uniform; therefore, a constant value could be assumed. Schematics of the experimental setup can be found in the cited study (Duran, et al., 2010b). The differential reactor was operated in a constantly aerated, re-circulating batch system. 500 mL of BA solution (prepared using ACS certified BA from Fisher Sci. and ultrapure water) with an initial concentration of ~5 mg/L was charged in a mixed tank (600 mL glass beaker), and then pumped through the reactor using a magnetic drive gear pump (Micropump 221/56C). The solution was run for 30 min without UV irradiation for BA absorption equilibrium to occur; after which, samples were collected from the well mixed tank every 20 min over a period of 120 min and their BA concentration was analyzed.

The previous procedure was repeated for different UV irradiance values which were adjusted by changing the distance of the UV lamps to the reactor. The lamp centerlines (20 mm away from each other) were located 5, 10, 15, 22.5 and 30 cm above the quartz plate. The UV irradiance over the catalyst-coated slides was measured using potassium ferrioxalate actinometry. For this, 500 mL of potassium ferrioxalate solution (0.02 M), prepared and utilized as described by Murov et al. (1993), was re-circulated through the differential reactor without TiO_2 coated-slides. All the chemicals employed were ACS certified, obtained from Fisher Sci., and used as received. The reactor quartz plate was covered with UV absorbent

electrical tape (3M) except for the area above the normal position of the coated glass slides. Samples were taken from the container beaker at different time intervals and the irradiance was calculated with the following formula (Murov, et al., 1993; Romero, et al., 2003):

$$E = \frac{4.72\times10^{5}\cdot V_T}{\Phi\cdot A_{window}}\cdot\frac{\mathrm{d}C_{Fe^{2+}}}{\mathrm{d}t}\cdot 0.89 \qquad (16)$$

where V_T is the total volume of liquid solution, Φ is the quantum yield of potassium ferrioxalate at 254 nm, A_{window} is the area of the irradiated window (which corresponds to the area of the coated slides), $\mathrm{d}C_{Fe}^{2+}/\mathrm{d}t$ is the slope obtained from the linear regression of Fe^{2+}-concentration versus time, 4.72×10^5 is a factor to convert Einstein to Joule (valid for 254 nm radiation), and 0.89 is a correction factor to deduct the contributions made by the lamp emitted radiation having wavelengths longer than 254 nm (Rahn, et al., 2003). The quantum yield used in the calculations was Φ=1.41 in accordance with a recent study by Goldstein & Rabani (2008).

5.3.3. Photocatalytic degradation performance of the annular reactors

The CFD-based model was evaluated against the experimental performance of annular reactor prototypes having the same dimensions as the geometrical models described in Fig. 5.1. The reactor structures were made of PVC and included a union that allowed for fitting catalyst-coated glass tubes in the inside (see Fig. 5.2). The TiO_2 photocatalyst was coated on the inner wall of previously sand blasted glass tube halves (76 mm long and 33 or 44 mm inner diameter) as shown in Fig. 5.2a. Six tube halves were put together using electrical tape to form 228-mm-long coated tubes with either 33 or 44 mm inner diameter. The reactor quartz sleeves had 20 mm inner diameter and 1.0 mm wall thickness (quartz type GE 124, CANSCI Glass Products Ltd.). The L-shape reactor was operated using a 165 mm-long lamp, whereas

the U-shape reactor was operated using two different lamps (165 and 207 mm). With the low-pressure mercury lamps (GPH357T5L/4P, Light Sources Inc.) having 277 mm arc lengths, the desired lamp lengths (165 and 207 mm) were obtained by covering the ends of the lamps with a layer of Teflon tape, topped by another layer of electrical tape.

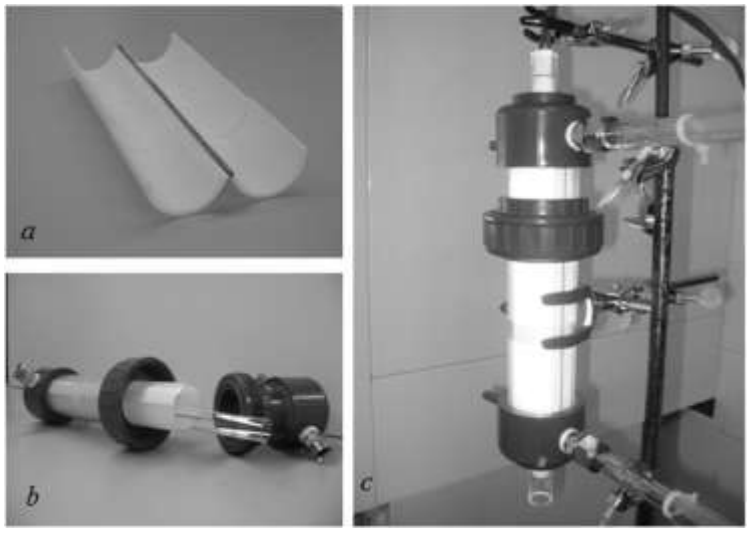

Fig. 5.2. TiO_2-coated U-shape annular reactor used in the experiments. (a) photocatalyst-coated glass halves, (b) photocatalyst-coated glass tube fitted in the PVC structure, and (c) U-shape annular reactor under operation. A similar reactor with modified inlet was used for the L-shape geometry.

The UV power output of the lamps under the actual operating conditions in the reactors was estimated as follows. First, the output of the lamps running in air was determined using the method proposed by Lawal et al. (2008). For this, the irradiance at 1 m perpendicular to the center of a lamp was measured using a radiometer (IL1700, SED240 detector, NS254 filter, International Light Tech.). Under these conditions, the power output (W) was calculated using the following formula:

$$W = \frac{E 2\pi^2 y \cdot H}{2\beta + \sin 2\beta} \tag{5.17}$$

where y is the normal distance from the lamp, H is the lamp length, and β is the half angle subtended by the lamp at the sensor position (i.e., $\tan \beta = H/(2y)$). The power values obtained in air were corrected to the operating conditions inside the reactor quartz sleeve surrounded by water at 25°C. For this, a temperature correction factor of 0.975 obtained in a separate study (Duran, et al., 2010c) was used.

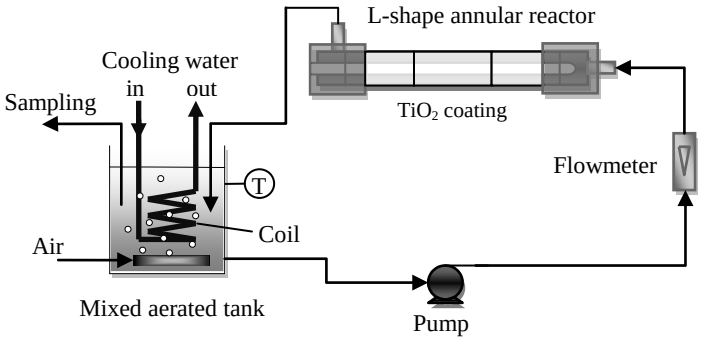

Fig. 5.3. Schematic of the experimental setup utilized for evaluating the photocatalytic degradation performance of the prototype annular reactors.

The TiO_2-coated annular reactors were operated in re-circulating batch mode using the experimental setup shown schematically in Fig. 5.3. The tank was a 3 L plastic beaker and the pump was a magnetic drive centrifugal pump (Flotec MDR6OT-X03). The temperature of the system was kept at 298.0 K ± 0.5 K, and was measured using a type-K thermocouple system (Digi-Sense, Cole-Parmer). Temperature control was achieved passing cold water through a copper coil submerged in the tank. The operation of the system involved re-circulating 2.5 L of constantly aerated BA solution (initial concentration ~5 mg/L) at constant flow rate through the reactor. At the beginning of each experiment, the solution was run for 30 min without UV irradiation for BA absorption equilibrium to occur. Following, the UV lamp (pre-operated for 30 min to achieve stabilized emission) was inserted in the reactor sleeve and samples were taken from the tank every 15 min for 90 min. The samples were analyzed for their BA content.

The procedure was repeated using flow rates of 1.0, 6.6, 11.4, and 24.6 L/min for the L-shape reactor and 1.0, 8.5, 20.0 and 27.4 L/min for the U-shape reactor.

5.3.4. Analytical methods

The concentration of Fe^{2+} formed during the actinometric measurements was determined via UV spectrophotometry at 510 nm (Murov, et al., 1993) (Cary 100 UV-Visible spectrophotometer, Varian). The concentration of benzoic acid was directly analyzed with a Waters 2695 HPLC. Separation was accomplished using a reverse phase Nova Pak C18 4 μm 3.9×150 mm separator column operated at 35°C. The compound detection was achieved using a Waters 2998 photodiode array detector with UV detection (detection wavelength = 230 nm). A sample volume of 100 μL was injected to the system and a 58% methanol/40% water/2% acetic acid solution was used as the mobile phase. The type of elution was isocratic with a flow rate of 1.23 mL/min. Empower Pro software was used to analyze the chromatographs.

5.4. Results and discussion

5.4.1. Photocatalyst characterization

In the preparation of the photocatalyst coatings, the coating surface density (thickness) was controlled with the withdrawal speed utilized in the dip-coating method. In this investigation, a withdrawal speed of 1.25 cm/min was employed for which the resulting coating surface density was estimated gravimetrically at 17.3 ± 1.7 g/m^2.

Fig. 5.4 shows SEM micrographs of samples of the composite sol-gel TiO_2 coating. As it can be seen, the coating is cracked in units approximately 50 μm long. These units seem not

to be well attached to the glass substrate contributing to low coating adhesion properties. In fact, great care had to be taken when manipulating the samples in order not to lose the coated surface. One possible factor that may have contributed to the cracking of the coating was the relatively rapid ramping up of the temperature during heat treatment. Also, the employed glass surface pre-treatment (sand blasting) produced sharp edges on the glass surface that seemed to induce the cracking of the TiO_2 material at those areas.

Even though it is realized that the coating method needs to be improved for reducing the coating cracking and hence enhancing the catalyst adhesion to the substrate surface, the mass loss of TiO_2 coating while running the system with water was not very significant. Through gravimetric measurements, it was determined that less than 12% of the coating was washed out after 30 hours of operation. This fact was also supported by the experiments (described below) that demonstrated that the photocatalyst coating activity did not considerably change even after 10 hours of continuous operation. As a result, the use of this TiO_2 coating was acceptable for the purposes of this investigation which focused on the evaluation of the CFD model in short term experiments (< 2 hours).

From the micrograph in Fig. 5.4c and others (not shown), it was estimated that the thickness of the coating is approximately in the range between 5-12 μm. Given that the density of TiO_2 is 4.23 g/cm^3 (Lide, 2008) and that the coating surface density was estimated at 17.3 g/m^2, the porosity of the coating was expected to be around 0.52.

The BET analysis reported a catalyst surface area of 22.3 m^2/g. This value is comparable to the ones obtained by Keshmiri, et al. (2004) for similar TiO_2 coatings. The catalyst pore size (13.5 nm) and the pore volume (0.104 cm^3/g) were also obtained from the BET analysis.

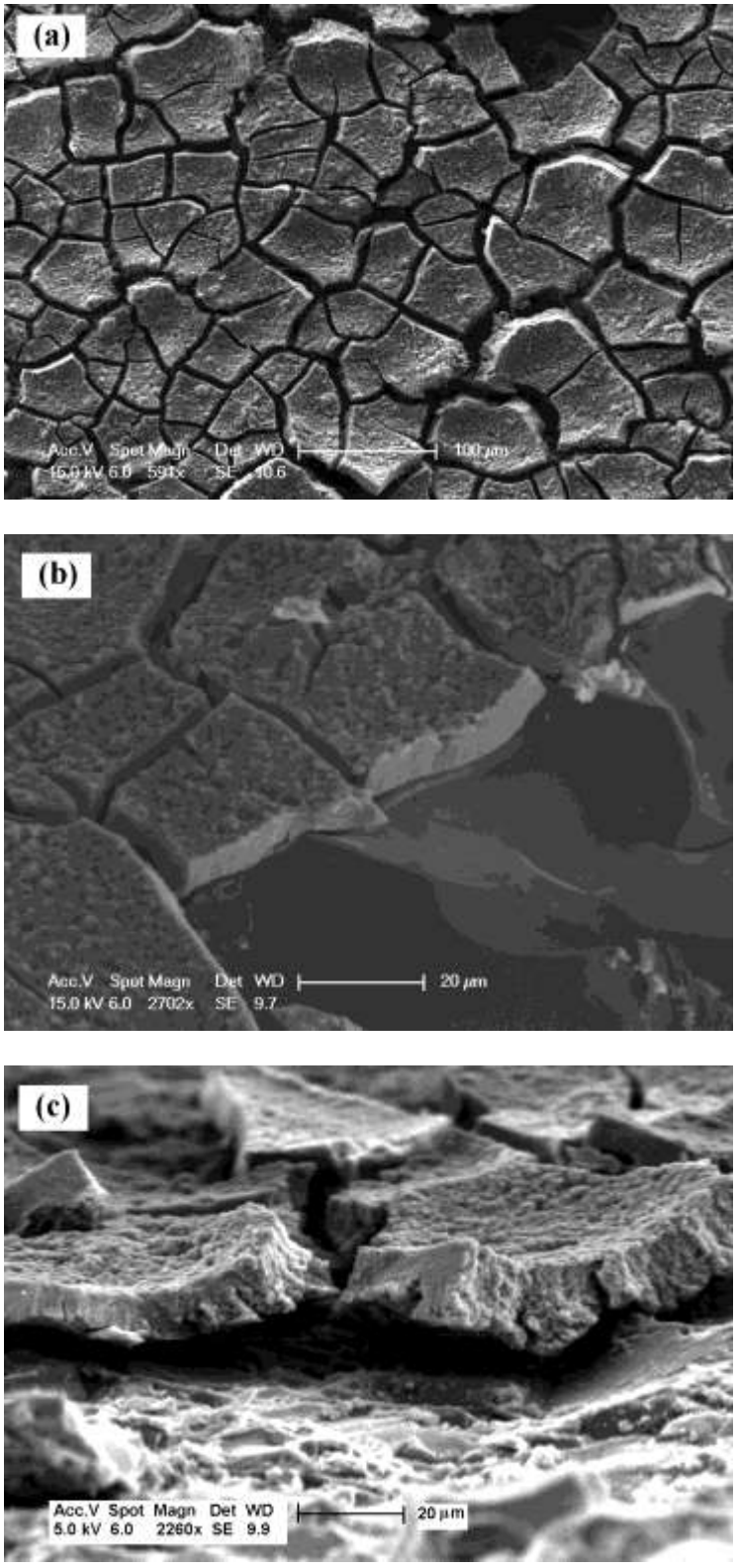

Fig. 5.4. SEM micrographs of the composite sol-gel TiO_2 coating. (a) Top view, (b) angled view, (c) side view.

The performance of the catalyst coating was also evaluated in terms of its loss of photocatalytic degradation activity with operation time. For this, several runs using the same set of TiO_2-coated slides were performed in the differential reactor setup. Each run lasted 2 hours, and for each of them, the photocatalytic activity of the coating was quantified in terms of the initial degradation rate of benzoic acid. The obtained results are reported in Fig. 5.5 and they showed that the photocatalytic activity of the TiO_2-coating remained constant (±10 %) for the first four consecutive runs.

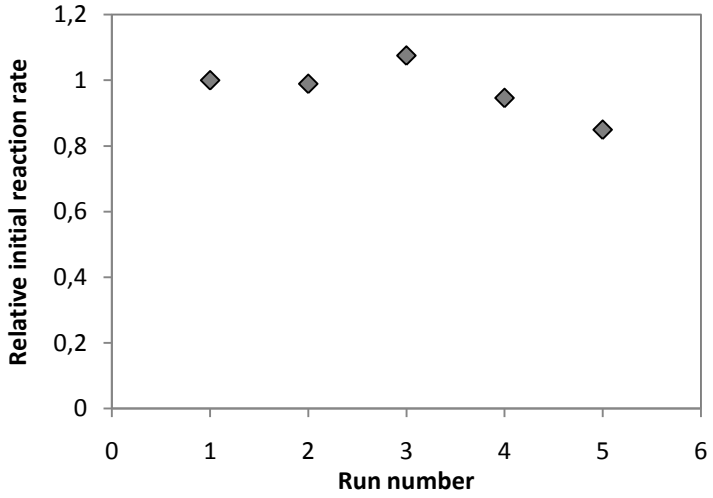

Fig. 5.5. Photocatalytic degradation activity of the photocatalyst coating after several consecutive runs. Each run lasted 2 hours.

5.4.2. Surface reaction kinetics

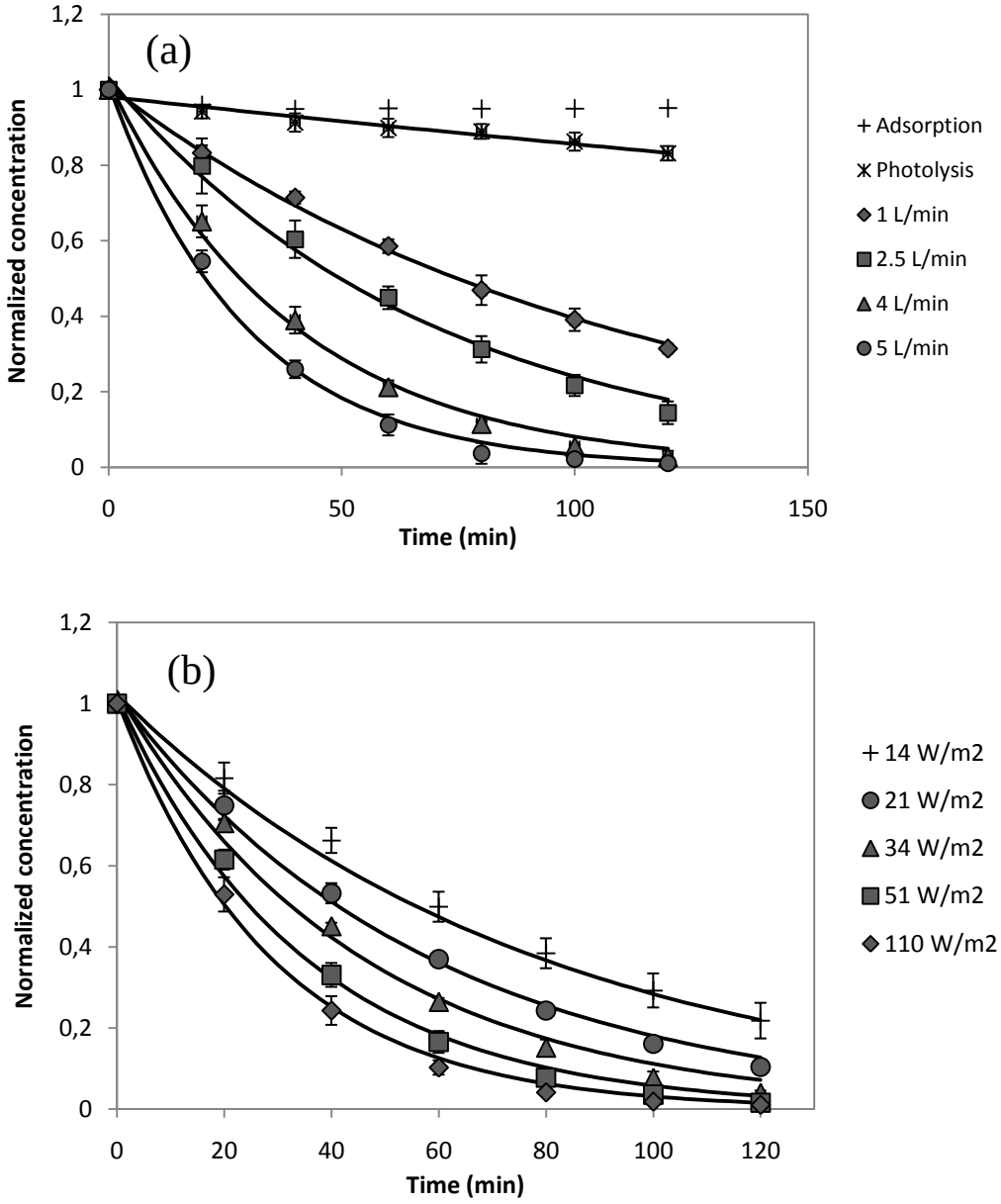

Fig. 5.6. Photocatalytic degradation of BA (initial concentration ~ 5 mg/L) obtained at 110 W/m^2 and different flow rates (a), and 5 L/min and different UV irradiances (b). The fitting lines correspond to an exponential decay.

Before investigating the surface kinetics of the photocatalytic reaction of BA, experiments were conducted to study the possible removal of the model pollutant by direct

photolysis and/or adsorption on to the photocatalyst surface. The direct photolysis experiments showed a small degradation of BA (<15% in 2 h) that presented first-order kinetics (see Fig. 5.6a). The photolytic reaction rate constants were quantified and used later for the determination of the photocatalytic surface reaction kinetics. On the other hand, only a small fraction of the initial BA (<5%) was adsorbed on the TiO_2 coating within the first 20 min of contact time. Based on this result, in the photocatalytic degradation experiments, the BA solution was circulated in the system for 30 min to achieve adsorption equilibrium before exposing the photocatalyst to the UV radiation.

Several runs at different UV irradiances and flow rates were performed in the differential reactor, each resulting in an exponential decay of BA concentration with time (see Fig. 5.6). This observed exponential decay implied that the surface reaction rate follows first-order kinetics with respect to the BA concentration (Duran, et al., 2010a). However, a dependence of the photocatalytic degradation rate on the flow rate was also observed, implying that the reaction rate was being partially limited by the rate of external mass transfer in the system. To obtain the surface kinetics under these circumstances, two approaches could be taken. One was to conduct experiments with increasing flow rates until mass transfer resistance was eliminated; however, due to the high pressures developed in the differential reactor at higher flow rates, it was not possible to increase the flow rate any further. The other approach consisted of calculating the surface reaction rate constants using the BA external mass transfer coefficients for the utilized system. In a previous study (Duran, et al., 2010b), the BA mass transfer coefficients were determined for the same differential reactor used in this investigation. In this way, the surface reaction rate constants (k'') were calculated as follow (Fogler, 2006):

$$k'' = \frac{k''_{eff} \cdot k_c}{k_c - k''_{eff}} \tag{5.18}$$

where k''_{eff} is the effective surface reaction rate constant, and k_c is the mass transfer coefficient for experiments performed using a flow rate of 5 L/min. k''_{eff} was obtained subtracting the rate constant associated with direct photolysis from the observed reaction rate constants. Fig. 5.7 shows the surface reaction rate constants obtained for different UV irradiances. The irradiances correspond to the values measured using the potassium ferrioxalate actinometer. The surface reaction rate constants presented a linear relationship with the UV irradiance ($k'' = 4.75\times10^{-6} \cdot E$); and overall, the molar photocatalytic degradation rate of BA ($-r''_{BA}$) followed first-order kinetics with respect to BA concentration and UV irradiance at the photocatalyst surface layer:

$$-r''_{BA} = 4.75\times10^{-6} \cdot E \cdot C_{BA,S} \tag{5.19}$$

Heterogeneous photocatalytic reactions of diluted substrate solutions with constant dissolved oxygen concentration are commonly found to follow pseudo-first-order kinetics with respect to the substrate concentration (Hoffmann, et al., 1995; Zhou & Ray, 2003). Also, linear dependence of the reaction rate with the UV irradiance is normally reported for systems under low UV irradiation (Brosillon, et al., 2008; Ollis, et al., 1991). For the particular case of BA, analogous results were reported in another investigation in which the concentration and irradiance conditions were similar to the ones used in this work (Mehrotra, et al., 2005).

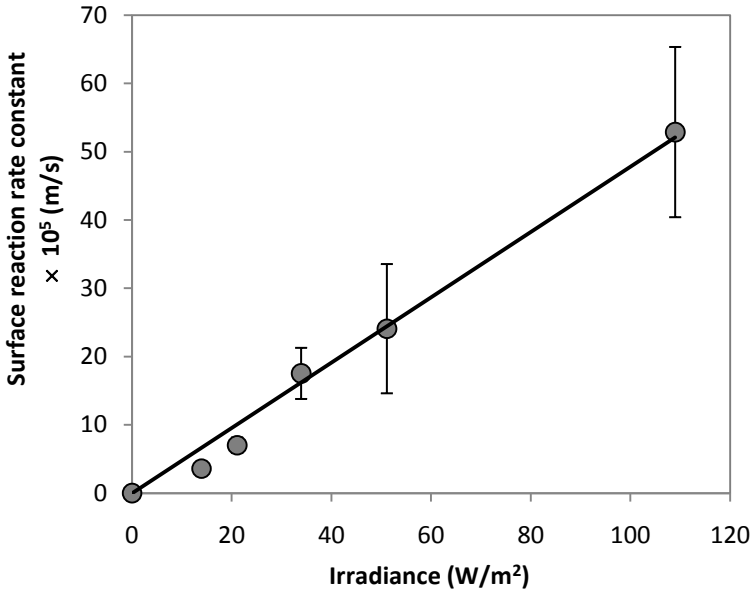

Fig. 5.7. Surface reaction rate constants obtained at different UV irradiances for the photocatalytic degradation of BA over the composite sol-gel TiO_2 coating. The error bars represent the 95% confidence intervals.

It is worth noting that even though the surface reaction rate expression (Eq. (5.19)) does not correspond to the intrinsic reaction kinetics, it is inherent to the photocatalyst coating and dissolved oxygen concentration used in the kinetic experiments (Camera-Roda & Santarelli, 2007; Chen, et al., 2000; Edwards, et al., 1996; Herz, 2004). Therefore, it is expected that this surface reaction kinetic expression can be utilized for predicting the BA degradation rate in any other immobilized system which uses the same TiO_2 coating (same preparation, coating technique, coating thickness) and dissolved oxygen concentration as in here. Similar methodology presented here can be applied to determine the surface kinetic expression for other conditions.

5.4.3. CFD simulations of the prototype annular reactors

Besides the surface kinetics expression, the other required experimental parameter for running the CFD simulations was the lamp power outputs. Due to the importance of this parameter, the comprehensive methodology described in the Experimental section was employed for obtaining reliable values. Following this method, the UV output of the 165 and 207 mm lamps were estimated to be 3.3 and 4.1 W, respectively.

Steady state CFD simulations of the prototype annular reactors were performed using different hydrodynamic models. Several operating flow rates which represented $350<Re<11{,}000$ were used to cover a range of laminar, transitional, and turbulent flow conditions. Even though the absolute values of the obtained results were different for each of the flow rates and turbulence models evaluated, the main patterns and local distributions of the analyzed variables (velocity, mass transfer coefficient, surface reaction rate, and external effectiveness factor) were somehow similar. These general results are described in the following paragraphs.

The obtained hydrodynamic results (Fig. 5.8) were very similar to the ones obtained in previous investigations of annular reactors (Duran, et al., 2009; Sozzi & Taghipour, 2006). Essentially, the velocity magnitude distribution along the annular space was more uniform for the L-shape than for the U-shape configuration. In the U-shape reactor, the fluid presented high velocities in the section opposite to the inlet and outlet ports, but low velocities on the same side of the ports. In the case of the L-shape reactor, the inner tube holder prongs generated a wake of low velocity behind them. These velocity distributions induced analogous local mass transfer coefficient distributions on the photocatalyst-coated surfaces, as presented in Fig. 5.9. The local mass transfer coefficients were calculated in Fluent using a custom field function defined as:

$$k_c = \frac{4.75\times10^{-6}\ E\cdot C_{BA,S}}{C_{BA,B} - C_{BA,S}} \qquad (5.20)$$

where $C_{BA,B}$ is the concentration of BA in the bulk fluid (assumed equal to the inlet concentration due to the small conversion of BA). Eq. (5.20) is obtained from equating the surface reaction rate (Eq. (5.19)) and the mass transport flux; this derives from the steady state assumption used for solving the governing equations.

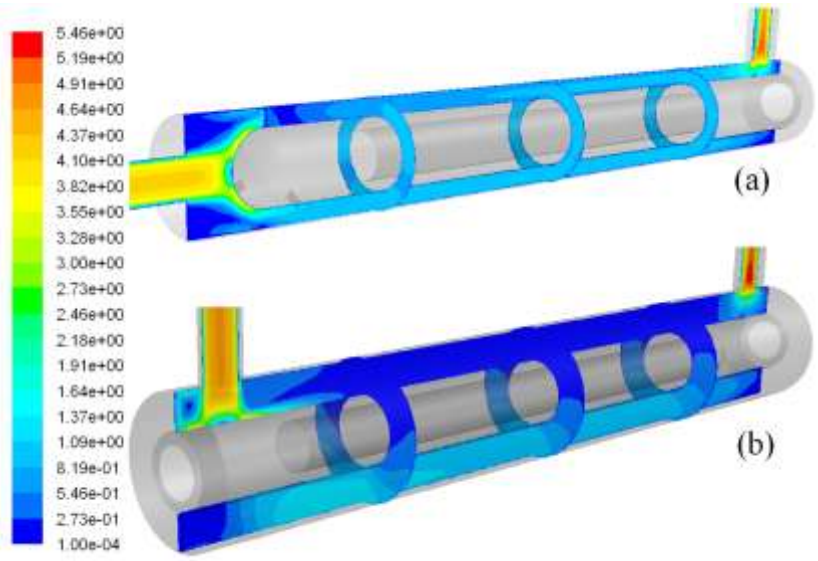

Fig. 5.8. Contours of velocity magnitude (m/s) in the L-shape (a) and U-shape (b) annular reactors calculated using the AKN turbulence model. The figure shows the longitudinal center plane and three transversal planes along the reactor volume. The results correspond to flow rates of 24.6 L/min (Re = 11,000) and 27.4 L/min (Re=10,000), respectively.

The local distribution of mass transfer coefficients is valuable for analyzing the performance of immobilized photocatalytic reactors. The overall reaction rate in these systems is usually limited by the rate of mass transport. Hence, identifying areas of low mass transfer, and finding alternatives for increasing the transport of species towards those photocatalyst-

coated areas will result in an increase of the degradation rate achieved in the photoreactor. For example, the U-shape annular reactor configuration presents a low mass transfer area in the top region of the reactor, towards the outlet port (see Fig. 5.9b). This situation could be improved, for example, with the insertion of internal baffles that generate fluid turbulence towards that region.

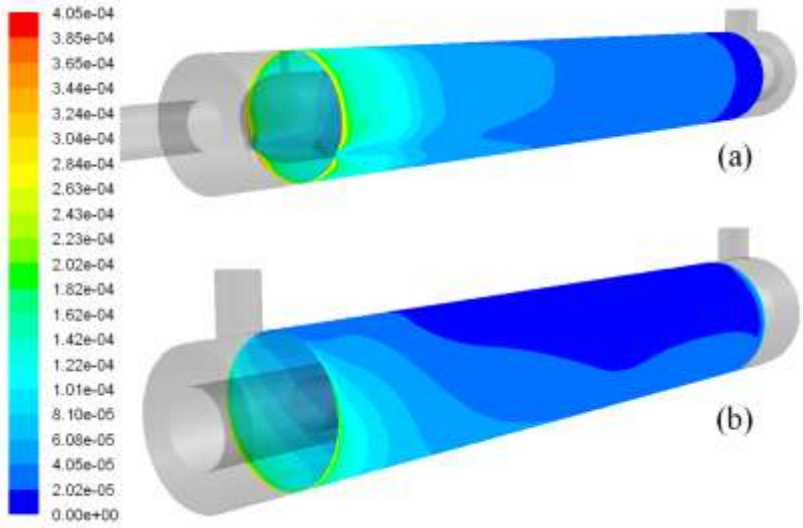

Fig. 5.9. Local mass transfer coefficient distributions (m/s) on the photocatalyst surface of the L-shape (a) and U-shape (b) annular reactors as calculated using the AKN turbulence model. The results correspond to flow rates of 24.6 L/min (Re = 11,000) and 27.4 L/min (Re=10,000), respectively.

The results of the radiation field simulations are presented in terms of irradiance distributions over the TiO_2-coated surface in Fig. 5.10. Due to the proximity between the photocatalyst surface and the lamps (<1.5 cm), the predicted irradiance profiles were nearly flat in the regions directly facing the lamps and then dropped drastically towards the ends of the coated-areas. These results agree with the experimental measurements of irradiance at the outer wall of an annular reactor reported elsewhere (Duran, et al., 2010c). As seen in Fig. 5.10,

the irradiance distributions and irradiance values on the photocatalyst layer of each reactor are very specific. For example, the irradiance values at the cental area of the reactors (areas with the highest irradiance) present differences of up to 50%. Evaluating the CFD model at different UV irradiance values and distributions is very important since during scale-up these quantities usually change.

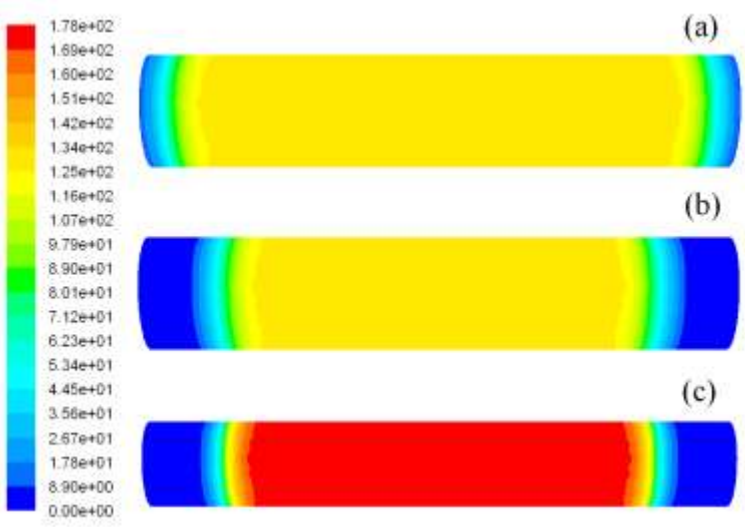

Fig. 5.10. Irradiance distributions (W/m^2) over the TiO_2-photocatalyst surface for: (a) U-shape reactor with 207 mm lamp, (b) U-shape reactor with 165 mm lamp, and (c) L-shape reactor with 165 mm lamp.

Fig. 5.11 presents the local surface reaction rate distributions over the photocatalyst surface. As expected, the areas combining high velocity gradients (and therefore, high mass transfer coefficients) with high UV irradiance resulted in high surface reaction rate, whereas low surface reaction rates were found in the areas having low mass transport and/or UV irradiance. The U-shape reactor with the 207 mm lamp (Fig. 5.11a) showed high surface reaction rates at the entrance region, particularly at the bottom of the annular space where the incoming fluid presented high velocity gradients. However, as expected from the local mass transfer analysis, this reactor showed low reaction rates in the top, outlet area. The U-shape

reactor with the 165 mm lamp (Fig. 5.11b) presented a similar behaviour, except for the two ends of the TiO_2-coated surface where the reaction rate was minimal due to the absence of sufficient UV irradiation. The L-shape reactor with the 165 mm lamp presented overall higher surface reaction rates due to the more uniform velocity and mass transfer distributions. However, regardless of mass transfer rates, the surface reaction rates at the end sections of the catalyst were close to zero because of the very low UV irradiance reaching the photocatalyst in those regions.

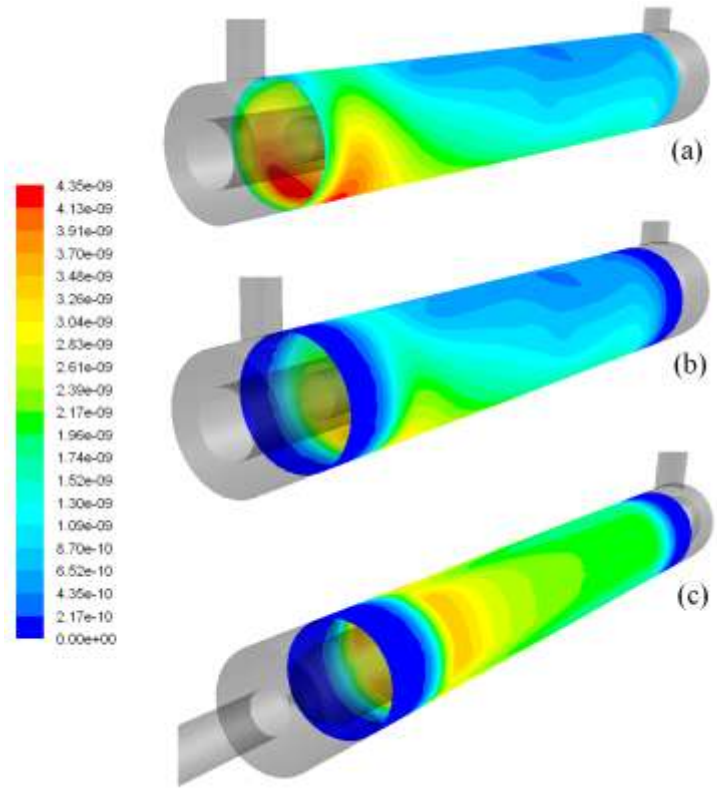

Fig. 5.11. Surface reaction rate (kmol s^{-1} m^{-2}) distributions over the TiO_2-photocatalyst surface for: (a) U-shape reactor with 207 mm lamp, (b) U-shape reactor with 165 mm lamp, and (c) L-shape reactor with 165 mm lamp. The results were computed using the AKN turbulence model for flow rates of 24.6 L/min (L-shape reactor) and 27.4 L/min (U-shape reactors).

The external effectiveness factor (E_{ex}) demonstrated to be a suitable parameter for analyzing the performance of turbulence and near-wall models in terms of their surface

reaction prediction capabilities (Duran, et al., 2010a). This factor is defined as the ratio between the observed reaction rate and the reaction rate without external mass transport limitations (Dekker, et al., 1995). In this work, E_{ex} was computed using a custom field function in Fluent as follows:

$$E_{ex} = \frac{k'' C_{BA,S}}{k'' C_{BA,B}} = \frac{C_{BA,S}}{C_{BA,B}} \tag{5.21}$$

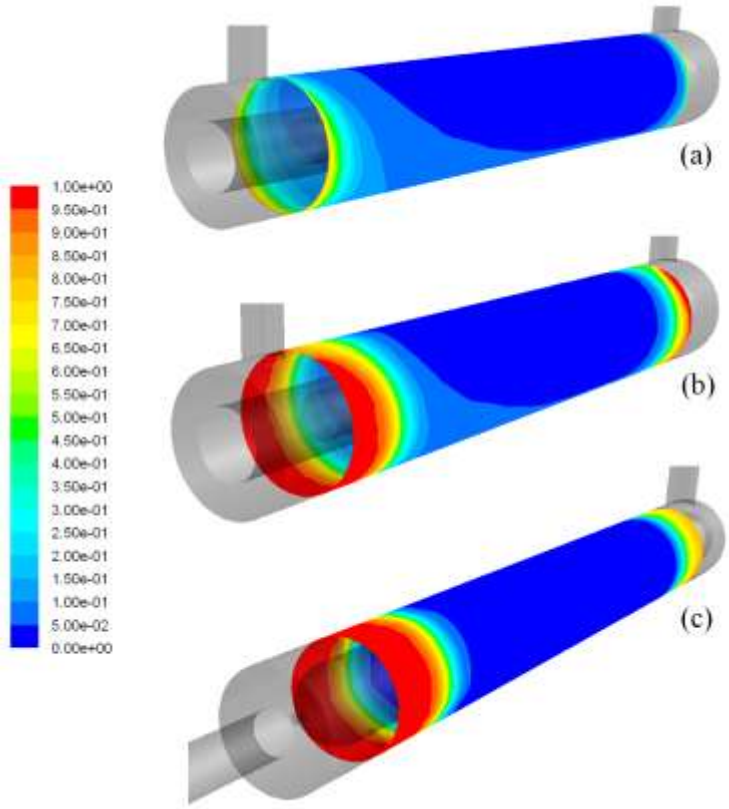

Fig. 5.12. External effectiveness factor (dimensionless) distributions over the TiO_2-photocatalyst surface for: (a) U-shape reactor with 207 mm lamp, (b) U-shape reactor with 165 mm lamp, and (c) L-shape reactor with 165 mm lamp. The results were computed using the AKN turbulence model for flow rates of 24.6 L/min (L-shape reactor) and 27.4 L/min (U-shape reactors).

Fig. 5.12 presents the local effectiveness factor distributions obtained for the analyzed annular reactors. The magnitude of E_{ex} ranges from 0 to 1 indicating the relative importance of

diffusion and reaction limitations. As E_{ex} approaches 1, the overall reaction is surface-reaction-limited, whereas when E_{ex} is much smaller than 1 (i.e., E_{ex} <<1), the overall reaction is diffusion-limited. A common criterion applied to heterogeneous reactions states that if E_{ex} is larger than 0.95, external mass transport limitation is negligible in the system (Dekker, et al., 1995). The analysis of the local E_{ex} distributions in the three reactors shown in Fig. 5.12 reveals that E_{ex} was very low at those areas where surface reaction was taking place (areas with significant UV irradiance). This result implies that at those regions, the surface reaction rate was much higher than the mass transport rate which induced overall a diffusion controlled process. E_{ex} values close to 1 were achieved only at the end sections of the catalyst surface for the 165-mm-lamp reactors, where the surface reaction rates were very low due to the lack of UV irradiation. These results confirm that overall, the pollutant degradation rates in immobilized photocatalytic reactors are strongly limited by external mass transfer. In such systems, the prediction of the overall reactor performance will be largely determined by the external mass transfer prediction capabilities of the hydrodynamic models utilized for the simulations (Duran, et al., 2010a).

5.4.4. Comparison of the CFD simulations with the reactor experimental performances

Several runs at different flow rates were performed operating the immobilized photocatalytic reactor prototypes in re-circulating batch mode. The photocatalytic degradation performance of the reactors was measured in terms of the apparent degradation rate constants (k_{app}) obtained under each experimental condition. These reaction rate constants corresponded to the photocatalytic degradation only and were computed subtracting the direct photolysis rate constants (obtained from control runs without the photocatalyst) from the observed reaction rates. The apparent reaction rate constants obtained from the experiments were

compared with the rate constants calculated by the model. The CFD-based apparent rate constants were calculated using the BA conversion per pass (X_S) achieved in the photoreactor as predicted by the steady state CFD simulations. This calculation was based on the analysis presented by Duran et al. (2010a) which derives from the fact that the conversion per pass X_S in any reactor (real or ideal) with first-order reaction kinetics is the same for the reactor operating in either continuous or re-circulating batch mode. Given this property, the apparent reaction rate constants for the re-circulating system were calculated using the following formula:

$$k_{app} = \frac{X_S}{\theta_T - X_S \theta_R} \tag{5.22}$$

where θ_T is the total residence time within the system ($\theta_T = V_T/Q$), θ_R is the residence time in the reactor ($\theta_R = V_R/Q$), V_T is the total fluid volume in the system, V_R is the reactor volume, and Q is the flow rate through the reactor.

Fig. 5.13 presents the results obtained for each of the prototype reactors and hydrodynamic models evaluated in this work. The experimental apparent reaction rates obtained for the three reactors presented a monotonic increasing tendency with respect to flow rate. These results confirmed that the overall photocatalytic degradation process was limited by the rate of mass transport within the range of the studied flow rates. When analyzing the performance predictions obtained using different hydrodynamic models, it can be noticed that the laminar model was able to predict the photocatalytic rate for all the studied annular reactors. This result agrees with those of previous studies (Duran, et al., 2009; Duran, et al., 2010a; Mohseni & Taghipour, 2004; Taghipour & Mohseni, 2005) in which the laminar model presented very good external mass transfer and surface reaction prediction performance.

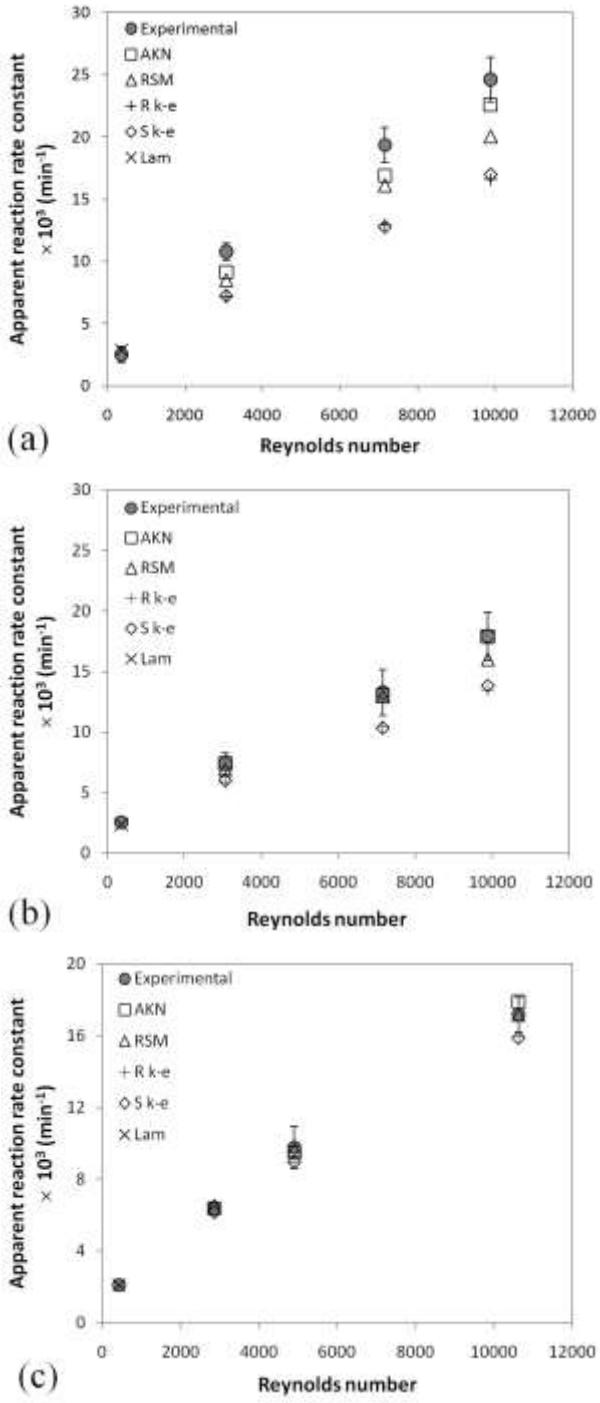

Fig. 5.13. Comparison of the apparent reaction rate constants estimated based on CFD simulations with the ones obtained experimentally for the U-shape reactor with 207 mm lamp (a), U-shape reactor with 165 mm lamp (b), and L-shape reactor with 165 mm lamp (c). The CFD predictions were computed using different hydrodynamic models and the error bars represent the 95% confidence interval obtained with triplicate runs.

The prediction performance of the turbulence models was different for each of the photocatalytic reactors. For the U-shape reactor with the 207 mm lamp, all the turbulence models underpredicted, to some extent, the apparent reaction rate constants (Fig. 5.13a). The predictions of the AKN model were in fair agreement with the experimental data (average error = 12%), RSM gave an average error of 19%, and R k-ε and S k-ε presented the largest deviation from the experimental results (average error = 33%). The CFD simulations of the external effectiveness factor for this reactor (see Fig. 5.12a) revealed that the BA degradation process was highly limited (and hence determined) by mass transfer over the entire photocatalyst surface. Under these conditions, the performance of the turbulence models for predicting the degradation of BA in the reactor was defined by their capability to predict external mass transfer in the system. In this sense, the results presented here are consistent with the ones obtained by Duran et al. (2009) in an investigation on external mass transfer prediction capabilities of different hydrodynamic models in annular reactors. According to the cited work, the studied turbulence models underpredicted the average mass transfer; however, AKN model provided better predictions of both average and local mass transfer rates. The overall underprediction was mainly attributed to an inappropriate prediction of mass transfer at the highly turbulent entrance section of the reactors. However, once the flow redeveloped through the annular space, model predictions, particularly those from the AKN and RSM models, improved significantly.

The results obtained for the other two reactors (U-shape and L-shape with 165 mm lamp) can also be discussed in the light of the previous analysis. The external effectiveness factor distribution for these reactors revealed that essentially no reaction, and hence mass transfer, took place at the end sections of the photocatalyst surface due to the absence of UV

irradiation (see Figs. 5.12b and 5.12c). According to this result, it could be expected that the overall performance of the turbulence models would be better for these reactors since no mass transport took place at the region where the models failed to predict mass transfer (entrance section of the reacto); all the species transport happened at the central region of the reactor, where turbulence models perform well predicting mass transfer. As it can be seen in Figs. 5.13b and 5.13c, the predictions of the turbulence models were in fact better for both reactors. AKN predictions presented an excellent match with the experimental data, RSM predictions were very close, but R k-ε and S k-ε continued underpredicting, to some extent, the degradation rate of BA.

Overall, AKN model presented better prediction of the degradation rate in the analyzed photocatalytic reactors. The better performance of the AKN model can be attributed to the large impact that near-wall region modeling has on interfacial phenomena predictions (Duran, et al., 2009; Wang & Mujumdar, 2005; Wang, et al., 1996). In this sense, it appears that for the systems under investigation, the low Reynolds number approach gives better results than the two-layer approach employed in the enhanced wall treatment utilized in the RSM, R k-ε and S k-ε models.

5.5. Conclusions

A CFD model for simulating immobilized photocatalytic reactors was developed and evaluated against experimental data. The evaluation of the CFD model was performed using several hydrodynamic models that incorporated different near-wall modeling approaches. The performance of the model was assessed in terms of its capability for predicting the photocatalytic degradation rate of BA, as a model compound.

Under the utilized experimental conditions, the photocatalytic degradation of BA followed pseudo-first-order kinetics with respect to both BA concentration and UV irradiance. The obtained kinetic expression is specific to the composite sol-gel TiO_2 coating, initial BA concentration, and dissolved oxygen concentration utilized in this study. This rate expression is expected to be applicable to other reactors as long as these variables remain similar to those in this work.

The experimental results and CFD simulations showed that the BA degradation rate in the analyzed photoreactors was limited by the rate of mass transport in the system. Under these conditions, the performance of CFD model was strongly determined by the external mass transfer prediction capability of the hydrodynamic models used. The CFD model photocatalytic reactor performance predictions were accurate when the laminar flow model, for laminar flow conditions, and the AKN or RSM turbulence models, for transitional and turbulent flow conditions, were applied.

The integrated model provided detailed description of the local photoreactor performance and identified the areas where improvement can be made. The model can be applied to better understanding of the reactor behaviour and design optimization.

5.6. Acknowledgments

The author acknowledges the Natural Sciences and Engineering Research Council of Canada (NSERC) for financial support and Alain Desprez for assisting with experimental and analytical work. J. Esteban Durán also thanks the support received from Universidad de Costa Rica.

5.7. References

Abe, K., Kondoh, T., & Nagano, Y. (1994). A new turbulence model for predicting fluid flow and heat transfer in separating and reattaching flows- I. Flow field calculations. *International Journal of Heat and Mass Transfer , 37* (1), 139–151.

Brosillon, S., Lhomme, L., Vallet, C., Bouzaza, A., & Wolbert, D. (2008). Gas phase photocatalysis and liquid phase photocatalysis: Interdependence and influence of substrate concentration and photon flow on degradation reaction kinetics. *Applied Catalysis B: Environmental , 78*, 232–241.

Camera-Roda, G., & Santarelli, F. (2007). Optimization of the thickness of a photocatalytic film on the basis of the effectiveness factor. *Catalysis Today , 129*, 161–168.

Cassano, A. E., Martin, C. A., Brandi, R. J., & Alfano, O. M. (1995). Photoreactor Analysis and Design: Fundamentals and Applications. *Industrial & Engineering Chemistry Research , 34* (7), 2155–2201.

Chen, D., Li, F., & Ray, A. (2000). Effect of Mass Transfer and Catalyst Layer Thickness on Photocatalytic Reaction. *AIChE Journal , 46* (5), 1034–1045.

Dekker, F., Bliek, A., Kapteijn, F., & Moulijn, J. (1995). Analysis of mass and heat transfer in transient experiments over heterogeneous catalysts. *Chemical Engineering Science , 50* (22), 3573–3580.

Denny, F., Scott, J., Pareek, V., Peng, G., & Amal, R. (2009). CFD modelling for a TiO2-coated glass-bead photoreactor irradiated by optical fibres: Photocatalytic degradation of oxalic acid. *Chemical Engineering Science , 64*, 1695–1706.

Duran, J.E., Taghipour, F., & Mohseni, M. (2009). CFD modeling of mass transfer in annular reactors. *International Journal of Heat and Mass Transfer , 52*, 5390–5401.

Duran, J.E., Mohseni, M., & Taghipour, F. (2010a). Modeling of annular reactors with surface reaction using computational fluid dynamics (CFD). *Chemical Engineering Science , 65*, 1201–1211.

Duran, J.E., Taguipour, F., & Mohseni, M. (2010b). Evaluation of model parameters for simulating TiO2 coated UV reactors. *Water Science and Technology: Water Supply* , In Press.

Duran, J.E., Taghipour, F., & Mohseni, M. (2010c). Irradiance modeling in annular photoreactors using the finite-volume method. *Journal of Photochemistry and Photobiology A: Chemistry*, In Press.

Edwards, M., Villa, C., C.G. Hill, J., & Chapman, T. (1996). Effectiveness Factors for Photocatalytic Reactions Occurring in Planar Membranes. *Industrial & Engineering Chemistry Research , 35*, 712–720.

Fluent-Inc. (2006a). *FLUENT 6.3 User's Guide. Chapter 12. Modeling Turbulence.* Lebanon, NH.

Fluent-Inc. (2006b). *FLUENT 6.3 User's Guide. Chapter 13.3. Modeling Radiation.* Lebanon, NH.

Fogler, H. S. (2006). *Elements of Chemical Reaction Engineering.* Upper Saddle River, NJ: Prentice Hall.

Goldstein, S., & Rabani, J. (2008). The ferrioxalate and iodide-iodate actinometers in the UV region. *Journal of Photochemistry and Photobiology, A: Chemistry , 193*, 50–55.

Herz, R. (2004). Intrinsic kinetics of first-order reactions in photocatalytic membranes and layers. *Chemical Engineering Journal , 99*, 237–245.

Hoffmann, M. R., Martin, S. T., Choi, W., & Bahnemannt, D. W. (1995). Environmental Applications of Semiconductor Photocatalysis. *Chemical Reviews , 95*, 69–96.

Imoberdorf, G., Taghipour, F., & Mohseni, M. (2008). Radiation field modeling of multi-lamp, homogeneous photoreactors. *Journal of Photochemistry and Photobiology A: Chemistry , 198*, 169–178.

Irazoqui, H., Cerdá, J., & Cassano, A. (1973). Radiation profiles in an empty annular photoreactor with a source of finite spatial dimensions. *AIChE Journal , 19* (3), 460–467.

Jarandehei, A., & Visscher, A. D. (2009). Three-Dimensional CFD Model for a Flat Plate Photocatalytic Reactor: Degradation of TCE in a Serpentine Flow Field. *AIChE Journal , 55* (2), 312–320.

Keshmiri, M., Mohseni, M., & Troczynski, T. (2004). Development of novel TiO2 sol-gel-derived composite and its photocatalytic activities for trichloroethylene oxidation. *Applied Catalysis B: Environmental , 53*, 209–219.

Launder, B., & Spalding, D. (1974). The numerical computation of turbulent flows. *Computer Methods in Applied Mechanics and Engineering , 3*, 269–289.

Launder, B., Reece, G., & Rodi, W. (1975). Progress in the development of a Reynolds-Stress turbulence closure. *Journal of Fluid Mechanics , 68*, 537–566.

Lawal, O., Dussert, B., Howarth, C., Platzer, K., Sasges, M., Muller, J., et al. (2008). Proposed Method for measurement of the output of monochromatic (254 nm) low pressure UV lamps. *IUVA News , 10* (1), 14–17.

Lide, D. (2008). *CRC Handbook of Chemistry and Physics, 89th Edition.* Boca Raton: CRC.

Mehrotra, K., & Ray, A. (2003). Performance Enhancement of Photocatalytic Reactor Utilizing Flow Instability. *International Journal of Chemical Reactor Enginnering , 1*, Article A12.

Mehrotra, K., Yablonsky, G. S., & Ray, A. K. (2005). Macro kinetic studies for photocatalytic degradation of benzoic acid in immobilized systems. *Chemosphere , 60*, 1427–1436.

Mills, A., Davies, R. H., & Worsley, D. (1993). Water Purification by Semiconductor Photocatalysis. *Chemical Society reviews , 22* (6), 417–425.

Mills, A.,Lee, S., Lepre, A., Parkin, I., & O'Neill, S. (2002). Spectral and photocatalytic characteristics of TiO2 CVD films on quartz. *Photochemical & Photobiolical Sciences, 1*, 865–868.

Mohseni, M., & Taghipour, F. (2004). Experimental and CFD analysis of photocatalytic gas phase vinyl chloride (VC) oxidation. *Chemical Engineering Science , 59* (7), 1601–1609.

Momentive. (n.d.). Retrieved 08 22, 2009, from http://www.gequartz.com/en/optical.htm

Murov, S., Carmichael, I., & Hug, G. (1993). *Handbook of Photochemistry* (Second ed.). New York: Marcel Dekker, Inc.

Nallasamy, M. (1987). Turbulence models and their applications to the prediction of internal flows: A review. *Computers & Fluids , 15* (2), 151–194.

Noulty, R., & Lealst, D. (1987). Diffusion Coefficient of Aqueous Benzoic Acid at 25°C. *Journal of chemical and engineering data , 32*, 418–420.

Ollis, D. F., Pelizzetti, E., & Serpone, N. (1989). Heterogeneous Photocatalysis in the Environment: Application to Water Purification. In N. Serpone, & E. Pelizzetti, *Photocatalysis: Fundamentals and Applications* (pp. 603–637). New York: John Wiley & Sons.

Ollis, D. F., Pelizzetti, E., & Serpone, N. (1991). Photocatalyzed destruction of water contaminants. *Environmental Science & Technology , 25* (9), 1522–1529.

Pareek, V. K., Cox, S. J., Brungs, M. P., Young, B., & Adesina, A. A. (2003). Computational fluid dynamic (CFD) simulation of a pilot-scale annular bubble column photocatalytic reactor. *Chemical Engineering Science , 58* (3–6), 859–865.

Pareek, V., & Adesina, A. (2004). Light Intensity Distribution in a Photocatalytic Reactor Using Finite Volume. *AIChE Journal , 50* (6), 1273–1288.

Periyathamby, U., & Ray, A. K. (1999). Computer Simulation of a Novel Photocatalytic Reactor Using Distributive Computing Environment. *Chemical Engineering Technology, 22*, 881–888.

Rahn, R., Stefan, M., Bolton, J., Goren, E., Shaw, P., & Lykke, K. (2003). Quantum yield of the iodide-iodate chemical actinometer: Dependence on wavelength and concentration. *Photochemistry and Photobiology , 78* (2), 146–152.

Raithby, G. (1999). Evaluation of discretization errors in finite-volume radiant heat transfer predictions. *Numerical Heat Transfer, Part B , 36*, 241–264.

Ranade, V. (2002). *Computational Flow Modeling for Chemical Reaction Engineering.* London: Academic Press.

Ray, A. (1998). A new photocatalytic reactor for destruction of toxic water pollutants by advanced oxidation process. *Catalysis Today , 44*, 357–368.

Romero, R., Alfano, O., & Cassano, A. (2003). Radiation Field in an Annular, Slurry Photocatalytic Reactor. 2. Model and Experiments. *Industrial & Engineering Chemistry Research , 42*, 2479–2488.

Romero-Vargas Castrillón, S., & Lasa, H. I. (2007). Performance Evaluation of Photocatalytic Reactors for Air Purification Using Computational Fluid Dynamics (CFD). *Industrial & Engineering Chemistry Research , 46*, 5867–5880.

Romero-Vargas Castrillón, S., Ibrahim, H., & Lasa, H. d. (2006). Flow field investigation in a photocatalytic reactor for air treatment (Photo-CREC-air). *Chemical Engineering Science , 61*, 3343 – 3361.

Salvado-Estivill, I., Hargreaves, D. M., & Li Puma, G. (2007). Evaluation of the Intrinsic Photocatalytic Oxidation Kinetics of Indoor Air Pollutants. *Environmental Science & Technology , 41* (6), 2028–2035.

Sengupta, T., Kabir, M., & Ray, A. (2001). A Taylor Vortex Photocatalytic Reactor for Water Purification. *Industrial & Enginnering Chemistry Research , 40*, 5268–5281.

Shih, T., Liou, W., Shabbir, A., Yang, Z., & Zhu, J. (1995). A new *k*-ε eddy viscosity model for high Reynolds number turbulent flows - model development and validation. *Computers Fluids , 24*, 227–238.

Sozzi, D. A., & Taghipour, F. (2006). Computational and experimental study of annular photo-reactor hydrodynamics. *International Journal of Heat and Fluid Flow , 27* (6), 1043–1053.

Spalding, D. (1971). Concentration Fluctuations in a Round Turbulent Free Jet. *Chemical Engineering Science , 26*, 95–107.

Taghipour, F., & Mohseni, M. (2005). CFD Simulation of UV Photocatalytic Reactors for Air Treatment. *AIChE Journal , 51* (11), 3039–3047.

Thormählen, I., Straub, J., & Grigull, U. (1985). Refractive index of water and its dependence on wavelength, temperature and density. *Journal of Physical and Chemical Reference Data , 14*, 933–945.

Turchi, C. S., & Ollis, D. F. (1990). Photocatalytic degradation of organic water contaminants: mechanisms involving hydroxyl radical attack. *Journal of Catalysis , 122* (1), 178–192.

Wang, S., & Mujumdar, A. (2005). A comparative study of five low Reynolds number *k*–ε models for impingement heat transfer. *Applied Thermal Engineering , 25*, 31–44.

Wang, Y., Postlethwaite, J., & Bergstrom, D. (1996). Modelling mass transfer entrance lengths in turbulent pipe-flow with applications to small cathodes for measuring local mass transfer rates. *Journal of Applied Electrochemistry , 26*, 471–479.

Wilcox, D. (2006). *Turbulence modeling for CFD.* La Cañada, Calif.: DCW Industries.

Yang, R., Zhang, Y., Xu, Q., & Mo, J. (2007). A mass transfer based method for measuring the reaction coefficients of a photocatalyst. *Atmospheric Environment , 41*, 1221–1229.

Yimer, I., Campbel, I., & Jiang, L.-Y. (2002). Estimation of the Turbulent Schmidt Number from Experimental Profiles of Axial Velocity and Concentration for High-Reynolds-Number Jet Flows. *Canadian Aeronautics and Space Journal , 48* (3), 195–200.

Zhou, S., & Ray, A. (2003). Kinetic studies for photocatalytic degradation of Eosin B on a thin film of titanium dioxide. *Industrial & Enginnering Chemistry Research , 42*, 6020–6033.

6. DESIGN IMPROVEMENT OF IMMOBILIZED PHOTOCATALYTIC REACTORS USING A CFD-TAGUCHI COMBINED METHOD [5]

6.1. Introduction

To improve the performance of an immobilized TiO_2 photocatalytic reactor prototype, many design factors (e.g., reactor geometry, service flow rate, UV lamp size and power output, number of UV lamps, incorporation of mass transfer enhancement elements) need to be analyzed. Using the one-factor-at-a-time approach for performing this complex analysis would be very time and effort consuming. Besides, the obtained results could have limited applicability since interactions between the factors may occur. A better and more efficient approach is the use of design of experiments (DOE) which allows for analyzing several factors in a set of experiments (simulations). DOE methods such as factorial design, response surface methodology, and Taguchi methods have been used in combination with CFD modeling to optimize the design of many different engineering systems (Frawley & Geron, 2009; Cheng, et al., 2006; Jian-hui, et al., 2009; Kim & Seo, 2004; Frawley, et al., 2009; Wang, et al., 2009; Cheng, et al., 2008; Yang, et al., 2005). Particularly, the Taguchi method (Taguchi, 1987) has been found to be a powerful optimization tool since the number of experiments (simulations) is reduced with respect to other techniques (e.g., factorial designs). Also, the sensitivity of each parameter can be analyzed allowing to investigate the factors that have more influence on the performance of the system.

The annular reactor geometry is considered to be perhaps the simplest and one of the most efficient configurations for photocatalytic applications using artificial radiation sources (Romero, et al., 2003). Most of earlier optimization studies have focused on operational

[5] A version of this chapter has been submitted for publication.
Duran, J.E., Taghipour, F., & Mohseni, M. Design improvement of immobilized Photocatalytic reactors using a CFD-Taguchi combined method.

factors (e.g., photocatalyst loading, pollutant initial concentration, aeration rate, pH, UV output, photocatalyst particle size, flow rate, etc.) of the TiO_2 slurry configuration (Vildozo, et al., 2010; Chong, et al.; Camera-Roda, et al., 2009). In the case of TiO_2 immobilized annular photoreactors, the pollutant degradation is more related to geometrical factors which determine the illuminated surface area-to-volume ratio and the external mass transfer in the system. However, little research has been conducted in this area. Imoberdorf et al. (2007) studied the effect of different configurations and design variables on the performance of single- and multi-annular photocatalytic reactors used for air treatment. The authors concluded that the performance of the photoreactor can be improved by constructing annular reactors of small annular width and large photocatalytic surface area.

This study utilized a CFD model (Duran, et al., 2010b) recently developed for the simulation of immobilized photocatalytic rectors to investigate the effect of different geometrical factors and mass transfer enhancement elements on pollutant degradation in an annular photoreactor. The annular reactor configuration studied was the one in which the inlet is parallel to the main reactor body (L-shape) with the photocatalyst coated on the inner wall of the outer tube. A Taguchi orthogonal test array design $L_9 (3)^4$ with 9 standard simulations (Taguchi, 1987) was used to analyze four design factors at three different levels. As a result of this analysis, the annular reactor design that achieved the highest performance could be determined. In addition, the factors with more influence on the performance of the system could be determined. Commercial CFD code Fluent® 6.3.26 was used to perform the simulations. The CFD model was experimentally evaluated using pesticide 2,4-D as a model pollutant.

6.2. CFD model

The CFD model utilized in this investigation is described in detail elsewhere (Duran, et al., 2010b). In the cited study, the CFD model was evaluated against experimental data obtained using benzoic acid as model pollutant and showed excellent performance. Based on the reported results, the laminar hydrodynamic model was used for simulations having laminar flow conditions, whereas the low Reynolds number k–ε turbulence model developed by Abe, Kondoh and Nagano (AKN) (Abe, et al., 1994) was used for transitional and turbulent flow conditions.

For the surface chemistry model in this work, the rate expression for the surface photocatalytic decomposition of 2,4-D ($-R^{S}_{2,4-D}$) was defined by:

$$-R^{S}_{2,4-D} = M_W \frac{2.26\times10^{-3}E}{136+E} C_{2,4-D,S} \qquad (6.1)$$

where M_W is the 2,4-D molar weight, E is the UV irradiance reaching the catalyst surface, and $C_{2,4\text{-}D,S}$ is the 2,4-D molar concentration at the catalyst surface exposed to the fluid medium. This expression was developed based on kinetic experiments conducted in parallel (refer to Section 6.6.1). Also, the diffusion coefficient of 2,4-D in the fluid was defined as D_m = 6.57×10^{-10} m^2/s (Gharagheizi & Sattari, 2009) and the overall reaction required to be set in the model was:

$$C_8H_6Cl_2O_3 + 15/2\ O_2 \rightarrow 8\ CO_2 + 2\ H_2O + 2\ HCl \qquad (6.2)$$

The inlet mass fractions of 2,4-D, dissolved oxygen, CO_2, and HCl were specified as 1×10^{-6}, 8.0×10^{-6}, 0, and 0, respectively. These conditions were defined considering that in a typical experimental run, the initial concentration of BA was around 4.41 ppm, the dissolved oxygen concentration was kept constant at saturation (8 ppm at 25°C) and no CO_2 was present

initially. These conditions were defined considering that in a typical experimental run, the initial concentration of BA was around 4.41 ppm, the dissolved oxygen concentration was kept constant at saturation (8 ppm at 25°C) and no CO_2 was present initially.

The UV-lamp (diameter = 15 mm, length = 165 mm) and the reactor operation temperature (25°C) used in this investigation were the same as the ones utilized in our previous study (Duran, et al., 2010b). Therefore, the lamp radiation output was set as 3.3 W as it was experimentally determined in the cited study.

All the details about the CFD model flow and radiation field governing equations, mesh structure, boundary conditions, physical properties, and numerical solution method and strategy are reported elsewhere (Duran, et al., 2010b).

6.3. Experimental

6.3.1. Determination of the surface reaction kinetics

The CFD model was experimentally evaluated against degradation data of 2,4-D (as model pollutant) obtained in prototype annular photoreactors coated with composite sol-gel TiO_2. However, the surface reaction kinetics for the degradation of 2,4-D over the TiO_2 coating was first determined in a separate study under controlled conditions. Experiments were conducted in a differential reactor equipped with three glass slides (25mm×75mm each) coated with the photocatalyst according to the method described elsewhere (Duran, et al., 2010b). The reactor was covered by a diffused quartz plate and was irradiated by two low-pressure mercury UV lamps (GPH357T5L/4P, Atlantic Ultraviolet) mounted under an aluminum reflector. The differential reactor was operated in a constantly aerated, re-

circulating batch system. 500 mL of 2,4-D solution (prepared using ACS certified 2,4-D from Fisher Scientific and ultrapure water) with an initial concentration of ~1 mg/L was charged in a mixed tank (600 mL glass beaker), and then pumped through the reactor using a magnetic drive gear pump (Micropump 221/56C). The solution was run for 20 min without UV irradiation in order for 2,4-D adsorption equilibrium to occur. The reactor was then placed under the UV lamps (pre-heated for 30 min) and samples were collected, for 2,4-D analysis, from the well mixed tank every 10 min over a period of 60 min. The procedure was repeated for different UV irradiances which were set by changing the distance of the UV lamps to the reactor. The lamp centerlines (20 mm away from each other) were located 5, 10, 15, 22.5 and 30 cm above the quartz plate. The UV irradiance over the catalyst-coated slides was measured using potassium ferrioxalate actinometry as detailed elsewhere (Duran, et al., 2010b).

6.3.2. Experimental evaluation of the CFD model

The CFD-based model was evaluated against the experimental performance of three annular reactor prototypes having the dimensions described in Fig. 6.1. The reactor sleeve holders consisted of three prongs (3 mm wide × 3 mm thick) located 120° one from another. The three reactors were coded as A (d_1 = 22 mm, d_2 = 33 mm), B (d_1 = 22 mm, d_2 = 44 mm) and C (d_1 = 22 mm, d_2 = 44 mm). Reactor C had repeated ribs of 1 mm in height (e) located every 12 mm (π) along the TiO_2-coated wall. The utilized reactor structures were made of PVC and included a union that allowed for fitting catalyst-coated glass tubes inside the reactor (see Fig. 6.2c). For reactors A and B, the TiO_2 photocatalyst was coated on the inner wall of previously sand blasted glass tube halves (76 mm long and 33 or 44 mm inner diameter). Six tube halves were put together using electrical tape to form 228-mm-long coated tubes with

either 33 (A) or 44 (B) mm inner diameter. For reactor C, the TiO_2 was coated on the inner wall of previously sand blasted 11 mm long glass tube pieces (see Fig. 6.2a). Nineteen glass pieces were put together with polytetrafluoroethylene (PTFE) washers (inner diameter = 42 mm, thickness = 1 mm) in between them to produce the desired ribs (see Fig. 6.2b). The reactor quartz sleeves had 20 mm inner diameter and 1.0 mm wall thickness (quartz type GE 124, CANSCI Glass Products Ltd.).

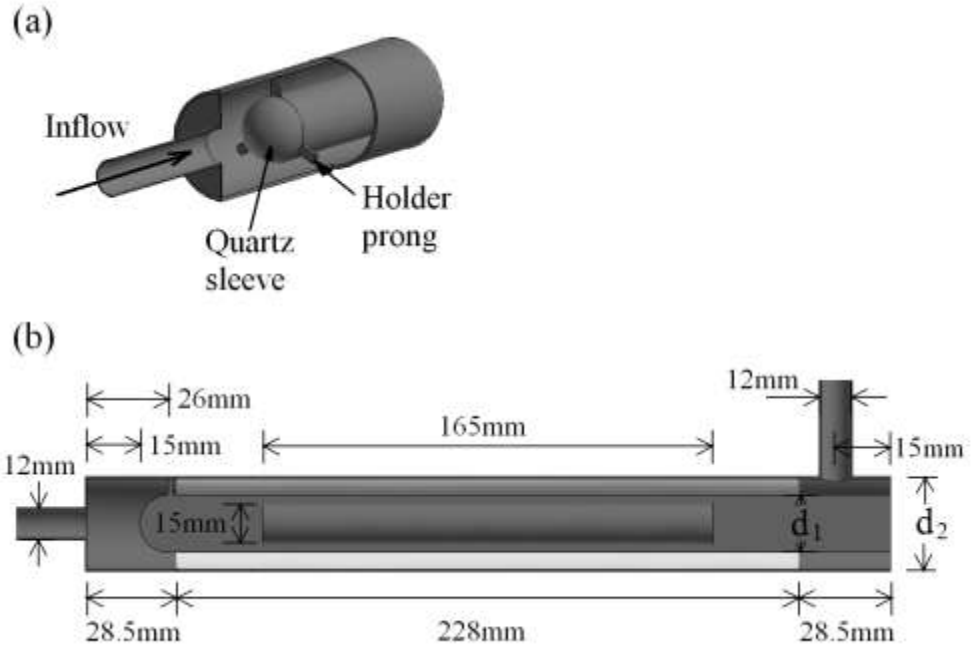

Fig. 6.1. Schematic diagram and dimensions of the studied TiO_2-coated annular reactor geometry: (a) reactor entrance details, (b) reactor dimensions. The 228 mm-long-white area shown inside the reactor corresponds to the photocatalyst coating. The cylinder inside the sleeve represents the UV lamp.

Fig. 6.2. TiO_2-coated annular reactor with repeated ribs: (a) photocatalyst-coated tube piece and PTFE washer, (b) coated glass pieces and PTFE washers put together forming a ribbed tube, (c) ribbed tube fitted in the PVC structure.

The TiO_2-coated annular reactors were operated in re-circulating batch mode. The temperature of the system was kept at 298.0 K ± 0.5 K. Temperature control was achieved passing cold water through a copper coil submerged in the tank. The operation of the system involved re-circulating 2.5 L of constantly aerated 2,4-D solution (initial concentration ~1 mg/L) at constant flow rate through the reactor. At the beginning of each experiment, the solution was run for 20 min without UV irradiation for the 2,4-D adsorption equilibrium to occur. Then, the UV lamp (pre-operated for 30 min to achieve stabilized emission) was inserted in the reactor sleeve and samples were taken, for 2,4-D analysis, from the holding tank every 15 min for 90 min. The procedure was repeated using flow rates of 1.0, 6.6, 11.4, and 24.6 L/min for reactor A and 1.0, 8.5, 17.0 and 24.6 L/min for reactors B and C.

6.3.3. Analytical method

The concentration of 2,4-D was directly analyzed with a Waters 2695 HPLC. Separation was accomplished using a reverse phase Nova Pak C18 4 μm 3.9×150 mm separator column operated at 35 °C. The compound detection was achieved using a Waters 2998 photodiode array detector with UV detection (detection wavelength = 280 nm). A sample

volume of 100 μL was injected to the system and a 58% methanol/40% water/2% acetic acid solution was used as the mobile phase. The type of elution was isocratic with a flow rate of 1.23 mL/min. Empower Pro software was used to analyze the chromatographs.

6.4. Evaluation of mass transfer enhancement elements

The performance of immobilized photocatalytic reactors is largely limited by the rate of mass transfer of the contaminants to the catalyst coating. Hence, incorporating external mass transfer promoters into the design of such reactors is desirable. In this investigation, two common promoters were evaluated for further consideration in the optimization analysis: repeated ribs on the photocatalyst-coated wall and static delta wing mixers. A schematic of these two enhancement elements are shown in Fig. 6.3. For performing the evaluation, reactors B (plain surface) and C (ribbed surface) were compared with a reactor of the same dimensions but with three delta wing mixers (isosceles triangles: base=19mm, height=22mm) placed in the middle of the reactor.

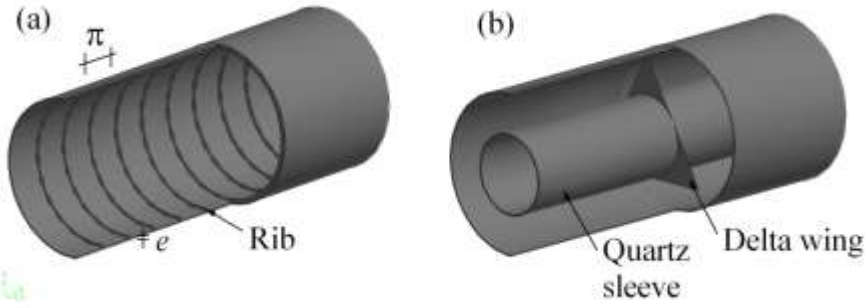

Fig. 6.3. Schematics of two external mass transfer enhancement elements: (a) repeated ribs of height *e*, separated a distance π, (b) delta wing static mixers.

6.5. Taguchi design

Four design parameters were chosen and their effects on the pollutant degradation performance of the immobilized annular photocatalytic reactors were investigated. The study was to establish proper values that improve the design of this type of reactor. The investigated design parameters were: F_1 = the annulus outer diameter (d_2), F_2 = the ratio between the annulus inner and outer diameters (d_1/d_2), F_3 = the ratio between the rib height and the hydraulic diameter ($e/(d_2-d_1)$), and F_4 = the ratio between the rib pitch and height (π/e). These parameters were studied at three different levels for identifying, if it exists, the non-linear relationship among them. The values of the parameters at each level are listed in Table 6.1. The levels of parameters F_3 and F_4 were chosen based on the recommended ranges reported in the literature on heat transfer enhancement with repeated-rib roughness (Webb, et al., 1971). Table 6.2 shows the standard $L_9(3)^4$ orthogonal array used in the present work. This array lists the values of the design parameters for each of the nine simulations needed for the corresponding statistical analysis. All the other reactor dimensions were equal to the values indicated in Fig. 6.1. For all the simulations, the lamp UV-output and the flow rate through the reactor were 3.3 W and 24.6 L/min, respectively.

Table 6.1. Design parameters with their values at three levels.

		Level		
Factor	Reactor parameter	-1	0	1
F_1	d_2 (cm)	4.4	7	9.6
F_2	d_1/d_2	0.5	0.65	0.8
F_3	$e/(d_2- d_1)$	0	0.045	0.09
F_4	π/e	6	12	18

Table 6.2. Taguchi's orthogonal array $L_9(3)^4$ for the analysis of geometrical factors influencing the performance of annular immobilized photocatalytic reactors.

Simulation	d_2 (cm)	d_1/d_2	$e/(d_2-d_1)$	π/e
1	4.4	0.50	0.000	6
2	4.4	0.65	0.045	12
3	4.4	0.80	0.090	18
4	7.0	0.50	0.045	18
5	7.0	0.65	0.090	6
6	7.0	0.80	0.000	12
7	9.6	0.50	0.090	12
8	9.6	0.65	0.000	18
9	9.6	0.80	0.045	6

In this investigation, the performance of the immobilized photocatalytic reactors was analyzed considering operation in a re-circulating batch system. The response variable (objective function) selected was the energy (pump + lamp) required to achieve a given contaminant degradation. For first-order-reaction systems, as in our case (refer to Section 6.1), this energy is proportional to the pressure drop (ΔP) across the reactor and inversely proportional to the apparent reaction rate constant (k_{app}):

$$Energy \propto \frac{\Delta P}{k_{app}} \tag{6.3}$$

The apparent reaction rate constant was calculated based on the steady-state CFD simulation results as presented by Duran et al. (Duran, et al., 2010a), using the following formula:

$$k_{app} = \frac{X_S}{\theta_T - X_S\,\theta_R} \tag{6.4}$$

where X_S is the 2,4-D conversion per pass in the reactor, θ_T is the total residence time within the system ($\theta_T = V_T/Q$), θ_R is the residence time in the reactor ($\theta_R = V_R/Q$), V_T is the total fluid volume in the system, V_R is the reactor volume, and Q is the flow rate through the reactor. The

optimization analysis was carried out maximizing a signal (response) function, *S*, of "the lower the better" type (Roy, 1990):

$$S = -10\log\left(\frac{\Delta P}{k_{app}}\right)^2 \tag{6.5}$$

Having the *S* values for each simulation, the average *S* values for each parameter (F_i) at each level were computed, so as the contribution ratios (*Co*) of each design parameter according to:

$$Co = Z_i / Z_{total} \tag{6.6}$$

where Z_i is the range of parameter i within the three levels:

$$Z_i = \max(average) - \min(average) \tag{6.7}$$

and Z_{total} is the total range:

$$Z_{total} = \sum_{i=1}^{4} Z_i \tag{6.8}$$

6.6. Results and discussion

6.6.1. Surface reaction kinetics

The 2,4-D direct photolysis and/or adsorption on TiO_2-photocatalyst was studied first. The direct photolysis experiments showed first-order degradation of 2,4-D even though the conversions were very small (<15% in 120 min), even under high irradiances (110 W/m^2). The photolytic reaction rate constants were quantified and accounted for when determining the photocatalytic surface reaction kinetics. The adsorption of 2,4-D on the TiO_2 coating was also small (<3% in 60 min).

Photocatalytic degradation runs performed in the differential reactor at different UV irradiances resulted in exponential decay of the 2,4-D concentration with time, implying that the surface reaction rate followed first-order kinetics with respect to the 2,4-D concentration (Duran, et al., 2010a). However, a dependence of the photocatalytic degradation rate on the operational flow rate was also observed, implying that the reaction rate was partially limited by the rate of external mass transfer in the system. Therefore, the surface reaction rate constants (k'') were calculated utilizing the 2,4-D external mass transfer coefficients in the employed differential reactor according to (Fogler, 2006):

$$k'' = \frac{k''_{eff} \cdot k_c}{k_c - k''_{eff}} \tag{6.9}$$

where k''_{eff} is the effective surface reaction rate constant, and k_c is the mass transfer coefficient obtained for experiments ran at 7 L/min. k''_{eff} was obtained subtracting the rate constant associated with direct photolysis from the observed reaction rate constant. The mass transfer coefficients of 2,4-D were estimated from the experimental mass transfer coefficients of benzoic acid determined for the same studied differential reactor (Duran, et al., 2010c), and using the equation:

$$k_{c,2,4-D} = k_{c,BA}\left(\frac{D_{m,2,4-D}}{D_{m,BA}}\right)^{2/3} \tag{6.10}$$

where $D_{m,2,4\text{-}D}$ (6.57×10^{-10} m^2/s) and $D_{m,BA}$ (9.32×10^{-10} m^2/s) are the molecular diffusion coefficients of 2,4-D and benzoic acid, respectively. Eq. (6.10) is based on the general dependence of mass transfer coefficients, with the diffusion coefficient to the power of 2/3 (Perry & Green, 1997).

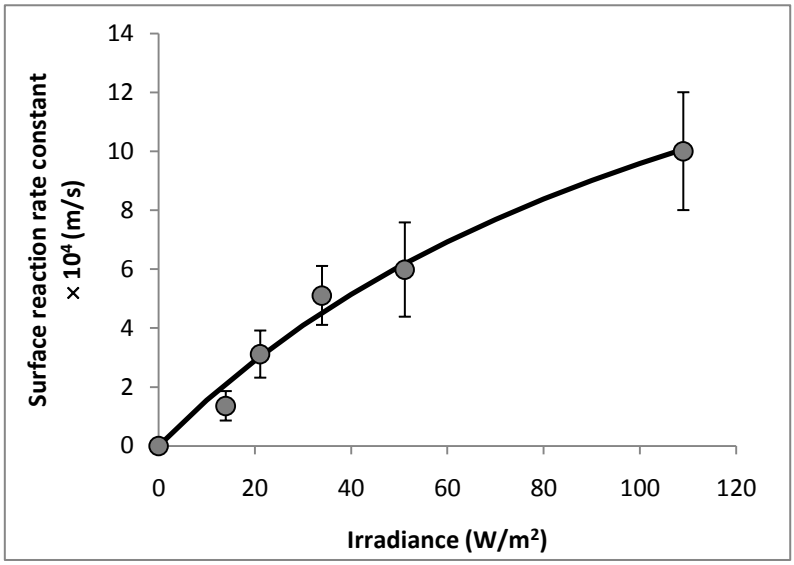

Fig. 6.4. Surface reaction rate constants obtained at different UV irradiances for the photocatalytic degradation of 2,4-D over the composite sol-gel TiO_2 coating layer. The error bars represent the 95% confidence intervals.

Fig. 6.4 shows the surface reaction rate constants obtained for different UV irradiances. The relationship between these two quantities was fitted with a saturation-growth model resulting in: $k'' = 2.29\times10^{-2}\cdot E/(113+E)$. Similar dependencies have been reported in other investigations (Modestov & Lev, 1998; Trillas, et al., 1995). Combining the results obtained, the molar photocatalytic degradation rate of 2,4-D ($-r''_{2,4\text{-}D}$) at the photocatalyst surface layer is given by:

$$-r''_{2,4-D} = \frac{2.26\times10^{-3}\cdot E}{136+E}\cdot C_{2,4-D,S} \qquad (6.11)$$

6.6.2. Experimental evaluation of the CFD model

Several runs at different flow rates were performed operating the immobilized photocatalytic reactor prototypes in re-circulating batch mode. The performance of the

photocatalytic reactors for degrading 2,4-D was quantified in terms of the apparent photocatalytic degradation rate constants (k_{app}) obtained under each experimental condition. These reaction rate constants were computed subtracting the direct photolysis rate constants (obtained from control runs without the photocatalyst) from the observed reaction rates. Fig. 6.5 presents the experimental results obtained for each of the prototype reactors, so as the CFD-based apparent reaction rate constants calculated using Eq. (6.4). The predictions based on the CFD simulations agreed fairly well with the experimental values over the entire range of flow rates studied, particularly for reactors A and B (average error < 9%). The CFD predictions for reactor C were rather higher than the experimental values (average error < 12%). This overestimation can be explained by the fact that the catalyst-coated area in the CFD model was about 8% larger than that in the experimental prototype. This was the case because the ribs in the CFD model were defined as faces without any thickness, whereas in the experimental prototype the PTFE washers were 1 mm thick. Based on these results, it was concluded that the present CFD model can give close predictions of the photocatalytic degradation performance of TiO_2-immobilized annular photoreactors with plain and ribbed surfaces.

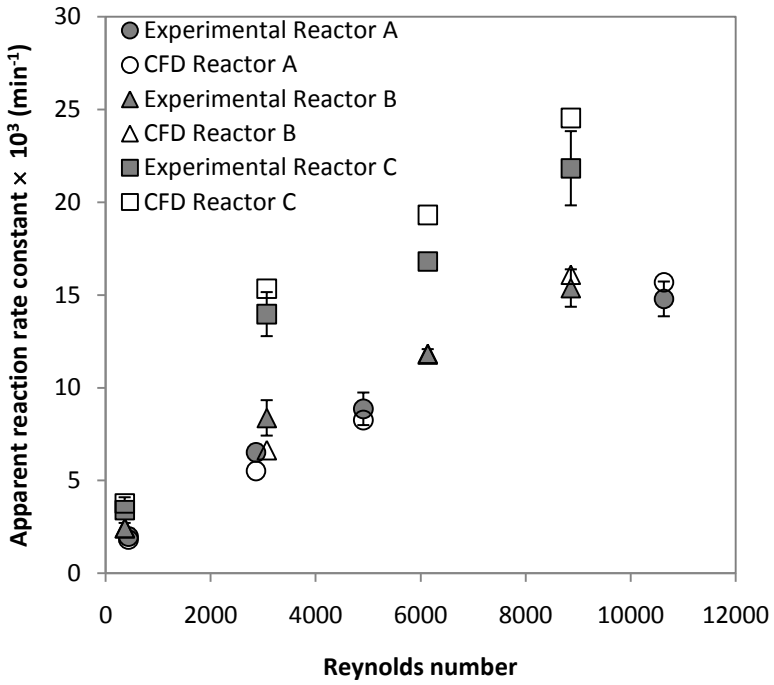

Fig. 6.5. Comparison of the apparent reaction rate constants estimated based on CFD simulations with the ones obtained experimentally for the three annular photocatalytic reactor prototypes (A, B and C). The error bars represent the 95% confidence interval obtained with triplicate runs.

6.6.3. Evaluation of mass transfer enhancement elements

Fig. 6.6 presents the CFD simulation results of the local surface reaction rate distributions over the photocatalyst surface of these three reactors at a flow rate of 24.6 L/min. The distribution in the ribbed coated surface (reactor C) showed higher values all along the wall, and as a consequence, higher pollutant degradation.

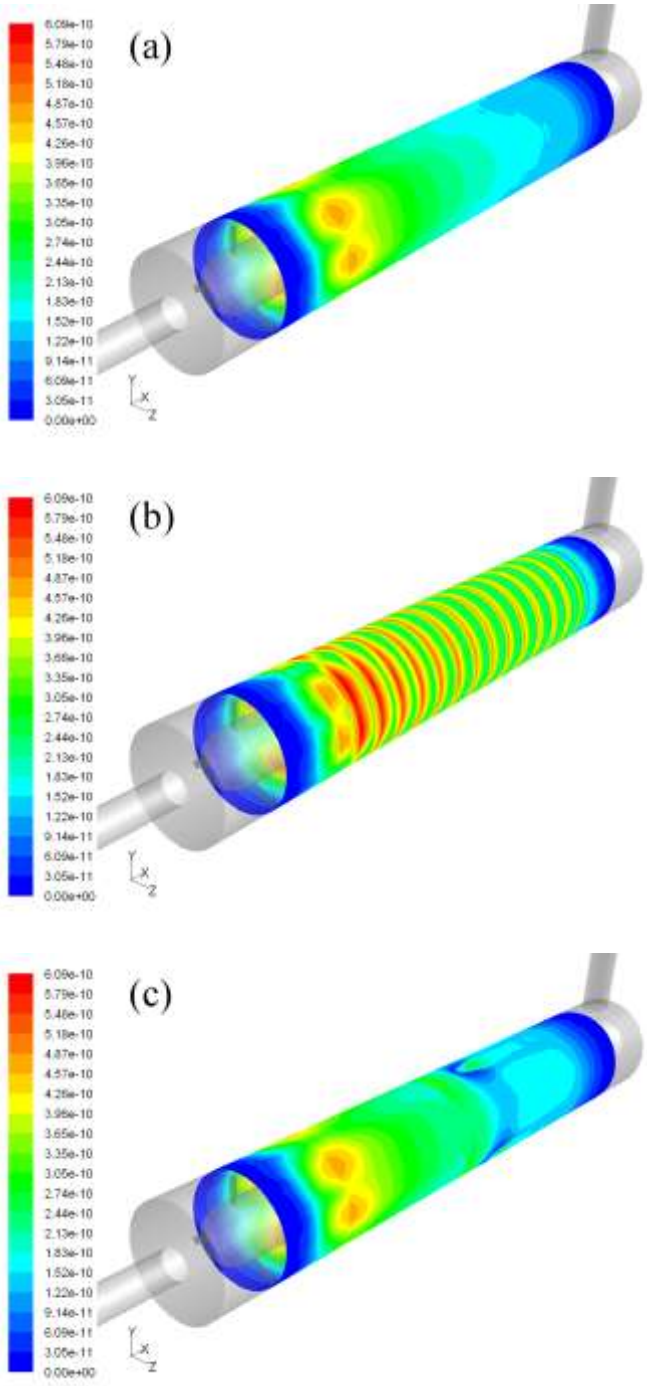

Fig. 6.6. Local surface reaction rate (kmol s^{-1} m^{-2}) distributions over the TiO_2-photocatalyst surface for: (a) reactor B (plain surface), (b) reactor C (ribbed surface), and (c) reactor with three delta wing mixers.

The distribution in the reactor with the delta wing mixers was not much different from that of reactor B (plain surface). These observations were substantiated when the data of apparent reaction rate constants, pressure drop and energy consumption for each case were analyzed (see data in Table 6.3). The reactor with repeated ribs presented a 53% higher apparent reaction rate constant and an increase of only 1% in the pressure drop when compared with the plain reactor. These corresponded to a decrease of 34% in the energy necessary for achieving a certain degree of pollutant degradation. The reactor with the delta wings presented only 8% increase in the apparent reaction rate constant and 1% increase in the pressure drop; the required energy decreased only 7%. The better performance of the repeated ribs over the delta wings is likely due to the fact that ribs produce turbulence very close to the wall, exactly where mass transfer is taking place. On the other hand, delta wings generate turbulence mainly in the core flow.

Table 6.3. Comparison of apparent reaction rate constants, pressure drop, and energy consumption for annular reactors with external mass transfer enhancement elements.

Reactor	$k_{app} \times 10^2$ (min^{-1})	ΔP (kPa)	E/E_{plain}
Plain	1.61	11.80	1.00
Ribbed	2.45	11.97	0.66
Delta wings	1.74	11.90	0.93

Under the studied circumstances, the use of repeated ribs on the TiO_2-coated wall appeared more promising for being introduced as an effective mass transfer enhancement element in the design of annular photocatalytic reactors. As a consequence, this enhancement element was further considered in the optimization analysis.

6.6.4. Taguchi design

The performance of the annular photocatalytic reactor was evaluated with different design parameters chosen for this investigation in accordance to the Taguchi standard array $L_9(3)^4$. The obtained results for the apparent reaction rate constants, pressure drop, and signal function values are presented in Table 6.4. Among the cases analyzed, the reactor design corresponding to simulation 3 was the one that presented the lowest energy consumption, and hence, the best reactor performance. In general terms, this design consists of small d_2 and large d_1/d_2, $e/(d_2-d_1)$, and π/e ratios. Small d_2 produces high radiation irradiance over the photocatalyst surface inducing higher reaction rates. Large d_1/d_2 generates higher velocity gradients in the reactor annulus, and hence, increases the rate of mass transfer. Large $e/(d_2-d_1)$ promotes the generation of turbulence (and thus, mass transfer) close to photocatalyst-coated wall. Finally, larger π/e allows the reattachment and subsequent redevelopment of the boundary layer downstream the rib (Webb, et al., 1971), increasing mass transfer.

Table 6.4. Performance of the annular photocatalytic reactor designs of the Taguchi analysis.

Simulation	$k_{app} \times 10^2$ (min^{-1})	ΔP (kPa)	S
1	1.61	11.8	-57.3
2	2.94	11.91	-52.2
3	4.11	14.52	-51.0
4	2.59	12.98	-54.0
5	2.73	12.65	-53.3
6	1.52	12.34	-58.2
7	2.70	14.04	-54.3
8	1.57	13.46	-58.7
9	3.52	12.95	-51.3

Fig. 6.7 shows the effects of each design parameter on the signal function, and hence on the photoreactor performance. Increasing d_2 resulted mainly in a decrease in S; increasing d_1/d_2 gave rise to S; increasing $e/(d_2-d_1)$ generated first an appreciable increase in S, but then the value tended to be constant; and π/e did not affected S significantly. From these plots, it was concluded that the design parameter combination at its corresponding "optimal" levels was: d_2 (-1), d_1/d_2 (+1), $e/(d_2-d_1)$ (0), and π/e (-1). A new CFD simulation of an annular reactor having these design parameter values was performed to confirm the more optimal performance of this reactor with respect to the other nine cases previously analyzed. The CFD simulation results gave k_{app} = 4.37×10^{-2} min^{-1}, ΔP = 14.27 kPa, and S = -50.3, corroborating that this particular design gives the best performance among all the designs evaluated herein.

Fig. 6.8 compares the performance of the ten analyzed reactor designs in terms of the energy required for achieving a specific degree of pollutant degradation. The energy required by the optimal case (identified as case 10 in Fig. 6.8) was taken as the reference value. As it can be seen, the energy required by all the reactor designs was higher than the one corresponding to the optimal case. For some cases (1, 6 and 8), the amount of energy was up to 2.5 times higher. Overall, these results demonstrate the effectiveness of the Taguchi method at finding better reactor designs that improve the performance of immobilized photocatalytic systems.

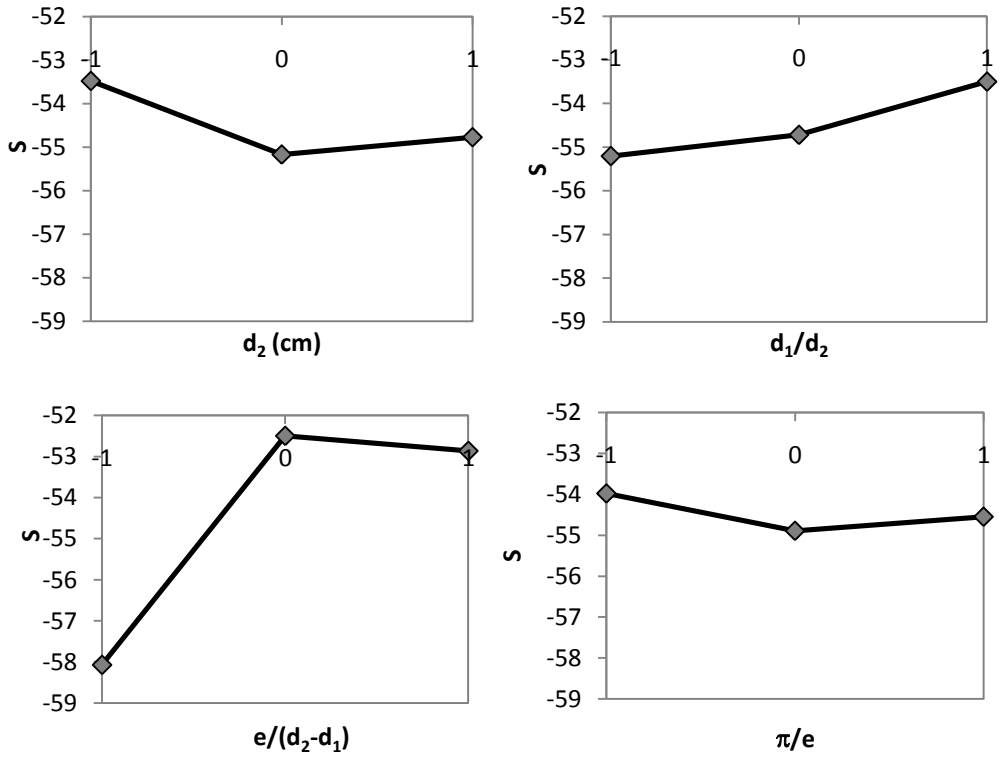

Fig. 6.7. Effects of design parameters (annulus outer diameter (d_2), annulus inner to outer diameter ratio (d_1/d_2), rib height to the hydraulic diameter ratio ($e/(d_2-d_1)$), and rib pitch to height (π/e) ratio) on the signal function (S)

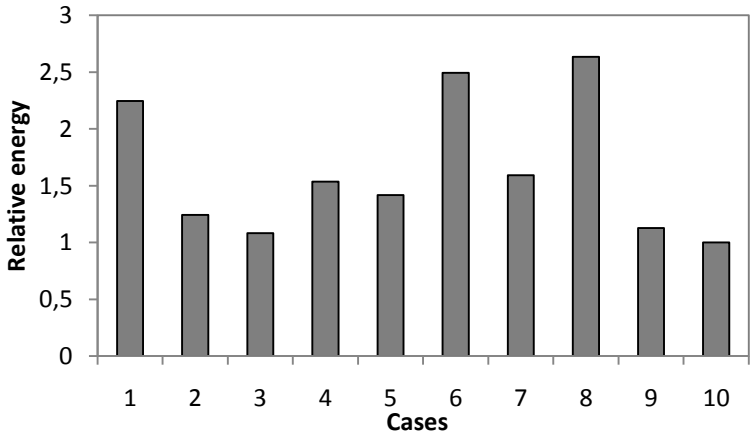

Fig. 6.8. Relative energy requiered for achieving a specific degree of pollutant degradation when operating the photocatalytic reactors in re-circulating batch mode. The reference energy corresponds to the optimal case (case 10) found in this study.

An important attribute of the Taguchi method is that it allows for determining the relative contribution of each design parameter to the change of the response variable. Fig. 6.9 shows the contribution ratio for each parameter. As seen, the $e/(d_2-d_1)$ ratio has the greatest contribution to the change in the reactor performance (57%), meaning that this parameter is the most significant one and should receive more attention during design optimization. The relative significance of the design parameters are as follows: $e/(d_2-d_1)$ (57%) > d_1/d_2 (17%) = d_2 (17%) > π/e (9%).

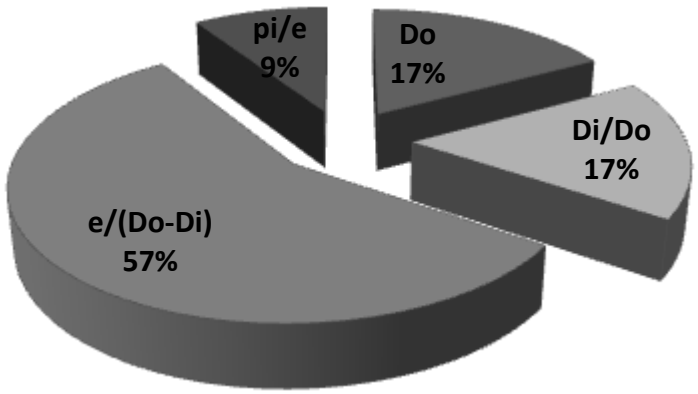

Fig. 6.9. Contribution ratios of the design parameters, annulus outer diameter (d_2), annulus inner to outer diameter ratio (d_1/d_2), rib height to the hydraulic diameter ratio ($e/(d_2-d_1)$), and rib pitch to height (π/e) ratio.

6.7. Conclusions

This work has demonstrated an effective optimization design approach for immobilized photocatalytic reactors, which combines CFD modeling and the Taguchi DOE method. The approach was applied for the case of annular reactors equipped with repeated ribs on the TiO_2-coated wall.

Under the utilized experimental conditions, the kinetic study of the photocatalytic degradation of 2,4-D followed pseudo-first-order kinetics with respect to 2,4-D concentration and presented a saturation-growth relationship with respect to the UV irradiance.

The experimental evaluation of the CFD model demonstrated its capability for giving proper predictions of the photocatalytic degradation of 2,4-D in immobilized annular photoreactors with plain and ribbed surfaces.

The preliminary CFD evaluation of external mass transfer enhancement elements revealed that the use of repeated ribs on the TiO_2-coated wall was more efficient than delta wing mixers.

The performed analysis showed that the performance of the studied annular photocatalytic reactors was improved using small values of *d2*, large d_1/d_2, intermediate $e/(d_2-d_1)$, and small π/e ratios. Among this parameters, $e/(d_2-d_1)$ was the one having the greatest impact on the reactor performance.

This study demonstrated that the application of CFD-modeling combined with the Taguchi method was effective for finding better reactor designs that improve the performance of immobilized photocatalytic systems.

6.8. Acknowledgments

The author acknowledges the Natural Sciences and Engineering Research Council of Canada (NSERC) for financial support and Alain Desprez for assisting with experimental and analytical work. J. Esteban Durán also thanks the support received from Universidad de Costa Rica.

6.9. References

Abe, K., Kondoh, T., & Nagano, Y. (1994). A new turbulence model for predicting fluid flow and heat transfer in separating and reattaching flows- I. Flow field calculations. *International Journal of Heat and Mass Transfer , 37* (1), 139–151.

Camera-Roda, G., Santarelli, F., & Panico, M. (2009). Study and optimization of an annular photocatalytic slurry reactor. *Photochemical & Photobiological Sciences , 8* (5), 712–718.

Cheng, W., Li, H., & Huang, C. (2008). Simulation and optimization of silicon thermal CVD through CFD integrating Taguchi method. *Chemical Engineering Journal , 137*, 603–613.

Cheng, Y., Xu, G., Zhu, D., Zhu, W., & Luo, L. (2006). Thermal analysis for indirect liquid cooled multichip module using computational fluid dynamic simulation and response surface methodology. *IEEE Transactions on components and packaging technologies , 29* (1), 39–46.

Chong, M. N., Jin, B., Chow, C. W., & Saint, C. P. A new approach to optimise an annular slurry photoreactor system for the degradation of Congo Red: Statistical analysis and modelling. *Chemical Engineering Journal , 152* (1), 158–166.

Duran, J.E., Mohseni, M., & Taghipour, F. (2010a). Modeling of annular reactors with surface reaction using computational fluid dynamics (CFD). *Chemical Engineering Science , 65*, 1201–1211.

Duran, J.E., Mohseni, M., & Taghipour, F. (2010b). CFD modeling of immobilized photocatalytic reactors for water treatment. *AIChE Journal , Submitted for publication*.

Duran, J.E., Taguipour, F., & Mohseni, M. (2010c). Evaluation of model parameters for simulating TiO_2 coated UV reactors. *Water Science and Technology: Water Supply* , In Press.

Fogler, H. S. (2006). *Elements of Chemical Reaction Engineering.* Upper Saddle River, NJ: Prentice Hall.

Frawley, P., & Geron, M. (2009). Combination of CFD and DOE to analyze and improve the mass flow rate in urinary catheters. *Journal of Biomechanical Engineering , 131*, 084501–1–084501–5.

Frawley, P., Corish, J., Niven, A., & Geron, M. (2009). Combination of CFD and DOE to analyse solid particle erosion in elbows. *International Journal of Computational Fluid Dynamics , 23* (5), 411–426.

Gharagheizi, F., & Sattari, M. (2009). Estimation of molecular diffusivity of pure chemicals in water: a quantitative structure-property relationship study. *SAR and QSAR in Environmental Research , 20* (3), 267–285.

Imoberdorf, G., Cassano, A., Irazoqui, H., & Alfano, O. (2007). Optimal design and modeling of annular photocatalytic wall reactors. *Catalysis Today , 129*, 118–126.

Jian-hui, Z., Chun-xin, Y., & Li-na, Z. (2009). Minimizing the entropy generation rate of the plate-finned heat sinks using computational fluid dynamics and combined optimization. *Applied Thermal Engineering , 29*, 1872–1879.

Kim, K.-Y., & Seo, J.-W. (2004). Shape optimization of a mixing vane in subchannel of nuclear reactor. *Journal of Nuclear Science and Technology , 41* (5), 641–644.

Modestov, A., & Lev, O. (1998). Photocatalytic oxidation of 2,4-dichlorophenoxyacetic acid with titania photocatalyst. Comparison of supported and suspended TiO2. *Journal of Photochemistry and Photobiology A: Chemistry , 112*, 261–270.

Perry, R. H., & Green, D. W. (1997). *Perry's Chemical Engineers' Handbook* (7th Edition ed.). New York: McGraw-Hill.

Romero, R., Alfano, O., & Cassano, A. (2003). Radiation Field in an Annular, Slurry Photocatalytic Reactor. 2. Model and Experiments. *Industrila and Engineering Chemistry Research , 42*, 2479–2488.

Roy, R. (1990). *A Primer on Taguchi Method.* New York: Van Nostrand Reinhold Int. Co. Ltd.

Taguchi, G. (1987). *System of Experimental Design.* New York: UNIPUB/Kraus International Publications.

Trillas, M., Peral, J., & Domenech, X. (1995). Redox photodegradation of 2,4-dichlorophenoxyacetic acid over Ti02. *Applied Catalysis B: Environmental , 5*, 377–387.

Vildozo, D., Ferronato, C., Sleiman, M., & Chovelon, J.-M. (2010). Photocatalytic treatment of indoor air: Optimization of 2-propanol removal using a response surface methodology (RSM). *Applied Catalysis, B: Environmental , 94*, 303–310.

Wang, Q., Chen, Q., & Zeng, M. (2009). A CFD-Taguchi combined method for numerical investigation of natural convection cooling performance of air-core reactor with noise reducing cover. *Numerical Heat Transfer, Part A: Applications , 55*, 1116–1130.

Webb, R., Eckert, E., & Goldstein, R. (1971). Heat transfer and friction in tubes with repeated-rib roughness. *International Journal of Heat and Mass Transfer , 14*, 601–617.

Yang, J.-T., Huang, K.-J., & Lin, Y.-C. (2005). Geometric effects on fluid mixing in passive grooved micromixers. *Lab on a Chip , 5*, 1140–1147.

7. CONCLUSIONS, CONTRIBUTIONS AND RECOMMENDATIONS FOR FUTURE WORK

7.1 Overall conclusions

A computational fluid dynamics (CFD) model for simulating immobilized photocatalytic reactors used for water detoxification was developed. For the model development, four fundamental phenomena that determine the physicochemical behaviour of the photoreactor (i.e., hydrodynamics, external mass transfer, surface chemical reactions, and UV-radiation field) were individually evaluated against experimental data and proper models were identified. The integrated CFD model was assessed in terms of its capability for predicting the photocatalytic degradation rate of benzoic acid and 2,4-D as model compounds and showed results in agreement with experimental data. Finally, the application of the developed model to the conceptual design of photocatalytic reactors was examined through an optimization approach that combined CFD modeling and the Taguchi design of experiments method.

The overall conclusions derived from this research are as follows:

Hydrodynamics and external mass transfer modeling in annular reactors

- The laminar model was able to predict successfully the mass transport in laminar flows, whereas the Abe-Kondoh-Nagano (AKN) low Reynolds number and the Reynolds stress (RSM) models predicted well the turbulent mass transfer in the analyzed annular reactors. A moderate underestimation at the entrance region where high turbulence and mass transfer rates take place was found.

- The core flow hydrodynamics predicted by the analyzed turbulence models (S *k*-ε, R *k*-ε, RSM and AKN) were in general agreement with previous PIV investigations of similar systems (Sozzi & Taghipour, 2006). However, important differences in the external mass transfer predictions among the models were found.
- Near-wall region modeling was found to have a large impact on surface mass transfer predictions. According to the results obtained in this study, it appears that the low-Reynolds-number approach simulates better the near-wall region than the two-layer approach employed in the enhanced wall treatment that is programmed in the commercial CFD code utilized in this investigation (Fluent).
- Although the L-shape (with the inlet parallel to the main reactor body) and U-shape (with the inlet normal to the main reactor body) annular reactor configurations presented different core flow distributions within the reactor volume, the mass transfer efficiency of both configurations were very similar. This fact indicated that in terms of mass transfer, there was no particular advantage for choosing one particular configuration over the other. However, if erosion of the surface material (e.g., catalyst) is an issue, the L-shape reactor might be a better option.
- Annular reactor models should include the reactor inlet sections since it was demonstrated that these play an important role in the reactor hydrodynamics, and consequently in its mass transfer performance.

Surface reaction modeling in annular reactors

- The performance of the hydrodynamic models in predicting the kinetic behaviour of a wall-coated annular reactor was found to be related to their efficacy to predict mass

transfer and consequently, the degree to which mass transfer limitation governs the system behaviour.

- The laminar model was able to predict the kinetic behaviour of the reactor under laminar flow conditions. For transient and turbulent flows, the performance of the turbulence models depended upon the degree to which the reacting system was limited by mass transfer. AKN and RSM exhibited good performance over the whole range of diffusion controlled conditions.

Irradiance modeling in annular reactors

- Goniometric far-field measurements showed that the predictions of isotropic-emission-based models (LSSE and ESVE) were in complete disagreement with the experimental data. Thus, these models are not recommended for far-field predictions. On the other hand, diffused emission models (LSDE and ESDE) predicted fairly well the irradiance distribution around the lamp. Moreover, incorporating reflection/refraction/absorption effects at the lamp quartz envelope to these diffused models allowed for even better irradiance predictions.
- Incorporating the high photon absorbance/re-emission effect produced by the Hg vapour inside the lamp to the ESVE model allowed predicting the diffused emission behaviour of the lamp. Moreover, adding reflection/refraction/absorption effects at the lamp quartz envelope resulted in a lamp emission model (ESVERA model) with excellent far- and near-field irradiance prediction capabilities.

- Near-field evaluation revealed that the radiation emission pattern (isotropic or diffused) has little effect on the irradiance prediction close to the lamp. However, important differences were observed for the fluence rate predictions.
- The surrounding temperature of lamps operating inside of quartz sleeves was found to have a strong effect on the lamp power outputs. For this reason, to perform accurate CFD simulations, it is essential to obtain and use a real estimate of the lamp power output under the actual operating conditions in the reactor. Methods such as the ones developed by Robinson (2007) or the one used in this study are recommended.

Integrated CFD model for simulating immobilized photocatalytic reactors

- The experimental evaluation of the integrated CFD model demonstrated its capability for giving proper predictions of the photocatalytic degradation of contaminants in immobilized annular photoreactors with plain and ribbed surfaces.
- Because the degradation rate of pollutants in the analyzed photoreactors was normally limited by the rate of mass transport in the system, the performance of CFD model was strongly determined by the external mass transfer prediction capability of the hydrodynamic models used. Hence, the CFD model showed accurate predictions of the photocatalytic reactor performance when the laminar flow model (for laminar flow conditions), and the AKN or RSM turbulence models (for transitional and turbulent flow conditions) were applied.
- Under the utilized experimental conditions, the photocatalytic degradation of BA followed pseudo-first-order kinetics with respect to both BA concentration and UV irradiance. Even though the obtained reaction kinetic expression did not necessary

correspond to intrinsic kinetics (the presence of internal mass transfer resistance in the photocatalyst coating was not verified), this expression is specific to the composite sol-gel TiO_2 coating, initial BA concentration, and dissolved oxygen concentration utilized in this study (Camera-Roda & Santarelli, 2007; Chen, et al., 2000; Edwards, et al., 1996; Herz, 2004). This rate expression is expected to be applicable to other reactors as long as these variables remain similar to those in this work.

- Under the utilized experimental conditions, the kinetic study of the photocatalytic degradation of 2,4-D followed pseudo-first-order kinetics with respect to 2,4-D concentration and presented a saturation-growth relationship with respect to the UV irradiance.

CFD-Taguchi combined method for optimizing photocatalytic reactors

- This research demonstrated that combining CFD-modeling with the Taguchi method is an effective approach for finding better reactor designs that improve the performance of immobilized photocatalytic systems.
- The CFD evaluation of external mass transfer enhancement elements revealed that the use of repeated ribs on the TiO_2-coated wall was more efficient than delta wing mixers.
- The statistical analysis showed that the performance of the studied annular photocatalytic reactors was improved using small outer tube diameters, large inner/outer tube diameter ratios, intermediate (rib height)/(hydraulic diameter) ratio, and small (rib pitch)/(rib height) ratios. Among these parameters, the (rib height)/(hydraulic diameter) ratio was the design parameter having the greatest impact on the photoreactor performance.

7.2. Significance and contributions of the research

Although purification of contaminated water by means of heterogeneous photocatalysis has demonstrated to be a promising technology, the development of commercial systems has not yet been successfully achieved. The development of such a commercial system would be of a great benefit to water treatment industry, since (i) photocatalysis is capable of degrading and even completely mineralizing the organic contaminants present in water without the production of any significant by-products or waste streams; (ii) the process is capable of inactivating pathogens including protozoa and viruses; and (iii) such a system would be a process with no consumable chemicals required (Mills et al., 1993; Ollis et al., 1991).

The model developed in this research is a robust CFD-based model capable of simulating heterogeneous photocatalytic reactors comprising of photocatalyst-coated surfaces used in water treatment applications. This model can be utilized as an engineering tool for the design, scale-up, and optimization of photocatalytic reactors. CFD simulations can give invaluable information about the performance of the photoreactor prior to the final experimental validation, and can minimize experimental effort and fabrication costs at the pilot-scale level (Adesina, 2004). Undoubtedly, the development of this model will significantly contribute to the research and development activities being done towards the implementation of such large-scale commercial photocatalytic treatment systems.

Another important contribution of this research was the approach undertaken for the model development. For developing the integrated CFD model, each of the fundamental phenomena that determine the photocatalytic degradation performance of the photoreactor was individually evaluated against experimental data and proper models were identified. This

approach brought robustness to the integrated model and allowed better understanding of the model performance and capabilities.

In addition to the contribution made to the field of water treatment applications, the findings obtained in this research can also be applied in other industrial fields. For example, the hydrodynamic turbulence models (AKN and RSM) identified to accurately predict external mass transfer can be apply in the simulation of other reactor configurations including tube wall reactors, membrane reactors, electrochemical reactors, and dialyzers; moreover, they can be used in wall-liquid heat transfer applications. The CFD-based lamp emission model (ESVERA) developed in this investigation can be easily applied in CFD simulations of any type of photoreactors utilized in areas such as UV disinfection, UV-based advanced oxidation processes, and photochemical reactors.

7.3. Recommendations for future work

- Experimental evaluation of the model using other reactor geometries and a larger range of highly turbulent operating conditions is desirable to further validate its applicability.
- Since most of the immobilized photocatalytic reactors operate under mass transfer limited conditions, several mass transfer enhancement techniques have been proposed for improving the pollutant degradation performance. Such techniques include the use of swirling (Shoukry & Shemilt, 1985), Taylor-Couette (Sengupta et al., 2001), and multi-phase (Trujillo et al., 2009) flows. It would be benefitial to expand the CFD-based model to the simulation of these types of systems. For this, finding of proper hydrodynamic models and multiphase modeling approaches is required.

- The CFD-Taguchi combined method presented in this investigation should be further utilized for obtaining improved reactor designs. The optimization of size, shape, and location of turbulence promoters inside the reactors should be carried out further. Other design of experiments methods (e.g., surface response method) can be utilized as well.
- The application of the developed radiation field model (using ESVERA lamp emission model) in multi-lamp photoreactors should be assessed.
- The applicability of the developed CFD-based model should be further evaluated for the simulation of photocatalytic reactors that utilize polychromatic radiation sources (medium pressure UV lamps).
- The incorporation of volumetric degradation processes to the CFD model is desirable. In this way, photoreactors with combined advanced oxidation processes (e.g., photocatalysis + H_2O_2/UV + Vacuum UV) could be simulated and optimized.
- The application of the CFD model for simulating reactors treating "real" contaminated water.

7.4. References

Adesina, A. (2004). Industrial exploitation of photocatalysis: progress, perspectives and prospects. *Catalysis Surveys from Asia , 8* (4), 265–273.

Camera-Roda, G., & Santarelli, F. (2007). Optimization of the thickness of a photocatalytic film on the basis of the effectiveness factor. *Catalysis Today , 129*, 161–168.

Chen, D., Li, F., & Ray, A. (2000). Effect of Mass Transfer and Catalyst Layer Thickness on Photocatalytic Reaction. *AIChE Journal , 46* (5), 1034–1045.

Edwards, M., Villa, C., C.G. Hill, J., & Chapman, T. (1996). Effectiveness Factors for Photocatalytic Reactions Occurring in Planar Membranes. *Industrial & Engineering Chemistry Research , 35*, 712–720.

Herz, R. (2004). Intrinsic kinetics of first-order reactions in photocatalytic membranes and layers. *Chemical Engineering Journal , 99*, 237–245.

Mills, A., Davies, R.H., & Worsley, D. (1993). Water Purification by Semiconductor Photocatalysis. *Chemical Society Reviews , 22* (6), 417–425.

Ollis, D. F., Pelizzetti, E., & Serpone, N. (1991). Photocatalyzed destruction of water contaminants. *Environmental Science & Technology , 25* (9), 1522–1529.

Robinson, J. (2007). Determination of the output of a UV lamp running in a quartz sleeve submerged in water. *World Congress on Ozone and Ultraviolet Technologies.* Los Angeles: International Ozone Association and International Ultraviolet Association.

Sengupta, T.K., Kabir, M.F., & Ray, A.K. (2001). A Taylor vortex photocatalytic reactor for water purification. *Industrial & Engineering Chemistry Process Design and Development*, *40*, 5268–5281.

Shoukry, E., Shemilt, L.W. (1985) Mass transfer enhancement in swirling annular pipe flow. *Industrial & Engineering Chemistry Process Design and Development*, *24*(1), 53–6.

Sozzi, D., & Taghipour, F. (2006). Computational and experimental study of annular photo-reactor hydrodynamics. *International Journal of Heat and Fluid Flow , 27* (6), 1043–1053.

Trujillo,F.J., Safinski, T., & Adesina, A.A. (2009). Solid–liquid mass transfer analysis in a multi-phase tank reactor containing submerged coated inclined-plates: A computational fluid dynamics approach. *Chemical Engineering Science*, *42*, 1143–1153.

APPENDIX A. EVALUATION OF MODEL PARAMETERS FOR SIMULATING TiO_2 COATED UV REACTORS [6]

A.1. Introduction

Heterogeneous photocatalysis is a particularly emerging and promising technology for water purification (Andesina, 2004; Herrmann, 2005). Photocatalytic oxidation processes involve the use of oxygen and nano-structured photocatalyst materials, predominantly titanium dioxide (TiO_2), activated by ultraviolet (UV) irradiation. The appeal of this technology for drinking water treatment lies mostly in its capability to potentially mineralize the pollutants, in addition to inactivating pathogens including protozoa and viruses. However, despite the many advantages of this technology and the extensive research done in this field, the development of large scale commercial photocatalytic oxidation reactors has not yet been materialized. Lack of proper models and simulation tools for predicting and analyzing the performance of full-scale systems, and therefore lack of adequate scale-up strategies, is among the key factors hindering the development of commercial water treatment systems utilizing this technology (Mukherjee & Ray, 1999; Adesina, 2004).

Development of models for predicting the behaviour of heterogeneous photocatalytic reactors is a complicated task. The complex interactions among transport processes, reaction kinetics, and radiation absorption lead to a strong coupling of physicochemical phenomena (Periyathamby & Ray, 1999). To model photocatalytic reactors, the conservation equations of momentum, mass and species, as well as the radiative transfer equation (RTE) should be solved (Cassano et al., 1995; Taghipour & Mohseni, 2005). This requires proper definition and incorporation of appropriate turbulence models for the hydrodynamics and mass transfer,

[6] A version of this chapter has been accepted for publication. Duran, J.E., Taghipour, F., & Mohseni, M. (2010). Evaluation of model parameters for simulating TiO_2 coated UV reactors. Water Science and Technology: Water Supply (in press).

ultraviolet (UV) radiation field model, and the intrinsic kinetics of the surface reactions in the photoreactor.

Computational Fluid Dynamics (CFD) has extensively demonstrated to be a very effective tool for the simulation of reacting systems (Kuipers & van Swaaij, 1998). In the field of photocatalysis, Pareek et al. (2003) simulated a suspended TiO_2 pilot-scale annular bubble column photocatalytic reactor, solving the RTE with a finite-volume-based discrete ordinate method. The simulated and experimental data showed good agreement indicating the applicability of the developed model in such systems. More recently, Trujillo et al. (2007) reported a study on the CFD analysis of the radiation distribution in an immobilized catalyst bubble column, externally illuminated photoreactor. The study showed that gas bubbling considerably increased the fluence rate in the gas-liquid mixture enhancing the absorbed radiation on the TiO_2-coated plates. Unfortunately, no experimental evaluation was done in the investigation.

CFD has also been successfully used for the simulation of photocatalytic reactors for air treatment. Mohseni & Taghipour (Mohseni & Taghipour, 2004; Taghipour & Mohseni, 2005) simulated and experimentally evaluated an annular photocatalytic reactor treating chlorinated VOCs. The information obtained could result in reactor design modification and performance improvement. Castrillón et al. (2006) made a flow field investigation in a photocatalytic reactor for air treatment and identified several design issues in the original unit. More recently, Salvadó-Estivill et al. (2007) presented a methodology for the evaluation of the intrinsic photocatalytic oxidation kinetics of indoor air pollutants. The method proposes the development of a rigorous CFD-based model that allow for deriving kinetic parameters directly from experimental kinetic data. In their article, they exemplified the use of this methodology for the case of the oxidation of trichloroethylene.

In the case of immobilized photocatalytic reactor for water treatment, to the best of our knowledge, there is only one study that reports CFD simulation analysis for this kind of system (Periyathamby & Ray, 1999). However, the publication neither offers much information about the CFD model (boundary conditions, radiation model, mesh quality, etc.), nor evaluates the simulation results against experimental data.

Most of the previous studies about CFD simulation of photocatalytic reactors have as common shortcoming the lack of experimental validation of their models. This research has focused on the development of a CFD-based model based entirely on experimental and/or analytical evaluation. The model includes aspects of hydrodynamics, mass transfer, UV radiation field and surface chemical reaction.

A.2. Methodology

A.2.1. Individual component evaluations

The development of a successful CFD-based model for simulating TiO_2 coated photoreactors relies on the proper definition of the models representing various phenomena affecting the rector performance (i.e. hydrodynamics, mass transfer, UV radiation field and surface chemical reaction). In this research, models were individually analyzed and analytically and/or experimentally evaluated for the individual phenomena involved in the photocatalytic reactors. In this way, the proper models can be defined and finally combined into an integral CFD model capable of modeling the performance of immobilized photocatalytic reactors. The commercial CFD package Fluent® (V6.2.16) was used to perform the simulations.

Three different hydrodynamic models (Laminar Model (Lam), Reynolds Stress Model (RSM) and Realizable *k*-ε Model (R *k*-ε)) (Fluent-Inc., 2005) were evaluated in terms of their mass transfer modeling capabilities. Mass transfer experiments were conducted in a differential reactor equipped with 25 mm wide glass slides coated with benzoic acid. Fig. A.1 shows the schematic of the reactor used, which consisted of a 63-mm-wide aluminum reactor designed to allow water to flow through a 225 mm long passage of 25 mm (width) and 3 mm (height), and over the coated glass plates. The reactor was covered by a clear acrylic plate. The glass slides were coated by dipping them into molten benzoic acid. On contact with the glass slides, the benzoic acid immediately solidified, yielding a uniform layer of the organic acid on the slide. The operation of the system involved injecting a flow of clean water into the reactor causing the dissolution of the slightly soluble acid into the bulk fluid. The average mass transfer coefficients of the system under different hydrodynamic conditions ($420<Re<5,300$) and at 25°C were determined by measuring the concentrations of dissolved benzoic acid in the outlet stream once steady state was reached. The concentration of benzoic acid was determined via a UV spectrophotometer (UV-Mini 1240, Shimadzu) at 231 nm. CFD simulations of the studied system were performed utilizing the three different hydrodynamic models and a comparison of modeling prediction of mass transfer with the experimental results was made.

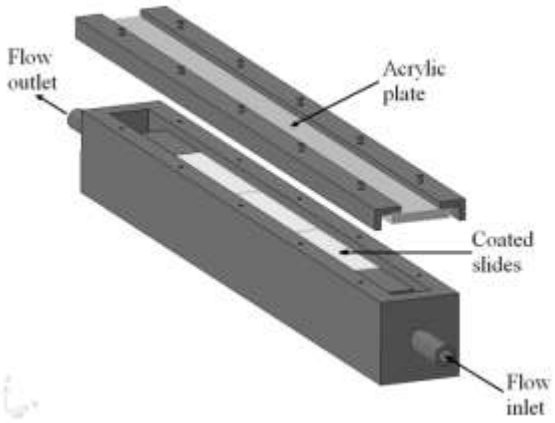

Fig. A.1. Schematic of the differential reactor used in the mass transfer experiments

The analysis of radiation field modeling involved solving the RTE using the finite-volume (FV) discrete ordinate (DO) method (included in Fluent®) and its comparison against an analytical solution of a simple emission source case. Some of the advantages of the FV-DO method are that it automatically allows the conservation of radiant energy and that the RTE is integrated over both the control angle and the control volume (Pareek & Adesina, 2004; Fluent-Inc., 2005). The radiation field generated from an emitting disc (diameter=10cm and radiant emittance=10 W/m^2) was analytically solved and numerically estimated for points along a perpendicular axis from the center of the disc. The transmitting medium was considered homogeneous, with no scattering or emission, but different absorption coefficients (a) were studied. Simulations of the analyzed system were performed and compared with the analytical results.

A first order heterogeneous reaction (not photocatalytic) taking place on the wall of a tubular reactor was simulated, under laminar flow regime, applying the surface reaction model available in Fluent (Fluent-Inc., 2005). The results of the simulation were compared with analytical solution found in the literature (Gill et al., 1975).

A.2.2. Integrated CFD simulation and experimental evaluation

Finally, a CFD model that integrated the hydrodynamics, mass transfer and surface chemical reaction models was evaluated experimentally using the same differential reactor shown in Fig. A.1. However, for this stage the acrylic plate and the benzoic acid coated glass slides were substituted by a diffused quartz plate and a composite nano-size sol-gel TiO_2 (Keshmiri et al., 2004) coated slides, respectively. The reactor was irradiated by two low-pressure monochromatic mercury UV lamps (5.7 W of UV-output at 254 nm) mounted under an aluminum reflector. The lamp centerlines were located 45 mm above the quartz plate and 20 mm away from each other. The differential reactor was set up in a constantly aerated and recirculated reacting system as shown schematically in Fig. A.2. Formic acid (FA) was chosen as the model pollutant for the degradation studies and its concentration was determined via a Total Organic Carbon (TOC) analyzer (ASI-VCPH TOC, Shimadzu). Experimental runs at different flow rates allowed for determining the intrinsic kinetics of the photocatalytic degradation of FA (at constant UV irradiation and dissolved oxygen concentration). In these runs, the FA concentration (2.5 mM initial concentration) was monitored for a period of three hours, in which a final conversion of at least 50% was achieved. The reaction rate constants for each set of experimental conditions were estimated by fitting the concentration-time data using an optimization method for non-linear parameter estimation in ordinary differential equation models (Gauss-Newton). Also, the results were compared with those of simulation using the integrated CFD model.

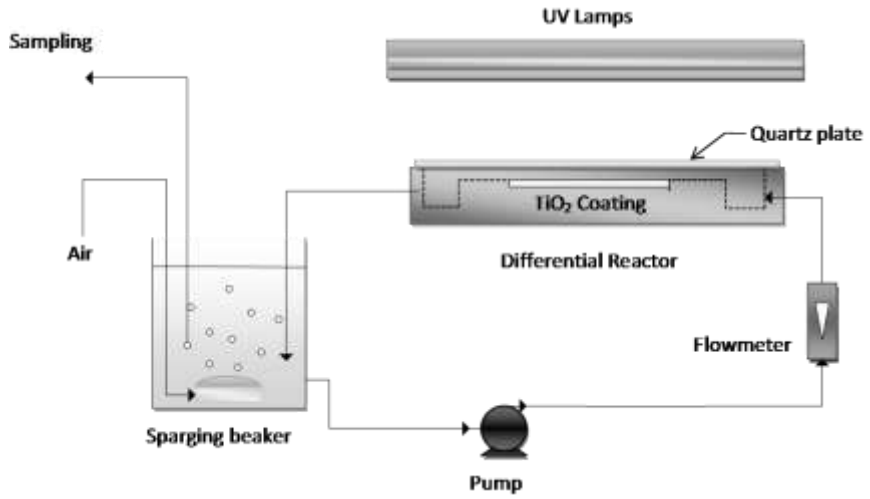

Fig. A.2. Schematic of the recirculated batch reactor used in the photocatalytic degradation studies of formic acid.

A.3. Results and discussion

A.3.1. Evaluation of the hydrodynamic models for mass transfer modeling

The data generated in the experiments performed with the differential reactor equipped with the glass slides coated with benzoic acid were used to calculate the average mass transfer coefficients (k_c) of the system. The mass transfer coefficients, presented in Fig. A.3, were calculated by computing a mass balance over the system. As expected, the experimental average mass transfer coefficients increased with increasing the flow rate over the studied range. It is important to note that the range analyzed covered the hydrodynamic conditions corresponding to the laminar, transition, and turbulent regimes. CFD simulations of the system were carried out using the three studied hydrodynamic models (Lam, R k-ε and RSM) and the results are also presented in Fig. A.3. Good agreement was obtained for the data with Re<2,000 or >5,000, i.e. those flows that were either in completely laminar or in completely

turbulent regime. These results were expected since the turbulence models studied (RSM and R *k*-ε) are applicable only when modeling completely turbulent flows. Since both turbulence models predicted accurately the mass transfer coefficient of the experimental runs under turbulent flow regime, the use of any of them in the integrated CFD simulation tool is supported. In a separate study, further research has been performed utilizing other turbulence models, reactor configurations and geometries, as well as a wider range of flow rates, for obtaining more comprehensive conclusions on the performance of turbulence models for predicting liquid-wall mass transfer (Duran, et al., 2009).

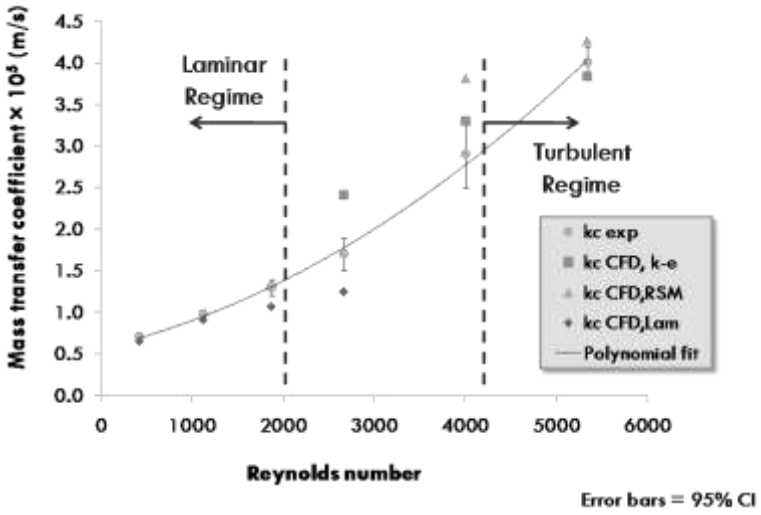

Fig. A.3. Average mass transfer coefficients (k_c) of benzoic acid in the differential reactor: experimental and simulation results.

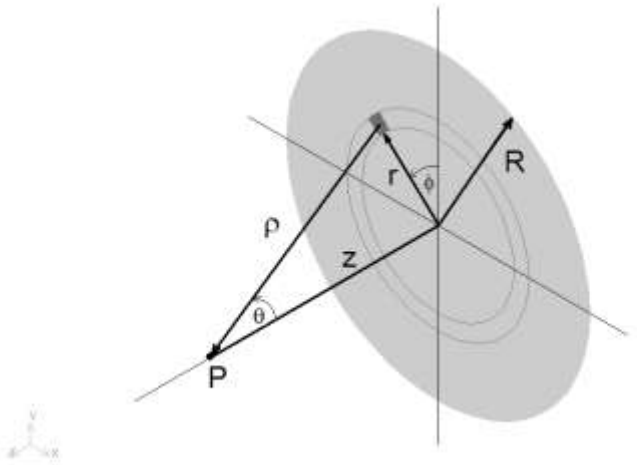

Fig. A.4. Geometry of definition for the calculation of the fluence rate in a point located perpendicular to the center of an emitting disc.

A.3.2. Evaluation of the FV-DO method with the analytical solution of an emitting disc

The fluence rate (G) in a point P located at a distance z perpendicular to the center of a radiation emitting disc (see Fig. A.4) can be calculated as follows. By definition, the fluence rate can be computed as (Cassano et al., 1995):

$$G = \int_{\Omega=4\pi} I \, d\Omega = \int_{\phi}\int_{\theta} I \sin\theta \, d\theta \, d\phi \tag{A.1}$$

where I is the specific intensity, Ω is the solid angle, and θ and ϕ are spherical coordinates. To calculate the contribution of an infinitesimal element of the disc located at a distance ρ from point P to the total fluence rate, this element can be considered as a point source emitter. The intensity coming from a point source emitter in a transmitting and absorbing medium (homogeneous, with no scattering or emission) decays exponentially with the distance as:

$$I = I_0 e^{-a\rho} \tag{A.2}$$

where I_0 is the specific intensity at the source and a is the absorption coefficient of the medium. Combining Eqs. (A.1) and (A.2), defining the integration limits, and recognizing that $\rho = z/\cos\theta$, the following is obtained for the fluence rate:

$$G = \int_{\phi=0}^{2\pi} \int_{\theta=0}^{\arctan(R/z)} I_0 e^{-\frac{a z}{\cos\theta}} \sin\theta \, d\theta \, d\phi \tag{A.3}$$

The solution of Eq. (A.3) is:

$$G = 2\pi I_0 \left[-e^{-a z \sec(\arctan(R/z))} \cos(\arctan(R/z)) - a z E_i(-a z \sec(\arctan(R/z))) + e^{-a z} + a z E_i(-a z) \right] \tag{A.4}$$

where E_i is the exponential integral function. Using Eq. (A.4), and computing the exponential integral function with a power series, the fluence rate values of the radiation field along the centered perpendicular axis are estimated. Fig. A.5 presents the results of the analytical solution compared with the simulated fluence rates using the finite-volume DO method available in the CFD software. For the three absorption coefficients of the medium that were analyzed, there was an excellent agreement between the analytical and simulation results, demonstrating the promising potentials of the finite-volume DO method in the CFD-based simulation tool being developed.

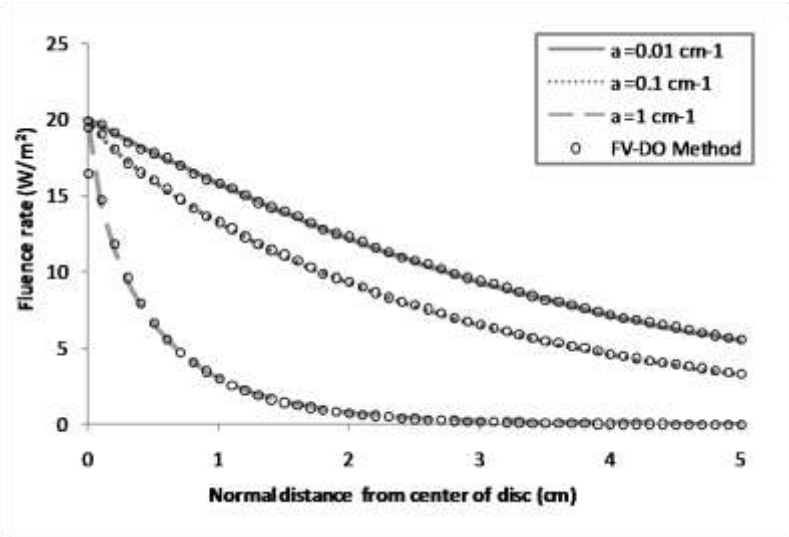

Fig. A.5. Fluence rates along the perpendicular axis from the center of an emitting disc in a transmitting medium with different absorption coefficients (*a*).

A.3.3. Evaluation of surface reaction model with an exact solution

Gill et al. (1975) obtained an exact solution for the concentration profiles in laminar flow reactors with first-order reactions at the wall. The solution reported by Gill et al. (1975) were compared with the results of CFD simulations for the specific case of β=10, X=0.03 and X=0.1. These parameters are defined as

$$\beta = \frac{k_s R}{D} \tag{A.5}$$

$$X = \frac{D\,x}{R^2\,u_0} \tag{A.6}$$

where k_s is the reaction rate constant per unit surface, R is the radius, D is the molecular diffusion coefficient, x is the axial coordinate, and u_0 is the axial velocity at the centerline of the tube. As it can be seen in Fig. A.6, the exact solution results and the CFD simulations showed excellent agreement.

More research on the evaluation of the surface reaction model under laminar, transitional and turbulent flow regime has been presented elsewhere (Duran, et al., 2010).

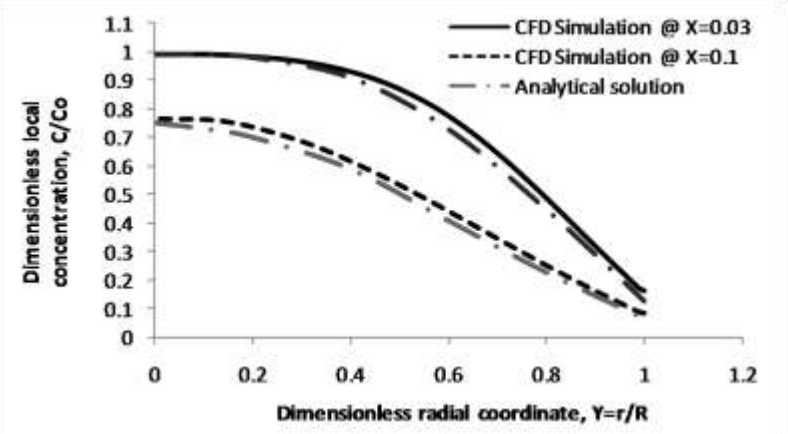

Fig. A.6. Radial distributions of dimensionless local concentration at dimensionless axial distances X=0.03 and 0.1 with β=10 in a wall tubular reactor.

A.3.4. Evaluation of the integrated CFD model simulating an immobilized photocatalytic reactor

CFD simulations of the UV-radiation field in the system utilized in the experiments demonstrated that the irradiance over the quartz plate (and consequently over the coated slides) is fairly uniform. Fig. A.7 shows the results obtained using the superficial emission model (Cassano et al., 1995) as boundary condition for the tubular lamps. The average value of irradiance computed for the analyzed area was 107 W/m^2 with deviations no greater than 10%. Based on these results and considering 5% of radiation loss due to reflection in the quartz plate, the irradiance across the whole photocatalytic area was assumed constant at 102 W/m^2 (2.17×10^{-4} Einstein s^{-1} m^{-2}).

Fig. A.7. UV irradiance (W/m^2) computed by the CFD simulation on the quartz plate above the catalyst-coated slides.

For determining the intrinsic kinetics of the immobilized photocatalytic reaction, it was necessary to make sure that the reaction was not affected by mass transfer limitation. In this sense, several experimental runs using different flow rates were made to find proper operating conditions. It was found that at Re > 2,600 no mass transfer limitation existed in the system and under those conditions, pseudo-first-order kinetics with an intrinsic surface reaction rate constant of 8.51×10^{-6} m/s (equivalent to 0.17 min^{-1}) was determined. This result is in accordance with the literature since photocatalytic reactions of diluted solutions are commonly reported to have pseudo-first-order kinetics (Herrmann, 2005). Since the irradiance over the photocatalyst was assumed constant, so as the dissolved oxygen concentration in the solution, the kinetic rate equation of the surface photocatalytic oxidation of FA ($-r''_{FA}$) was considered to depend only on the concentration of FA (C_{FA}) according to:

$$-r''_{FA} = 8.51\times10^{-6} m/s \cdot C_{FA} \qquad \text{(A.7)}$$

Utilizing Eq. (A.7) as boundary condition at the photocatalyst coated surface, CFD simulations of the differential reactor operating under the same hydrodynamic conditions of the experimental runs were performed. Fig. A.8 shows the contours of the mass fraction of

formic acid at the photocatalyst surface as computed with different hydrodynamic models. The results present higher concentration decrease of FA along the photocatalyst-coated slides as Re decreases in the system. This behaviour can be explained as a result of the longer contact time of the fluid with the photocatalytic surface. Also, three peaks in the transversal profile of FA concentration along the catalyst plates are noticeable in all the simulations performed. These higher concentration regions are consequence of higher fluid velocity gradients in these zones. This condition was verified through analysis of the velocity field in the system which showed a recirculation zone at the channel entrance that induces these three high velocity gradient regions in the flow distribution.

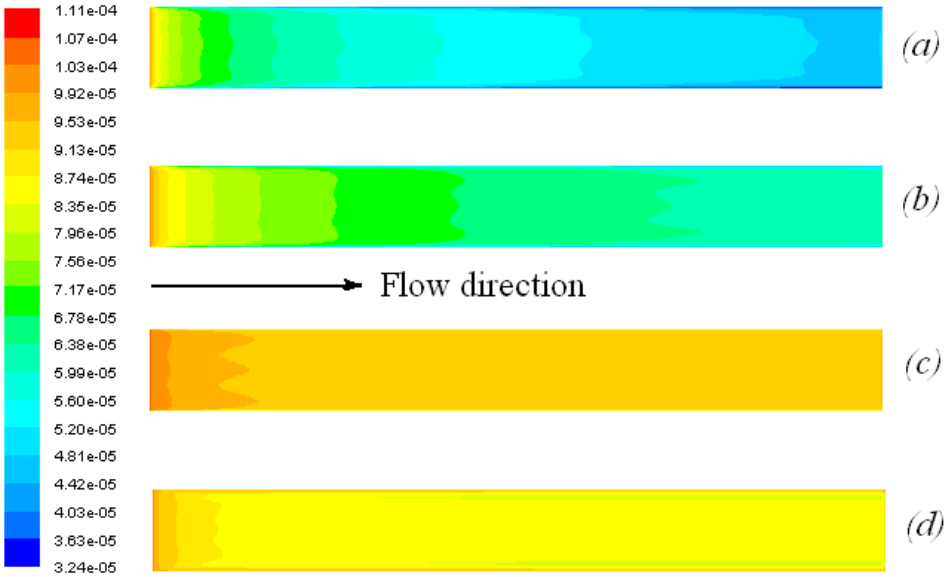

Fig. A.8. Contours of the mass fraction of formic acid at the photocatalyst surface as computed with different hydrodynamic models for the system operating at various Re numbers: (a) Laminar model at Re=422, (b) Laminar model at Re=1123, *(c)* R *k*-ε at Re=5337, *(d)* RSM at Re=5337.

By knowing the experimental rate constant (apparent or intrinsic) of a first-order reaction taking place in the differential reactor it is possible to estimate the conversion (ξ) for one pass in the reactor using:

$$\xi = 1 - e^{-k\tau} \tag{A.8}$$

where k is the volumetric reaction rate constant and τ is the space time (defined as the volume of reactor coated with catalyst divided by the volumetric feed rate of reactants). In this way, the conversions for one pass for the experimental runs performed were estimated and are reported in Table A.1. These values are compared with the corresponding conversions per pass computed by the CFD simulations. As reported in Table A.1, the relative difference between the results for the case of laminar flow is minimal, whereas in the case of turbulent flow it is in the order of 10% for both turbulence models.

Table A.1. One-pass experimental conversion estimations versus CFD-based model predictions

Re	k (min^{-1})	Hydrodynamic model	Experimental conversion of FA (%)	CFD computed conversion of FA (%)	Relative error (%)
422	0.109	Lam	0.580	0.561	3.3
1123	0.125	Lam	0.251	0.246	2.0
5337	0.170	R k-ε	0.072	0.063	12.5
5337	0.170	RSM	0.072	0.066	8.3

A.4. Conclusions

- In terms of mass transfer modeling capabilities, the analyzed hydrodynamic models performed well. It was also evident that these models do not perform well simulating fluids under transition flow regime.

- The FV-DO demonstrated promising potentials for being used for simulating radiation distribution in photocatalytic reactors; nevertheless, further evaluations with experimental data are needed.
- The photocatalytic degradation of formic acid followed pseudo-first order kinetics under the operating conditions used in this investigation.
- The CFD simulations of the immobilized photoreactor showed good agreement with analytical and experimental results.
- The approach presented here was demonstrated to be an effective way for integrating a CFD model for simulating immobilized photocatalytic reactors.

A.5.References

Adesina, A. (2004). Industrial exploitation of photocatalysis: progress, perspectives and prospects. *Catalysis Surveys from Asia, 8* (4), 265-273.

Cassano, A. E., Martin, C. A., Brandi, R. J., & Alfano, O. M. (1995). Photoreactor Analysis and Design: Fundamentals and Applications. *Industrial & Engineering Chemistry Research, 34*, 2155-2201.

Castrillón S., R.-V., Ibrahim, H., & de Lasa, H. (2006). Flow field investigation in a photocatalytic reactor for air treatment (Photo-CREC-air). *Chemical Engineering Science, 61*, 3343 – 3361.

Duran, J. E., Taghipour, F., & Mohseni, M. (2009). CFD modeling of mass transfer in annular reactors. *International Journal of Heat and Mass Transfer, 52*, 5390-5401.

Duran, J. E., Mohseni, M., & Taghipour, F. (2010). Modeling of annular reactors with surface reaction using computational fluid dynamics (CFD). *Chemical Engineering Science, 65*, 1201-1211.

Fluent-Inc. (2005). *FLUENT 6.2 User's Guide*. Lebanon, NH.

Gill, W. N., Ruckenstein, E., & Hsieh H. P. (1975). Homogeneous models for porous catalysts and tubular reactors with heterogeneous reactions. *Chemical Engineering Science, 30*(7), 685-694.

Herrmann, J. (2005). Heterogeneous photocatalysis: state of the art and present applications. *Topics in Catalysis, 34* (1-4), 49-65.

Keshmiri, M., Mohseni, M., & Troczynski, T. (2004). Development of novel TiO_2 sol-gel-derived composite and its photocatalytic activities for trichloroethylene oxidation. *Applied Catalysis B: Environmental, 53*, 209-219.

Kuipers, J. A., & Van Swaaij, W. P. (1998). Computational fluid dynamics applied to chemical reaction engineering. *Advances in Chemical Engineering, 24*, 227-328.

Mohseni, M., & Taghipour, F. (2004). Experimental and CFD analysis of photocatalytic gas phase vinyl chloride (VC) oxidation. *Chemical Engineering Science, 59*(7), 1601-1609.

Mukherjee, P. S., & Ray, A. K. (1999). Major Challenges in the Design of a Large-Scale Photocatalytic Reactor for Water Treatment. *Chemical Engineering & Technology, 22*(3), 253-260.

Pareek, V. K., Cox, S. J., Brungs, M. P., Young, B., & Adesina, A. A. (2003). Computational fluid dynamic (CFD) simulation of a pilot-scale annular bubble column photocatalytic reactor. *Chemical Engineering Science*, *58* (3-6), 859-865.

Pareek, V. K., & Adesina, A. A. (2004). Light intensity distribution in a photocatalytic reactor using finite volume. *AIChE Journal*, *50*(6), 1273-1288.

Periyathamby, U., & Ray, A.K. (1999). Computer Simulation of a Novel Photocatalytic Reactor Using Distributive Computing Environment. *Chemical Engineering & Technology*, *22*, 881-888.

Salvado-Estivill, I., Hargreaves, D.M., & Li Puma G. (2007). Evaluation of the Intrinsic Photocatalytic Oxidation Kinetics of Indoor Air Pollutants. *Environmental Science & Technology*, *41* (6), 2028-2035.

Taghipour, F., & Mohseni, M. (2005). CFD Simulation of UV Photocatalytic Reactors for Air Treatment. *AIChE Journal*, *51*(11), 3039-3047.

Trujillo, F. J., Safinski, T., & Adesina A.A. (2007). CFD Analysis of the Radiation Distribution in a New Immobilized Catalyst Bubble Column Externally Illuminated Photoreactor. *Journal of Solar Energy Engineering*, *129*, 27-36.